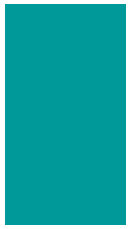# Enhancing the Structural Stability of α-phase Hybrid Perovskite Films through Defect Engineering Approaches under Ambient Conditions

ADAM URWICK

Thesis Submitted for a PhD in New and Sustainable Photovoltaics

The Department of Chemical and Biological Engineering

April 2023

Executive Summary

This thesis investigates methods whereby perovskite solar cell power conversion efficiency and material stability may be improved. Hybrid perovskites have gained increased attention for optoelectronic applications due to favourable properties such as strong absorption, facile processing, and changeable band-gap. Despite excellent improvements in power conversion efficiency of devices, perovskite films are unstable, degrading with relative ease in the presence of moisture, oxygen, light, heat, and electric fields. The focus of this thesis is on ambient atmosphere stability, concerned with the influence of moisture in particular on perovskite film fabrication, degradation, and device functionality. In order to shed light on the impact of ambient atmosphere on perovskite films, experiments are designed to investigate films during fabrication and degradation. The influences firstly of stoichiometry during ambient fabrication, and then ionic substitution (with caesium and formadinium) upon moisture-induced degradation are investigated. Finally, films and devices with a novel composition incorporating Zn are fabricated under ambient conditions to investigate the effect of Zn addition on perovskite film stability.

The reader is primed in broad terms on perovskites solar cells, giving a grounding in solar cell operation, the perovskite crystal structure, solution processing for perovskite films and various aspects of degradation and instability. The Experimental and Theoretical Methods portion outlines the experimental methods used, including both solution and sample preparation, and characterisation methods. The theory underpinning characterisation methods is discussed, and analytical methodologies are discussed and justified on the basis of these theoretical understandings, with particular emphasis on time-of-flight grazing incidence small angle neutron scattering and wide angle X-ray scattering.

In the results section, findings are presented and discussed, addressing the questions raised in the aims and objectives. Each results chapter is presented in a pseudo paper style allowing an informed reader to broadly engage with them as standalone texts (besides references to fabrication and characterisation methods used).

Novel understanding is produced regarding the influence of methylammonium iodide on the formation of the crystalline solvent-intercalated intermediate in ambient conditions, and methylammonium lead triiodide devices comparable to the literature are fabricated under all-ambient conditions (from solution to solar cell).

Neutron Scattering experiments reveal exceptional resistance to phase segregation in formamidinium rich perovskites containing caesium as an A-site substitution cation, exposed to moisture in the dark. Results also suggests more rapid degradation of perovskite films occurring in the bulk as opposed to the surface of the film, supporting theories of moisture induced decomposition being initiated in the bulk.

Studies into the incorporation of zinc chloride and caesium iodide into methylammonium lead triiodide perovskite films under ambient conditions reveals the formation of several secondary phases, exacerbated by exposure to moisture, O_2, light and heat, and concentrated at the surface. The presence of these phases is then associated with higher thermal instability in these films compared to regular methylammonium lead triiodide films, despite improved moisture resilience.

It is found that:

1. MAI addition enhances the DSMO-intercalated solvent formation rate, leading to the formation of larger crystalline intermediate domains during spin-coating in ambient atmosphere.
2. Results provide evidence indicative of mixed FA rich perovskite-hydrates forming in a humid atmosphere. They also show reduction of humidity induced phase segregation in Cs containing perovskites.
3. Evidence of the deleterious effect of $ZnCl_2$ additive on $MAPbI_3$ thermal stability when used as an additive in film formation under ambient conditions.

— Adam Urwick

Contents

5

List of Figures

List of Tables

Introduction to Perovskite Solar Cells

1 Background

1.1 Motivation

This thesis builds upon ongoing investigations into a class of materials with high potential for photovoltaic applications; perovskite solar cells (PSCs). Photovoltaics are seen as an integral technology in strategies to mitigate climate change, due to the abundance of solar energy, the ease and speed of solar panel deployment, and plummeting costs. PSCs are currently limited by relatively poor long-term stability, and difficulties in retaining high efficiency when scaling up from the lab. This work adds to the growing understanding of the factors holding PSCs back; factors stemming from the prevalence of undesirable defects in the material arising during processing and operation.

In its report on climate change in 2018, The Intergovernmental Panel on Climate Change (IPCC) stated that in order to limit the catastrophic impact of rising temperatures this century upon millions of people and natural ecosystems, policymakers need to effect changes that would limit global warming to 1.5°C. In November 2021, Climate Action Tracker, an independent research group providing advice for policymakers worldwide, calculated current policies and action to result in ~2.7°C of warming above pre-industrial levels.[1] The UN Secretary-General Antonio Guterres warned at the most recent COP-27 summit that "we are on a highway to climate hell with our foot on the accelerator".[2]

Anthropogenic climate change occurs due to the excessive emission of greenhouse gases we produce relative to background levels of greenhouse gases emission due to natural processes — according to the IPCC report global anthropogenic CO_2 emissions would need to fall to ~45% of 2010 levels by 2030, reaching 'net zero' around 2050 to limit warming to 1.5°C.[3] At the same time there is increasing demand for energy across the world, with rapidly industrialising economies across Africa and Asia and a population set to hit almost 10 billion by 2050.[4] There is a desperate need for energy sources which do not produce CO_2 or other greenhouse gases and have a minimal carbon footprint from 'cradle to grave'. Photovoltaics are a promising technology for addressing this problem, capable of turning light into electricity. Enough energy reaches the earth's surface from the sun over 1.5 hours to fulfil the world's energy requirements for a year.[5,6] Increasing the fraction of this we harvest directly will play a significant role in the future as renewable energy sources are made more ubiquitous. Crystalline Si modules — possess ~ 95% of the PV market share (2021).[7] The best research cell efficiencies of multi-crystalline silicon (Si) cells is 24.4% , while mono-silicon has attained 26.7% efficiency; recent research-scale hybrid perovskite thin films have surpassed multi-crystalline Si cells, reaching 25.7% a positive sign for the development of perovskite photovoltaic cells.[7,8]

Research into hybrid perovskites for optoelectronic applications has gained significant momentum over the past decade due to desirable properties such as good charge carrier lifetimes, high defect tolerance, tuneable optical band gap, strong optical absorption, and high carrier mobilities.[9] PSCs can even be tuned for indoor conditions, achieving ~31% efficiency at 1000 lux, or semi-transparent building integrated PV applications.[10–14] In addition, relatively simple and cheap processing routes such as spin coating have made them readily accessible to many researchers. Much of the research focuses on tackling stability issues and understanding thin film properties to facilitate development of scalable processing routes to take perovskites from the lab to the roof. This thesis has endeavoured to build upon and add to the current knowledge of PSCs, focusing on approaches to improve device performance and stability by manipulating stoichiometry and homo-valent ionic substitute additives. Careful material selection and design will enable the reduction of deleterious structural defects, reducing the rate of degradation under exposure to air, heat and light.

'Swanson's Law' was devised to describe the photovoltaics industry in the 90 s, observing that module prices dropped around 20% for every doubling of cumulative shipped volume. The price of Si-cells in $/Watt(W) dropped from $76/W in 1977 to less than $10/W in 2000.[15] Conservative modelling from NREL assuming decreasing R&D predicts utility scale solar to drop to $0.73/W by the end of 2050, while an advanced scenario

with increased R&D projects $0.46/W. In the US in the 4th quarter of 2022, fixed-tilt utility scale solar was at $0.91/W, confirming previous projections of utility scale solar to drop below $1/W by the end of 2020.[16,17]

NREL keeps track of record research cell efficiencies for various cell designs and materials, which is a useful way of following the development of photovoltaics. 'Research cell' refers to small lab-made devices with efficiencies confirmed by independent and recognised testing labs. The given efficiencies are under standard test conditions, defined as AM 1.5 and 1000W/m^2 at 25°C. Notable trends in recent years are the rapid rise of certain emerging PV technologies such as Quantum Dot cells, Organic cells, and Perovskite cells, shown in Figure 68 by the yellow filled red circle.

Both Japan in the late 1990s and Germany in the 2000s heavily subsidised the adoption of PV, swelling production of solar cells. China spotted the significant potential to be had in cornering the production market, and today supplies approximately 60% of the world's PV cells.[18] The price of solar cells has continued to decline, with spot prices dropping to as little as $0.2/W in March 2023, with predictions expecting the cost to drop below that of coal based power plants in many countries around the world.[19–22] With concern about the consequences of anthropogenic climate change growing to a fever pitch in the scientific community, research into alternative technologies for providing renewable and sustainable energy with lower associated greenhouse gas emissions has increased. Solar energy has received considerable favourable attention for reasons including abundance as well as less socio-political opposition stemming from environmental, societal and aesthetic concerns when compared to power sources such as nuclear reactors and wind turbines. In addition, the increasing cost of energy from fossil fuels has pushed many energy firms to diversify into alternative energy technologies, which has been a boon for research investment. Energy prices in the UK are significantly exposed to energy cost increases associated with fossil fuel energy sources; gas fired power stations generate around 40% of the UK's electricity, while 85% of households use gas boilers to heat their homes.[23] The post-COVID re-opening of the economy, coinciding with the Russian invasion of Ukraine ramped up gas prices as supplies to Europe were squeezed. Rising wholesale gas prices than drove up gas and electricity prices for energy providers, increasing the final cost to consumers.[24] The wholesale cost of electricity increased from £50/MWh to almost £600/MWh between October 2020 and October 2022.[25] Diversifying away from fossil fuels to renewables such as PV has become a matter of not only environmental but also economic sustainability. Greater investment and deployment of renewable energy sources including PV will be crucial to avoiding similar crises in the future.

Today's photovoltaic materials can be divided into first generation cells; made of crystalline Si, second generation cells; thin film technologies such as CdTe and Copper Indium Gallium Selenide (CIGS), and third generation cells; emerging thin film technologies currently still in research and development. Hybrid organic-inorganic perovskites have been of particular interest, increasing in efficiency from 3.8% in 2009 (not shown in Figure 1 as was not verified by NREL) to 25.7% in thin films (see Figure 1). PSCs have the potential to be even cheaper than Si when produced at scale; Si wafer production wastes as much as 50% of the input material as Si sawdust and requires energy intensive processing at high temperature. In comparison perovskite can be solution processed with capability for low cost and room temperature fabrication processes, and comparable power conversion efficiencies.[26,27] However, PSCs suffer from instability issues which are influenced by practically every aspect of processing, from the atmosphere of solution preparation through to annealing time and temperature. Their initially high efficiencies as measured on lab-scale devices after fabrication dwindle over time under operation without effective encapsulation and sufficient process control. Efficiencies also fall as cells are scaled up to modules.[28] Hundreds of researchers endeavour to conquer these challenges, as the opportunity afforded by these materials could make a significant impact on renewable energy adoption. Hence improving their efficiency, performance stability and scalability of production is of prime interest.

Access to efficient sustainable and renewable energy sources is becoming more and more important to the national energy security of nations. Some countries are finding it in their interest to move away from dependence on imported fossil fuels or reliance on minerals and materials from unpredictable markets. In addition, the production of many materials used in conventional photovoltaic technologies (besides a vast array

of modern technologies), such as Cd, Ge, Ga, In, and Te is dominated by China, raising concerns of material resources dependence.[29,30]

1.2   What is the Photovoltaic effect?

Solar panels absorb light and convert it into electrical energy through the excitation of electrons by absorption of photons. Electrons are extracted to an external circuit where they provide power. The quantum of light energy is called a photon. The energy of a photon is dependent on its frequency, and in the visible range of wavelengths can be denoted by colour, with higher energy photons (and therefore higher frequency photons) being toward the blue end of the spectrum. Upon absorption of a photon the photon's energy can excite electrons from the valence band (also understood as bound states in the binding orbitals of molecular solids) across an energy gap (E_g, termed the band gap in crystalline semiconductors) to the conduction band (unoccupied conducting states in the anti-binding orbitals) at a higher energy. When electrons are excited in this way an electron-hole pair is generated, creating a hole in the valence band.

Photovoltaic materials are semiconductors, where the size of the energy gap is in the range of 0.5-3 *eV*. An energy gap of this size between the valence band and conduction band permits absorption of visible light. The maximum energy that can be captured by a single junction solar cell falls within this energy range, described by the Shockley-Queisser limit. Light with energy exceeding this range can damage solar cells, whereas infrared light has less energy. Insulators cannot absorb visible light because they have an E_g that is too large, while metals possess a continuous distribution of energy levels which permit fast decay from any given excited energy level down to the ground state by releasing heat in the form of phonons (vibrations of the crystal lattice). In a typical semiconductor, if the photon energy of the incident light on a material is sufficient to excite an electron in this way (photon energy exceeds E_g), the electron rapidly relaxes to the edge of the energy gap via phonon emission (thermalisation). It would eventually drop back down to its prior energy level (ground), by recombining with the hole created upon excitation and emitting a photon with energy $E = E_g$. This would happen despite the energy separation of the band gap, to restore equilibrium. In a photovoltaic material, a built-in asymmetry in the energy levels of the charge carriers hinders radiative recombination across the energy gap. Instead, carriers are made to do work as electric current in an external circuit before recombining. This is achieved by engineering an in-built driving force which separates the electron-hole pair. Charge carrier separation via application of an external bias (V) gives rise to photocurrent. As the size of the band gap increases, when $V < E_g$, recombination current drops, and therefore V_{OC} increases. In a device with large E_g, V_{OC} decreases due to low J_{SC}.

The various conditions which enable separation rely on spatial gradients in the electronic environment. Gradients in the vacuum level or work function for example can be utilised, by doping different regions of a single semiconductor differently (homojunction), as in a *p-n* junction- the classical model of a solar cell. The *p* side is doped with acceptor impurities (shown as the negatively charged acceptor ions plus holes in Figure 2, representing a positively charged dopant species), which attract free electrons, and become negatively charged at the junction of the *p* and *n* doped materials. Meanwhile the *n* side is doped with donor impurities, which attract free holes, becoming positively charged at the interface. The charge carriers involved in setting up this space charge region (depletion width) are called the majority carriers. For example, the *p* facing side of the depletion region is the result of the recombination of free electrons from the *n* type region with holes on the *p* type acceptor ions. The depleted region of the junction acts as a barrier against further diffusion of majority carriers. An electrostatic field is setup across the junction between the *p* type and *n* type material due to lower electrostatic potential (work function) on the *n* side of the junction. This built-in field (V_{BI}) has a voltage *ΔV* equal to the difference between the fermi levels (E_f) of the doped regions relative to the vacuum energy level ($V_{BI} = \Delta V = E_{f,n} - E_{f,p}$) Photogenerated electrons move towards the *n* type material, and holes towards the *p* type material. The photogenerated carriers are minority carriers, with holes and electrons generated throughout the *p* and *n* regions respectively but driven by diffusion towards the junction. At the junction drift due to the in-built field separates them. Figure 2 summarises this information.
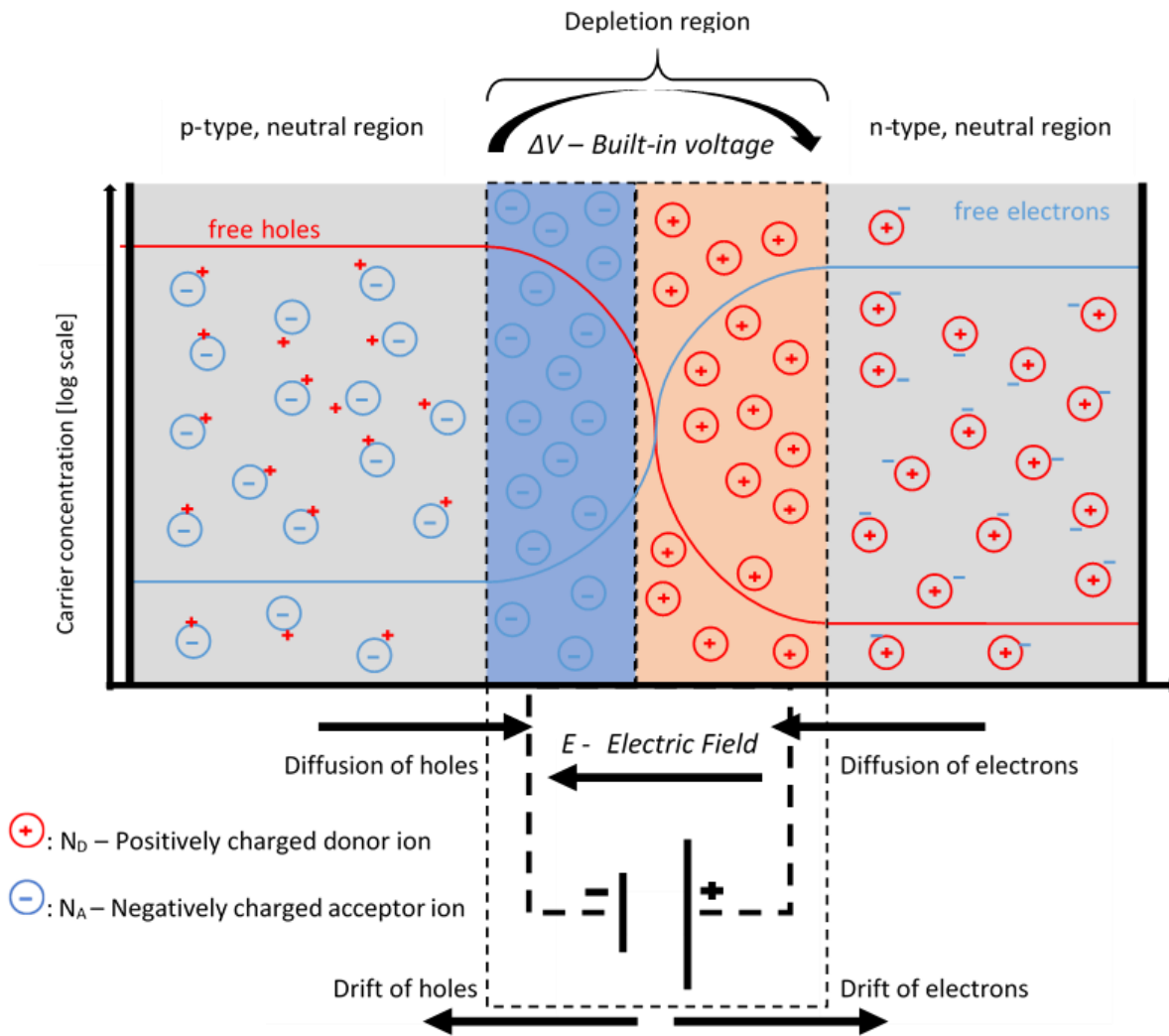
Figure 1: Drift-diffusion model of a p-n junction. In a p-i-n junction, an intrinsic absorber is sandwiched between p-type and n-type selective contacts, from which minority carriers are depleted by selective charge transfer. Blue '-' are electrons, red '+' are holes. Built in voltage arises from formation of depletion width. This sets up an electric field which assists charge separation. Diffusing charge carriers separated with drift assistance to respective junctions.

Another way of achieving charge separation is by designing a gradient in the electron affinity or band gap, resulting in effective fields which act on the charge carriers. Examples of this include the heterojunction at the interface between two materials and compositional gradients in an alloy.

A typical *p-i-n* cell has a larger undoped and therefore intrinsic (*i*) depletion region (and hence wider electric field region) between smaller *p* and *n* regions. This junction design has the effect of increasing photocurrent because minority charge carriers — which have a short diffusion length— are more likely to reach their respective junctions and be separated due to the drift-field assistance. In perovskites, a *p-i-n* or *n-i-p* architecture is used. Here the perovskite acts as the intrinsic (*i*) absorber between two charge carrier selective contacts, creating a pseudo *p-i-n* junction. The intrinsic region is akin to the depletion width, wherein minority charge carriers are generated when photons are absorbed. Under operation they diffuse towards their respective contacts and are assisted by drift due to the in-built field between the charge transport layers (CTLs). Electrons are collected by the n-type electron transport layer (ETL), while holes are collected by the p-type hole transport layer (HTL). Electrons flow through an external circuit and do work, before recombining with holes in the p-type layer. This is called the recombination current.

There is an upper limit to the light-to-electrical power conversion efficiency (PCE) for any solar cell, defined as the ratio of total incident solar photon energy: electrical energy output. This can be determined by the Shockley-Queisser (SQ) Model and formalism, which defines the SQ limit, also known as the detailed balance limit (See

Figure 69).[31] This model has several assumptions, including a planar geometry and blackbody radiation from the source. It also assumes all electron-hole recombination events are radiative (recombination emits a photon of the same energy as the photon that generated the electron-hole pair), and that there are perfect charge selective contacts. Essentially all photons with $E > E_g$ create free electrons and holes, yielding 1 electron per absorbed photon. The SQ limit only takes into account thermodynamic constraints; the optical absorption edge, solar spectrum (i.e. AM 1.5) and operating temperature are used as the only inputs for the PCE calculation. Real materials do not strictly follow such a simplified model however, and will always be below the SQ limit. In a real material, the absorption edge is rarely a perfect step function for example, and will often have a tail, or inter-band states. This is a property research focuses on improving material performance. Another significant factor is the occurrence of non-radiative recombination centres in real materials — recombination can occur at defects where the excess energy is converted to heat by phonon emission. Operating losses in a real system within the SQ limit can thus be approximated with the following: (Operating losses = *SQ loss + radiative losses + non-radiative losses+ maximum power point operating losses + contact losses*) [32]:

2   Hybrid Perovskites

Perovskites are the world's most abundant class of minerals and have long been of interest to geoscientists as they try to understand the formation of the Earth. Perovskites are researched widely in many materials fields, from ferroelectrics, superconductors, and fuel cells to spintronics, thermoelectrics and recently, photovoltaics. They owe this wide variety of applications to their renowned chemical tolerance and structural flexibility complimented by good physical and chemical properties. This tolerance and flexibility stems from their ABX_3 crystal structure. Their extensive adaptability and applicability forms the basis of a $20-billion-dollar electro ceramics industry in applications such as catalysts, insulators, semiconductors, superionic conductors and superconductors.[33,34]

Table 1: Applications of Perovskites

Lasers	Water Splitting	Solar Paint	Building Integrated PV
Space Applications	Hydrogen Storage	Detectors/Sensors	Gamma ray detection/ harvesting
Thermochromic devices	Transistors/Memristors/ Artificial Synapses	Liquid Crystal Devices	Photoreceptors

2.1   Crystal Structure

The basic perovskite crystal ABX_3 has two metallic, positively charged cations (A&B) and one non-metallic negatively charged anion (X). The larger A cation sits at the centre of the tetragonal unit cell, while 8 B cations occupy the corners. The X anions fill the midpoints along the edge of the cell. If this is presented as an assembly of polyhedrons, the cell can be interpreted as an A cation surrounded by 8 corner sharing B cation centred octahedrons, with X anions at the points of each octahedron (as shown in Figure 2A). This is typically described as a body-centred cubic (bcc) structure, but relates to the face-centred cubic (fcc) structure as the A site cations and the X-site anions comprise a fcc lattice (Figure 2B). The B-site cations situated in the octahedrally coordinated corners are surrounded by 6 X-site anions. The crystal structure of methylammonium lead triiodide ($MAPbI_3$), the stereotypical hybrid perovskite system is shown in Figure 3A, where the purple spheres at the corners of the grey octahedra represent the corner shared Iodide (I^-) anions, the centre of the octahedra are the Pb^{2+} cations, and the MA^+ cations sit in the A-site. This organic-inorganic perovskite was first generated in 1978 by Dieter Weber when he replaced caesium as per HL.Wells *et al.* with MA cations.[35] The octahedra share their vertices but not their edges, making the perovskite structure flexible; the octahedra can rotate and tilt cooperatively. Stabilising of this octahedral tilting has been linked to improved PV performance.[36,37]

These sites can be occupied by a vast array of elements in the periodic table, with 24 elements identified as capable of occupying the A-site, while almost 50 can occupy the B-site, and not only oxygen but halides can occupy the X-sites. This large flexibility accounts for the incredible structural variety encapsulated by the broad

perovskite family. An A-site cation which is too small with respect to its B-site neighbours for example can lead to a deviation from the ideal cubic structure to tetragonal or orthorhombic structures, resulting in twisting and tilting of its surrounding octahedrons to lower energy, or even off-centring of cations resulting in a weakening of the interaction between the A-site cation and B-X lattice with a resulting polarity. The sites can also be occupied by a mix of cations i.e. varying elements, or varying charged ions of the same element, where the material can be consequently tuned along a continuous series of compositional variance.
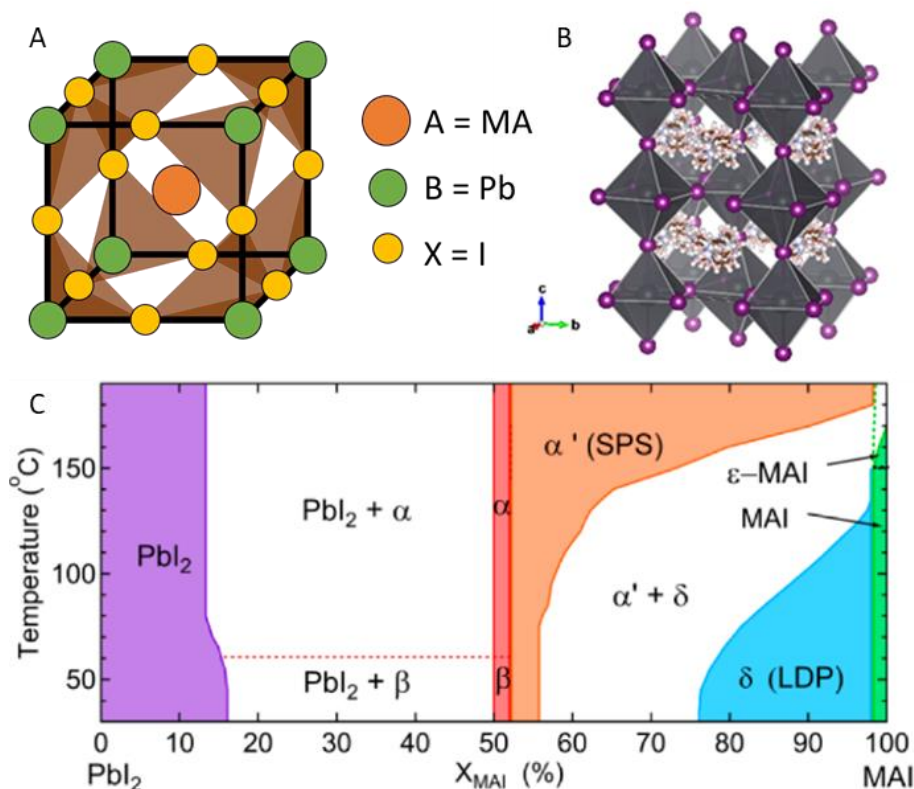
Figure 2: (A) BCC perovskite structure of $CH_3NH_3PbI_3$ (MAPbI$_3$). Methylammonium cation ($CH_3NH_3^+$) occupies the central A site surrounded by 6 Pb^{2+} corner cations and 12 nearest-neighbour iodide anions (I$^-$) in corner-sharing PbI_6 octahedra. (B) MAPbI$_3$ crystal structure as it relates to the FCC crystal structure with A-site cations surrounded by 8 I$^-$ anions, and showing how the organic cation can freely rotate around its axes in the A-site (Reproduced from 10.1038/ncomms8497 under Creative Commons Attribution 4.0 International License) (C) Pseudo-binary phase diagram of MAPbI$_3$. (Reproduced with permission from doi/10.1021/acs.chemmater.5b01017 Copyright 2015 American Chemical Society.)

How well a combination of ions conforms to the ideal and highly symmetric ABX_3 cubic structure can be quantified by ideality factors. For example, the Goldschmidt tolerance factor, t;[38]

$$t = (r_A + r_X)/\{\sqrt{2}(r_B + r_X)\}$$

Equation 1

Where, r_A, r_B, and r_X are the ionic radii of the A, B and X ions respectively. The phase stability of the perovskite phase increases the closer t is to 1. Lower t can lead to lower symmetry orthorhombic or tetragonal phases, while larger values can lead to layered structures, where the 3D network deviates into 2D structures, consisting of alternating planes of the inorganic metal-halide octahedra and monolayers or bilayers of organic cations. Mixing very large and small cations can result in quasi-2D structures, where variable thickness perovskite layers are terminated by large organic cations. These are commonly referred to as Ruddlesden-Popper phases when the large cation is monovalent or Dion-Jacobson when the large cation is divalent.[39] For hybrid perovskites, stability of the perovskite phase is expected for $0.813 < t < 1.107$.[40]

The octahedral factor (μ) is another parameter used to predict structure stability and is defined as the ratio between the ionic radius of the B cation and the X anion ($\mu = R_B / R_X$). Generally, the formation of halide perovskites occurs when the octahedral factor $\mu > 0.442$. The formation of halide perovskites does not occur when μ is below this value due to instability of the (BX_6^-) octahedron (Q. Chen *et al.*, 2015).

17

Hybrid Perovskites - Crystal Structure

The pseudo-binary phase diagram (see Figure 2C) for the prototypical hybrid perovskite $MAPbI_3$ system, shows how altering the ratio of PbI_2 to MAI during synthesis changes the phase composition as a function of temperature. $MAPbI_3$ has an *I4/mcm* tetragonal structure (β) at room temperature, where the c-axis is elongated due to the polar organic cation $CH_3NH_3^+$ (MA^+). Above 60°C, relaxation of the structure as the degree of disorder decreases makes a secondary tetragonal phase (α) stable. Above 60°C MA^+ rotates freely; when the structure is averaged over time (as per typical crystallography experiments) overall it looks like a high symmetry cubic structure. As a result, the α phase has often been conflated with a high temperature cubic phase due to the small elongation along the c-axis, which can be difficult to resolve.[41] Total Scattering Experiments suggest the cubic structure matches $MAPbI_3$ scattering well over lengths >10 Å, whereas the lower symmetry tetragonal structure is more accurate for short lengths (1-10 Å).[42] Clarity regarding the structure also comes from models and high resolution X-ray inelastic scattering, which suggest the cubic phase represents an energetic saddle point between equivalent tetragonal distortions. This local disorder is not observed in Bragg diffraction where long-range order is preserved (non-finite resolution). It is this high temperature pseudo-cubic α-phase which is desirable for PSCs. The atomic arrangement of MA^+ in its lattice site has also been linked to the preferred <110> directionality of crystal stacking in MA-based thin films; H-bonding between the NH_3 group and PbX_6 octahedra create an energetically favourable orientation for the crystal.[43,44]

Structural alterations will also arise from compositions which are non-stoichiometric, where there are vacancies of cations or anions in the structure, extra species squeezed into the crystal at interstitial sites, or antisite defects.[45] Collectively these can be referred to as point defects. These defects can locally dope the perovskite, introduce trap states, and mediate current-voltage (I-V) hysteresis. Photogenerated carriers fall into traps at interfaces, while ions migrate through atomic vacancies and interstitial sites towards contacts. The accumulation of charged species at the interfaces with selective contacts leads to charge screening and hence hysteresis, where there is a difference in forward and reverse bias current.

These changes will affect physical and optoelectronic properties such as conductivity and photoluminescence and therefore device performance. Solution processed hybrid perovskites have a high density of defects due to the imperfect crystallisation inherent in the highly dynamic processing. Despite their high defect density perovskites remain remarkably efficient photovoltaics, and this is due to their high defect tolerance; despite having remarkably high defect densities, defects infrequently form within the band gap, and as a result have minimal effect on the desirable optoelectronic charcteristiscs.[46] Point defects will form transition level states either near the valence band maximum (VBM) or conduction band minimum (CBM), or — less frequently — states within the band gap of the perovskite. These are called trap states, and those which trap two types of carrier become recombination centres for free electrons and holes. Trap states near the band edges are called shallow-level traps, and de-trapping of carriers occurs more readily, as there is a lower energy offset. In perovskites, intrinsic defects such as vacancies most commonly form shallow level trap states. Transition levels deep in the band gap form deep-level traps and are called Shockley-Read-Hall (SRH) recombination centres. SRH defects are responsible for trap-mediated non-radiative recombination and more typically arise at grain boundaries and surfaces. In perovskites these defects can be related to interstitial and antisite defects.[47–50] Many approaches to improving the performance of hybrid perovskites as photovoltaics attempt to remove these trap states or counteract them, for example by improving crystallinity (film quality), passivation, and interfacial engineering.[51–53] Thus, increases in radiative efficiency are typically correlated with a reduction in deep-level trap states.[54]

Pb substitution with Zn

Motivations to reduce lead content in perovskite solar cells stem primarily from its toxicity. It readily reduces to PbI_2, which is itself photoactive and undergoes photolysis under operating conditions, which introduces detrimental trap states. Homo-valent metals, such as Zn^{2+}, have been extensively explored as alternative B-site cations to substitute for Pb^{2+} (with one screening effort replacing up to 25% of Pb with 9 different metal species).[322] Zn is non-toxic, and is a stronger lewis-acid than Pb^{2+} meaning it coordinates more strongly with the MA^+ cation and I^- anion. Combining this with the smaller ionic radius of Zn^{2+} relative to Pb^{2+} results in enhanced

crystallisation with larger grain size and increased crystallinity along the {110} set of planes. According to XRD and EDS data by Zhao *et al.*, and Chen *et al.* respectively, Zn is completely dissolved in the perovskite phase when used as a cation partially substituting the B-site.[323,324] Zn also acts as a strong reducing agent, reacting with I_2 to mitigate the oxidation of iodide ions in the perovskite solutions.[325] Addition of a reducing agent in the precursor solution ensures an accurate stoichiometric ratio of precursor salts in solution reducing the prevalence of iodide vacancies (V_I) and iodine inclusion (I_i) defects in the final film. The reducing agent, Zn^{2+}, reacts with I_2 formed in solution reducing the prevalence of defects.[327] The importance of accurate stoichiometry has been demonstrated by various authors, and is discussed subsequently.[83,84,328–330] This reduces both non-radiative recombination centres in the form of V_I and I_i, which have been linked to accelerated degradation, hysteresis, and lower carrier lifetime.[79,216,331,332] Zn addition strongly enhances the charge carrier collection efficiency of perovskite solar cells, showing there is a reduction in non-radiative carrier recombination.[323,325,333–335] This stems from improved crystalline quality, increased grain size (and hence reduced grain boundary area), and reduced pinholes.[318,323,334,336] Zn addition has also been shown to significantly slow down hot-carrier cooling in caesium lead halide perovskites.[337]

2.2   Thin films

High quality perovskite thin films are crucial for the development of high performing perovskite photovoltaic devices. In this context that means that morphologically the film will have uniform coverage of the substrate, with high areal density (the presence of pinholes will be minimised) and grains large enough to span the gap between the HTL and ETL in a single grain. For clarification, a grain is a unit of material in which the crystal structure is the same throughout and is bounded on all sides by grain boundaries (GBs) with other grains, interfaces, or a surface. This is important as for devices pinholes will present shunt paths through which there will be leaking current, and the surface needs to be uniform in its coverage to ensure the conformal deposition of succeeding device layers. Pinholes are also regions where light is not absorbed. Optimal coverage can be obtained by having widespread, uniform and dense nucleation. This can be achieved through solvent engineering of the precursor solution, and optimisation of the deposition and annealing processes in terms of time, temperature, and atmosphere. Grains of comparable size to the thickness of the perovskite film will reduce the number of GBs. GBs are typically more disordered than the grain bulk, possessing defects such as vacancies or inclusions which act as trap states to charge carriers. A higher density of trap states (particularly SRH defects) favours recombination of charge carriers and will hence reduce the performance. GBs also facilitate migration of ions or environmentally introduced species such as oxygen.[55] Furthermore, films with smaller grains have shown lower fracture resistance, with the GBs providing favourable paths for crack propagation.[56] Grains which are oriented preferentially relative to the substrate also boost charge carrier extraction. A film with more ordered grains and higher crystallinity is typically desirable, and this is an aspect routinely measured using X-ray diffraction techniques, transmission electron microscopy (TEM), and to a lesser extent, scanning electron microscopy (SEM), and this will be explored in later sections. Large grains oriented preferentially with regards to the substrate (or charge transfer layer (CTL)) hence generally lead to better performing PSC's, although there are examples of high performing PSC's with small grains where crystallinity is high and GB recombination negligible in comparison the grain interior.[57,58]

Charge carrier lifetime, which can also be interpreted in terms of diffusion length is a metric typically used to characterise thin films for photovoltaics. This reflects the average time it will take or distance a photogenerated carrier will cover before it can be expected to undergo recombination with another carrier — either radiatively emitting a photon, or non-radiatively, where the energy is either lost as heat in the form of a phonon propagating through the lattice as the carrier falls to a lower energy trap state (trap-mediated recombination), or to another charge carrier in the CB or VB (Auger recombination). Long carrier lifetimes and long diffusion lengths are typically interpreted as being indicative of low trap-state density and low rates of non-radiative recombination. These values can be measured and explored using measurements of photoluminescence quantum yield (PLQY), time-resolved photoluminescence spectroscopy (TRPL), and surface photovoltage (SPV) measurements.[59–61]

The reactivity of metal halide perovskites is particularly important during processing, deposition and formation of films. Compositional changes or doping effects can occur due to reaction with O_2, H_2O, and additives to the

precursor solution, or even simply due to the volatility of the species in the film, with MA halides being particularly volatile. This can lead to detrimental changes to optoelectronic properties due to the formation of traps. Redox chemistry is also important in the decomposition of perovskite films, with Zhao *et al.* observing the spontaneous reaction of perovskites with Al, Cr, Ag, and Yb, reducing the Pb^{2+} cations to Pb^0. This occurred even in the absence of typical triggering factors such as H_2O, light or O_2.[62] Degradation of hybrid perovskite films will be elaborated upon in section 2.5. For $MAPbI_3$, the thermodynamic stability of the pure 3d perovskite phase lies within a very narrow range of compositions of its binary halide components. Local decomposition can easily occur due to these reactions, typically leading to by-products such as PbI_2. PbI_2 is often observed passivating the perovskite at GBs and interfaces, reducing the number of trap states. PbI_2 is itself photoactive and may contribute to charge carrier generation. However too much of this phase presents an obstacle to charge carrier transport and stability, and if included it needs to be optimised to maintain high film quality.[63–65] Other secondary phases and impurities at best will act as dead zones in the film, but at worst will act as non-radiative recombination centres, as well as nucleation points for the further degradation of the film into the non-perovskite phase. These phases need to be controlled to maintain homogenous film properties and retain high charge carrier lifetimes, mobility, and extraction.

2.3 Solution Processing

2.3.1 Importance of correct stoichiometry

Correct stoichiometry is important in PSC fabrication, as it ensures a complete reaction between the precursors and reduces the prevalence of residual PbI_2, Iodide vacancies, film longevity, and device performance.

Excess PbI_2 has commonly been cited as being beneficial in perovskite films due to a passivation of recombination centres.[66] The excess iodide passivates predominantly bulk iodide ion vacancies ($V_I^\bullet$), increasing charge extraction in the short term.[67] Termination of perovskite crystals with Pb and I and excess PbI_2 on grain boundaries and surfaces may also provide moisture resistance, with delayed formation of the monohydrated perovskite phase compared to stoichiometric samples evidenced by Petrus *et al.*.[68] However, photolysis of PbI_2 creates voids in the film, introducing trap states that reduce device performance under long-term operation.[69] Unreacted, residual PbI_2 has also been shown to have a detrimental effect on PSC's, seeding degradation under operating conditions.[70]

The addition of excess MAI has been shown to improve the crystallinity of the perovskite grains.[71] In an experiment to generate high quality spin-cast $MAPbI_3$ films on warmed substrates Liao *et al.* diagnosed this as due to a more complete conversion of PbI_2 to $MAPbI_3$.[72] They also found increased grain size, improved crystallinity, decreased defect density, and carrier concentration enhancement. Devices had higher fill factor (*FF*) and J_{SC}. Moreover, the generation of perovskite films using an MA-gas mediated perovskite precursor method was shown to create $MAPbI_3$ films with larger crystal grains, lower roughness, and a preferred (110) crystal orientation, which is associated with higher PCE.[73,74] This film preparation methodology ensured the complete reaction of the PbI_2 precursor with MAI, and minimised the presence of moisture during spin-casting. Films with dominant (110) orientation were shown to have improved morphology and optoelectronic properties by Kavadiya *et al.*, with reorientation of crystals from (002) to (110) occurring during annealing at 100°C.[75] Dhamaniya *et al.* showed that films dominated by (110) orientation crystallites had lower decomposition rates in a 70-80%rH atmosphere compared to films rich in (100) planes, wherein a hydrated phase forms, leading to faster decay.[76] Interestingly, Petrus *et al.* showed that upon prolonged exposure to a humid atmosphere, $MAPbI_3$ films with an MAI excess showed an increased photocurrent and photovoltaic efficiency, resulting from solvent-annealing with water vapour.[68] Recrystallisation, and grain reorientation (increasing the intensity of the (110) reflections) reduced the electronic disorder. Similarly, Enhanced solvent retention in films with excess MAI was previously found in $MAPbCl_2$ films in work by Munir *et al.*, which would also be beneficial for grain growth.[77] In a key in-situ XRD study, Yang *et al.* have shown that $MAPbI_3$ exhibits a diffusion controlled, one dimensional growth mechanism during annealing in accordance with the Avrami model. Nuclei form at a constant rate, growing perpendicular to the solvent air interface. The growth rate is mediated by the diffusion rate of MAI to the crystal growth front. Subsequent growth occurs by coalescence.[78]

Both the addition of excess PbI_2 and excess MAI results in Iodine-rich conditions; conditions which according to Zhang *et al.* leads to Iodine interstitial defects. Under I-rich conditions these defects are largely responsible for

defect-assisted non-radiative recombination, with capture coefficients of 0.7 x 10^{-8} cm^3s^{-1}.[79] The use of excess MAI can lead to the formation of the I-rich phase PbI_6, shown to aggravate hysteresis issues in PSCs.[80] On the other hand, I poor conditions due to degradation or halide segregation leads to a larger concentration of hydrogen vacancies, formed by the breaking of either N-H or C-H bonds in MA molecules. Hydrogen vacancies have an even higher capture coefficient of 10^{-4} cm^3s^{-1}.[81] The net effect on devices is a decrease in J_{SC}.

Fan *et al.* found that grinding perovskite precursor salts in H_2O leads to the formation of α-phase pure perovskite. Solvation of the organic salt in moisture enhanced the reaction rate with PbI_2. Films produced from powders synthesis in this way had less residual PbI_2, increased grain size, lower roughness, and fewer trap states when compared to standard films. This technique also increased the shelf-life of the films, with lower chemical degradation of the precursor solution and larger colloids in solution.[82] This work emphasises the importance of ensuring a complete reaction between the precursors to obtain high quality perovskite films. The importance of stoichiometry for encouraging formation of high quality perovskite films for high performance devices was also demonstrated by Kostas *et al.* in their work investigating PbI_2; films made from sub-stoichiometric PbI_2 (deficient in Iodine) lead to lower performing devices. This negative effect could be corrected by using an excess of MAI in film preparation.[83] Belous *et al.* identified distinct film formation pathways dependent on the ratio of MAI:PbI_2 precursors in DMF solutions.[84] When the ratio was 2:1, perovskite formed via an intermediate compound; MAI_2PbI_4. When increased to 3:1 perovskite formed via both MA_3PbI_5 and MA_2PbI_4. The different pathways impacted final crystal structure and morphology, though the effect on device performance was not explored. The importance of precursor stoichiometry in precursor solution on film quality is discussed, evaluated and investigated further in section 6.

2.3.2 One Step Deposition

In order to obtain a high-quality film, an optimum between nucleation density and crystal growth must be reached. If the nucleation density is too high, a very fine-grained structure will form, requiring subsequent heat treatment in order to grow grains and reduce GBs, defects, and interfacial strain. If nucleation density is too low, large grains with gaps between them will develop. These gaps provide shunting paths where current will be lost in a device, or even shorting paths if selective CTLs come into contact through these holes in the photoactive film layer. To control the film formation and prevent these issues, many approaches have been developed, from solvent engineering and thermal engineering (controlling the heating regime) to surface and interfacial engineering (manipulating the chemistry of surfaces in order control film formation) using post-deposition treatments or use of additives in the precursor solution.

One step deposition via spin coating of a precursor solution is one of the simplest and most accessible techniques for preparing perovskite thin films for solar cells. The solution is prepared by dissolving precursor materials such as MAI and PbI_2 in polar solvents such as dimethylformamide (DMF) or dimethyl sulfoxide (DMSO), or mixtures thereof. The solution is dropped onto a spinning substrate spinning at thousands of rotations per minute (rpm), which centrifugally spreads the solution over the wetted surface. Initially, removal of excess solution is dominated by the angular force as the substrate spins, while in the latter stages of spin casting evaporation

dominates. As coordinating solvent is removed, the precursors increase in concentration until they become super-saturated in the remaining solution and begin to precipitate out of the solution, nucleating and beginning the conversion to perovskite as they react. Depending on when spinning stops, evaporation may continue during subsequent drying or annealing stages. Excess uncoordinated solvent evaporates during spinning, with the residual coordinated solvent (conjugated in intermediate solvate-precursor complexes) driven off during drying or annealing. Some perovskite systems, such as $MAPbI_3$ in γ-butyrolactone (GBL) and $MAPbBr_3$ in DMF show inverse solubility, where solubility decreases with an increase in temperature, allowing for rapid crystal growth at elevated temperature.[85] According to Mohammad et al. this occurs as at low temperature, precursor molecules are bound in solvent complexes, while as temperature rises, the concentration of unbound precursors increases due to complex dissociation, and the concentration approaches the super saturation limit, permitting precipitation of the perovskite nuclei.

Hybrid Perovskites - Solution Processing

The nucleation process can be described using the Lamer model as shown in Figure 3A of homogenous nucleation; homogenous nucleation assumes nucleation of spherical crystals within solution without the requirement of a third phase. First solvated precursor molecules in solution increase in concentration above the saturation or solubility limit (C_S) as solvent evaporates until they hit the super-saturation limit, C_{SS}.[86] At the super-saturation limit, nucleation occurs as the concentration of precursors hits a critical level which allows the perovskite formation reaction to occur. The nucleation rate of perovskite will eventually surpass the precursor formation rate at the critical super-saturation limit (C_{SMax}), resulting in a decrease in precursor concentration. The conversion of precursor solvates to the nucleating perovskite phase reduces the concentration of precursor in solution, reducing it below the super-saturation concentration, and reducing the nucleation rate. At this point growth of existing nuclei dominates. Beyond the supersaturation limit, the precursor solution becomes thermodynamically unstable and decomposes spontaneously, with phase separation to precursor salts occurring resulting in the formation of residual salts such as lead halides. In practice, a combination of homogeneous and heterogeneous nucleation occurs, with heterogeneous nucleation dominating at low saturation, and homogenous nucleation dominating at high saturation and above the super saturation limit. Heterogeneous nucleation occurs on a third phase such as the substrate surface. For controlled nucleation and growth of precursors from solution usually heterogeneous nucleation of the perovskite nuclei on the substrate material is required, as opposed to homogenous nucleation within solution, as the latter can result in poor film coverage. The substrate reduces the energy barrier for nucleation by reducing the interfacial energy of the liquid and crystal interface.[87] A useful model for describing heterogeneous crystal growth is the Volmer-Weber model (see Figure 3), where the nucleating phase forms as separate islands on the substrate, and therefore a high density of nuclei arising from the evaporating solution is required to ensure a dense, uniform thin film forms.[88]
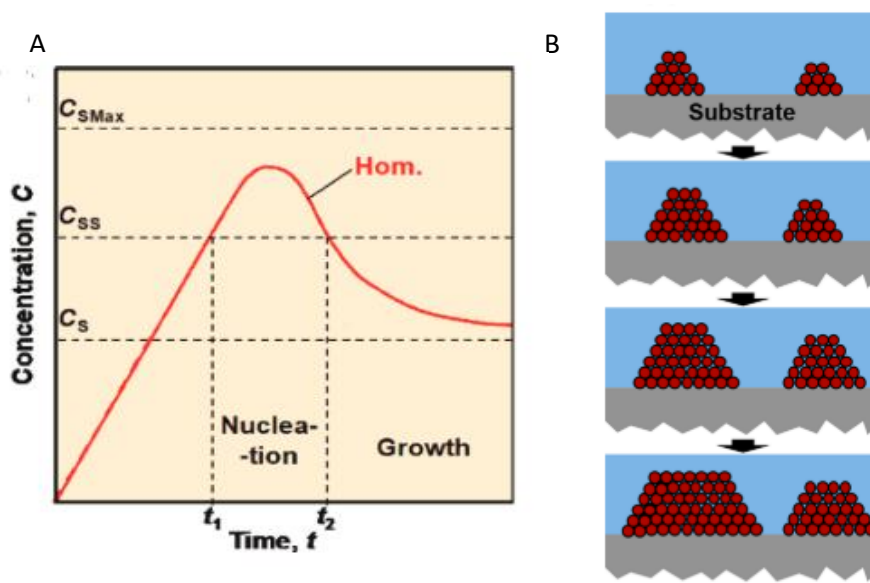
Figure 3: (A) Graph of Lamer model of crystal growth assuming homogenous nucleation. (B) Volmer-Weber mode Island Growth of crystallites (Adapted with permission from doi/10.1021/acs.chemrev.8b00318. Copyright 2019 American Chemical Society.)

However, this model was designed to describe deposition from a gaseous phase and not from a solvent, and so can't capture the full picture of perovskite crystal growth. Yet the Volmer-Weber model does not require an epitaxial relationship with the substrate, and is hence still useful for describing perovskite film growth, where crystallisation may begin at the solvent-air interface for example. Besides the growth of nuclei by diffusion of precursor monomer species to the perovskite, growth can occur via Ostwald Ripening whereby larger crystals grow at the expense of smaller ones. Here small crystals dissolve back into the solution, saturating it locally. The solvate species then deposit on larger crystals nearby.[89] Growth can also occur via coalescence where nuclei fuse together. Eventually these small crystals grow to a size at which we begin to describe them (generally interchangeably) as crystallites or grains.

Hybrid Perovskites - Solution Processing

Evidence for crystallisation of perovskite at the solvent-air interface came from work by Chen *et al.*, who show that perovskites prepared by one-step solution coating methods such as spin coating and blade coating can follow downward grain growth.[90] Downward vertical grain growth perpendicular to the film surface is induced by the evaporation of coordinated-solvent at the solvent-intermediate-gas interface as intermediate phases are converted to perovskite. This growth is found to be less sensitive to perovskite composition or substrate wettability. The nature of the intermediate crystallisation was not investigated in their work, with the crystalline film designated as MAI-PbI$_2$-DMSO with peaks at 6.6°, 7.2° and 9.2° (assigned to the (002), (021) and (022) planes respectively. Zheng *et al.* observed two stages in perovskite crystallisation during annealing; 1) solvent-evaporation mediated transformation of the solvent-intermediate phase to brown β-perovskite, and 2) directional growth of the perovskite phase with loss of residual solvent and transition to black α-perovskite.[91] The directionality of the intermediate nucleation and how this influences perovskite grain growth has been is summarised in Figure 4.[91]
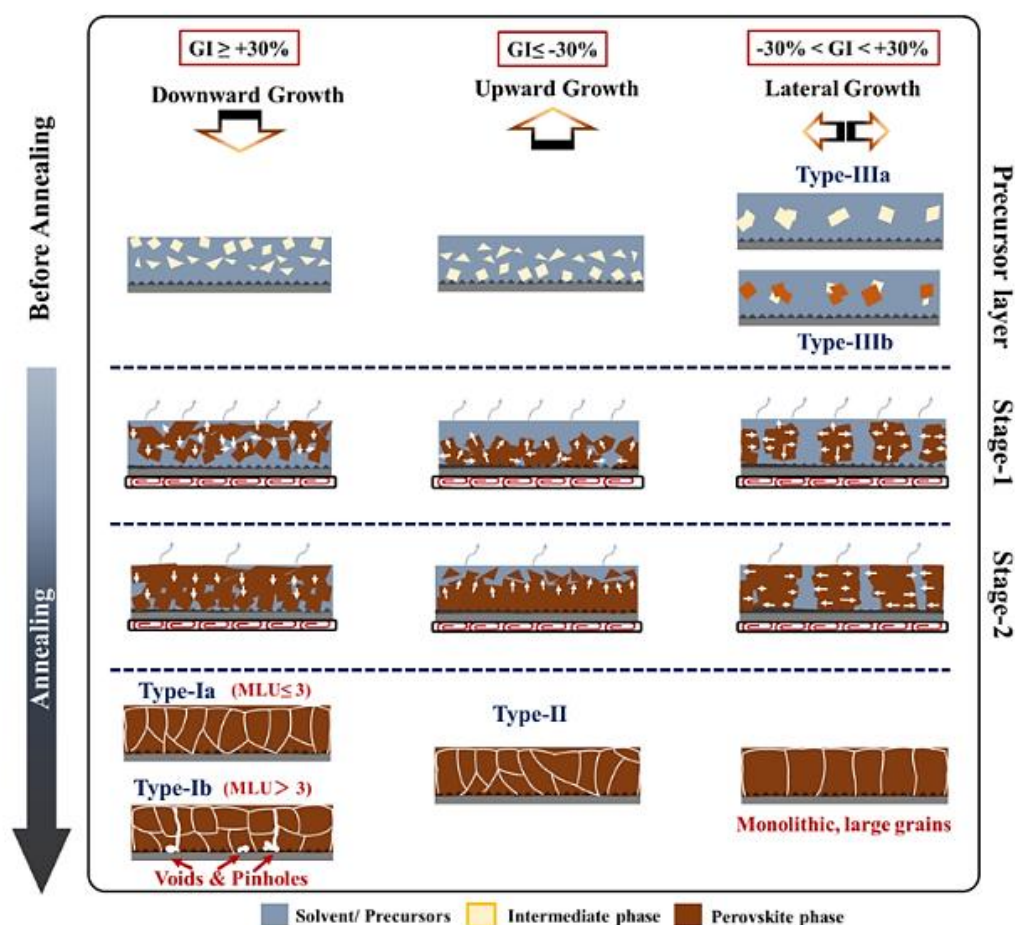
Figure 4: "Parameters and typologies of perovskite layers growth models.".[91] The parameter 'GI' stands for Gap Index and relates to the percentage difference in solvent elimination rate between the upper and lower layers of the film. Large GI, ≥30% results from downward growth, and –ve GI, ≤-30% results from upwards growth. Lateral growth occurs when GI is between these modes. The parameter 'MLU' stands for Multiple of Lower layer residual solvent ratio (RSR) over Upper layer (RSR) at a critical annealing time. When MLU >3, a perovskite crust forms at the film surface which traps solvents, leading to the formation of voids at the substrate surface and pinholes in the perovskite surface when it bursts through and is released. Reproduced from DOI: 10.1038/s41467-022-34332-3 under a Creative Commons License.

Zheng *et al.* have proposed a universal typology to distinguish between three film growth modes depending on the preferential growth direction of perovskite grains. This was validated by a study across a large range of perovskite compositions using glow-discharge-optical emission spectroscopy, XRD, and SEM. They identify downward (Type I), upward (Type II), and lateral (Type III) growth modes. They are further subdivided into sub-types depending on the growth rate or presence of perovskite nuclei in the as-spun film. Type III films with vertically oriented GBs and a monolithic structure favours charge transfer from the perovskite film to the CTLs,

and should be targeted for high efficiency devices. The grain growth (here composed of two main stages) has two main stages: 1) solvent-evaporation mediated transformation of the solvent-intermediate phase to brown intermediate/perovskite, and 2) directional growth of the perovskite phase with loss of residual solvent and transition to black perovskite. Similarly too Zheng et al., Mrkyvkova *et al.* demarcated two corollary stages in perovskite grain growth using in-situ measurements of photoluminescence (PL): first the nucleation of perovskite crystallites and 'free growth' (unconstrained by neighbouring crystals) accompanied by monotonously increasing PL intensity; and second, the formation of GBs as perovskite grains impinge upon each other with the loss of solvent.[92] Defective crystallite surfaces form at GBs introducing defect states that quench PL intensity, and increase non-radiative recombination.

The growth of grains can either proceed via a solid-state mode or a matrix-phase-mediated Ostwald ripening process, where large grains will grow at the expense of smaller grains (in a similar process to that of the growth of perovskite nuclei from precursor solution, mediated by the liquid solution phase). In the solid-state growth process, monomer species in smaller grains diffuse across the solid-state GB from the smaller to the larger grain, depleting the smaller grain till it disappears.[93] This growth stagnates as grain diameter approaches film thickness, because at this point, drag forces exerted on the GBs by the bottom interface with the substrate and the top intersection with the surface hinder further growth of isotropic thin films. However, in anisotropic thin films, secondary coarsening may occur, where grains favourably oriented with regards to the substrate grow rapidly at the expense of unfavourably oriented grains. [87] The rate of grain growth is sensitive to the heating regime, with perovskites such as the prototypical $MAPbI_3$ suffering decomposition to PbI_2 if annealing is done for too long at too high a temperature.[94–96] Grain size typically increases with annealing temperature until the onset of thermal degradation at which point material at GBs typically degrades to secondary phases due to the higher crystal disorder (semi-amorphous GBs) facilitating transport of decomposing species.[93] Despite its ease of use in the laboratory, hot-plate annealing is not a very scalable annealing technique, due to the difficulty in obtaining uniform heating throughout the area and thickness of the film. Variations in atmospheric chemistry, air flow, convective heat transfer, variations in thermal coefficients (thermal expansion, thermal transfer) of the hot-plate material, substrate, CTL, and perovskite, and many other effects make it an inconsistent annealing method which results in irreproducible films. An alternative is convective annealing, which raises uniformity of films due to a more homogenous heating environment. However, both processes are relatively time consuming, requiring untenable space requirements for annealing the film if scaled up for roll-to-roll processes. Radiative annealing methods could provide an opportunity for scalable processing, due to their high ramp rates, fine temperature control, and consistency.[97]

To address the issue of large, poorly connected grains, solvent engineering methods have been developed which mainly aim to stimulate a high rate of nucleation over as short a time span as possible, reducing the time available for undesirable structures to grow (such as dendritic morphologies which lead to a discontinuous film), and ensuring a high areal coverage of the film. One way this can be achieved is by application of antisolvents during spin casting. Antisolvents rapidly raise the saturation of the solute by simultaneously reducing the solubility of the precursors in the solution and increasing the evaporation rate of the solvent (as solvent molecules are less strongly conjugated with solute molecules they will more readily evaporate). Examples include toluene, chlorobenzene, and ethyl acetate.[98–100] The rapid nucleation that results from the application of an antisolvent leads to a desirable, compact, dense grain structure. Another approach to achieving this is through vacuum drying after spin casting. This has been used to quickly remove solvent from the film.[101–103] Gas quenching to accelerate solvent evaporation and rapidly raise supersaturation of the solution has also been used.[104] The solvent itself can be changed to achieve the desired rate of supersaturation; for example, the spin-casting from a mixture of methylamine (ME) and acetonitrile (ACN) delivers films with uniform, compact microstructure of large, smooth grains. The perovskite nucleates very rapidly during spin-coating as the solvents rapidly evaporate. Furthermore, the deposited films have carrier lifetimes 20x as long as those from films prepared using DMF, suggesting the use of this method also reduces defects.[101] Solvent annealing methods are yet another technique developed to improve thin film microstructure and morphology. Annealing in a solvent vapour atmosphere results in a larger grain size and increase crystallinity.[105] It is thought that this may occur due

to the dissolution of material at GBs and surfaces in a solvent phase, allowing the reordering of crystals, and GB migration. Huang *et al.* used DMF solvent vapour during annealing of MAPbI3 to obtain 1 μm grains with dramatically improved electrical properties in comparison to films which were simply thermally annealed. The champion device had a PCE of 15.6%.[105] It is common to use a mixture of solvents to attain the desired nucleation and growth of the perovskite phase, most typically DMF and DMSO. The high solubility of precursors in DMF is combined with the longer film drying times offered by solvents like DMSO. As a result many researchers have sought to understand the influence of solvent choice on perovskite film formation.[106]

2.3.3 Precursor Solvents and Importance of DMSO Intermediate

Solvents with a high boiling point have lower evaporation rates and hence suppress nucleation of the perovskite phase from solution, which can lead to non-uniform and rod-shaped grains. A good example of this is the spin coating of stoichiometric mixtures of MAI and PbI2 from DMF.[107,77] Munir *et al.* suggest that the precursor solvate formed during solution processing incorporates solvent molecules in an MAI-PbI2-DMF complex, complexes which are crucial to the formation of the perovskite film. These intermediate complexes either lead to nucleation through the formation of clusters within the solution upon which perovskite nucleation occurs, or continuous precursor thin films in which the perovskite nucleates. Intermediate solute-solvent complexes have varying effects on crystallisation kinetics depending on the solvent molecules. The ease with which perovskite can revert to intermediate species under 100°C is likely responsible for the irreproducibility of devices across a wide range of publications, while also crucial for the growth of perovskite crystals required for high performing devices.

Jeon *et al.* added DMSO as a complexing agent as it complexes more strongly with lead halides than DMF.[98] This led to DMSO-PbI2-MAI or DMSO-PbI2 complexes forming upon spin coating, which were subsequently converted to smooth, compact perovskite films. According to Guo *et al.* there are a wider range of complexes based on DMSO than DMF in terms of the stoichiometry of the crystalline precursor which incorporates it, as shown in Figure 5.[108]
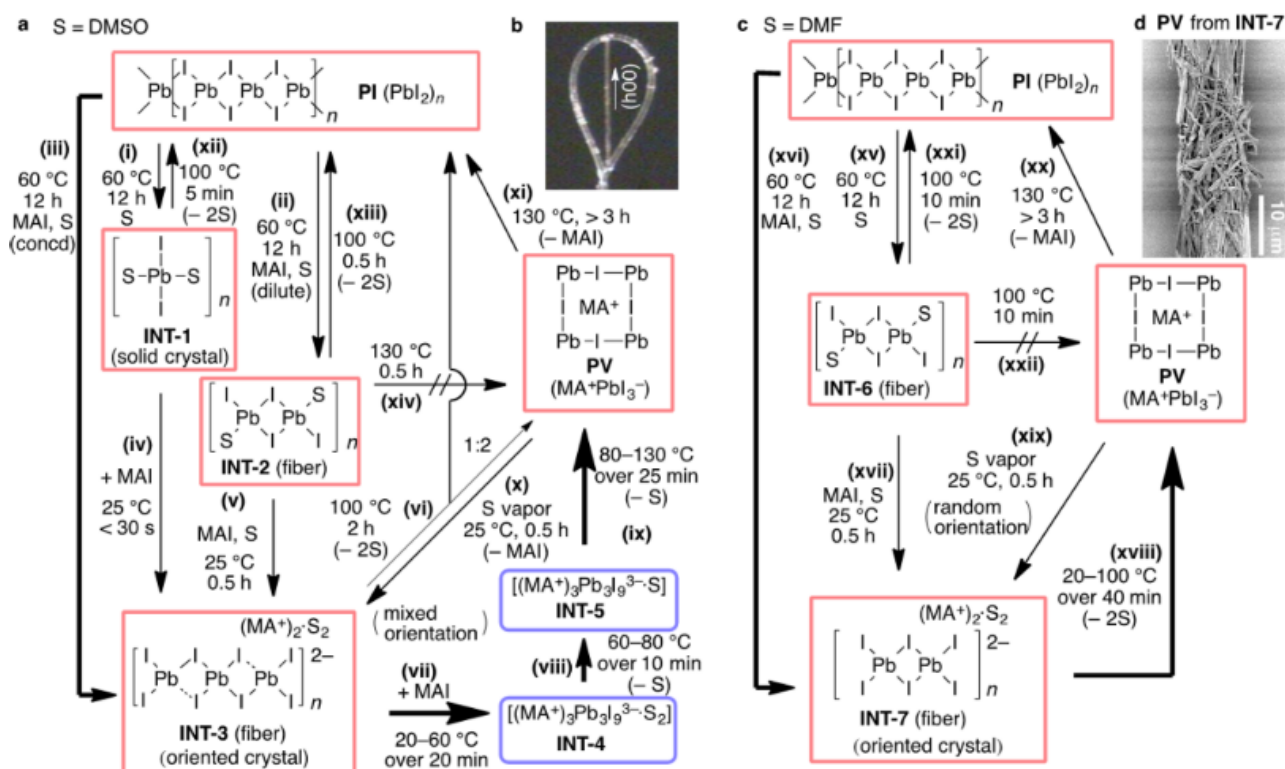
Figure 5: Chemical Reactions and crystalline intermediates occurring during conversion from MAI and PbI2 (PI) to MAPbI3 (PV) when meditated by either DMSO or DMF. Mobile equilibria among various chemical species are established under 100 °C until the solvent is lost from the system by evaporation. Bold arrows denote productive pathways during single crystal formation. (a) DMSO mediated pathways. (b) optical microscope image of an intermediate 3 (INT-3) crystal fibre. (c) DMF-mediated pathways. (d) SEM image of P fibre obtained by annealing INT-7. (Reproduced with permission from doi/10.1021/jacs.5b10599. Copyright 2015 American Chemical Society.).

25

Hybrid Perovskites - Solution Processing

Use of DMSO has been demonstrated to produce more reproducible and higher efficiency devices, and various explanations have been offered for this.[109] Briefly, the MAPbI$_3$-DMF complex is less stable at room temperature than the DMSO equivalent (MA)$_2$Pb$_3$I$_8$-2DMSO (INT-3). This is partially because the DMSO complex will have lower strain (which would arise from the volume difference between the intermediate phase and MAPbI$_3$ perovskite), and additionally because the DMSO complex has a slower crystallisation process (MAI molecules need to diffuse to the growing perovskite phase, as opposed to simple evaporation of excess solvent). The result is a lingering solvent phase which encourages grain growth by solvent annealing. Together, reduced strain and solvent annealing effects reduce defect densities and improve crystallinity of the perovskite film.

Rong *et al.* found that slower diffusion of the DMSO leads to a higher fraction of the intermediate phase (INT-3), and subsequently a smoother surface morphology.[110] According to their research, balanced diffusion of DMSO and MAI at an optimal temperature leads to the formation of fewer pinholes within the film. Rong *et al* found that the rate of exchange of DMSO with MAI governs the formation of the perovskite, as shown in Figure 6A. Figure 6B shows the process can proceed via three different routes during annealing as solvent is driven off the film by evaporation, depending on temperature (reproduced from Rong *et al.*).[110] Investigating the role of intermediate phases in the growth of perovskite crystals, Bai *et al.* highlighted the importance of obtaining the INT-3 phase to grow aligned and high quality perovskite layers on NiO.[111] The addition of DMSO to their solutions of precursor salts and DMF resulted in the preferential nucleation and growth of perovskite along the 110 direction from the substrate upwards during annealing, as opposed to the top-down nucleation in films with only DMF complexes when the antisolvent was applied (the antisolvent induced perovskite nucleation occurred preferentially to the heat induced nucleation.
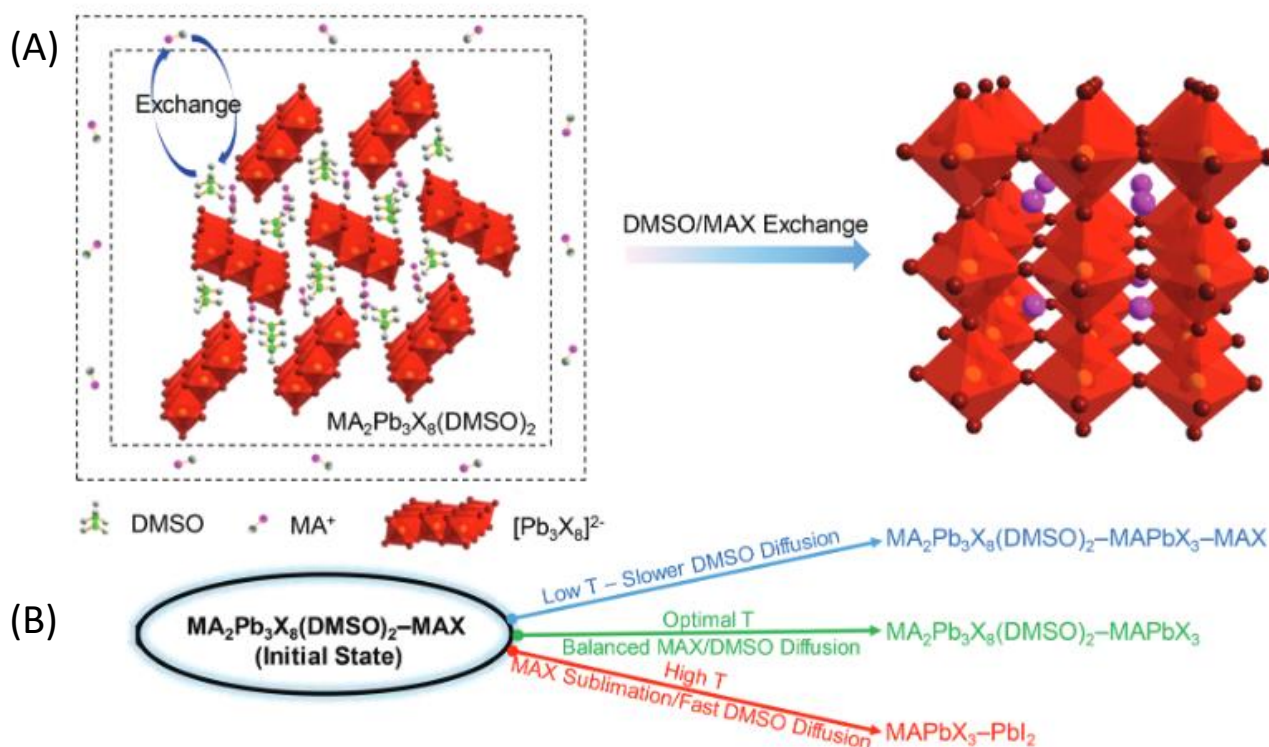
Figure 6: (A) Schematic crystal structure and composition of the intermediate phase and perovskite phase after exchange of DMSO and MAI. (B) Three diffusion pathways to perovskite films showing effect of annealing temperature on final film composition.[110] Reproduced with permission from doi/10.1039/c6nr00488a

DMSO helps to suppress the formation of perovskite, instead leading to the uniform distribution of INT-3 nanorods on the surface which later convert to perovskite. A DMSO: PbI$_2$ ratio of 10:1 delivered the highest performing devices. The utility of INT-3 in grain growth was further displayed by Xiao *et al.,* finding the vapour phase DMSO can react with MAPbI$_3$ at GBs to form an INT-3 phase between crystalline domains. The interconversion between this intermediate and other intermediates facilitates GB migration and hence grain

coarsening.[112] Many routes to obtaining high performing perovskite films for PSCs utilise the DMSO intermediate.[98,108,113,114] Another study by Ozaki *et al.* found the enhanced stability of solvent-intercalated MAPbI$_3$-DMF precursor complexes when dissolved in DMSO widened the timing-critical processing window for antisolvent (in this study toluene) application, allowing for more reproducible films after spin coating.[115] The ratio of DMSO: PbI$_2$ was approximately 9:1, similar to the ratio in the study by Bai *et al.*.

However, Cao *et al.* found that high quality films can be fabricated without exploitation of the Pb$_3$I$_8$ intermediate. In their two-step film deposition method, a mesoporous PbI$_2$ film is first generated by deposition of a DMSO: PbI$_2$ solution in a 1:1 or 2:1 ratio (the as-deposited film containing various precursors) and subsequent heating at 80°C. MAI-IPA solution was then dripped on the film, penetrating the mesoporous channels and resulting in full conversion to perovskite films from PbI$_2$ with negligible lattice expansion.[80] They suggested that the benefit of DMSO was in facilitating the production of a high quality precursor film. Although intermediates can be exploited in producing high quality films, specific intermediates in themselves are not the only approach to high quality perovskite films.

2.3.4 Use of Antisolvents

Preparation of high performing and stable PSCs in ambient air is an important step in developing scalable processing methods for perovskites, as many researchers prepare PSCs in such conditions, and methods to facilitate this production environment will enable wider accessibility. Due to deleterious effects of H$_2$O and O$_2$ on PSC devices, and sensitivity of these films to atmosphere during processing, it is necessary to devise processing methods that produce high quality films resilient to moisture ingress in operation, while also optimising against the presence of moisture during film formation.[116] Deposition is heavily humidity dependent, as demonstrated by Jeong *et al.*, who found MAPbI$_3$ films deposited in a two-step process under 40% relative humidity (rH) had PCE's approximately 10x greater then films deposited at 20%rH.[117] Moisture concentrated at GBs facilitates both lateral and vertical grain growth. This helps neighbouring grains merge via a dissolution and recrystallization process, while also increasing surface roughness due to the 3-dimensional nature of the growth. There is a reduction in GBs area due to grain growth, reducing the presence of non-radiative recombination centres. This reorientation and growth also leads to preferential crystal orientations, as the variation in crystal orientation is reduced, as evidenced by GIWAXS.[117] Moisture activates the reaction between MAI and PbI$_2$. Intermediate perovskite hydrate phases provide faster diffusion pathways due to their larger structural spacing, and the ionisation of MAI increasing its reactivity with PbI$_2$.[116] Aranda *et al.* have suggested that competition between H$_2$O and DMSO to coordinate with Pb atoms limits the formation of the intermediate PbI$_2$:MAI:DMSO complex responsible for the final film properties. As rH rises above 30%, PCE decreases due to the formation of hydrates in the film, leading to pinholes and shunting of devices. Carefully optimising the ratio of DMSO to adjust for the atmosphere rH allows for fabrication of high efficiency devices in ambient conditions with PCE's approaching 19%.[118] For the curious reader, an in depth review of the influence of moisture on perovskite solutions, thin films, and devices has been written by Huang *et al.*.[116]

Fabrication of PSCs with antisolvent in ambient air has become a popular method of mitigating the influence of ambient air.[99,119–123] The spin-casting approach is combined with an antisolvent-induced crystallisation step, where an antisolvent is dripped on the substrate during spinning to increase the precursor solvent removal rate and encourage the nucleation of the crystalline DMSO-intermediate (Lewis-adduct) MA$_2$Pb$_3$I$_8$(DMSO)$_2$, from which the black pseudo-cubic α-perovskite phase forms upon annealing.[13,108,124,125] Further addition of antisolvent (for example ethyl acetate) can induce the nucleation of room temperature stable brown tetragonal β-perovskite by further increasing the solvent removal rate.[109] The desired α-phase is subsequently obtained upon thermal annealing. Taylor *et al.* have demonstrated that antisolvents can be categorised intro three groups depending on their ability to dissolve the organic precursor components, and their miscibility with the precursor solution solvents.[126] A high quality perovskite film can be obtained from any antisolvent when applied at the optimal rate for that specific solvent. Troughton *et al.* proposed that the selection of antisolvent is crucial, observing ethyl acetate (EA) produces better films than chlorobenzene (CBZ), toluene, or diethyl-ether (DE) under ambient conditions. EA has a high affinity for H$_2$O (3.3 vol%) in comparison to DE (1.5%), toluene (0.033%) and CBZ (0.04%). This reduces the formation of hydrated perovskite as more moisture adsorbed into the

precursor film and in the ambient atmosphere will be absorbed by the antisolvent when annealing in air. This was evidenced by diminished XRD perovskite peaks in films treated with toluene, CBZ and DE. SEM supported this, showing greatly reduced pinholes and less variation in grain size, even at 75%rH. Obtaining pinhole free, highly crystalline ordered perovskite films processed under very high humidity conditions when using EA as an antisolvent during deposition demonstrated the feasibility of PSC production without strict atmosphere control. However, the influence of ambient humidity on films processed with EA remained unclear as films produced at an rH of 0% had higher PCE than films produced at 30%rH, which had lower PCE than films produced at 50% and 75%rH.[127]

EA treated MAPbI$_3$ devices have been widely characterised.[119,120,123,127–129] Kim *et al.* sought to understand the effect of EA volume on the formation of perovskite morphologies during fabrication. They found an optimal volume of 40 μl for a substrate of size 2.5x2.5 cm at 20%rH. Insufficient EA didn't remove DMF completely, with residual DMF in the precursor-DMSO complexes producing coarse perovskite morphologies. Excess EA removed DMSO, leading to perovskite crystals forming too early, as there was insufficient solvent to form the intermediate complex required for optimal film formation. At higher rH, the optimal volume of EA increases. Slower evaporation of DMF in the humid atmosphere means more EA is required to remove it. [123] Bu *et al.* emphasised the non-toxicity of EA in comparison to carcinogenic CB, in their work where they showed that the use of EA as a solvent for the HTL (spiro-OMeTAD) as well as an antisolvent for the perovskite produced higher performing devices than CB-dissolved-HTL/EA-treated-perovskite or CB-dissolved-HTL/CB-treated-perovskite devices. EA has an ideal polarity, less than 4.5 — making it miscible with DMF and not perovskite — while greater than 2, allowing it to dissolve spiro-OMeTAD.[129] Zhang *et al.* showed that their ethyl acetate treatment increased the contact angle of water droplets to 89.8° — almost 45° more than ether treated films. This would suggest a more hydrophobic film surface has been obtained. Un-encapsulated devices retained 84.80% of their original PCE after 80 days of ambient storage.[119] They showed using AFM that EA treated films gave a smooth surface, with lower surface roughness and larger grains than ether treated films, which would facilitate reduced interface resistance between the perovskite and CTLs. Additionally, the reduction in GBs means there are fewer defects, and hence reduced ion migration, resulting in better performance and stability. They also use Fourier Transform Infrared Spectroscopy (FTIR) to find that hydrogen bonding occurs between EA and DMSO, which may help ensure regular growth of the intermediate phase by reduced evaporation of the antisolvent and slowed perovskite nucleation. EA treated films have enhanced optical absorption, enhanced photoluminescence intensity, and slower photoluminescent decay, showing the treatment reduces the presence of nonradiative recombination centres, and reduced scattering losses. This is corroborated by devices made by Bu *et al.* who found more efficient carrier extraction and greater carrier lifetimes in EA treated devices, suggesting reduced recombination centre density.[129] The EA treated devices showed better long term air stability, both due to a more hydrophobic film surface (greater water droplet contact angle), and fewer paths for ingress of moisture. Finally, the films showed greater thermal stability due to impeded ion migration as a result of passivated defects.[119] This reduces decomposition of the film (decomposition of films is explored in greater depth later).

Its high boiling point and strong affinity for water are greatly responsible for the desirable interaction of ethyl acetate with precursor films among various antisolvents. Theoretically an antisolvent with even high vapour pressure and greater water solubility within the correct polarity range (2-4.5) would produce an even better film. This would be due to shorter perovskite formation time reducing exposure of the intermediate phase to exposure. This is explored by *Yang et al.* who look at the dependency of films on different acetates. Methyl acetate (MA), with the highest vapour pressure, lowest boiling point, and greatest H$_2$O solubility, produces dense smooth films with even fewer pinholes than films treated with EA. Longer chain acetate solvents are less effective at inducing the perovskite transformation prior to annealing, with more intermediary DMSO remaining in the pre-annealed films. Grain size also increased, supporting the notion that the DMSO-precursor intermediate facilitates grain growth, and that a high evaporation rate leads to a high density of nucleation. The presence of a residual PbI$_2$ phase in the films reduces as the acetate length increases, from MA->EA->PA->BA. This supports the theory the intermediate phase helps coordinate PbI$_2$ to MAI, ensuring more complete conversion to perovskite.[120]

Hybrid Perovskites - Solution Processing

Wang *et al.* developed a theoretical model for the evaporation dependent crystallisation to try and explain the interaction of ambient moisture with the antisolvent during film processing. Using this model, they proposed a humidity insensitive antisolvent method for anti-solvent assisted crystallisation. They earmark the turbid point as a crucial time point during fabrication at which the appearance of the precursor film changes from transparent to turbid – a state defined as cloudy, opaque or thick with suspended matter. It indicates the precursor film is in a state appropriate for antisolvent induced crystallisation, with best results found when the antisolvent dropping occurs several seconds before the turbid points ends. This defines an important processing window for antisolvent application. In their evaporation-crystallisation model, they considered the possibilities that either adsorbed gaseous H_2O changes the perovskite film composition, or H_2O accelerates the reaction between PbI_2 and MAI. A small amount of H_2O in the MAI precursor solution was found to encourage the formation of high quality perovskite films due to enhanced MAI ion mobility by Adhikiri *et al.*[130] Gao *et al.* found that spin coating at higher rH leads to films with poor coverage due to low nucleation density. They proposed that adsorbed moisture acts as a solvent, suppressing the nucleation of the perovskite phase.[131] However, Wang *et al.* showed that H_2O was a relatively poor solvent for perovskite precursors and instead suggested that variation in the results of spin coating induced crystallisation at different rH levels is caused by the suppression of evaporation of precursor solvent by atmospheric humidity. Thus suppression may be related to H_2O and the solvents used (DMF/DMSO) both being polar solvents.

In brief, at low humidity (<70%rH), solvent evaporation is fast, and the solution quickly super-saturates, hence leading to a high rate of nucleation as opposed to nuclei growth. This results in densely aggregated nuclei, and hence the film morphology has numerous small grains. These scatter light strongly, making the turbid point easily observable. At high humidity, evaporation is slow, and hence nuclei growth dominates. The film has fewer, larger grains, with a less obvious turbid point as scattering is weaker. Identification of the turbid point allowed them to determine when the film was in an appropriate initial nucleation state for antisolvent treatment. The turbid point and hence the antisolvent window are increasingly delayed as rH increases. At 70%rH, the initial nucleation state of their films has a nucleation density below the critical amount needed for successful antisolvent treatment. This is likely due to the higher ratio of DMF to DMSO used in their precursor solution (9:1) in comparison to Troughton *et al.* (4:1), as well as their use of DE and CBZ as opposed to EA. As aforementioned, these solvents do not dissolve as much H_2O as EA, and hence more solvent is required for the antisolvent treatment, both to absorb moisture and remove the solvent DMF. The high boiling point of the DMF means DMF remains conjugated to precursor ions for longer, suppressing the formation of the initial nucleation phase appropriate for antisolvent assisted crystallisation of the perovskite phase.

Wang *et al.* theorised that increasing the solvent evaporation rate would allow them to overcome the issue of a delayed and disappearing turbid point as rH increases. They resolve to decouple the turbid point from atmospheric humidity by preheating the substrate. Preheating the substrate thermodynamically favours nucleation in spin coating induced crystallisation. They explain this by considering the free energy of nucleation ΔG^* and critical nucleus radius, r^* using classical nucleation theory for homogenous nucleation, which dominates at high saturation. ΔG^* is composed of a surface term ΔG_S and volume term ΔG_V, and determines whether stable (nuclei do not redissolve) nucleation can take place. Nuclei with $r < r*$ are unstable and will dissolve back into solution.[131] ΔG^* decreases as the volume free energy change per unit (ΔG_V) increases, which increases with increasing temperature, T. Meanwhile r^* decreases as the surface free energy per unit surface area σ decreases, which decreases with increasing T. Preheating followed by antisolvent treatment at the turbid point in an ambient atmosphere leads to films with better optoelectronic performance due to compact, highly crystalline grains. PCE increased as rH increased, and they attributed this to a solvent annealing affect, where the humid atmosphere helps to passivate grain defects in films.[132]

Antisolvents do however have their drawbacks. Their use leads to increase solvent waste requiring safe disposal. Alternative techniques can reduce this — rescinding the need for antisolvents altogether, as in flash infrared annealing as per Sanchez *et al.*, use of quenching gas assisted crystallisation, vacuum flash crystallisation or vacuum assisted annealing, additive assisted (e.g. Acetate, (Ac)) crystallisation, and hot casting.[102,133–137]

2.3.5   Hot casting and Grain Growth

In the hot casting method, the substrate is heated above room temperature prior to spin-coating, with the aim of increased grain growth. The hot substrate causes partial de-wetting (higher contact angle between the solution and substrate surface) of the precursor solution due to the high interfacial energy, as well as a thermal gradient between the substrate surface and the thickness of the deposited solution, which is at a much lower temperature. Nie *et al.* use such a technique, heating the substrate to 180°C and observing large, millimetre scale leaf-like structures composed of smaller micron-scale sub-grains covering the substrate surface.[138] Deng *et al.* observed a similar microstructure in films made using a doctor-blading process on preheated substrates, and attributed the morphology to convection driven crystallisation. The thermal gradient between the substrate and ambient air creates fluid convection, developing a microstructure of concentric rings of crystals.[14] It is proposed they form by Raleigh-Bénard convection: Hot solution heated by the substrate rises to the surface, and when it does it cools, flowing back to the bottom. Multiple convection cells form within the film, all pushing against each other to form polygons containing concentric rings of crystals.[14] This approach has clear potential in one-step spin deposition methods, with Nie *et al.* reporting champion PCE of 18%.[138]

2.3.6   Effect of Ambient Temperature

While the use of antisolvents somewhat ameliorates the deleterious impact of ambient humidity on film formation, there is also the issue of ambient temperature variation when processing under ambient conditions. Molenda *et al.* showed that a temperature increase of 10°C (20°C-30°C) was sufficient to reduce PCE of MAPbI$_3$ devices cast from DMF from an average of ~11% to ~4%, while also increasing the standard deviation between samples. Increasing temperature increases the evaporation rate of the solvent, increasing the partial pressure of solvent vapour and thereby influencing the perovskite crystallisation. They found a higher abundance of structural defects in the samples fabricated at higher ambient temperatures, evidenced by decreased electroluminescence, higher Urbach energy, and greater prevalence of PbI$_2$ impurities in XRD.[139]

2.4   Investigating Film Evolution from Deposition to Decomposition

Investigating the film evolution from the point of deposition to the end of perovskite conversion and thereafter to degradation is a challenging prospect due not only to the complexity of the structures under investigation, particularly during the early stages of film formation, but also due to the wide-ranging factors which can affect the final film microstructure and morphology. Such factors include the temperature of the substrate and the concentration and composition of the precursor solution, to annealing time, intrinsic instability of the perovskite phase, and damage due to the measurement process itself.[140] Deconvoluting all these factors to try and understand the contribution of any one to the crystallisation process is made even more difficult by the limited reproducibility in film formation methods used, and comparisons between findings are often further complicated by differences in material systems used. Even when there is consistency in the perovskite stoichiometry investigated (for example MAPbI$_3$), findings may not always be directly applicable to perovskite systems that would be used in up-scaled, real world devices, which may follow different processing routes or consist of different elements.[141] In many investigations, 2D X-ray diffraction techniques (XRD) or grazing incidence X-ray diffraction techniques are invaluable in probing the crystal structure. These measurements can be done on samples as they are deposited and annealed *in situ*, allowing continual monitoring of the phase transformations and structural changes occurring during film evolution. Grain size, disorder, preferred orientation, and phase analysis can all be measured.[142] These techniques can be further complimented by microscopy techniques to elucidate morphology and crystal structure, luminescence and impedance measurements to understand optoelectronic characteristics, or even *in operando* current-voltage (J-V) measurements.[143]

2.4.1   Crystallisation Kinetics of MAPbI$_3$ based films

Tan *et al.* used *in situ* grazing-incidence wide angle spectroscopy (GIWAXS) on MAPbI$_{3-x}$Cl$_x$ in mesoporous Al$_2$O$_3$ to characterise the material evolution of three distinct compound structure stages during thermal annealing; a crystalline precursor, a 3D perovskite, and finally the degradation product of PbI$_2$ after annealing. This was one of the first attempts to characterise the crystalline precursor to perovskite transformation in hybrid perovskite films. The power of this technique is immediately clear, allowing the probing of microstructure of thin films while

avoiding the substrate bulk.[144] In previous work by our group, Alhazmi *et al.* used WAXS to investigate the crystallisation dynamics in $MAPbI_{3-x}Cl_x$ and fit the normalised intensity of the various phases present to an Avrami model. The $MAPbI_3$ film formed upon annealing from a 1D intermediate, with Cl ions not present in the $MAPbI_3$ crystals. A similar WAXS methodology is applied in this manuscript in Section 6. In another prior work by our group, Pineda *et al* used GISAXS and optical microscopy to characterise the nucleation and growth of $MAPbI_{3-x}Cl_x$ bar coated films with addition of 1,8-diiodooctane (DIO) and hydroiodic acid (HI).[145] They revealed that while the pristine $MAPbI_{3-x}Cl_x$ film has a reaction-controlled growth mode, limited by the slow nucleation rate; the film with addition of HI and DIO follows a diffusion-controlled growth mode, where growth of crystals is limited by the aggregation of neighbouring crystals rapidly nucleated by the additive. The high nucleation density itself acts as barrier to crystal growth, with neighbouring nuclei competing to accumulate material. They identify 3 stages in perovskite crystallisation in bar coated films deposited on a substrate at 60°C.

The influence of annealing time and temperature was further studied by Dualeh *et al.* investigated the conversion from a precursor solution of (MAI: $PbCl_2$ in a molar ratio of 3:1 in DMF, deposited on mesoporous TiO_2 ($mTiO_2$) to perovskite in terms of the annealing temperature. The effect of annealing temperature on film formation, morphology, and composition was correlated using a combination of UV-Vis spectroscopy, SEM and XRD. These experiments found the incomplete conversion of the precursor to perovskite at lower temperatures (<80°C) and the occurrence of PbI_2 at high temperature (≥120°C). Device characterisation was done using J-V curves with the best performing devices being those annealed at the optimum temperature of 100°C. Finally, impedance spectroscopy (in the dark) was used to study the effect of annealing time on the charge transfer properties of the film. Recombination resistances and chemical capacitance were extracted from impedance data and from this data it was inferred that the formation of a barrier to electron extraction at the $mTiO_2$ interface causes injection limitation. This band misalignment's origin is linked to the presence of either precursor or PbI_2 phases, dropping the CB of the perovskite while also acting as electron sinks, reducing the build-up of charge in the $mTiO_2$. Under forward bias, the chemical capacitance shows typical exponential behaviour for films annealed at 80°C, but as annealing temperature is increased above 80°C, the effect of band misalignment on reducing the capacitance becomes more dominant and occurs at lower forward bias. This is correlated with increased PbI_2 formation and larger perovskite grains, however an explicit dependency is not proven.[96]

The effect of specific lead halides on the precursor-perovskite transformation has been studied by numerous researchers. Notably Moore *et al.* found that crystallisation kinetics of perovskite formation were rate-limited by the removal of excess organic salt from the precursor in deposition of non-stoichiometric ratios of Pb and MA salts in DMF. The activation energy (E_a) for removal of excess organic salt was directly related to the lead salt used.[137] This was further confirmed by Munir *et al.* and Stone *et al.*, finding the $PbCl_2$ derived precursor in $PbCl_2$-derived $MAPbI_3$ didn't incorporate the solvent phase, with perovskite formation slowed by the gradual evaporation of excess MACl.[77,146]

Moore *et al.* investigated the effect of the lead halide anion on the crystallisation kinetics through analysis of *in situ* wide angle X-ray scattering (WAXS). They developed a kinetic model from extracting data on the transformed fraction of hybrid perovskite films and used this to find the E_a for the precursor to perovskite transition for a variety of lead salts. They showed that the first step in perovskite formation from non-stoichiometric ratios of Pb and MA salts deposited from a solution of DMF was the removal of excess organic salt from the precursor, and that the E_a depended on the lead salt used. This understanding was used to inform processing, allowing the optimisation of crystal growth and film morphology through selection of the appropriate lead salt for the precursor solution.[137]

Moore *et al.* and Munir *et al.* both found that the $PbCl_2$ derived precursor likely does not incorporate the solvent phase. Unger *et al.* suggested the existence of a complex precursor phase, which was later probed using X-ray absorption near-edge structure measurements by Pool *et al.* revealing the precursor likely contains MACl and other species containing Pb-Cl bonds.[147,148]. The precise precursor structure remained elusive until Stone *et al.* approached the problem, using a combination of *in situ* grazing-incidence XRD (GIXRD) during annealing at 100°C of spin cast films, as well as extended X-ray absorption fine structure measurements (EXAFS). GIXRD differs from GIWAXS in that it operates over a larger range of angles, from 5-90° as opposed to 1-45° in GIWAXS (WAXS and GIWAXS are discussed in detail in Section 5.2. With evidence from these experiments they identified a crystalline

precursor to be MA_2PbI_3Cl, existing in equal fraction to a disordered MACl phase in the as spun film. They then performed *in situ* X-ray fluorescence (XRF) during the phase transformation, and developed a self-regulating model to describe the transformation, where the conversion from precursor to perovskite is slowed and rate-limited by the gradual evaporation of excess MACl. This prevents rapid crystallisation upon solvent drying, enabling the formation of compact, high quality films.[146] The importance of removal of the organic salt was demonstrated by Zhang *et al.* in their systematic study of the role of the anions in the lead salt, enhancing perovskite film smoothness and surface coverage through accelerated growth kinetics using the readily volatile MA(Ac) by-product.[78]

Hu *et al.* investigated the perovskite crystallisation kinetics and growth mechanism in real time from liquid precursor to final perovskite film for $MAPbI_3$ films spin cast from a solution of $Pb(Ac)_2$ and MAI in 3:1 ratio in DMF. Using *in situ* GIXRD and FTIR (Fourier Transform Infrared Spectroscopy) to reveal the structure transformation of the film phases, they identified the presence of $[PbI_6]^{-4}$ centred ion cage intermediate structures in the as-deposited film. They propose a nano-assembly model to describe the stacking of intermediate cages as solvent evaporates, and their transformation to stable perovskite crystals. Complimentary to this, SEM and AFM were used to reveal the periodic banding of the sub-granular structure — akin to ripples in water. They explain the periodic crystallisation growth during annealing at elevated temperature with a crystallisation depletion mechanism, and with this understanding create a kinetically trapped morphology by rapidly increasing solvent evaporation using hot-air-quenching to obtain smooth, compact films.[149] However kinetically trapped morphologies are often in a state removed from equilibrium where kinetic processes such as ordering or phase segregation are favoured, which could result in changes in performance during operation under the stimulus of light, heat, and electrical fields.

The rate of removal of $PbAc_2$ has been linked to improved crystallinity, grain size, and uniformity of coverage by various authors.[150–152] In research by Sanni *et al.*, pre-anneal 'ageing' (drying in air) time could be optimised to improve the film quality. [152]They found 200 s to be better than immediate thermal annealing and better than 600 s of ageing for the film quality, with fewer pinholes, higher crystallinity and a larger PCE with less variation in results across cells. They attributed this to the partial nucleation of perovskite during the end of spin-coating and pre-annealing, leading to less abrupt removal of $Pb(Ac)_2$ in subsequent annealing at 90°C. Besides emphasising the importance of optimising nucleation vs growth, this highlights the sensitivity of the perovskite film to conditions during every stage of film fabrication. Where possible, all these conditions should be reported in a paper concerned with repeatability of its findings (See Appendix, 13.1, Table 3).

2.4.2   Crystallisation Kinetics in Mixed Perovskites

The crystallisation pathways of mixed perovskites have been an important area for the research field to understand, due to their tuneable band gap, making them ideal for application in tandem solar cells. Three stage in the formation of mixed perovskite (containing a mixture of FA, Cs, MA on the A-site, and I and Br on the X-site) films have been identified. Following spinning of the initial precursor solution, a hexagonal delta phase forms which possesses a sensitive annealing window. Annealing during this window mitigates the formation of hexagonal polytypes during crystallisation. Cs cations promote the formation of the desirable α phase, and inhibit formation of intermediary polytypes. Incorporation of MA^+ also stabilises the cubic phase through lattice contraction. Br^- incorporation changes the crystallisation kinetics due to its lower solute-interaction, enhancing the nucleation rate.[153] Failure to promote formation of the α-phase during this annealing window leads to the appearance of a complex phase mixture of hexagonal polytypes, $MAI-PbI_2-DMSO$, intermediate, and the perovskite α-phase.[154] The crystallisation sequence of mixed ion perovskites has been identified as a transformation from the 2H phase (δ-phase hexagonal polytype) to 4H, then 6H, and then finally 3C, a transformation sequence typically found in inorganic metal oxide perovskites under extreme conditions.[155] It has been shown that addition of mixed cations and halide ions to $MAPbI_3$ delays the production of secondary phases and by-products during spin-coating, facilitating the conversion to perovskite after dripping CB.[156] The window for antisolvent application increases from seconds to several minutes. This is useful as the conversion to perovskite is heavily influence by the quality and crystallinity of the intermediate film. The formation of perovskite intermediates is also related to the relative humidity during fabrication, with perovskite appearing

more readily at <5%rH then at 40%rH, where perovskite doesn't occur (without application of antisolvent). In FACs, with application of antisolvent to films prior to annealing, the perovskite phase nucleated immediately without generation of undesired phases even at moderate levels of rH.[157]

2.4.3   Strain effects in thin films

Grain rotation or reorientation and lattice expansion/contraction was explored by Lilliu *et al.* using a novel method of tracking texture evolution during deposition and thermal annealing of $MAPbI_3$ using a self-organising map which tracks the diffraction spots of single crystallites from *in situ* GIWAXS. They found that during deposition and annealing of films deposited via spray coating and spin coating, single grains underwent rotation or reorientation. The number of spots increased with precursor film hydration or relative humidity. The statistical picture of texture evolution their method produced could likely be driven by strain in the film arising from film processing and formation.[158] Jones *et al.* made progress explaining this, using correlative synchrotron XRD and time-resolved photoluminescence (TRPL) on the same scanning area to reveal lattice strain is associated with a high defect concentration and non-radiative recombination. They propose the strain arises during the cubic to tetragonal phase transition (57°C) due to constrained (or unconstrained) local environments established in the initial steps of film growth and crystallisation, where heterogeneous nucleation and growth lead to inhomogeneous crystallites. They also find the strain heterogeneity ranges across varying length scales, from the nanoscale sub-grain to long-range super-grain clusters (regions of grains with similar orientations on the scale of 10 s of microns). It raises the question of whether focusing on single grains in hybrid perovskites is sufficient to understand the interplay of strain and optoelectronic performance.[159] Strain in these films had also been traced back to the thermal expansion mismatch between the perovskite material and substrate during annealing by Zhao *et al.*, who found it to be an intrinsic source of instability in perovskite films which reduced the E_a for ion migration. This can be related to the presence of more defects in strained films, which opens channels along which ions and other external species such as H_2O or O_2 may migrate, accelerating the decomposition rate under illumination.[160]

Zhu *et al.* expanded the understanding of strain in the films by studying the evolution of residual strain in mixed perovskite films using depth dependent GIXRD. They identified a gradient distribution of in-plane strain perpendicular to the substrate, where tensile strain decreases from the surface of the film to the substrate. This strain heterogeneity was confirmed with TEM at different depths, showing an increase in lattice constant with depth from the surface. This was correlated with changes in composition from the surface to the bottom of the film, with time-of-flight secondary ion mass spectrometry (TOF-SIMS) and transmission electron microscopy/energy dispersive X-ray spectroscopy TEM/EDX mapping revealing the gradient distribution of MA^+ which substantially decreases from the surface to the bottom. Compositional distribution and gradient thermal stresses are both linked to gradient residual stress. The effect of residual stress on charge carrier dynamics and photovoltaic properties are also investigated. Depth dependent PL spectra show a decreasing band gap with depth of the perovskite film, while it is found through first principle calculations that the strain induces band bending on the perovskite, reducing hole carrier transport and extraction. As the film grows from the substrate surface up, a thermal gradient between the hotplate and ambient may be partially responsible for the observed strain in the film, driving crystallisation in material nearer the heat source and hence limiting the diffusion of MA^+ into the non-stoichiometric perovskite.

These studies amongst scores of others have made significant progress towards explaining perovskite film formation, but there remains work to be done in providing a holistic and complete explanation of the film formation process which is generally applicable to all hybrid perovskites while considering the process alterations and variations from the wide range of internal and external factors. And how can the film microstructure and morphology be related to perovskite instability, degradation, hysteresis, and ion migration?

2.5   Devices

Perovskite devices are typically planar stacked structures, where the perovskite absorber is placed between a p-type hole transport layer (HTL) and n-type electron transport layer (ETL), which respectively contact a cathode and anode. The regular n-i-p structure (see Figure 7) and inverted p-i-n structure are planar heterojunction

architectures, and commercially the most prevalent amongst thin film solar cells architectures in organic and inorganic devices. The inverted structure swaps the positions of the electron and hole selective layers with respect to the substrate. In this work, regular perovskite devices will be chiefly fabricated with an architecture as shown in Figure 7A, where the HTL is PTAA, the ETL is SnO_2 and a cathode of Ag or Au is used. Other device architectures include mesoporous devices, the parent structure of the now typical planar stacked structures, inverted planar heterojunctions and interdigitated back contact devices.

Mesoporous devices (Figure 7D) use a porous ETL transport layer as an intermediary surface-area enhancing matrix between the photoactive material and a compact ETL. This structure is typically used when fabricating cells with ink-based methods, penetrating the mesoporous layer with the ink before annealing to remove solvent. Interdigitated back contact devices position the electron and hole selective electrodes on the backside of the cell in an interdigitated pattern, as shown in Figure 7B. The active layer is deposited on the electrodes. This architecture prevents optical losses due to the top electrical contact, as the device can be illuminated from the top surface.[161] It also allows surface sensitive in-operando studies to be done, allowing characterisation of optoelectronic and structural properties of the perovskite active layers post-fabrication using methods such as GIWAX, Focused ion beam- SEM (FIB-SEM) and Laser-beam-induced current (LBIC), as demonstrated by Alsari *et al.* and Wong-Stringer *et al.*[143,162]
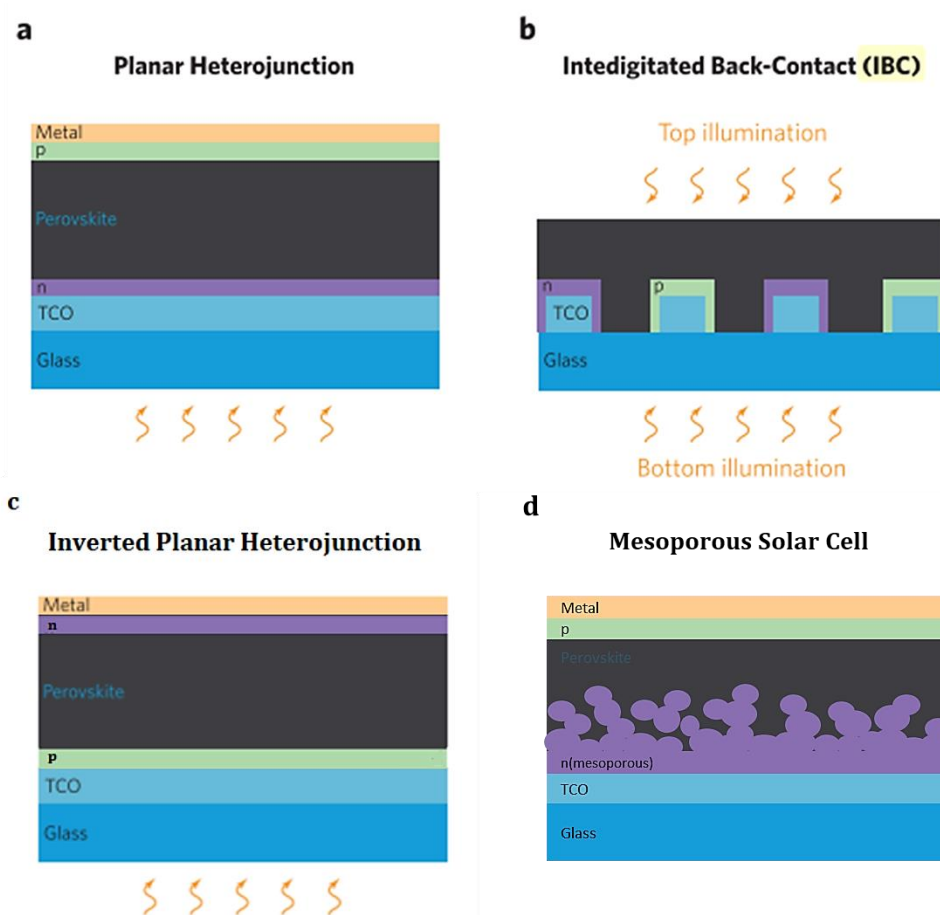
Figure 7: (A) A regular n-i-p planar heterojunction device and (B) Interdigitated back contact device. In both structures' 'p' is the hole selective material, and 'n' the electron selective material. The TCO is a Transparent Conducting Oxide allowing light to pass through while also conducting electrons and acting as the cathode. The Metal acts as the anode. (Reproduced from 10.32386/scivpro.000005 under Creative Commons License) (C) Inverted planar heterojunction, (d) Mesoporous solar cell schematic. Circles represent the porous scaffold.

2.6   Film and Device Degradation

Unpackaged PSCs degrade within a few hundred hours of exposure to air with rH>50%.[163] Moisture induces a combination of reversible and irreversible changes in the film, depending on the extent of exposure. Resistance to oxidation is also beneficial; while many metal halide perovskites are relatively stable when left in the dark,

they will rapidly degrade when in the presence of O_2 and light, through the light-accelerated process of photo-oxidation.

Rand *et al.* performed a comprehensive study of the chemistry of perovskite optoelectronic devices.[62] They found redox chemistry plays an underlying role in determining the degradation processes in perovskite devices with Ag/Al/Yb/Cr metal contacts. In-situ XRD revealed the spontaneous reduction of Pb^{2+} to Pb^0 in the presence of Al^0, converting $MAPbI_3 \rightarrow MA_4PbI_6 \cdot 2H_2O \rightarrow MAI$. In-situ SEM shows that H_2O facilitates ion diffusion, enabling the continued reaction of the Al and perovskite layers. While not necessary for the redox reaction to occur, it facilitates the diffusion of unreacted PbI_2 to the Al^0 electrode. As shown in Figure 8, the redox reaction occurred for all metal contacts except Au.

While Ag showed evidence of the reaction, the peaks from Pb^0 were relatively small, and due to the lower price of Ag compared to Au, Ag is chosen for device studies in this thesis. There are exceptions where Au is used due to the higher expected PCE associated with these devices (see Section 6). Unlike certain previous research Al is not used due to the rapid redox chemistry and resulting degradation would impact device characterisation and in particular studies of device degradation. The use of an interlayer between the perovskite and Ag (a PTAA based hole transport layer to enhance charge extraction) further acts as a buffer against metal contact induced degradation. This study has emphasised that degradation investigations need to focus on the whole device and not just thin films, as critical chemical reactions can stem from intrinsic interfacial interactions between layers. Moisture's role as a decomposition reagent in perovskite films is only secondary to the more dominant device degradation pathways at metal contact interfaces, where moisture facilitates reduction of the perovskite.
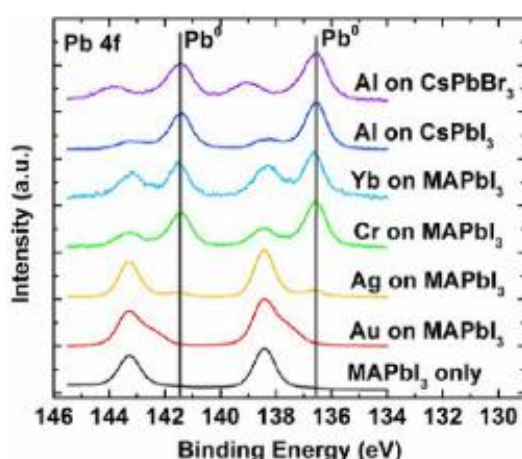
Figure 8: Pb 4f Xray Photoelectron Spectroscopy spectra of samples with Al, Yb, CVr, Ag, and AU metals deposited directly on various perovskite films. All perovsite/metal interfaces show evidence of redox chemistry with the presence of Pb^0 peaks except for the MAPbI3/Au interface. (Reproduced with permission from doi/10.1021/jacs.5b10599. Copyright 2015 American Chemical Society.)

2.6.1   Moisture and O_2 stability

Boyd *et al.* reviewed the understanding of degradation mechanisms in perovskites for photovoltaic applications.[164] Their review of the literature on humidity showed that H_2O can easily penetrate the perovskite crystal structure and form intermediary monohydrate and dihydrate perovskite phases, shown in Figure 9. These changes are generally reversible, with hydrate structures being shown to covert back to crystal perovskite after 48 hours in dry air, evidenced by an XRD study by Legey *et al.*.[165] Schlipf *et al.* found that the trend of water uptake exhibits a plateau between 30%rH and 60%rH attributed to crystal surfaces becoming saturated with adsorbed water.[166] At higher humidities, this water is incorporated into the crystal and hydrates form. Toloueinia *et al.* using dark pulse discharge measurements similarly found that at 60%rH there is no penetration of water into perovskite film whereas at 100%rH the number of ionic species increases with the formation of PbI_2 and aqueous MAI.[167]
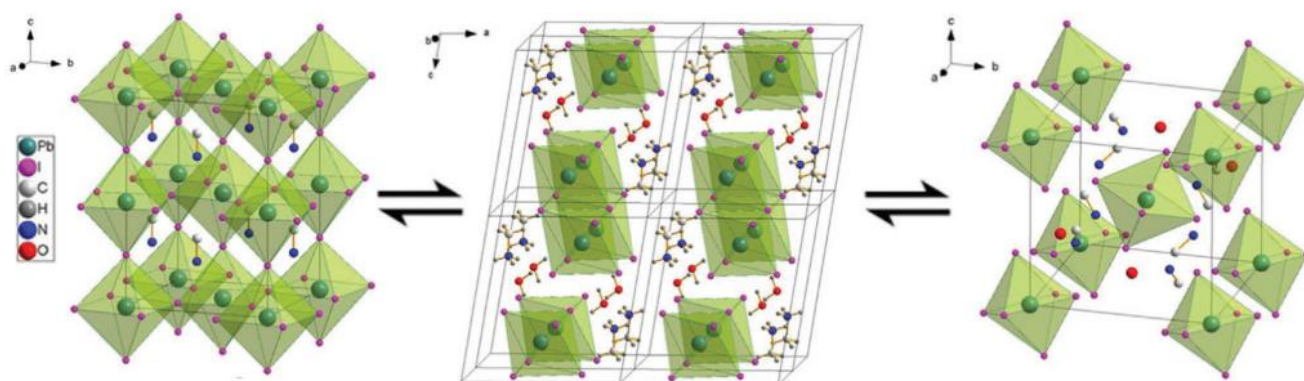
Figure 9: Structure of MAPbI$_3$ (left), monohydrate MAPbI$_3\bullet$H$_2$O (middle), and dihydrate (MA)$_4$PbI$_6\bullet$2H$_2$O (right). (Adapted with permission from doi/10.1021/acs.chemmater.5b00660. Copyright 2015 American Chemical Society.)

H$_2$O molecules in the perovskite form strong H-bonds with organic cations, weakening the bond between the cation and PbI$_6$ octahedral cage. This enables more rapid deprotonation (removal of hydrogen) of the organic cation, which leaves the perovskite more susceptible to the deleterious effects of exposure to electrical fields or heat.[95,168] Water reacts with Iodide (I$^-$) to create hydroiodic acid. The reaction of perovskite with H$_2$O leaves PbI$_2$ after decomposition. Ab initio calculations by Azpiroz *et al.* suggest that PbI$_2$ terminated surfaces have a lower degradation rate than MAI-terminated surfaces, which readily react with the hydroxide ions to form a hydrate phase.[169] Frost *et al.* propose the decomposition pathway in Figure 10. H$_2$0 is required to initiate the reaction (a), producing soluble HI (b), volatile, gaseous Methylamine (CH$_3$NH$_2$, c), and finally H$_2$O and PbI$_2$ (d).[170]
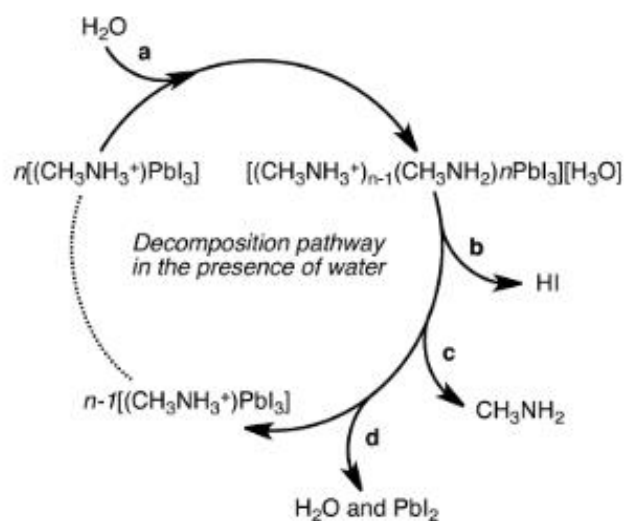
Figure 10: Potential moisture-initiated decomposition pathway presented by Frost et al., Reproduced under ACS Author Choice/Editors' Choice usage agreement from doi/10.1021/nl500390f

MAI-terminated surfaces are more prevalent at GB regions than between grains. GBs act as initiation sites for the decomposition to moisture, and provide a rapid diffusion pathway for moisture into the perovskite bulk. Liao *et al.* performed nanoscale mapping of the humidity induced degradation of polycrystalline MAPbI$_3$ films. Their findings suggest that the reaction proceeds initially through the humidity induced grain growth and atomic rearrangement, followed by formation of a monohydrate layer in the GB region which, due to its low stability at room temperature, degrades to PbI$_2$ through the evaporation of MAI and H$_2$O over the course of 2 days. Moisture continues to diffuse through the semi-amorphous hydrated GBs repeating this process, and these GBs are the last surfaces to develop PbI$_2$. PbI$_2$ eventually covers surfaces(facets contacting the air, substrate or other layers) and GBs, limiting further moisture ingress, or loss of the metastable hydrated phase. [171] The whole process takes several days. Films with smaller grains have as such been shown to degrade faster, with this trend holding true regardless of the film fabrication method.[172]

Hybrid Perovskites - Film and Device Degradation

Haque *et al.* have thoroughly investigated the decomposition reaction of lead halide perovskites, finding that diffusion of O_2 into bulk MAPbI$_3$ films occurs immediately upon exposure to air, and is complete within an hour.[55,173–175] Molecular O_2 adsorbs at iodide vacancies on the surface and diffuses through iodide vacancies in the bulk.[55] I$^-$ vacancies (V_I^+) have an intrinsically high concentration, and are rapidly generated upon photoexcitation (outlined in section 2.7.1). Once adsorbed at vacancy sites, O_2 in V_I^+ sites act as traps for photo-excited electrons in the conduction band. The O_2 becomes reduced to a superoxide species; O_2^-. The negatively charged species reacts with highly positively charged A-site protonated cations in an acid-base reaction that creates H_2O, deprotonated A-site gas such as methylamine, PbI$_2$ and I$_2$, as per the reaction:[176]

$$4CH_3NH_3PbI_3(s) + O_2(g) \xrightarrow{light} 4PbI_2(s) + 4CH_3NH_2(g) + 2H_2O(g) + 2I_2(g)$$
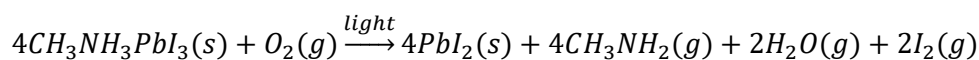
This is also found by Liao *et al.*, who build upon their understanding of ambient humidity degradation in their work exploring photo-degradation of MAPbI$_3$. Using in-situ scanning probe microscopy they find PbI$_2$ — as opposed to a hydrated perovskite phase — forms at the surface after aging under light in humid air. The reaction of photo-excited MAPbI$_3$ with the superoxide species is energetically favourable. O_2 diffuses through the PbI$_2$ layer to react with the MAPbI$_3$ beneath, growing a porous PbI$_2$ nano-layer. H_2O, which forms as a reaction by-product both catalyses the degradation reaction by stabilising the superoxide species, but also promotes densification of the PbI$_2$ layer. This densification is enhanced by ambient humidity which rapidly diffuses along GBs to the PbI$_2$ layer, facilitating recrystallisation and densification. Eventually this layer blocks the in-diffusion of O_2 and humidity from the environment, by capping GBs and stifling diffusion.[177]

It would follow that less acidic A-site cations such as formamidinium (FA) or caesium will be more stable to photo-oxidation. It is also critical to control the density of iodide ion vacancies in perovskite films in order to suppress the adsorption of O_2 at these sites, and diffusion through the bulk. This can be achieved by atomic substitution to increase the strength of the interaction between cations and halide anions, as described before, as well as surface passivation techniques.[52] Atomic substitution is also an effective strategy for improving moisture resilience. X-site and A-site substitution can enhance the interaction between the A-site cations and Pb ions reducing the lattice cell parameters and ensuring the crystal retains the perovskite crystal structure upon extended moisture exposure. The instability of the MAI cation in the presence of moisture and light irradiation is due to facile oxidation of the iodide anion.[326] Replacing the MA$^+$ cations with less acidic cations such as FA$^+$ (CH(NH2)2$^+$) or Cs$^+$ also reduces deprotonation and stabilises the perovskite lattice.[164,184] Substitution of MA$^+$ with FA$^+$ has been investigated due to a favourable band gap and greater thermal and photo-stability.[185,186] Due to inherent volatility of the MA$^+$ cation the mixed MA$_x$FA$_{1-x}$PbI$_3$ perovskite has been further stabilised by addition of Cs$^+$ by various researchers, or the removal of MA$^+$ in favour of a Cs$^+$ component.[184188–190] A-site substitution with Cs$^+$ has been show to increase moisture, thermal, and photo-stability in FA$_{1-x}$Cs$_x$PbI$_3$, FA$_{1-x}$Cs$_x$PbI$_{1-y}$Br$_y$ and Cs$_x$(FA$_{0.83}$MA$_{0.17}$)$_{100-x}$Pb(I$_{0.83}$Br$_{0.17}$)$_3$)$_{0.95}$.[191,192] The small ionic radius of Cs$^+$ (1.67 Å) in contrast to FA$^+$ (2.53 Å) and MA$^+$ (2.16 Å) improves bonding between the organic cation and [PbI$_6$]$^{2-}$ octahedra.[184] It also prevents I$^-$ migration, a crucial factor in device instability.[16] The lattice parameter can be further tuned by halide substitution of I$^-$ with Br$^-$ (X-site substitution) There is a linear relationship between the Br content and the lattice parameters of MAPbI$_{3-x}$Br$_x$ phases, with a tetragonal-cubic transition between x = 0.13 and 0.20.[195]

Black photo-active α-FAPbI$_3$ is thermodynamically unstable below 150°C, converting to a yellow non-perovskite hexagonal phase δ-FAPbI$_3$ at room temperature.[187] In humid and dark conditions FAPbI$_3$ typically transforms to its constituent salts or its δ-phase. At 50%rH, the α-phase FAPbI$_3$ degrades into yellow δ-phase and PbI$_2$. After 6h at 85%rH, the FAPbI$_3$ perovskite degrades completely to PbI$_2$.[178] The moisture-induced phase change is initiated at GBs and proceeds towards the grain interior. According to Raval *et al.*, the α-δ phase change involves a surface initiated local diffusion and precipitation mechanism, with H_2O acting as the solvent.[179] In contrast to FAPbI$_3$, FAPbBr$_3$ is thermodynamically stable under the same conditions.[179,180] Although single A-site cation perovskites based on FA$^+$ cations readily transition from the α phase to δ phase under ambient conditions, when FA$^+$ is alloyed together with Cs$^+$ and MA$^+$ in optimal ratios they produce a much more stable cubic perovskite lattice.

In CsPbI$_3$ films degradation is similarly induced by moisture. H_2O adsorbed on α-CsPbI$_3$ films may catalyse the phase change by inducing halide vacancies and lowering the free-energy barrier for nucleation. The high

solvation enthalpy of halide ions coupled with low vacancy formation energy means halide vacancy concentration increases with humidity as Halide ions react with Hydrogen and volatilise (e.g. HI). The presence of vacancies lowers the formation energy of an interface between α and δ phases, facilitating conversion.[178] Evidence for the action of moisture also comes from Cordero *et al.*, who show H_2O diffuses both along perovskite GBs and via interstitial sites. They claim H_2O both catalyses the interconversion between the α-δ phases, and forms bonds with the FA (or MA) cation, increasing its effective size and shifting the structural equilibrium towards the δ and hydrated phases.[181] Hidalgo *et al.* found that when air acted as the carrier gas for humidity, the formation of δ-phase $FAPbI_3$ was accelerated; while this work is still in exploratory stages, it is plausible that O_2 plays a role in this enhanced reaction.

Kazemi *et al.* found that in triple cation mixed halide perovskite, degradation under 85%rH of the perovskite follows two concomitant pathways. The first leads to formation of PbI_2, while the second leads to a combination of $CsPb_2Br_5$ nanocrystals and Cs-poor I-rich perovskite.[182] According to Hidalgo *et al.*, intriguingly, for mixed iodide-bromide halide perovskites degradation proceeded through non-perovskite hexagonal phases such as 4H and 6H. Bromide addition hindered degradation.[183] Despite these observations it is not clear whether a hydrated perovskite phase arises during the moisture induced decomposition in mixed cation mixed halide, FA based perovskites.

While these strategies are effective in reducing degradation, a performance reduction persists even in encapsulated devices over hundreds of hours of illumination under dry conditions. There have been many contributions to understanding the degradation routes in some mixed cation perovskite films. Ho *et al.* found that under light and high relative humidity, $FA_{0.85}Cs_{0.15}PbI_3$ degradation follows a multistage pathway.[196] In the first stage between 0-11 hours, PbI_2 rich depressions form as FAI evaporates. The mixed cation phase separates into $CsPbI_3$ needles and large $FAPbI_3$ grains. Degradation stops for a couple hours, before proceeding in the second stage with the shrinking of the $FAPbI_3$ grains. However, at 85%rH in the dark, depressions are not formed, and instead large grains develop after 80 hr exposure. This suggests a different pathway in the dark. Similarly, Li *et al.*, identify photo-inactive, current blocking Cs-rich clusters after ageing $FA_{0.9}Cs_{0.1}PbI_3$ under operating conditions.[197] Maniyarasu *et al.* investigated the moisture degradation of $FA_{1-x}Cs_xPbI_3$ at 30%rH. Using photoelectron spectroscopy, they found that Cs was depleted from the surface alongside the organic cations. While the FACs based perovskite stabilised with Rb shows a ratio of Cs to Pb close to nominal, for FACs the Cs/Pb ratio is about half the nominal concentration at the highest depth probe, reducing towards the surface. XPS also suggests the surface is easily depleted of alkali cations due to decomposition of the perovskite lattice.[198] Addition of RbI fills iodine vacancies and stabilises the perovskite, and it is possible that triple cation, FA-MA-Cs compositions may have a similar response. Hu *et al.* looked at triple cation perovskites at 75%rH in the dark using XRD and after exposure to 90%rH using energy dispersive X-ray spectroscopy (EDX). According to XRD, there was minor degradation of $FA_{0.83}MA_{0.17}Pb(I_{0.83}Br_{0.17})_3$ and $Cs_{0.05}FA_{0.83}MA_{0.17}Pb(I_{0.83}Br_{0.17})_3$ to PbI_2 after 1hr exposure. After 5 days exposure at 90%rH they found moisture induced phase segregation and degradation in 5% Cs doped $FA_{0.83}MA_{0.17}Pb(I_{0.83}Br_{0.17})_3$. The degraded region of the film had a Cs and Br rich phase identified as $CsPb_2I_4Br$.[199] Interestingly they didn't find a change in the elemental stoichiometry of FAMA or phase segregation after 90%rH exposure for 2 days.

2.6.2   Thermal stability

Thermal stability of perovskites is an important property to understand as the films will undergo various heat treatments during manufacture and may operate at elevated temperatures during operation for extended periods of time. During fabrication films are annealed, leading us to require a deep understanding of the phase transformations taking place within the relevant range. Further down the chain, the perovskite could experience temperatures exceeding 140°C depending on the module encapsulation method, for short periods of time as the encapsulant material (typically a polymer sheet) is heated to polymerise the polymer and bond the module together. This is important as soft perovskites like $MAPbI_3$ begin to irreversibly degrade above 140°C (in vacuum).[96] The thermal decomposition pathway is as follows:

$$MAPbI_3(s) \xrightarrow{heat>60°C} PbI_2(s) \; + \; [CH_3NH_3^+ \; + \; I^-];$$

OR $MAPbI_3(s) \xrightarrow{140°C} PbI_2(s) + CH_3NH_2(g) + HI(g)$ OR $CH_3I(g) + NH_3(g)$
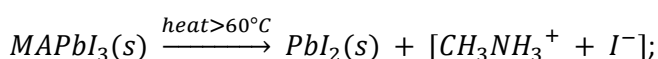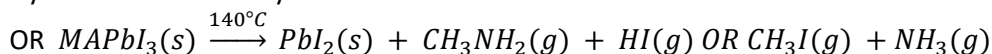
Operating temperatures can rise as high as 65°C, which over the lifespan of the device may slowly lead to reduced performance. Testing at high temperature is useful experimentally as it allows the investigation of these chemical reactions and degradation processes that would otherwise occur over months or years in the field, and which can be accelerated to occur more rapidly.

Structural stability is indicated by the Goldschmidt factor as previously described in section 2.1. While MAPbI$_3$ and other MA-based perovskites have a tolerance factor of 0.91, existing in a tetragonal or pseudocubic crystal structure over the relevant operating temperature range (-15→ 65°C), they are not as resistant to thermal decomposition as FA or Cs based perovskites.[200] These latter perovskites form metastable phases upon annealing and quenching to room temperature; after a matter of hours or days they will decompose to a photoinactive δ phase. This happens because the too-large FA cation, and too-small Cs cation lead to a weaker, distorted perovskite unit cell. To ameliorate the disorientation caused by either alternative A-site cation, it is beneficial to use a mixture of both. The mixture's tolerance factor (as calculated using average site radii) allows for structurally stable perovskite phases that are also thermally stable. They also offer the capacity for tuning to attain desirable optoelectronic properties.[201,202]

A-site cation substitution has the largest effect on thermal stability due to the structural effect of the cation on the lead halide octahedra interactions and the reduced volatility of inorganic compared to organic salts. FAMA, FACs and FAMACs compounds are resistant to thermal degradation across a wide alloying range with higher PCE's than their single cation counterparts. Recently Rubidium has been used in addition to these three cations in quadruple-cation perovskites with PCE's of 21.6% and 500h stability at 85°C by Saliba *et al.*.[203,204] Improved stability may be due to an additional site for hydrogen bonding in FA, which would lower the acidity of FA (as H will bond to this site as opposed to the Iodide ion, suppressing HI formation), and the reduced volatility of both FAI and CsI.[184] The same research group also showed an MA-free RbCsFa composition with an efficiency of 19.3%. This composition shows similar stability to the Rb-stabilised CsMAFA compositions, and this may be attributable to the removal of the volatile MA cation, as well as entropic stabilisation of the solid solution.[191] However, partial substitution of MA doesn't prevent it's volatilisation. Tan *et al.* analysed the decomposition of $Cs_{0.05}(MA_{0.17}FA_{0.83})_{0.95}Pb(I_{0.17}Br_{0.83})_3$ using an Arrhenius model of the changing perovskite peak height in XRD. They found that it decomposed in a two-step process during annealing at 150°C in air, with first of these showing similar decomposition kinetics to MAPbI$_3$, suggesting the first stage involved the reaction of MA$^+$ and the second the reaction of FA$^+$.[205] Indeed, the photoactive α perovskite phase of these FA and Cs based materials can spontaneously transform into a photo-inactive hexagonal δ non-perovskite phase. This intrinsic structural instability arises from deviation from an optimal octahedral tilt of the PbI$_6$ octahedra at decreasing temperature, making the α-phase thermodynamically unstable.[178]

Besides A-site cation substitution, X-site Anion mixing is also used, particularly mixtures of Br and I.[195,206,207] Adding Br to CsPb(Br$_x$FA$_{1-x}$)$_3$ for example shrinks the space available for the A-site cation, making it a better fit for the smaller Cs cation, remaining stable at room temperature.[141,189] Fa$_{0.83}$Cs$_{0.17}$Pb(I$_{1-x}$Br$_x$)$_3$ compounds form a single phase across the Br-I range and have good thermal stability.[208] However as will be explored in section 2.7.1, mixed halide perovskites can suffer from halide segregation in the presence of light and electrical fields. Despite the potential of ionic substitution, efforts can decrease the phase stability the perovskite material, and reversible or worse irreversible phase segregation leading to localised differentiation in performance will occur. Other means of stabilising the octahedral tilt of the PbI$_6$ cages are being explored. Doherty *et al.* demonstrated the importance of stabilising the ocatehdral tilt by treating the surface of FAPbI$_3$ with ethylenediaminetetraacetic acid. They achieved stabilisation of the octahedral cage without cation additives, creating films resistant to external stressors.[209]

2.7 Hysteresis

Snaith *et al.* first reported current-voltage (*I-V*) hysteresis in PSCs in 2014. Where hysteresis occurs there is a marked difference in the current delivered from a solar cell under forward and reverse bias. According to their

findings, hysteresis was dominant in the perovskite material as opposed to the charge selective contacts, although these CTLs did play a role in modulating the degree of hysteresis depending on material and morphology.[210] The timescale over which the hysteresis occurs (~100 s) rules out typical charge generation or recombination process(which are of the order of ps) as being responsible. They also found hysteresis strongly depended on scanning parameters such as scanning rate, amplitude of the applied field, scanning direction, and the conditions of the material prior to scanning. Various explanations for this were developed, from ferroelectric models, to charge trapping and detrapping, and ion migration. Several arguments against the ferroelectricity model have largely ruled this out as the dominant mechanism. The ferroelectric effect present is incredibly small, and hence difficult to ascertain.[211] It occurs over a timescale of ns, as opposed to ~100 s for hysteresis.[212] The current understanding generally has reached a consensus that it is combination of charge trapping/detrapping processes and ion migration.[213] Charge trapping and detrapping occurs due to the presence of trap states. These stem from defects in the crystal structure and serve as major sites of carrier recombination. These same defects also act as pathways for migrating ions, mediating diffusion through the availability of different pathways (for example site vacancies or interstitials).[45] Halide ions are widely regarded as the main ionic conductors in hybrid perovskites, with modelling and experiments on halide-ion vacancy conduction from as far back as the 1980 s supporting this.[214–216] Halide ion migration and the presence of trap states are intricately linked and should both be present to observe significant hysteresis.

Hysteresis can be described with the drift-diffusion model of a p-i-n junction presented in section 1.2. The depletion width in a typical ~300 nmperovskite film extends ~100 nm from the contacts into the bulk, with a bulk region wherein the in-built field is zero or a minimum. Under forward bias (+ve V), the depletion layer contracts. In order to maintain charge neutrality within the neutral region as ionic charges migrate under the influence of the electrical field, charge carriers rapidly adjust their distributions. Charge carriers will move in a direction opposite to the photo-current in order to screen ionic charges. This screening reduces ionic drift due to coulombic attraction, and hence ionic migration may mainly be through diffusion. This screening also reduces the net current while the process is occurring. Eventually the ions and charge carriers will reach a new equilibrium. Under reverse bias the opposite will occur, with the depletion region expanding and charge carriers moving in the direction of photocurrent as well as a possible reduction in ionic charges (for example $I^- + V_I^+$). This has the effect of raising the net current relevant to the forward bias condition. This has an impact on the type of non-radiative recombination occurring, with enhanced Shockley-Read-Hall recombination occurring due to the presence of deep level defects such as V_I^+ during diffusion under forward bias, and enhanced Auger recombination when there is a large polarity in the electron-hole distribution. [217]

2.7.1 Understanding Ion Migration

Walsh *et al.* provided a useful collation of the current understanding of the factors which govern or stimulate ion migration. These factors can be split into intrinsic factors stemming from the structural properties of hybrid perovskites, and extrinsic factors due to environmental factors.[218]

Intrinsic Factors

Hybrid perovskites have a high density of point defects as outlined earlier. These can act as mobile species, moving through the lattice under the influence of stress, temperature, chemical and electrical gradients. Point defects are typically in an ionised charge state, for example a positively charged iodine vacancy (V_I), but can also occur as charge neutral pairs. Of these there are two types: Schottky defects, and Frenkel defects. Schottky defects occur where an anion and cation vacancy occur together, cancelling out each other's charges. Frenkel defects occur where an ion vacancy is accompanied by the formation of an interstitial of the same ion species.[219] Other metastable states can form under illumination, as charged defect sites can trap charge carriers for prolonged periods of time (for example the trapping of e^- by a V_I^+). The low formation energy for iodine Frenkel defect pairs has been suggested a likely mechanism to explain electrostriction in $MAPbI_3$ by Chen *et al.*.[220] They propose that the small point defect formation energy allows the formation of additional defects under bias, generating an electromechanical response. Density Functional Theory (DFT) computations show induced compressive strain in the c-axis of -0.6%, similar to experimental values under an electric field of 3.7 μm^{-1} of -

1%. An Arrhenius relationship between the electrostrictive response and temperature as well as a reduction in the E_a for ion migration as the magnitude of the applied field increases further provides connections between electrostriction and defect formation and annihilation. As temperature increases, defect density increase, while as the strength of the field increases more defects are produced, and ion migration is made easier.

Evidence supports the notion that vacancy-mediated iodide diffusion is the main diffusion mechanism present in hybrid perovskites, with Eames *et al.* calculating E_a values for the migration of an iodine vacancy in MAPbI$_3$ at ~0.6 eV. MA$^+$ diffusion was calculated to have an E_a value of ~0.8 eV, and so while less likely, cannot be ruled out as a migrating species at room temperature. Pb^{2+} however was calculated to have an E_a of 2.3 eV.[216] Haruyuma *et al.* determined E_a values for V_I^+ and V_{MA}^- of ~0.3 eV and ~0.6 eV respectively, while Azpiroz *et al.* found these to be ~0.1 eV, ~0.5 eV and for V_{Pb} ~0.8 eV.[169,221] Differences in these values can be attributed to the different DFT modelling approaches and assumptions made, although they all describe the same order of reactivity.

In polycrystalline thin films, point defects can accumulate as extended defects in the form of GBs or on external surfaces. These can provide rapid diffusion paths for ions, as the highly defective regions provide a lower barrier to ion migration. GBs have been found to support fast iodide diffusion in MAPbI$_3$ (using conductive-AFM) reducing the effective E_a for I$^-$ diffusion in the dark. GBs and surfaces have high concentrations of charged point defects as a result of the crystallisation process (crystal lattice disorder at the edge of the crystallites has lower formation energy). This has been supported by observations of enhanced charge carrier recombination, and reduced charge carrier mobility over these regions. [222–224]

Extrinsic Factors

Ions are susceptible to the influence of an applied electric field, with observations being made of ion migration under electrical bias.[225] Recent work also shows that the combination of field-induced ion migration and charge carrier injection leads to the formation of trap states.[226] Under prolonged poling, the bias can lead to degradation of the perovskite to PbI$_2$ and MAI, with the volatilisation of MA or I$_2$.[168,227] Furthermore, electrical biasing without injection of charge carriers has been shown to cause halide segregation in mixed perovskite films, evidenced by a photoluminescence blue-shift, which is similarly observed under laser excitation.[228]

A homogenous thin film placed in a chemical gradient (such as a specific halide atmosphere) experiences ion exchange until a new chemical equilibrium is established between the atmosphere and the crystal lattice. For halides in hybrid perovskite thin films this has been shown to occur over seconds, showing ease of ion diffusion at the surfaces and GBs.[229] Evidence supporting the mobile nature of sub-lattices in perovskites is further provided by evidence of A and B cation exchange, although this occurs over the timescale of hours. [230,231] Additionally the susceptibility of the films to H$_2$O and O$_2$ in solution and during film deposition, crystallisation, and degradation has been observed, having various effects on microstructure, and charge carrier dyamics.[55,68,232,233] The large number of defects facilitates the ingress of H$_2$O and diffusion of oxygen atoms.

During operation, a photoactive material will lose a significant portion of energy as heat, due to thermodynamic constraints as outlined by the Shockley-Queisser limit.[31] Photons with energy greater than the band gap will generate hot carriers (carriers above the CBM) which will thermalize, cooling down to the conduction band edge and releasing their energy by multiphonon emission.[234] Non-radiative recombination can cause local heating which can activate defect formation and ionic transport, as excess energy is dissipated as phonons which provide enough energy to overcome the energy barriers. Decomposition (MAPbI$_3$ → MAI + PbI$_2$) has also been shown to be triggered by commonly used wavelengths of Raman lasers (532 nm and 633nm) and device degradation accelerated by absorption of the infrared component of the solar spectrum during operation under sunlight.[168,235,236] Hybrid perovskites have a low thermal conductivity, which means local temperature gradients will have a significant effect on the formation of defects and ion migration, as they provide pathways for reducing this energy.[237,238] This also means that in a closed system a concentration gradient can form, where heterogeneity will increase in an initially homogenous film due to thermally activated structural disordering, until the influence of local ion concentration gradients counteracts it. An equilibrium between the competing influences of thermodynamic activity and local ion concentration is reached.

Hybrid Perovskites - Hysteresis

Hybrid perovskites are infamously unstable under illumination; photo-induced phase separation has been extensively studied in mixed halide perovskites, commonly termed the 'Hoke Effect', as well as photo-induced mobility in single-halide hybrid perovskites (both thin films and single crystals).[239–244] Low intensity long wavelength visible light, in the near-IR from a red-laser has been shown to be sufficient to accelerate degradation, even in an inert N_2 atmosphere.[177] The importance of mixed halide hybrid perovskites for tandem photovoltaics incorporating these thin films has spurred research into this effect.[245–248] A key observation in the migration of halide ions is their motion away from the illuminated surface and into the bulk.[239,244]

Illumination of films results in electrical and thermal changes, influencing the previously discussed intrinsic factors responsible for the films optoelectronic properties. Walsh *et al.* surmised four main processes by which photo-induced halide migration may occur as summarised in Figure 11. It remains an open question as to which is the correct, or most dominant mechanism, and hence there is an impetus to derive a holistic explanation of the phenomena.
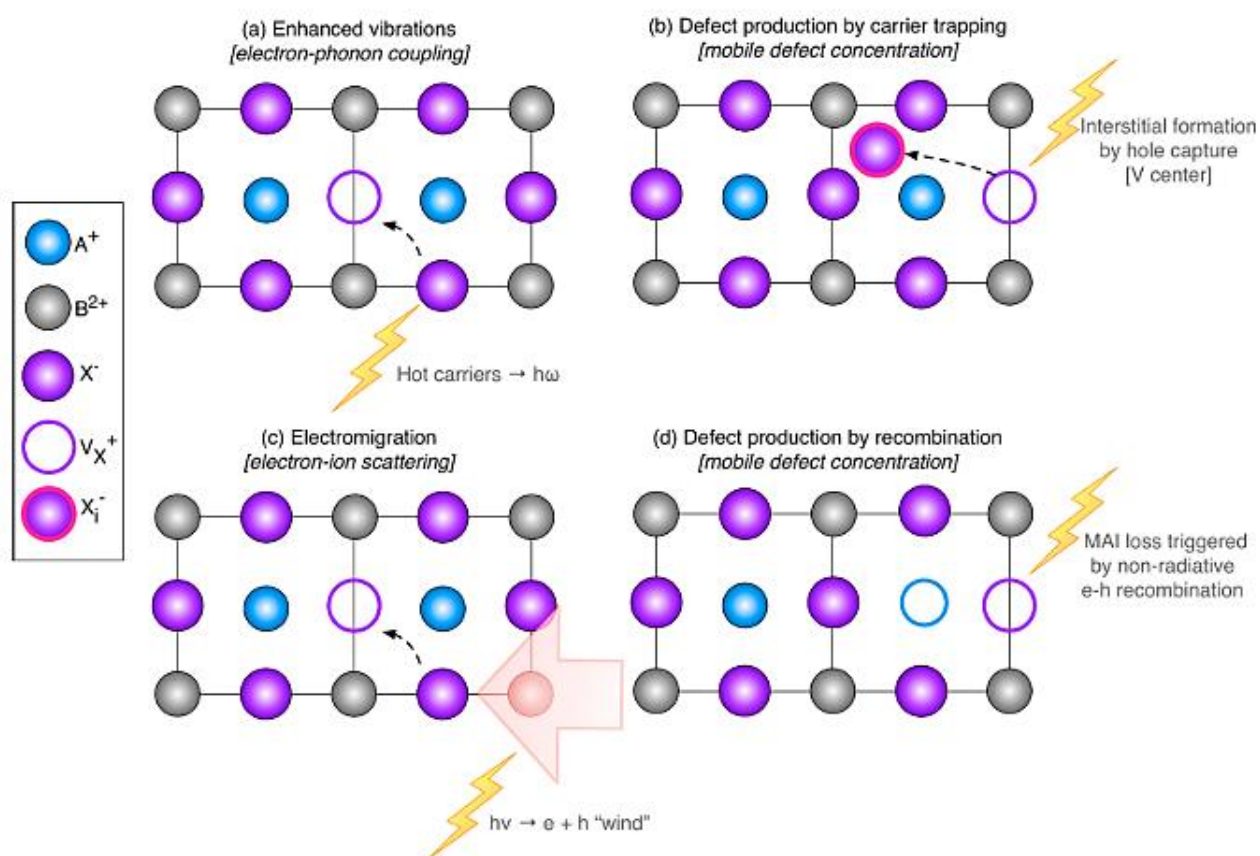
Figure 11: Four possible process by which photo-induced ion migration may occur. (Reproduced with permission from 10.1021/acsenergylett.8b00764, Copyright 2018 American Chemical Society.)

1) When light is absorbed hot carriers are generated which cool to the lattice temperature by phonon emission, leading to an enhanced rate of ion migration. 'electron-phonon coupling' transfers excess energy from hot carriers to mobile ions.
2) Illumination generates photo-induced charge carriers which become trapped, with the gain in potential energy offsetting the energy cost of defect formation. For example, the formation of an interstitial by hole capture.
3) Illumination generates charge carriers with a polaronic nature which transfer their momentum to ions.
4) Non-radiative electron-hole recombination provides sufficient energy to stimulate the formation of enhanced mobile defect concentrations.

Light has also been shown to lead to structural changes in the material, with evidence of photostriction and strain relief, the latter of which would likely require ionic rearrangement to occur.[249,250] Evidence for b has come

from Tiede *et al.*, who find a correlation between I-rich region formation and defect density under illumination. Photo-generated charge carriers are trapped by I-related defects, ultimately leading to the recombination of I-related defects (i.e. I_2 interstitial with I^- vacancy) and formation of I-rich regions.[251]

There are various techniques through which ion migration can be monitored or studied, exploiting changes in photoluminescence, conductivity or optical properties in response to the aforementioned extrinsic factors. *In situ* studies are a powerful tool, allowing the influence of external factors to be correlated directly with observed property variations. *In situ* studies can be designed to simulate *in operando* conditions, for example by steady state illumination or thermal cycling of thin film samples.[252] Li *et al.* used wide-field PL microscopy and impedance spectroscopy *in situ* to investigate spatial and transient evolution of thin films under electrical bias. Formation of defects accompanying ion migration under the applied field was invoked to explain PL inactive domains of the film. Another oft used technique is X-ray photoemission spectroscopy (XPS), which has been used *in situ* as an electrical field is applied to map changes in elemental composition and photoluminescence in both single crystals and thin films.[253–255] Other *in situ* methods used to try and resolve chemical and optoelectronic changes in thin film which may arise due to ion migration and ion segregation include electro-absorption spectroscopy, spatially resolved PL, SEM,TEM, Cathodoluminescence, EDX, and X-ray Absorption Spectroscopy (XAS).[61,229,256–264] There is scope for further studies using methods such as these, though mindfulness is required of damage which can be incurred in the sample due to high energy electron or laser beams used.[265]

3 Aims and Objectives

Hybrid perovskites have become a vast topic of research, with the immense quantities of literature producing many different models and theories to explain complex and interlinked processes. A narrative is emerging of the key processes that occur during crystallisation, with the role of precursors, and intermediate complexes becoming more clearly defined. Aspects of processing such as annealing, atmosphere, and solvent evaporation have been vigorously explored. Ion migration has been identified as a key process governing hysteresis, and several theories as to how photo-induced ion migration may occur have been put forward. Ion migration is closely intertwined with the quality of the film following film formation due to the presence of defects and GBs. Defect engineering of perovskite thin films through the mixing of multiple ions on A and X sites in the perovskite crystal has been a promising method for achieving high performing, long lifetime PSCs, but has not received as much attention as simpler single cation compositions with regards to the characterisation of film formation and degradation. The wide variety of hybrid perovskite compositions provides ample space for further research, design and improvement to hybrid perovskite thin film properties. As such there are specific question which I will be looking to answer or contribute to solving within this space.

1. **How does precursor stoichiometry manipulation influence the formation of MAPbI$_3$ films processed under ambient conditions?**

Manipulating stoichiometry in MAPbI$_3$ precursor solutions films influences the morphology of the fabricated film. Indeed, previous work by our group has shown the importance of PbI$_2$ stoichiometry on device performance, as well as the demonstrable effects of Iodide additives on film formation. MAI enriched films have larger grains as grain growth is mediated by the diffusion of MAI. PbI$_2$ enriched films have residual PbI$_2$, mostly at surfaces and grain boundaries (GBs), which serve to passivate defects and improve carrier transport properties. Both effects are desirable for high performing perovskite devices, where we want to reduce the presence of defects such as iodide ion vacancies and reduce GB area.

Another aspect of film formation crucial for obtaining high quality films is sufficient nucleation density to reduce the occurrence of pinholes (which can result from the formation of an incontiguous film morphology during annealing, as well as the escape of trapped solvent). This is made possible using antisolvents such as ethyl acetate which reduce the precursor solubility and causing the solution to reach super saturation, while also encouraging formation of the DMSO solvent intermediate, and hence the contiguous crystallisation of the perovskite phase upon annealing. Examples of devices fabricated with EA are shown in Appendix 13.1, Table 4. Can the combined influences of excess precursor salts and optimised antisolvent induced crystallisation be used to obtain uniform, dense, passivated and large-grain perovskite thin films under ambient conditions?

The impact of stoichiometry with and without EA antisolvent application will be investigated through WAXS during in-situ spin-coating and annealing, SEM and UV-Vis Spectroscopy. X-ray scattering is typically used for crystallographic and structural characterisation, and can be combined with in-situ measurements during processes such as spin-coating and annealing to monitor the evolution of thin films. Crystallographic systems, crystallite size, preferred phases among other features can be investigated. SEM can be used to characterise morphological features such as grain size and prevalence of pinholes. This will be useful for investigating the influence of stoichiometry on microstructure. UV-vis spectroscopy will be useful for optoelectronic characterisation of thin films, providing information on absorption, band gap, and disorder at the band-edge, related to the prevalence of defects. Finally, optimised EA antisolvent application will be used to fabricate devices under ambient conditions for comparison between MAPbI$_3$ compositions.

2. **How and why does replacement of MA with Cs and FA improve the resilience of perovskite films to moisture-induced decomposition?**

Our understanding of moisture induced decomposition of FA based perovskites has progressed rapidly due to the increasing popularity of FA based perovskites for high performing mono and multi-junction solar cells. FA-based PSCs have higher PCE due to a favourable band gap. While the conversion from α-perovskite to photo

Aims and Objectives

inactive δ perovskite is well documented, as well as the interconversion between various hexagonal polytypes during degradation, the formation of hydrated FA perovskite phases is less certain. Using GISANS there presence can be investigated by utilising the unique contrast mechanism in Neutron Scattering, facilitating sensitivity to light elements. There also remains the question of how feasible preparation of FA rich perovskites in ambient atmosphere is, due to the facile α-δ transformation. Antisolvent application has gained traction as a process for kinetically stabilising solvent-precursor intermediate phases and ensuring the development of perovskite films with continuous coverage and high crystallinity, their efficacy can be limited by poor moisture affinity, sub-optimal or supra-optimal polarity and toxicity. Ethyl acetate (EA) has emerged as a convincing alternative to chlorobenzene, toluene or di-ethyl ether. This is due to its high moisture affinity, high volatility, and optimal polarity. EA has been demonstrated as an effective antisolvent for facilitating the conversion of the intermediate film to perovskite in $MAPbI_3$ devices under various humidities, and in mixed cation, mixed halide perovskites, when processed under an N_2 airflow, as shown in Table 4. However, synthesising these doped perovskite films under ambient conditions with ethyl acetate in order to mitigate the influence of moisture (as well as to increase crystallinity) has seen little investigation. This could be a valuable area of research as doped perovskite compositions provide an avenue for tuneable, high efficiency single-junction or multi-junction devices. Some of the highest performing devices as shown in Table 4 surpass 20% PCE using a combination of Cs, MA and FA cations on the A-site, and I and Br on the X-site. And if they can be manufactured under ambient conditions this will relax the requirements for an inert processing atmosphere. This will be investigated using SEM, and UV-vis spectroscopy.

3.   Can EA induced crystallisation of $MAPbI_3$ films be combined with ionic substitution to improve stability under exposure to moisture?

In $MAPbI_3$, decomposition to hydrated phases is initiated by the reaction of MA^+ cations on the surface with hydroxide ions. This leads to lattice strains which generate more defects, and consequentially further decomposition. Reducing GB area should enhance resilience to moisture induced degradation. Alternatively, reducing the ability of moisture to permeate the film initially could be a powerful approach. Ethyl acetate appears to be useful during film fabrication, with this treatment also reducing the rate at which the PCE decreases for devices made with treated films. This may be associated with improved structural and morphological properties, such as increased crystallinity, low surface roughness, reduced GB area, and the specific nature of surface defects. Tuning the crystal structure through ionic substitution has been shown to improve moisture resistance through stabilisation of cubic-phase and reduction in surface defects, but can treatment with ethyl acetate be used in conjunction with this method under ambient conditions to decrease moisture ingress? Similarly, substitution strategies have been shown to increase thermal stability, but can this be combined with antisolvent application for a further enhancement? The effect of cation substitutes for MA and Pb will be investigated through a combination of GIWAXS, UV-Vis, Ellipsometry, and SEM on synthesised thin films. Device analysis as a function of PCE, J_{SC}, V_{OC}, and *FF* overtime will be conducted.

Experimental & Theoretical Methods

4 Experimental

4.1 Perovskite Solution Synthesis

The synthesis procedure is the dissolution of the perovskite precursor salts to be reacted in an organic solvent. Herein a mixture of DMF:DMSO in a 4:1 volumetric ratio is used, and solutions are made up to 1.3M concentration. The 4:1 ratio is used to ensure sufficient nucleation density under ambient conditions as per Troughton et al (see section 2.3.4).[127] This concentration could be optimised, with research suggesting differing concentrations (from 0.9 - 2 M) resulting in higher performance devices; as there are so many factors to control in optimising this aspect (constituent precursors, solvent, antisolvent, spin coating parameters, age of solution, fabrication environment), and a lack of consensus on the optimum, it merits further research and review, but is outside the scope of this work.[266–268] Precursors are measured out with a digital analytical balance scale onto weighing paper folded into weighing boats, before being transferred to vials and dissolved in the DMF:DMSO solvent mixture. Solutions are mixed with a magnetic stirrer bar on a magnetic stirrer hotplate for specific lengths of time at $\leq 70°C$, to encourage mixing and homogenisation of the perovskite solution. In some instances, due to agglomeration and poor mixing of precursors, a 0.45 µm hydrophobic PVDF filter is used to remove residual unreacted Pb salts from the solution before deposition. This is a convention in the field to reduce deposition of unreacted Pb on the film substrate. During stirring, vials are capped and sealed with a parafilm sealing tape. All preparation was done in ambient air (measurement of salt masses) with an extraction hood placed above the scales to avoid inhalation of toxic dust such as PbI_2, or in the fumehood (mixing and stirring).

4.1.1 Perovskite Solution Preparation for Investigation of Super-stoichiometric $MAPbI_3$ compositions

Methylammonium Iodide (MAI, Sigma Aldrich) and Lead Iodide (PbI_2, mechanochemically synthesised to ensure correct ratio of Pb to I as per Tsevas *et al*.[83]) were measured and mixed together as per the stoichiometric requirements for the following compositions $MAPbI_3$ ((1):206.66 mg MAI+ 599.32 mg PbI_2), $MAPbI_3$ + 10wt% excess MAI ((1)+20.67 mg MAI), and $MAPbI_3$ + 10wt% excess PbI_2 ((1)+59.93 mg PbI_2) with the molar ratios (1:1), (1:1.1) and (1.1:1) respectively. The mixture was dissolved in a solvent mixture of DMSO and DMF in a volumetric ratio of 1:4, to make up 1.3M, 1.4M and 1.4M solutions, respectively. The solutions were stirred at 70°C for approximately a day before use to ensure a homogenous distribution of precursor species and complete mixing.

4.1.2 Perovskite Solution Preparation for Investigation of Moisture Induced Decomposition of Perovskite Films

For GISANS experiments, perovskites were prepared according to the stoichiometries described in Results Section 6, and detailed in Table 2. They were dissolved in a solution of DMF:DMSO in volumetric ratio of 4:1, and stirred for at least an hour at room temperature prior to deposition.

Table 2: Table of precursor salt massed mixed for each perovskite composition in Section 5

Perovskite Composition	Precursor salt mass added(mg)					
	MAI	MABr	FAI	CsI	PbI_2	$PbBr_2$
$MAPbI_3$	206.66	-	-	-	599.32	-
FAMA	-	22.93	171.97	-	505.12	82.69
CsFAMA	-	21.79	163.37	16.80	481.76	78.56
FACs	-	-	185.56	57.42	509.43	71.57

4.1.3 Perovskite Solution Preparation for Investigation of $ZnCl_2$ and CsI addition to Perovskite Films

A 1.3M solution of $MAPbI_3$ in a 4:1 volumetric ratio of DMF:DMSO solvent was prepared by measuring out stoichiometric quantities of MAI and PbI_2 salts and dissolving them in the solvent mixture. A 1.3 M solution of $MA_{0.97}Cs_{0.03}Pb_{0.97}Zn_{0.03}(I_{0.97}Cl_{0.03})_3$ ($MACsPbZn(ICl)_3$) in a 4:1 (v:v) solvent mixture of DMF:DMSO was prepared by dissolving 200.46 mg of MAI, 581.34 mg PbI_2, 10.13 mg CsI, and 5.32 mg of $ZnCl_2$ in a 1 ml solution of DMF/DMSO.

Experimental - Substrate preparation

ZnCl$_2$ was added separately to the perovskite from a prepared solution of 1.3 M ZnCl$_2$ in DMF:DMSO (4:1, v:v), due to the high hydrophilicity of ZnCl$_2$ powder (adsorbs moisture from the air).

4.2   Substrate preparation

Either plain glass (for materials characterisation) or pre-patterned glass substrates (for devices) with eight indium tin oxide (ITO) pixels (surface resistivity = 20 Ω / square (sq), 20 mm x 15 mm) were sonicated for 10 min in a solution of 1 ml of Hellmanex III in 250 ml of boiled deionized water (DI H$_2$O). Any residual detergent was subsequently washed off by rinsing the substrates in 3 baths of 100 ml of DI H$_2$O. The glass/ITO substrates were sequentially sonicated for 10 minutes each in 250 ml of acetone and then 250 ml of isopropanol. Cleaned substrates were dried with an air gun and then treated with oxygen plasma for 10 minutes to remove remaining organic compounds. Clean glass/ITO substrates were transferred to a fume cupboard and covered. Perovskite solutions were deposited within an hour of cleaning the substrates for use in film characterisation.

4.3   Perovskite Film Preparation for Characterisation

The generic procedure used in this work is spin coating of films using specific spin programmes (programmable speed, time, ramp rate, and stages) in a portable vacuum free Ossila spin coater. After spin coating (which may include an antisolvent application step), samples are transferred to a hotplate and annealed for set lengths of time between 60-100°C depending on the experiment. All sample preparation is done under a fumehood.

4.3.1   MAPbI$_3$ Perovskite Film Preparation for Investigation of Super-stoichiometric MAPbI3 compositions

For SEM and UV-Vis spectroscopy in Section 5, 40 µl of perovskite solution are either spun at 1000 rpm for 10 s and 5000 rpm for 20 s (Program 1) or at 3000 rpm for 30 s (Program 2) as per the experiment. Ethyl acetate anti-solvent was dynamically applied drip-wise to the substrate centre between 10 and 25 s after the start of spinning (the volume and timing was varied, and is discussed in Section 5). The spin coated films were placed on a hotplate to anneal at 100°C for various anneal times.

4.3.2   Mixed Cation Mixed Halide Perovskite Film Preparation for Investigation of Moisture Induced Decomposition of Perovskite Films

The Silicon (Si) substrates were cleaned prior to deposition by polishing the deposition surface, and sequentially rinsing with acetone and 2-propanol. Before deposition of perovskite the Si wafer surface was functionalised with O$_2$ plasma treatment. 100 µl of perovskite solution was dripped on 50 mm diameter, 4 mm thick Silicon Wafer substrates and spun at 3000 rpm for 30 s in a fume cupboard with an rH of 30% and ambient temperature of 20°C. Si has a small absorption cross-section and negligibly scatters neutrons, reducing interference with measurements. The perovskite films were annealed on a hotplate at 100°C for 30 minutes and then transferred to the humidity chamber containing an LiCl salt solution, which maintains rH at ~25%. After the first measurement in LiCl (0 hrs), the salt solution was swapped for an NaCl solution, which raised humidity to ~90% and the hydration measurements were taken. It took approximately 20 minutes to reach rh ~80% and 100 minutes to reach rH ~90%. The maximum beam diameter was 15 mm.

For UV-VIS and SEM, samples were prepared from precursor salts, dissolved to make 1.3M solutions in a solution of DMF and DMSO in a volumetric ratio of 4:1. Samples were stirred overnight at 70°C in the fume cupboard. 40 µl of perovskite solution was deposited on a spin coater statically and spun through a two-phase one-step deposition process of 1000 rpm for 10 s followed by 5000 rpm for 20 s. In the case of samples with antisolvent, 100 µl of ethyl acetate was applied 15 s after the start of spinning. Films were annealed on a hotplate at 100°C for 30 minutes.

4.3.3   Preparation of MAPbI$_3$ and [MACsPbZn(ICl)$_3$] films for Investigation of ZnCl$_2$ and CsI addition to Perovskite Films

To prepare the perovskite solutions for spin-casting, the solutions were stirred for approximately 24 hours before statically casting on room temperature substrates with a two-speed spin coating process. The films were first spun at 1000 rpm for 10 s and then at 4000 rpm for 20 s. Approximately 20 s after the beginning of spinning,

100 µl of ethyl acetate was pipetted upon the film approximately 1 cm above the centre of the film to wash away excess solvent and adsorbed moisture, and to promote the formation of the beneficial DMSO-intercalated intermediate. [124] Films were then transferred to a hotplate and annealed. The anneal was 10 minutes at 100°C for the humidity experiments, and at various times and temperatures for the annealing temperature and thermal ageing experiments. The humidity and temperature of the fume cupboard fluctuated between 45-50%rH and 20-22°C.

Films were thermally aged on the hot-plate underneath a foil covered petri dish to block incident and scattered light. Enclosing the annealing environment in this way also promotes grain growth by slowing the escape of evolved MACl vapour.[269]

Films were exposed to a moist, dry or ambient atmosphere controlled by Salt Solutions of NaCl (75%rH) or LiCl (25%rH) as per Young.[270] Films in the dry and moist atmospheres were enclosed in polypropylene containers which reduce transmitted UV light, reducing the rate of photodecomposition of the perovskite. Films exposed to ambient humidity were also exposed to ambient lighting, testing the stability of these films under the effect of ambient humidity, oxygen and UV-light.

5   Theory and Characterisation Methods

5.1   Scattering Theory

Grazing incidence scattering techniques allow the investigation of surface and near surface structures in thin films at different length-scales. Sensitivity to certain features and structures can be tuned by experimental design — both by choice of radiation source, and manipulation of the incident beam such that it interacts with the measured material at different depths or scatters at different structural length-scales. These particles can be either photons or neutrons, with varying frequency and intensity. Different investigations will call for different beam set-ups and it is important to optimise experimental conditions to increase the signal: noise ratio, i.e., amplify coherent scattering (although there are certain techniques which can utilise diffuse, incoherent scattering for analysis). The theoretical examination in 5.1.1 is applicable in both neutron and X-ray scattering. Concepts such as the Bragg Condition, Ewald Sphere, and grazing incidence geometries are underlined by the same equations, though different physical interactions are responsible.

5.1.1   Grazing Incidence Small Angle Neutron Scattering

Grazing incidence small angle neutron scattering (GISANS) as a technique is sensitive to the morphology as well as the alignment of lateral and vertical structures at a nanometre scale.[271–273] It utilises concepts from grazing incidence diffraction (GID), small angle scattering (SAS), and reflectometry to explore scattering from the sample, generally utilising an area detector. In comparison to X-rays, electrons or visible light, neutron scattering presents significant advantages under certain conditions: X-rays are weakly scattered by elements with low atomic number — contrast is correlated with the electron density around atoms, and so light elements scatter very weakly. Visible light has wavelengths longer than size of features of interest (10^{-6}), while both light and electrons suffer from opacity issues — they are typically readily absorbed by the sample. Finally, electrons can damage samples, with evidence for degradation of thin films under applied electron beams in perovskite thin films.[265,274]

In neutron scattering, contrast arises from interactions either via the short-range nuclear force between the incident neutrons and the nucleus or dipole-dipole interactions between magnetic moments of the neutron and unpaired electrons. This is very different to X-ray scattering, wherein contrast arises from the interaction of the photon with electrons in the atomic shell, and can thus be modelled theoretically (i.e. heavier atoms scatter more strongly). On the other hand, while neutrons are much more penetrating than X-rays and visible light — suffering less attenuation as scattering centres are 100,000 times smaller than the distance between scattering centres — the interactions are inherently weaker than electrical interactions, and neutron beams have low flux, constraining the signal attainable by instrument design. The strength of the interaction dictates the amplitude of the neutron wave scattered by the nucleus. Scattering length is a measure of this, denoted by b, and related to the interaction area cross-section σ by $\sigma = 4\pi b^2$.

Theory and Characterisation Methods - Scattering Theory

For all nuclei, *b* will vary with the energy of the incident neutron radiation because compound nuclei with energies close to those of excited nuclear states are formed during the scattering process. This gives rise to complex values of *b*, where the real part corresponds with scattering while the imaginary part corresponds with absorption of incident neutrons by the nucleus. However, neutron beams used to probe structures usually do not incur this effect due to their low energy (new nuclei are not formed or make a negligible contribution to *b*), so the imaginary component is usually not of concern. *b* must be determined experimentally, as it does not correlate with any fundamental constant that can be modelled, such as atomic number. However, once values of *b* have been determined, its variation from one isotope to another can be utilised in isotopic labelling to investigate structures. By substituting one isotope for another, the scattering of the differentiated constituents can be resolved to reveal their positions relative to other constituents.

Scattering alters both the momentum and the energy of the neutrons and the matter being probed. Momentum transfer to the sample by the neutron is equivalent to the wave-vector of the incident neutrons (k_0) minus the wave vector of the scattered neutrons (k), known as the scattering vector Q, where $Q = k_0 - k$. The magnitude and direction of Q is determined by the magnitude of the incident and scattered wave vectors, and the scattering angle *2θ* through which a neutron is deflected. The intensity of the scattered neutrons for a specific sample is measured as a function of Q and ϵ, the energy transfer, which will be 0 for elastic scattering, referred to colloquially as the *I* (Q, ϵ), the neutron-scattering law.

Van Hove showed the existence of two types of scattering in 1954, namely, coherent scattering where the scattered waves from different nuclei constructively interfere, and incoherent waves where they do not interfere but intensities from each nucleus instead summate.[275] The simplest type of coherent scattering is diffraction. Making the assumptions that all incident neutrons have the same incident wave vector k_o, the scattering is elastic, and armed with the knowledge that interference will result in scattered neutrons travelling in well-defined directions (determined by the symmetry and structural spacing), Van Hove's formulation of the scattering law reduces to Equation 2:

$$I(Q) = \sum_{j,k} b^2{}_{coh} e^{iQ.(r_j - r_k)} = \left| \sum_j b_{coh} e^{iQ.r_j} \right|^2 \equiv S(Q) \qquad \text{Equation 2}$$

For a three-dimensional lattice with one isotope. Here $S(Q)$ is the structure factor (describing how a material scatters incident radiation in terms of interference of scattered waves from all atoms in the lattice), b_{coh} is the coherent scattering length, and r_j and r_k are the position vectors of the atom *j* and *k* in the lattice. Values of Q for which $S(Q)$ is non-zero must satisfy $Q \cdot (r_j - r_k) = Qd = 2\pi n$ where $|r_j - r_k| = d$, *d* is the inter-planar distance and *n* is an integer. When Qd is a multiple of 2π then each exponential term in (Equation 2) will be unity ($e^{i2\pi} = 1$). Therefore, Q must be perpendicular to the planes of atoms in which *j* and *k* are situated. These Q values are governed by the same laws as applies for X-rays, known as the Bragg condition. The following understanding is generally applicable for both neutron and X-ray scattering. When combining the above conditions for diffraction with the elastic scattering condition one gets Equation 3:

$$Q = \frac{4\pi \sin\theta}{\lambda} \qquad \text{Equation 3}$$

Equating Equation 3 to $Q = 2\pi n/d$ yields Equation 4 : Bragg's Law.

$$n\lambda = 2d\sin\theta. \qquad \text{Equation 4}$$

Bragg's law relates *2θ* (the angle between the incident and scattered plane waves) to inter-planar spacing and also shows that for constructive interference to occur between waves scattered by adjacent planes, the path-length difference must be a multiple of λ, as shown in Figure 12A. When the sample is oriented correctly to the incident beam such that Bragg's condition is satisfied, a Bragg peak in the signal will be obtained at that scattering angle. Since the incident and scattered waves have the same length due to elastic scattering, Q will lie on the surface of a sphere of radius $2\pi/\lambda$. Points at which the Bragg diffraction condition are satisfied

(reciprocal lattice vectors where the momentum transfer is conserved) will therefore occur where the Q equals a reciprocal lattice vector.
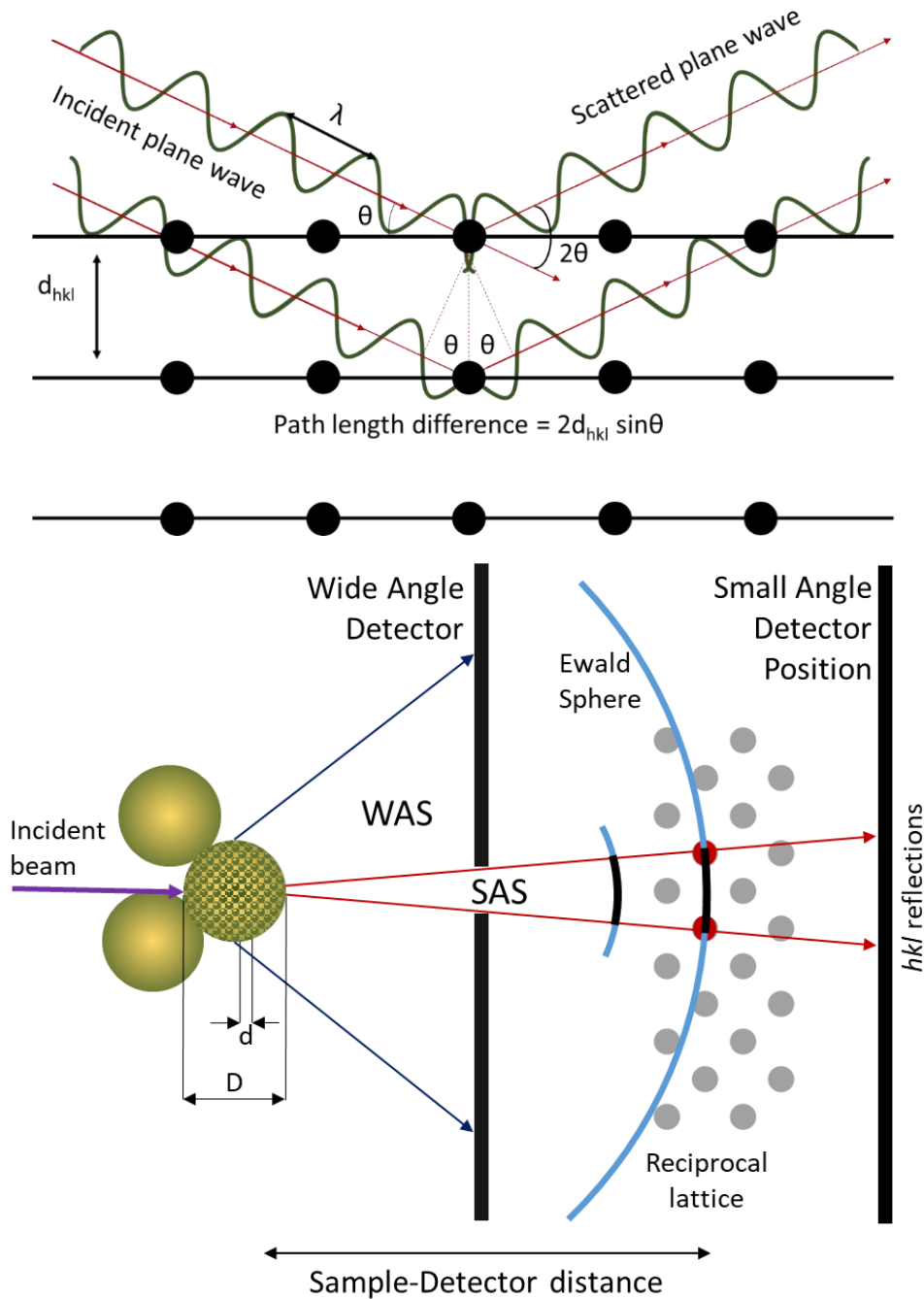
Figure 12: (A) Origin of Bragg scattering peaks. When the path length difference is an integer multiple of the plane spacing, d_{hkl}, constructive interference of the scattered plane waves will occur. (B) Ewald Sphere: Surface that satisfies the Bragg scattering condition. Red arrows: Small Angle Scattering diffracted beams. Blue arrows: Wide Angle Scattering diffracted beams. When the reciprocal lattice points are too near one another (i.e. detector too close to sample, there may be overlap of diffraction spots, making resolution of data more difficult. Real space (d, D) is inversely correspondent to reciprocal space (1/d, 1/D). As D>d, 1/D<1/d

The Ewald sphere is the surface in reciprocal space on which all experimentally observed elastic scattering occurs. If the origin of the Ewald Sphere is taken to be the centre at which the incident ray is scattered, then diffraction will only occur for reciprocal lattice points on the surface of the Ewald Sphere, as shown in Figure 12. Rotating the crystal allows all reciprocal lattice points intersecting the Ewald sphere to be measured (or alternatively varying θ or λ of the beam to attain essentially the same effect, which is sometimes easier to do

experimentally). Samples may often be polycrystalline where the incident beam will penetrate multiple crystals with random orientations, eroding the necessity of sample rotation to interrogate the entirety of the 3D space. Different crystal systems have distinct peaks in reciprocal space due to their defined periodicity. Equation 2 implies that the intensity of scattering is proportional to the square of the density of atoms responsible. Thus, the position and intensity of Bragg peaks enable one to determine crystal structure (hkl), the spacing of planes (d_{hkl}), and the density of atoms in them.

This understanding enables a variety of scattering experiments, exploiting the different length scales and features interrogated at different incident angles and wavelengths. Table 5 (Appendix 13.1) shows which experimental techniques are used within each incident angle range, although these are not consistent throughout the literature and are given as guidelines as opposed to definitive boundaries.

5.1.2 Reflectometry and Small Angle Scattering

Different neutron scattering effects can be observed at different scattered angle ranges. The exiting scattered beam angle resolves in either transmitting or reflecting modes. Reflectometry is a diffraction technique where the angle of the reflected beam equals the angle of the incident beam. Typically used when investigating extremely flat surfaces such as those of thin films, the shape of the reflectrometry profile provides structural information such as density, thickness and roughness. In some thin films, the scattering volume is often too small in the transmission geometry to produce a diffraction signal with a sufficient signal: noise ratio at small angles. In these instances, changing to a grazing incidence geometry overcomes the noise problem. This technique is described as grazing incidence diffraction (GID), where the scattering volume is increased due to the in-plane propagation of the incident wave.

Probing surface structures with neutrons becomes possible when small angle scattering (SAS) is combined with grazing incidence geometries (GISAS). In general, the smaller the scattering angle, the larger the structures under scrutiny. The resolution of the data is therefore improved by choosing a sample-detector distance which magnifies the scattering of interest. At short sample-detector distances for example, small-angle scattering data will be hard to resolve as scattering vectors (small variation in q_z) are concentrated within a smaller area on the Ewald Sphere (small variation in q_y and/or q_x). Increasing this distance spreads out data over a larger surface and allows for adequate Q resolution on the 2D detector. Small angle neutron scattering (SANS) uses scattering angles less than 1° and wavelengths greater than 5 Å to probe larger structures. The Von Hove formulation can be manipulated for neutrons scattered at small angles to give Equation 5 for intensity:

$$\mathrm{I}(Q) = \left| \int b(r) e^{iQ.r} d^3r \right|^2 \equiv S(Q) \qquad \text{Equation 5}$$

Where $b(r)$ is the neutron scattering length density and is a sum of b_{coh} for all scattering atoms divided by the molecular volume (V_m, cm^3 mol^{-1}) in which they occur.

$$b(r) = \frac{\Sigma b_{coh}}{V_m} \qquad \text{Equation 6}$$

Where V_m is the molar volume divided by Avogadro's Constant: v_m/N_a.

If the horizontal scattering angle φ is equal to zero, and the angle of reflection θ_r equals the angle of incidence θ_i then the scattering is described as specular, whereas if there is a horizontal component, or θ_r otherwise deviates from θ_i then the scattering is defined as off-specular or diffuse. Off-specular scattering features reflect lateral variations in $b(r)$. This is summarised in Figure 13.

Perfect reflections of the incident beam occur for $\theta_i <$ the critical angle θ_c, defined for neutrons as Equation 7:

$$\theta_c = \lambda \sqrt{\frac{b(r)}{\pi}} \qquad \text{Equation 7}$$
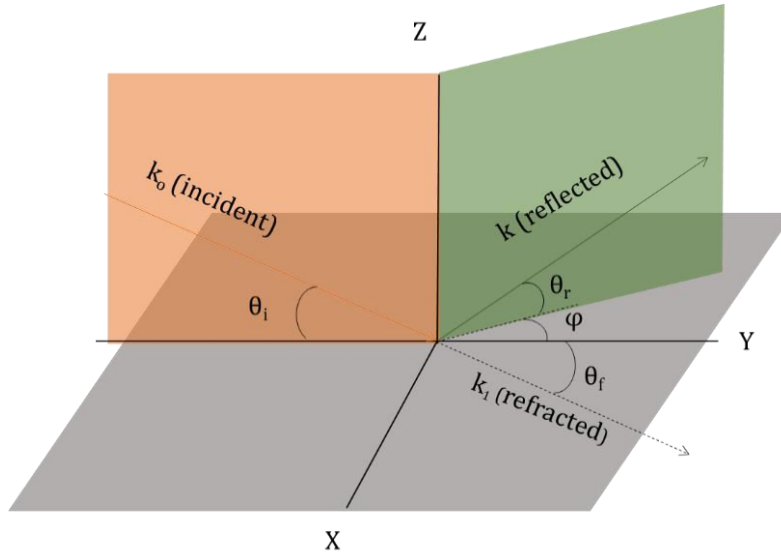
Figure 13: Simplified view of scattering at the surface of a material. k_0 & θ_i are the incident wave vector and angle, k_1 & θ_f the refracted wave vector and angle, and k & θ_r the reflected wave vector and angle, with φ the horizontal component of k (all θ in z-direction, ϕ in y-direction)

As the incident angle θ_i increases above θ_r, fewer neutrons are reflected. Reflectivity (R) of neutrons follows Fresnel Law (which is valid for smooth, flat homogenous surfaces). R is the ratio of the reflected beam energy to the incident beam energy, and is therefore a measure of the magnitude of Q normal to the surface. R can then be analysed as a function of Q to obtain information about variation in $b(r)$ as a function of depth from the surface. When there are variations in $b(r)$ in the direction parallel to the surface plane, due to an inhomogeneous, rough surface, scattering in non-specular directions may be significant. Off-specular, i.e. diffuse or incoherent scattering will reach a maximum at θ_c, and result in a so-called Yoneda peak, after its discoverer.[276] This is also measured in terms of Q with a finite q_x or q_y component.

The reflected and refracted waves are effectively described using the principles of optics when the refractive indices of the media involved are known. For (X-rays and) neutrons, the refractive index $n = 1 - \delta + i\beta$, where the dispersion coefficient is: $\delta = \lambda^2 b(r)/2\pi$, and the absorption contribution: $\beta = \lambda\mu/4\pi$, where the linear absorption coefficient (an intrinsic property of the material denoting the probability of the (photon or) neutron being absorbed while traversing the material per unit length): $\mu = N\alpha_{abs}$, where N is the atomic number density and α_{abs} is the total absorption cross-section.

The scattering length of protons is negative (measured empirically), and therefore substances with a high concentration of hydrogen can exhibit an $n > 1$. The imaginary component of n will only be significant when the material is absorbing. For neutrons, μ is so small that β is usually negligible and can be ignored.

5.1.3   Components of GISANS

In a typical GISANS experiment, the above interactions with the sample will produce a 2D image on the beam detector consisting of the specular reflection, diffuse reflections, the direct incident beam (straight through the sample), diffracted, and transmitted beams. These components are shown in

detail in Figure 14. In GISANS the intensity of the direct beam component will often be so high (due to the weak interaction of neutrons as aforementioned) that it will necessitate the use of a beam stop. When $\theta_i < \theta_c$ the specular peak has almost the same intensity as the direct peak. Additionally, the specular reflection may be so intense that it also requires a point beam stop in the z-axis. A high intensity beam may saturate the detector, making it difficult to pick out features with magnitude-lower scattering intensities. However, in GISANS the signal of interest (relating to mesoscale structures and larger at small values of q_y) is located above the sample horizon, and as such will not be near the specular or direct peaks. Strong scattering features will result from the periodic distribution of structures on the nanoscale, arising from Bragg-like scattering in diffraction.
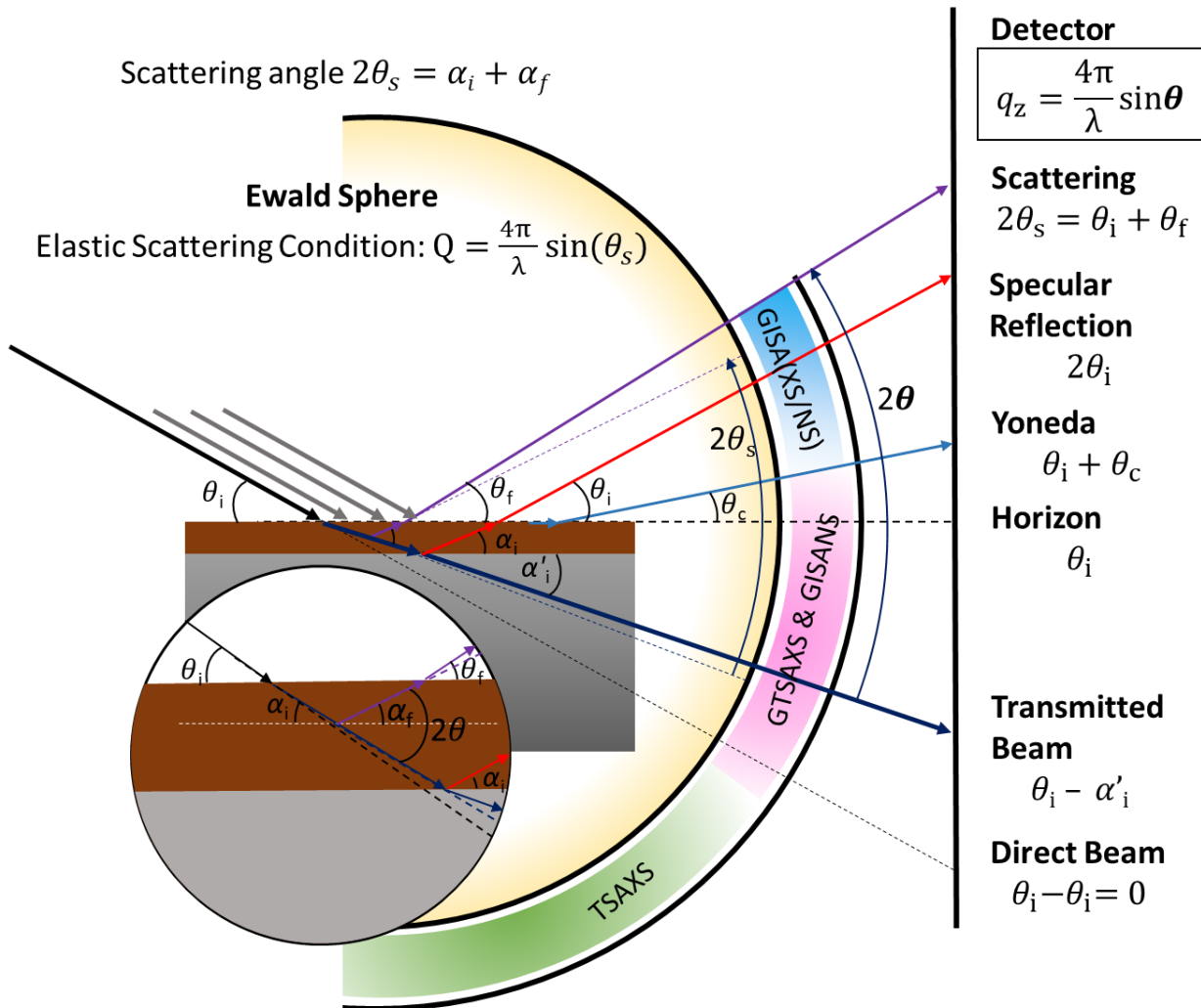
Figure 14: 2D representation of Ewald Sphere and geometries of different techniques in small angle X-ray scattering(XS) and Neutron Scattering(NS). Experiments utilising Transmission(T) takes place for beams scattered through the substrate where $\theta < \theta_i$. Grazing Transmission X-ray techniques (GT) utilise transmission at the sample edge to reduce refraction effects from the substrate while averaging through the sample bulk. Adapted from http://gisaxs.com/index.php/GISAXS.

The horizon line splits the 2D image into the transmitted and reflected beam contributions. Taking a horizontal or vertical cut through the 2D image at a fixed exit angle will give different information on the structures related to those intensity measurements. At the small angles used in GISANS, the 2D detector mostly probes the q_y and q_z contributions, as q_x is very small due to the solid angle probed on the Ewald sphere being small, and therefore curvature is negligible. Small values of q_y correlate with larger structures, so a horizontal cut gives information on distribution and relative proportion of lateral structural features at differing length scales depending on the q_y value. A vertical cut will give information in vertical changes in structure, such as those occurring at the interface between laminar layers of materials.

Grazing incidence geometry allows a depth sensitivity during measurements by varying θ_i or λ. Below the θ_c, although most of the incident beam is reflected, there is still some penetration of the film by an imaginary component, and thus has low intensity. This transmitted wave travels at the surface in an evanescent wave, exponentially damped with regards to propagation in the z-direction. As it travels along the surface, it samples a larger scattering volume, increasing the strength of the scattering intensity. Above θ_c, neutrons penetrate deeply into the film. Thus, surface or near surface, and bulk film structures can be separated out by changing the incidence angle. This can be particularly useful when the specular peak and the Yoneda peak are in a similar position on the area detector. Careful tuning of θ_i below θ_c allows depth profiling of features.

Alternatively, λ can be changed by using time of flight (TOF) detectors. Here a broad neutron wavelength band is used instead of a fixed neutron wavelength. For each wavelength within the band a scattering data set is obtained simultaneously. Providing the gap between pulses is long enough to prevent overlap, then as the initial position and velocity of the neutrons is known, measuring the final position on the detector and the time to reach it allow neutrons of different wavelength (inversely proportional to energy) to be assigned (high energy neutrons in the pulse will reach the detector faster). Hence neutrons which have elastically scattered according to the Bragg condition should reach the detector before neutrons which scatter in an inelastic fashion (as energy is lost in momentum transfer to the sample), and as different features will satisfy this condition at different wavelengths, all that needs to be done to investigate different features is the selection of the appropriate wavelength within the band. With a single optimised incident angle this can be used to take a measurement of which one parts has surface sensitivity (longer λ), while another has bulk sensitivity (shorter λ). Off specular (diffuse) scattering reaches a maximum when the exit angle equals the θ_c, shown as the Yoneda Peak. If the incident angle is fixed, and wavelength increases, then the exit angle will increase and the Yoneda will eventually coincide with the specular peak in q_z. Where diffuse scattering is of interest, the Yoneda and specular peaks can be separated by choosing a wavelength from the pulse at which the exit angle is below the θ_c. TOF-GISANS was demonstrated by *Wolff et al.* in their depth-resolved study of block co-polymer micelles close to the surface of silicon substrates.[277] TOF-GISANS is used in this work for investigation of moisture induced decomposition of perovskite films.

5.1.4 GISANS Methodological Summary

Grazing incidence small angle neutron scattering (GISANS) as a technique is sensitive to the morphology as well as the alignment of lateral and vertical structures at a nanometre scale.[271–273] It

utilises concepts from grazing incidence diffraction, small angle scattering, and reflectometry to explore scattering from the sample in all directions, generally utilising an area detector. Grazing incidence geometries typically exploit incident beam angles (θ_i) below the critical angle (θ_c) of the thin film (the angle below which perfect reflections of the incident beam will occur) which causes the imaginary component of the incident beam to spread out along the surface, allowing interrogation of a large scattering volume. Above θ_c, the neutron beam penetrates deeply into the bulk. Hence surface or near-surface and bulk film structures can be inspected separately by changing the incident angle. The penetration depth varies with the wavelength of the incident beam, meaning depth sensitivity can also be varied by changing the incident wavelength (λ) around a single optimised incident angle.

Broad neutron wavelengths are used in combination with Time-of-Flight (TOF) detectors to investigate both surface and bulk characteristics of perovskite films. For each wavelength within the band a scattering data set is obtained simultaneously. Providing the gap between pulses is long enough to prevent overlap, then as the initial position and velocity of the neutrons is known, measuring the final position on the detector and the time to reach it allow neutrons of different wavelength to be assigned. Hence neutrons which have elastically scattered according to the Bragg condition should reach the detector before neutrons which scatter in an inelastic fashion, and as different features will satisfy this condition at different wavelengths, all that needs to be done to investigate different features is the selection of the appropriate wavelength within the band.

Taking a vertical or horizontal cut (Figure 15A or B respectively) through the 2D image at a fixed exit angle will give different information on the structures related to those intensity measurements. Mesoscale structures of interest at small values of q_y can be identified from scattering features which result from the periodic distribution of structures on the nanoscale, arising from Bragg-like scattering in diffraction. A vertical cut (q_z) will give information in vertical changes in structure, such as those occurring at the interface between laminar layers of materials, and phase changes through the bulk of the film. This is depicted in the cartoon in Figure 16 and summarised by Pipeline 1.

Contrast arises from interactions between incident neutrons and nuclei or unpaired electrons. The strength of these interactions dictates the amplitude of the scattered neutron wave, and is measured using the scattering length density (b). b is determined experimentally and its variation from one isotope to another can be utilised in isotopic labelling to investigate structures. Herein we use a D_2O (dideuterium oxide i.e. heavy water) atmosphere to characterise the uptake of moisture by perovskite films. As D_2O displaces organic cations and deuterated phases form, the different b of the corresponding phases will produce scattering peaks on the GISANS detector, emerging from the perovskite and revealing their position over time relative to the phases containing nominally intrinsic H isotopes. H has a negative b (-3.739) whereas D has a positive b (6.671).

GISANS experiments were carried out at Sans2d at the ISIS neutron source to investigate the uptake of moisture in different perovskite films. The high flux and wide q range enable the characterisation of particles as small as 0.5 nm. The analysis investigates the extent of degradation in terms of changing particle size (swelling due to uptake and adsorption of moisture in perovskite crystals) and due to chemical degradation (to perovskite components such as the constituent salts and hydrated phases). Performing the experiment in the dark allows us to eliminate the contribution of UV induced degradation of perovskite to Lead Halides.[278] Herein we use GISANS to analyse both the phase

evolution and characteristic distances in different perovskite chemistries. Scattering data is plotted using Kratky plots of (Ixq^2) vs. q, as shown in Figure 15.
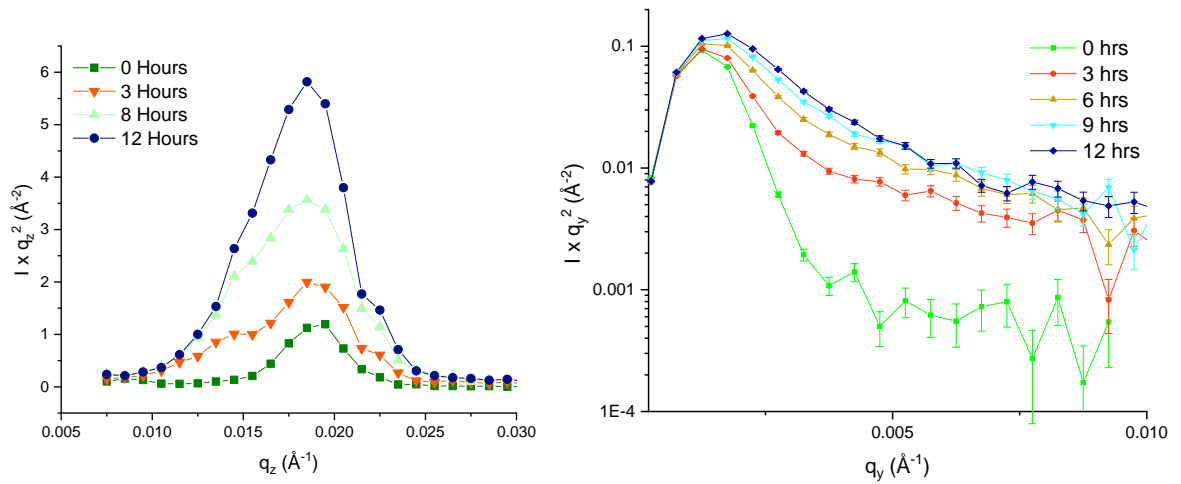
Figure 15: Kratky plots of (Ixq^2) vs. q as used in A) Horizontal cut for phase identification and B) Vertical cut for determination of characteristic lengthscale r_g in SasView. Axes scaled logarithmically for fitting as would be seen in SasView.
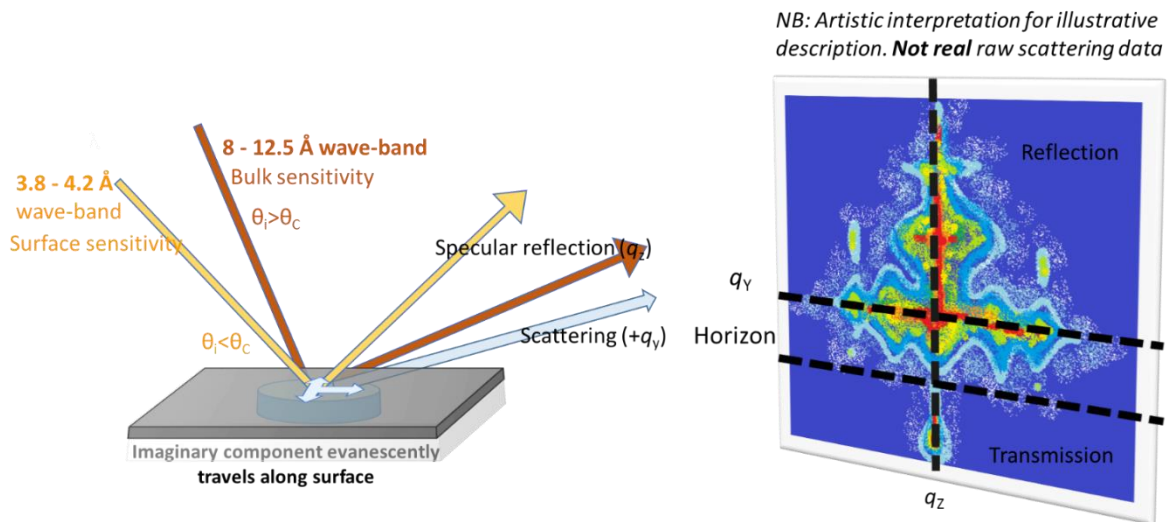
Figure 16: Cartoon depicting neutron scattering from the sample. Scattering intensity is integrated either horizontally (q_Y) or vertically (q_Z), and the incidence angle will determine the region of the sample being investigated as well as the type of analysis which can be performed (as per Pipeline 1).
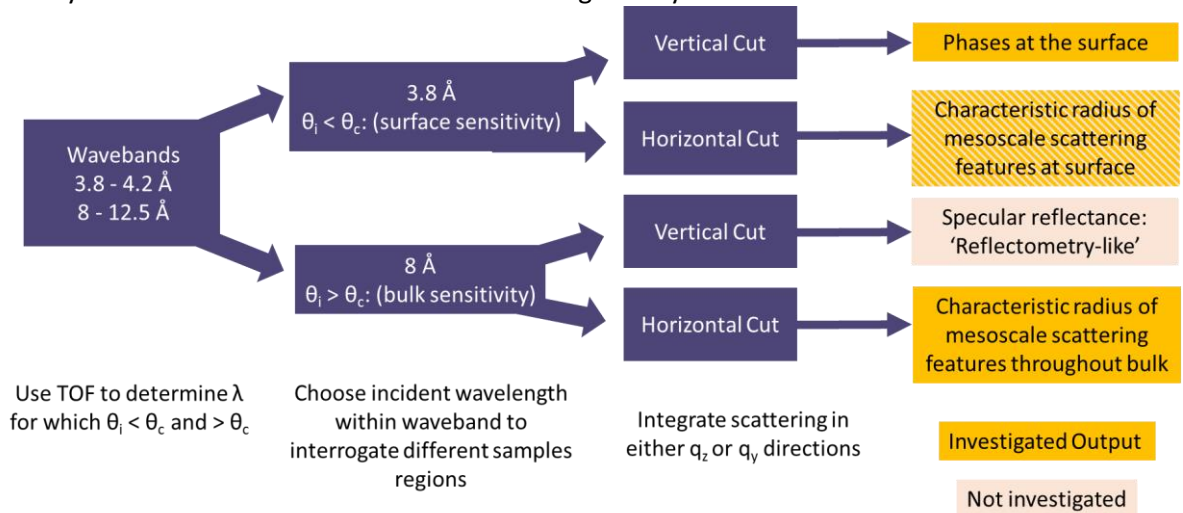
Pipeline 1: TOF-GISANS Analytical Pipeline

Kratky plots normalise scattering profiles by mass and concentration reducing the scattering intensity decay and making features more obvious. I(q) scales with q as the sensitivity of scattering to fine microstructural features such as interfaces, surfaces, pores and nanoparticles becomes more significant, leading to interference and scattering effects which decrease I(q). We model horizontal cuts through a 2D scattering intensity image from a neutron band of 8—12.5 Å (using TOF analysis we optimise the incident beam at 8 Å) using a simplistic sphere model in SasView to estimate the characteristic length-scales associated with mesoscale features on the order of hundreds of nanometres. The sphere model is justified due to symmetry of crystallites observed in SEM before and after degradation, and due to the desirability of assigning a single size parameter.[279] Similarly, horizontal cuts of scattering data induced by a 3.8 Å incident beam are used to interrogate particle dimensions at the surface of the films, and modelled with a Guinier model. This model provides a universal and shape-independent method of determining particle sizes from SAS data.[279]

In this work, off-specular scattering from perovskite thin films in q_y is modelled with specific functions in SASview in order to investigate the particle size distribution over time during exposure to moisture. The intensity of bulk scattering (resulting from a longer, 8 Å incident beam) from horizontal cuts (off-specular scattering integrated in q_y) within the range 1E-4—3E-2 Å^{-1} is fitted with the sphere model (see example fit in Figure 17A):[280]

$$I(q_y) = \frac{scale}{V} \cdot \left[3V(\Delta\rho) \cdot \frac{\sin(q_y r) - q_y r \cos(q_y r)}{(q_y r)^3} \right]^2 + background \qquad \text{Equation 8}$$

Where scale is the scale factor or volume fraction, V is the volume of the scattering phase, *r* is the sphere radius, background is the background level, and $\Delta\rho$ is the difference in *b(r)* between the scattering phase and the solvent. The model allows us to determine the radius *r* associated with characteristic length-scales. Chi-squared (χ^2) values for this model's fits vary between 1-10, giving the highest significance among models tests (including the Guinier model).

Theory and Characterisation Methods - Scattering Theory

For surface scattering, a Guinier model (See Figure 17B) is used to fit the horizontal cut scattering intensities from a 3.8 Å beam within the range 1E-3—3E-2 Å^{-1}:[280]

$$I(q_y) = scale \cdot exp\left[\frac{-q_y{}^2 \, r_g^2}{3}\right] + background \qquad \text{Equation 9}$$
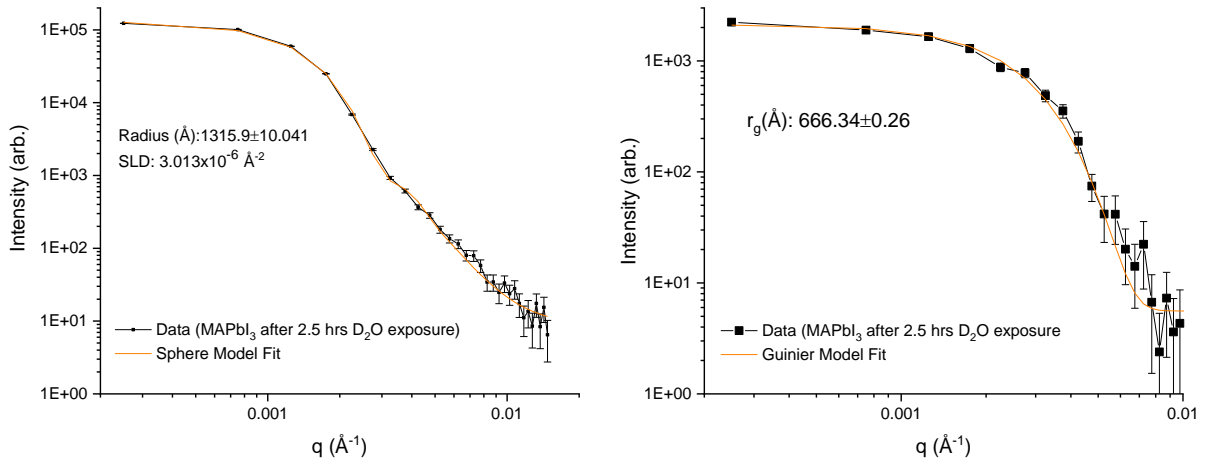
Figure 17: (A) Example of sphere model fit to scattering data from in-plane scattering from an 8 Å incident beam. (B) Example of Guinier model fit from in-plane scattering from a 3.8 Å incident beam.

Where r_g is the radius of gyration, quantifying the scatterer's distribution of *b(r)* (scattering length density as opposed to mass density*)* from its *b(r)* centre of mass. As r_g decreases, this implies a reduction in the distance of scatterer's from the scattering centre of mass, from which we can infer a decrease in inter-particle distance. In this work this corresponds with characteristic distances associated with fragmenting grains due to moisture induced degradation. χ^2 values vary between 0-1 (which implies high significance).

We use scattering peaks from vertical cuts from a waveband of 3.8—4.2 Å in combination with calculated *b's* for predicted degradation products of the various perovskites to determine the evolved state of the film moisture exposure. Vertical cuts from scattering patterns induced by an 8 Å beam chiefly show scattering above the critical angle, allowing reflectometry-like diffraction experiments. The shape of the reflectometry profile provides structural information such as density thickness and roughness.

The phases present in the evolving perovskite films are evaluated by comparing the peak positions in Kratky plots (*q* vs *Iq²*) too *q*-values corresponding with calculated θ_c values for predicted phases in the film. This approach has been demonstrated previously by Schlipf *et al.*.[281] Using Equation 6 and Equation 7 we can determine θ_c by inputting the molecular volume V_m calculated from referenced species densities, and the $\sum b_{coherent}$ values from the publicly available list of neutron scattering lengths from the National Institute of Standards and Technology Centre for Neutron Research.[282] The calculated *q*-positions for predicted phases are shown in Table 6 (Appendix 13.2). Kratky plot peaks

are fitted as per the examples of MAPbI$_3$ after 12 hours exposure in Figure 18 and FA$_{0.83}$Cs$_{0.17}$Pb(I$_{0.83}$Br$_{0.17}$)$_3$ after 8 hours exposure to 90%rH in Figure 19 using OriginPro.

As previously outlined, scattering experiments at different angular ranges will return different structural information. This is exploited to investigate different characteristics of perovskite films under the varying conditions associated with processing of films, degradation, and during operation.

BaseLine:Constant

Chi^2=1.23815E-003	Adj. R-Square=9.99567E-001	# of Data Points=40
SS=2.22866E-002	Degrees of Freedom=18	
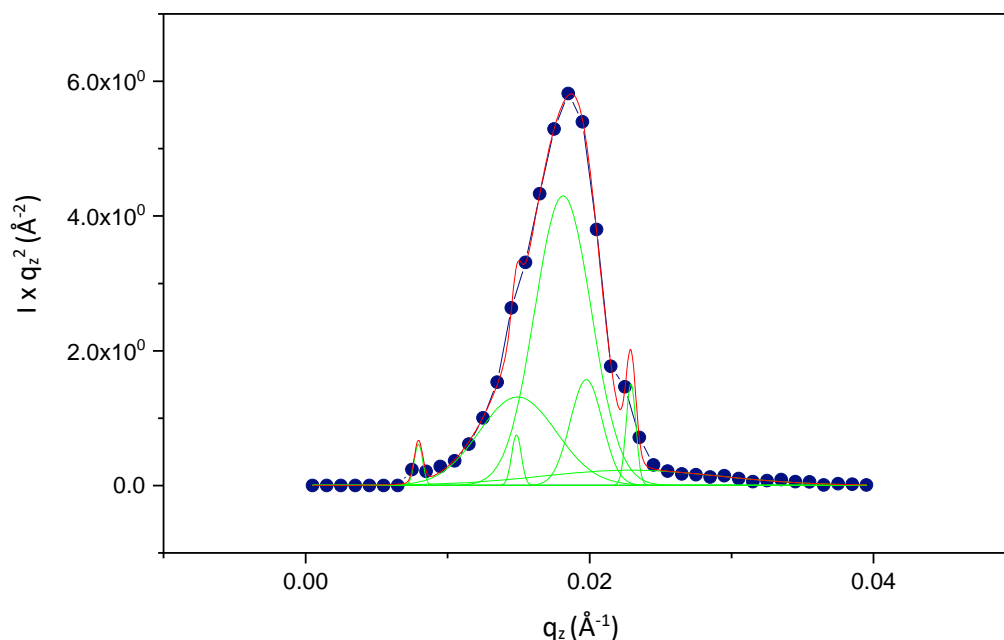
Fitting Results

Peak Index	Peak Type	Area Intg	FWHM	Max Height	Center Grvty	Area IntgP
1	Gaussian	6.39655E-4	8.05472E-4	0.74604	0.01485	1.57116
2	Gaussian	0.00894	0.00641	1.31134	0.01494	21.96291
3	Gaussian	0.02139	0.00468	4.2957	0.01813	52.54368
4	Gaussian	0.00445	0.00267	1.56848	0.01977	10.93153
5	Gaussian	4.54902E-4	6.99893E-4	0.6106	0.00795	1.11736
6	Gaussian	0.00353	0.0148	0.22491	0.02291	8.66597
7	Gaussian	0.00131	8.15973E-4	1.50339	0.02291	3.20739

Figure 18: Example fitting of Kratky plot of Horizontal scattering from a 3.8-4.2 Å incident neutron wavelength band. This shows MAPbI$_3$ after 8 hrs of degradation. The peaks relate to different phases respectively for Peak indices 1-6; (5) 0.00795: MAPbI$_3$ mixed hydrogen isotope (D+H) hydrate, (1) 0.01485 (MAPbI$_3$ mono-heavy-hydrate +PbOH$_2$), (2) 0.01494 (PbOH$_2$ + PbI$_2$), (3,4) 0.01813,0.01977 (Deuterated MAPbI$_3$/ Mono-heavy-hydrate), (6,7) 0.02291 (Deuterated (6 Deuterium) MAPbI$_3$

BaseLine:Constant

Chi^2=1.07735E-005	Adj. R-Square=9.99835E-001	# of Data Points=40
SS=1.29282E-004	Degrees of Freedom=12	
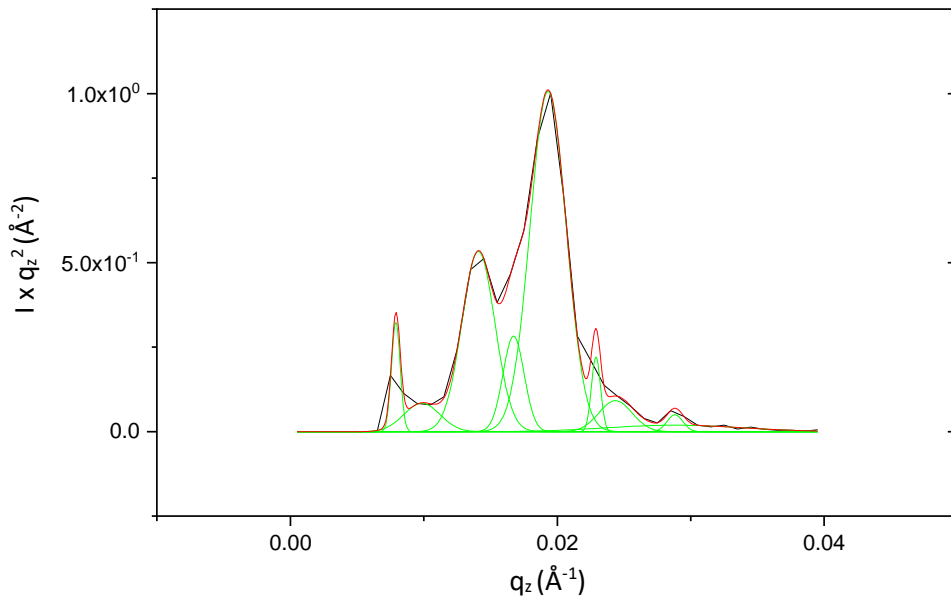
Fitting Results

Peak Index	Peak Type	Area Intg	FWHM	Max Height	Center Grvty	Area IntgP
1	Gaussian	0.00165	0.00291	0.53324	0.01409	23.76754
2	Gaussian	5.60517E-4	0.00186	0.28268	0.01672	8.06111
3	Gaussian	0.0034	0.00318	1.00718	0.01931	48.96346
4	Gaussian	2.8422E-4	0.00317	0.08413	0.00986	4.08753
5	Gaussian	7.39734E-5	0.00139	0.04996	0.02882	1.06385
6	Gaussian	2.39312E-4	0.01183	0.01933	0.02882	3.44168
7	Gaussian	1.87701E-4	8.00092E-4	0.22039	0.0229	2.69943
8	Gaussian	2.86418E-4	0.00293	0.09168	0.02436	4.11914
9	Gaussian	2.63968E-4	7.68275E-4	0.32278	0.00791	3.79627

Figure 19: Example fitting of Kratky plot of Horizontal scattering from a 3.8-4.2 Å incident neutron wavelength band. This shows $FA_{0.83}Cs_{0.17}Pb(I_{0.83}Br_{0.17})_3$ after 8 hrs of degradation. The peaks relate to different phases respectively for Peak indices 1-6; (1) q=0.01409 (**$FAPbI_3$+$CsPb_2I_4Br$**), (2) 0.01672 (CsI+$FAPbI_3$ mono-heavy-hydrate), (3) 0.1931 ($PbBr_2$ + Deuterated $FAPbI_3$),(7) 0.0229 (Deuterated FACs in which 4-5 Hydrogen atoms are replaced by Deuterium), (8) 0.02436 (PbO or Deuterated $FAPbBr_3$) (5,6)0.02882 ($PbOD_2$)

5.1.5 Experimental setup for GISANS Experiment

An in-situ degradation study of perovskite films upon exposure to a relative humidity of 90% levels was done using GISANS. Degradation of thin films is associated with hydrated phases moisture, change in particle size and q-scale. The experimental setup for these in-situ measurements is shown in Figure 20. Precursor solutions were made up and were spun on cleaned Si wafers. Samples were placed in a humidity chamber containing saturated salt solution baths of either NaCl or LiCl and an Arduino connected hygrometer which was linked to a laptop. The chamber was provided by ISIS, while the humidity measurement system was devised in-house (hygrometer + Arduino code and laptop control). The chamber had neutron-transparent windows, facilitating in-situ GISANS measurements of the film as moisture is adsorbed on the surface and chemical and morphological

changes occur. Salt solutions of NaCl were used to attain a relative humidity of 90%, while LiCl was used to dry the experimental chamber, and create a constant base humidity of approximately 25%. The issue of humidity measurement was resolved with measured humidity as per expectations from review of humidity control in the laboratory using Salt Solutions by Young.[270] Plots of humidity are shown in Figure 21 (measurements at ISIS).
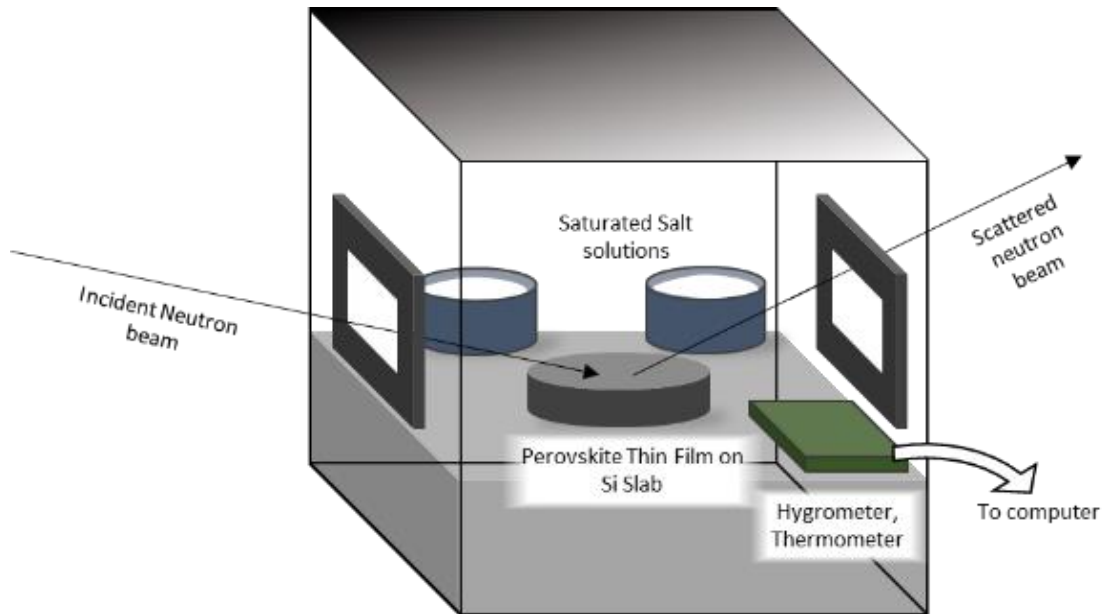
Figure 20: Small Angle Neutron Scattering experiment setup for in-situ moisture degradation
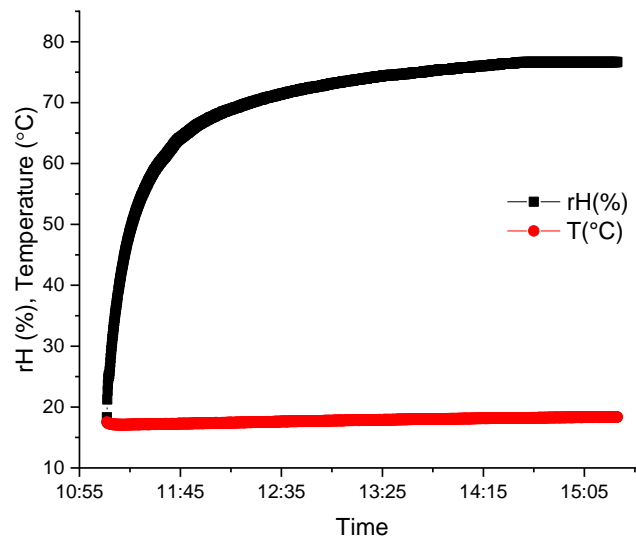
Figure 21: Plot of relative humidity over time for hygrometer during the ISIS experiment. Also shown is temperature. A saturated salt solution was used (NaCl), giving an rH slightly higher than the predicted 70%.

5.2   Wide Angle X-ray Scattering

X-ray scattering is used for structural investigation of perovskite thin films in either transmission or grazing incidence geometries. X-rays are scattered from thin film samples with intensity peak positions and spacing determined by the specific crystal structures present. Different crystal structures will provide solutions to Bragg's law (see Section 5.1.1) at different sets of characteristic exit angles or q-values, allowing the determination of phases. The 2D scattering intensities can be reduced to 1D diffractograms which can be fitted in various software (or technically through manual calculation) to determine lattice parameters defining inter-planar spacing; space-groups, and thereby crystal systems. Different phases will possess distinct space groups (describing the symmetries) and lattice parameters. By comparing the fitted peak positions to diffraction patterns available in the literature or various libraries, peaks can be assigned millers indices which denote the family of lattice planes from which the peak originates, as well as the phase possessing those planes. Peaks with higher intensity will occur for lattice planes with greater order — this may arise due to the orientation of the planes with regards to the incident beam resulting in a greater density of scattering centres, or typically will increase due to preferential formation of the crystal in that orientation due to conditions specific to the growth process of the phase. GIWAXS and WAXS experiments were performed on the I07 beamline at the Diamond Light Source, Didcot, UK. Beam energy was 12.4keV.

5.2.1   Understanding peak broadening and shifting

The position, intensity and width of the scattered peak is also influenced by the ordering and size of the crystallites interacting with the incident beam. As crystalline packing density increases the intensity of the scattered beam also increases due to a greater volume of interaction meaning a greater proportion of the beam is reflected. As crystalline ordering increases this will increase the intensity of peaks satisfying the Bragg equation, producing more pronounced phases in the X-ray diffractogram against the background scattering. Preferential orientations can occur during processes such as annealing where a particular growth direction is thermodynamically favoured for the crystallites. Peak broadening occurs due to micro-strains in the crystal lattice (due to defects and concentration gradients). Broadening is exacerbated by the instrumental contribution which arises due to the finite size of the beam spot — the diffracting volume is therefore also finite and diffraction will always occur off the true centre of the incident beam.

Broadening and crystallite size are reciprocally related — as the number of scattering centres tends towards infinity the scattering interference increases leading to sharper and sharper peaks until it reaches a fundamental limit such as the inherent instrumental broadening. Broadening will hence be largest for small crystallites and generally decrease as they grow. Growth can also reduce the prevalence of defects in some materials as domain boundary reorientation and atomic motion restores a regular lattice and mitigates the formation of point and line defects. Crystallite strain, arising for example due to mismatches in thermal expansion coefficient between perovskite and contacting layers and substrates also impacts peak position. Compressive strain, which reduces the distance between lattice atoms, results in an increase in q-positions of lattice peaks (an increase in reciprocal space), whereas a tensile strain, expanding the distance between atoms results in a decrease in q-position of lattice peaks.

This theoretical understanding is useful in deducing the mechanisms underway during thin film crystallisation and decomposition, and is used to interpret phase evolutions in perovskite thin films during spin-coating and annealing.

5.2.2 Methodological Summary for WAXS

Wide-Angle X-ray Scattering performed in transmission geometry enables in-situ structural characterisation of liquid and solid surfaces at interatomic and intermolecular length scales. Complex liquid surfaces involving self-assembling nanoparticles aptly describes perovskite film formation.

A major challenge in understanding such systems is probing both local nanoscale structure and mesoscale heterogeneities (such as multiple phases and morphologies). Typical specular reflectivity and grazing incidence experiments for probing surfaces rely on small incidence angles, which cast large beam footprints on the order of mm. This makes it difficult to resolve heterogeneities on the order of nm and μm. Another issue is the need to sample a large parameter space: the conversion to perovskite is influenced by thermodynamic factors arising from atmospheric conditions (partial pressures, heat), chemical composition, and processing variables such as spin-speed and drying time. Taken together, a high signal-to noise ratio is needed to collect statistically significant data from which these can be investigated. Using a transmission geometry increases sensitivity to ordering in the in-plane direction, while also increasing the interrogated sample depth, which can be powerful for investigating phase changes in the vertical direction in the film.[283] It also reduces losses arising from multiple interfacial scattering events in Grazing-incidence methods.

A rotating stage helps to compensate for the smaller scattering volume relative to a grazing incidence experiment. As the X-ray beam is offset from the axis of rotation of the sample, the beam precedes in a circular path, and probing a larger number of crystallites. This has the effect of averaging out counts across the detector area during the integration stage of data reduction and helps to compensate for the relatively low signal of the scattered beam. A larger number of crystallites are interrogated in a dynamic experiment when compared to a static one. As long as the liquid phase does not severely attenuate the incident beam, and background scattering in the region of interest is low, data should be analytically useful. In this experiment, the microscope slides used produced significant broad background scattering upon the area detector. Subtracting the glass background was done using the DAWN Pipeline briefly outlined in Schema 1. As the scattering from the glass substrate is broad it can readily be subtracted without affecting the peaks of interest. Scattering beam intensities, measured as a function of the scattering vector in terms of q can be readily manipulated using the Bragg equation to give values of θ, d, and phase information through comparison to diffraction spectra in the literature. However, it is less sensitive to vertical heterogeneity and poor in spatially resolving these features. Furthermore, it cannot investigate the preferential orientation of crystallites relative to the substrate surface or investigate different sample depths. Scattering data will be a product of all interacting phases. This makes this technique complimentary to grazing incidence techniques. Some researchers have in fact combined the techniques to take advantage of the best aspects of both in Grazing Incidence Transmission X-ray scattering where measurements are taken at a small incident angle near the edge of the sample in order to avoid refraction effects while also sampling a larger scattering volume and small q_z.[284]

Theory and Characterisation Methods - Wide Angle X-ray Scattering

Schema 1 outlines the reduction methodology for converting the 2D distribution of scattering intensities at the detector to 1D diffractograms. This was designed after studying the i22 DAWN user manual and guidelines by Filik et al.[285] In brief, this method of reducing the data first converts Bragg scattering peaks distributed in reciprocal space and intersecting with the Ewald Sphere into a 2D detector image. This image is then azithumally integrated to give a 1-dimensional plot of scattering peaks as a function of 2θ. Finally, the x-scale is converted from 2θ to q, measured in 1/Angstroms ($Å^{-1}$), and measurements are plotted in time-series with intensity as either a tertiary z-axis or colour-coded in a contour plot. Figure 22 shows 1D diffractograms for $MAPbI_3$ after 100 s of spin coating before and after removal of the glass substrate background. The code for generating contour plots was written in Python and ran using a Jupyter Notebook (see Appendix). Phase determination is approached through comparison with existing datasets where possible.

Schema 1: Reduction Methodology for WAXS

1. Detector Calibration (Silver Behenate Reference

2. Threshold Mask

3. Dilate Mask

4. Set Poisson Error

5. Self-Absorption

6. Import Mask from File

7. Subtract Frame

8. Solid Angle Correction

9. Azithumal Integration

10. Export Results

1. Imports the detector calibration file. The data is calibrated using a silver behenate reference in the powder calibration perspective.

2. The threshold mask defines invalid pixels (dead and hot or overexposed) on the detector, so they are not considered in subsequent corrections.

3. The dilate mask applies the hot pixel correction to neighbouring pixels within a defined radius.

4. Calculates the Poisson (photon counting) error for each pixel on the detector face, this is done with the Set Poisson Error processing step, which has no options and simply has to be placed into the pipeline to calculate the required error values

5. Self-absorption corrects for the increased probability of scattered rays that are absorbed as they travel through slightly increased amounts of sample after the scattering event. This accounts for transmission effects due to the measurement geometry

6. Applies beam block mask

7. Subtracts Substrate background

8. Corrects for projection of 3D scattering on 2D detector

9. Reduces the data from a 2D image to a line plot with the Azimuthal Integration processing step to produce I vs. q data. Data is averaged through the entire detector area.

Figure 22: Scattering from a MAPbI$_3$ sample after 100 s of spin coating before and after application of the substrate frame subtraction operation in Schema 1. Broad scattering from the glass background is clear before.

5.2.3 Experimental Setup for transmission mode WAXS

A transmission mode WAXS experiment was designed to investigate the process of perovskite formation during different steps in the widely used and basic spin-coating-plus-annealing fabrication method. A bespoke, in-house designed vertical spin-coater was used to take measurements during spin-coating of perovskite precursor solution as shown in Figure 23A. The spin-coater was replaced with a hot-plate in the same geometry, and in-situ annealing data was taken for films which were spin-coated in the lab prior to the experiment.

All samples were fabricated following a one-step deposition process. Samples fabricated in the lab prior to annealing during in-situ WAXS were prepared using Program 2 described in 4.3.1. 40 µl of solution was dripped on the static substrate surface, and 100 µl of ethyl acetate was applied 15 s after the beginning of spinning. In the case of the in-situ spin coating experiment, 50 µl of solution is dripped onto the surface, and the sample was spun at 4000 rpm for 30 s. The in-situ spin coater was optimised prior to use to determine the voltage-rpm relationship, as shown in Figure 23B, with a linear relationship.

A substrate was mounted on the custom-built spin coater which has a hollow shaft to allow the propagation of X-rays to the detector. Rotation occurs in a vertical plane approximately perpendicular to the incident X-ray beam. As the X-ray is perpendicular to the sample surface, it is sensitive to in-plane ordering through the depth of the sample, but less sensitive to out of plane ordering. For in-situ spin coating, 50 µl of precursor solution was dripped onto the substrate surface with a pipette just above the measurement point, filled from a remotely operated syringe injection pump. The spinning process was started shortly after the solution begins to run down the static surface, dynamically spreading the material over the surface. The spin-coater was surrounded by a custom built chamber in front of a beam-stop and after a series of slits to reduce background

65

scattering and to ensure solvent vapour is extracted by a ventilation system placed directly above the chamber. Kapton windows are used as they are transparent to X-rays and prevent the splashing of ejected lead-containing material outside the chamber. Wiping the Kapton windows is avoided, as this smears material and scratches the Kapton, but when necessary this is done. A splash guard captures the majority of excess material which is lost centrifugally during spinning. The chamber is not air-tight, and thus the inner atmosphere will be a combination of He (overpressure applied in chamber), air and solvent vapour. When the sample is static, the scattering is restricted to a few spots on the 2D WAXS images, because only a small volume of crystallites being measured. By spinning the sample during measurement, a greater volume of material passes through the beam (as the beam is offset relative to the centre of rotation of the spin coater by ~2mm), more crystals are probed. Thus, in the dynamic spinning experiment, a much larger number of crystallites are sampled, and the WAXS data is more representative of the sample. Additionally, beam damage is limited as a fast shutter is used to block the beam when the 5 s measurements are not being taken.
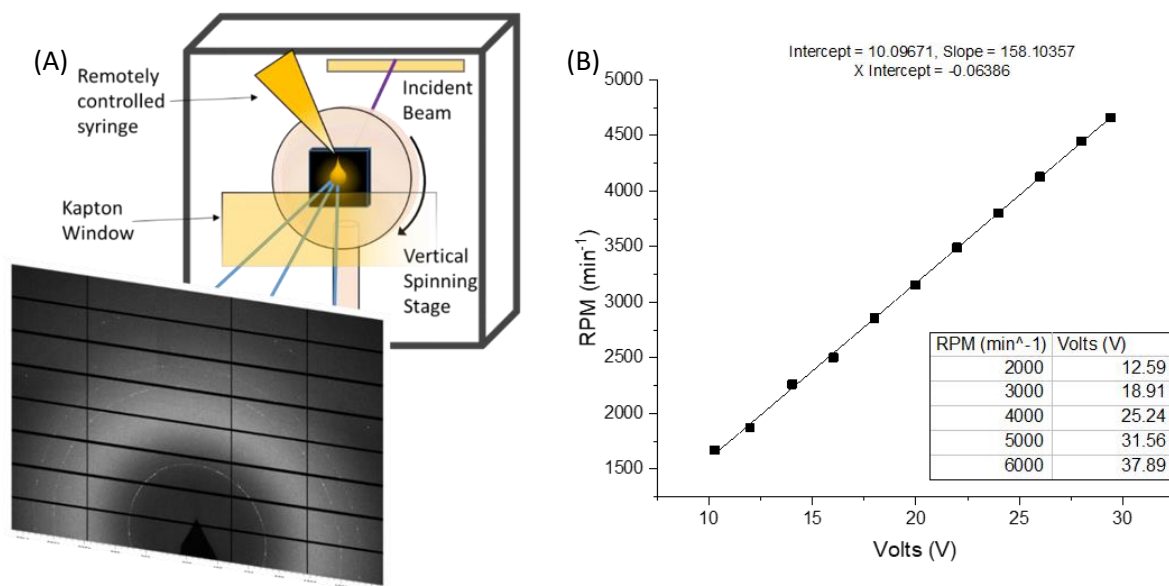
Figure 23: WAXS stage setup with 2D detector image and spin coater calibration.

In the in-situ annealing experiments, the spin-coater is replaced with a hot-plate, once again taking advantage of the transmission geometry via a hollow shaft through which the measurement is made. The hotplate takes approximately 2-3 minutes to reach 100°C. Samples are placed on the hotplate, and then the beam and the hotplate are turned on. The q-values and intensity scale were calibrated using a sample of silver behenate, which has a well-defined structure with well-defined peak positions and intensities. The samples were interrogated with a 10.5 keV beam, over the wide-angle 2θ range 1-40°, and converted to q (0-3.5 Å^{-1}). The beam resulted in a spot size on the sample which was approximately 100 µm high by 200 µm wide. Data is shown as a function of q in Angstroms as this will not change with instrument parameters or beam wavelength for a given sample. Relative humidity in the beam hutch was 55-57%, and the temperature varied between 22-27°C. WAXS data was reduced using DAWN. Individual spectra were fitted in DAWN to determine FWHMs and peak

areas for peaks at different times. Fits were undertaken with a pseudo-Voigt model. 2D contour plots were generated via Python from 2D X-ray spectra in time series.

5.2.4   Methodological Summary for GIWAXS

In this experiment the incident angle was varied in order to explore the depth dependence of various phase's prevalence, as well as strain effects in perovskite thin films. GIWAXS experiments were performed on the I07 beamline at the Diamond Light Source, Didcot, UK. Beam energy was 12.4 keV. The angle of incidence was varied between 0-0.5°. Decreasing θ_i has the effect of increasing surface sensitivity as the resultant scattering becomes dominated by waves scattered from the imaginary component of the incident wave which becomes evanescently coupled to the surface. Measurements at 0.3° were used for comparison between samples as it gave the highest scattering intensity, suggesting it was close to the θ_c. During measurement samples were housed inside a custom built sample chamber flooded with a continuous overpressure of dry He to prevent the samples reaction with ambient air affecting samples during measurement.

Phases are assigned to peaks by comparing their q-positions to q-positions of peaks as shown in calculated diffraction patterns of expected phases according to materials project.org.[286] These simulated peaks are benchmarked as much as possible against experimental values from peer-reviewed publications, accessible from the website. Peak fitting was done using DAWN. Space Groups were determined by fitting diffraction spectra exported from DAWN in GSAS II. Plots were made in OriginPRO. The pipeline in DAWN was relatively simple. The pipeline was the same as Pipeline 2, though the frame subtraction is not necessary in this geometry as the beam does not interact with the substrate.

5.3   Spectroscopic Methods

5.3.1   Ultraviolet-Visible Spectroscopy

UV-Vis spectroscopy is a method for characterising the optical properties of a thin sample. This technique uses light in the visible, near UV, and near IR spectral regions to characterise absorption and reflectance. Absorption of photons in the visible light range of the electromagnetic spectrum causes transitions of electrons from the ground state to the excited state — the lower the energy gap between the ground state and the excited state, the longer the wavelength of light absorbed i.e. lower energy photons.

The Beer-Lambert law relates the absorbance of light to the concentration of absorbing species in the direction of light propagation. For clarification, the measured absorbance is the attenuation of light, which can be caused by absorption, reflection, scattering and other processes, whereas absorption refers to the physical process of absorbing light (the above-described electronic transition to an excited state). Assuming a uniform concentration of absorptive species, this expression is:

$$A_\lambda = log\left(\frac{I_0}{I_t}\right) = -\log(T) = \alpha_\lambda lc \qquad \text{Equation 10}$$

T is the transmittance, logarithmically proportional to absorbance A, and I_o and I_t are incident and transmitted intensity respectively. α is the absorptivity of the attenuating species (molar attenuation or absorption coefficient as a function of wavelength), l the optical path length, and c the

concentration of attenuating species. Hence, for a fixed path length, UV-Vis spectroscopy can be used to determine the concentration of the absorber in a solution, if α is known. However, this does not account for species which are highly scattering as opposed to absorbing, which will also attenuate the transmitted beam. In a uniform perovskite film, under flux normal to the surface there will be negligible scatter. For some of the samples in this work this is not the case, and scattering contributes to the absorbance, most obviously recognisable where the baseline of the data appears above zero.

In semiconductors, there are different mechanisms for this absorption to occur. There can be inter-band (responsible for colour), intra-band (free carriers excited within a band), or excitonic absorption. Absorption can also occur in dopants in the lattice. Excitonic absorption differs from inter-band absorption in that the electron-hole pair produced by absorbing a photon is still loosely bound. Not enough energy has been transferred to overcome the coulomb attraction between them. In materials where this occurs, the optical band gap can be distinguished from the electrical band gap as the threshold for absorbing photons, whereas the electrical band gap is the threshold for creating an unbound electron-hole pair. In MAPbI$_3$ free carriers predominate while coexisting with excitons at room temperature. D'Innocenzo *et al.* modelled that high photoexcitation (generating a state density in excess of 10^{15} cm^{-3}) at room temperature will lead to a reduced ratio of carriers to excitons, as the opportunity for free electron-hole capture events increases.[287] Nonetheless, excitons in perovskites tend to be loosely bound with exciton binding energies between 20-45 meV at room temperature.[288] For most perovskites this means room temperatures measurements of optical band-gap with UV-Vis spectroscopy will give a fairly accurate estimate of the electrical band gap (~1.5-1.6 eV for MAPbi$_3$).

Inter-band transitions in semiconductors can be either direct or indirect due to differences in band structures arising from the overlaps of bonding (valence band) or antibonding (conducting band) orbitals. In materials with an indirect transition, photons require the assistance of phonons (oscillations of the crystal lattice) to shift to the high energy state. Whether a band gap is direct or indirect can be simply determined by plotting absorption coefficient against photon energy and using the following equations:

For a direct band gap, assuming only inter-band excitations and roughly parabolic bands:

$$\alpha_\lambda \approx A^* \sqrt{h\nu - E_g} \qquad \text{Equation 11}$$

Where h is plank's constant, ν is frequency, k_B is the Boltzmann's constant, T is temperature, A^* is a frequency-independent constant that is characteristic of the material and related to the effective masses of the carriers, and E_p is the energy of the phonon which facilitates the transition. A Tauc plot of $h\nu$ versus $(\alpha h\nu)^{1/r}$ allows determination of the band gap occurring in the material (See Figure 70, Appendix 13.3). Here r is a fitting parameter that can be used to interpret the behaviour of the material absorption spectrum near the band-edge. The plot will show a distinctly linear region which can be extrapolated to the x-axis where $\alpha = 0$ to determine the onset of absorption, giving the energy of the optical band gap. If a linear plot is yielded from a plot with $r = 0.5$ then there is a direct band gap while for $r = 2$, there is an indirect band gap.

Theory and Characterisation Methods - Spectroscopic Methods

The degree of structural disorder (defects arising from non-stoichiometric chemistries, impurities, and other factors) in the semiconductor introduces localised states within the optical band gap that have the effect of smearing the absorption edge. Urbach energy (E_U) also indicates the disorder of electronic states in the film. The absorption coefficient can be related to the Urbach energy as:

$$\alpha_\lambda = a_o \exp(\frac{h\nu}{E_U})$$
<div align="right">Equation 12</div>

Where a_o is a constant. Plotting $ln(\alpha)$ against incident photon energy $h\nu$ (See Figure 71, 13.3) will allow E_U to be obtained from the slope of the graphical fit, $1/E_U$. A higher E_U implies a disordered absorption edge.

In this work, UV-Vis absorbance spectra of films were obtained using a spectrometer (USB2000+UV–VIS–ES) equipped with a deuterium halogen light source (UV–VIS-NIR_DT–MINI–2-GS), both from Ocean optics. Data was collected using the Ocean Optics SpectraSuite software and the recorded data was plotted using Origin Pro v 8.1 software. UV-Vis spectroscopy is used to measure films of approximate thickness between 200-400nm. By analysing the shape of the Absorbance plot the presence of absorbing species can be deduced by peaks in the absorbance plot or steep absorbance increases coinciding with absorption at a band gap. Low transmittance in the absence of strong absorption can typically be attributed to a high level of scattering as a result of a film with poor morphology. A rough surface can scatter incident light in different directions, reducing both absorption and transmittance. Scrutinising the absorption onset through Tauc and Urbach plots allows comparison of band gap energy and disorder of the band-edge across samples.

5.3.2   Ellipsometry [289]

In an Ellipsometry experiment, a beam of known polarisation is reflected or transmitted from the sample, and the output polarisation is measured. The polarisation state of the output beam can be split into its s and p components, where the amplitude of each are r_s and r_p (r: reflected) respectively. s refers to being perpendicularly polarised light relative to the plane of incidence, while p is polarised parallel to the plane of incidence. The change in polarisation (ρ) is measured in terms of the amplitude component (Ψ) and phase difference (Δ) in degrees.

The detector will convert elliptically polarised light from the material to electronic signal to determine the overall final reflected polarisation. This is compared to the known input polarisation to determine the difference. From this, properties such as thickness and optical constants n (real refractive index) and κ (extinction coefficient or imaginary component) may be determined using a valid physical model. κ corresponds with absorption, indicating the amount of attenuation that occurs when the incident light propagates through the material. κ is related to the absorption coefficient (α) as:

$$\alpha = \frac{4\pi\kappa}{\lambda}$$
<div align="right">Equation 13</div>

Materials typically consist of more than a single bulk layer – i.e. multiple thin film layers on a substrate, and so data analysis is usually conducted using a regression analysis:

Theory and Characterisation Methods - Spectroscopic Methods

1.   Sample is measured, obtaining a dataset of Ψ and Δ values
2.   Model is constructed to describe the sample layers and materials.
3.   Model used to calculate the predicted response from Fresnel's equations which describe each material relating Ψ and Δ to n, κ, thickness and roughness. OR an estimate is given.
4.   Calculated values are compared to empirical experimental data. Unknown material properties can be integrated to improve the match between experimental data and model-calculated data. This is achieved using regression, where a minimisation method such as the Mean Squared Error method is iteratively used to quantify the difference between curves (for example property versus wavelength). Finding the global minimum in the estimator allows the correct material property to be determined for a given property measurement dataset.

Thickness measurements require that a portion of light travel through the entire film and return to the surface. Ellipsometry is used for films of thickness ranging from sub-nm to a few µm. Above this range, interference oscillations are difficult to resolve, except at long wavelengths (IR). Also, as a result of this, phase information from Δ is very sensitive to films down to sub-monolayer thickness.

Thickness affects the path length of light, but n determines phase velocity (v) and refracted angle, thus both n and thickness contribute to the delay between the output beam and input beam. Both n, κ and thickness must be known to get the correct results. These constants vary depending on λ, and so fitting calculated data to experimental data can use a dispersion relationship of optical constant versus λ to fit the model.

For transparent materials, the refractive index is often described using the Cauchy relationship in Equation 14, where three terms (Amplitude (A), Broadening (B) and Centre Energy (E_C)) are adjusted to match n for a given material:

$$n(\lambda) = A + \frac{B}{\lambda^2} + \frac{E_C}{\lambda^4} \qquad \text{Equation 14}$$

The absorbing region must account for both n and κ, for which oscillator theories can be used to describe absorption, such as Lorentz, Harmonic and Gaussian oscillators. An offset to the real component is added to account for absorption outside the measured spectral region. A Lorentz oscillator could be used to model an absorbing material as per Equation 15:

$$n(v) = \varepsilon_{1\text{ offset}} + \frac{AE_c}{E_c^2 - E^2 - iBE} \qquad \text{Equation 15}$$

Where $\varepsilon_{1\text{ offset}}$ is the offset index (explained in the Optical Model section) and E is the energy ($E = hv \cong 1240/\lambda_{nm}$). More advanced optical dispersion models will also account for absorption at the band gap energy. In this work, the absorbing region is modelled using a B-spline dispersion model consistent with Kramers-Kronig dispersion relations given in Equation 16, appropriate for modelling optical constants of semiconductor materials.[290–292] Kramers-Kronig consistency is used to calculate the shape of the real component after the imaginary behaviour is described by the oscillator.

$$n(v) - 1 = \frac{c}{\pi} \mathrm{P} \int_0^{\infty} \frac{\kappa(\tilde{v})}{\tilde{v}^2 - v^2} d\tilde{v} \qquad \text{Equation 16}$$

Theory and Characterisation Methods - Spectroscopic Methods

The real refractive index (n) can be determined at any frequency (v) by the values taken by the extinction coefficient κ for all frequencies (a complex variable). $\mathcal{P}$ denotes the Cauchy Principal value, which is a method of assigning values to the improper integral which Equation 16 becomes when approaching infinity. By measuring one part of the complex refractive index ($\tilde{n} = n + i\kappa$), the Kramers-Kronig relations allows the other to be determined.

Variable angle spectroscopic ellipsometry has been used by other researchers to determine the complex refractive index and dielectric function of perovskite thin films, to investigate changes in optical constants during hydration as perovskite react with moisture to form hydrate phases, and to compare MAPbX$_3$ single crystals optical properties as the halide species X varies.[165,293,294] Ellipsometry can also be used to determine roughness by modelling the surface of the film as a mixed layer of absorbing material and air. It is important to note that roughness induces an extra phase shift (Δ). So if the surface roughness layer increases in thickness, the increased Δ will have a knock on effect, increasing κ and therefore the calculated α.[295] This can be understood as optical in-coupling from surface roughness increasing the extrinsic or effective absorption coefficient.

Optical model:

Modelling simultaneously takes into account three incident angles (65°, 70°, 75°). It incorporates the 3 layers shown in

Figure 24; a glass slide modelled using a Cauchy model, absorbing layer modelled with the B-spline dispersion, and a roughness layer which assumes 50% of the layer being composed of air (same refractive index as air). The model defines a new B-spline layer for each sample, determining thickness and surface roughness in conjunction with optical constants. The B-Spline layer specifies the optical constants versus wavelength using a series of nodes which are equally spaced in eV. The approximate spacing of the nodes is controlled by the resolution, set to 0.1 eV. A transparent region is set by applying the transparent wavelength range above 800 nm (this doesn't need to be exact and the software will refine this). The model is allowed to fit the parameters "E Inf", "IR Amp", and IR Br to model the absorption. The parameter "E Inf" is the value of ε_1 at infinity and is added as a constant offset to the ε_1 curve, accounting for effects of absorption at energies far above the measured spectral range. "IR Amp" is the value of the zero-energy oscillator accounting for the effects of absorption at low energies outside the measured spectral range, for example due to free carrier absorption. "IR Br" refers to the broadening of the oscillator referred to in IR Amp. This can be set to zero, which will make the IR Amp act as an IR Pole, tilting the ε_1 curve down at lower wavelengths. However here it is fitted, allowing IR Amp to account for a Drude absorption tail; there is evidence of photo-induced lattice fluctuations leading to carrier localization that impacts the absorption profile.[296,297] In this work a J.A. Woollam alpha-SE ellipsometer is used alongside their CompleteEASE software for ellipsometry measurements. Ellipsometry is thus a useful non-destructive method for determining optical constants n and k, from which absorption α can be calculated. From $\alpha(\lambda)$ E_g and E_U can be determined using the approaches outline in 5.3.1 and compared to UV-Vis spectroscopy. It can also be used to measure thickness and surface roughness, though ideally these values could be corroborated with other characterisation methods to verify them, such as profilometry or atomic force microscopy.

Figure 24:Ellipsometry Model showing glass substrate, perovskite absorber layer, and surface roughness layer assuming 50% void space, 50% perovskite.

5.3.3   X-ray Photoelectron Spectroscopy:

X-ray photoelectron spectroscopy (XPS) is an elemental and chemical composition characterisation technique based on the photoelectric effect. It has surface sensitivity within the top 10-20 nm of material. In short, XPS shows both what elements are present and what elements they are bonded too. A (typically) conducting sample is irradiated with monochromatic X-rays. (1-2 keV), emitting photoelectrons originating from either core shells or the valence band (with respectively distinct binding energies). An electron population spectrum is acquired from the emitted photoelectrons incident on the detector — a plot of the number of electrons detected at specific kinetic energies (E_k). Specific chemical states and their abundance are determined by calculating the electron binding energy (E_B) from E_k and measuring the number of ejected electrons. E_K of emitted photoelectrons relates to the binding energy by Equation 17:

$$E_K = hv - E_B - \Phi_S$$

Equation 17

Where hv is the energy of the incident X-ray photons, and Φ can be thought of as an adjustable instrument correction factor accounting for the few eV of E_K given up the photoelectron as it is emitted from the bulk and absorbed by the detector.

Elements produce characteristic XPS peaks with positions corresponding to the chemical state of their atoms. The number of electrons detected (intensities) relates to the amount of element present within the sampling volume. Raw XPS intensities are divided by a relative sensitivity factor (RSF) and normalised over all elements. A wide survey spectrum is obtained showing peaks across all binding energies within the measurement range. The intensity can be approximated by the Beer-Lambert Law in Equation 18, to express the intensity of photoelectrons escaping the sample surface and being detected.

$$I_d = I_o e^{\frac{-d}{\lambda cos\theta}}$$

Equation 18

The photoemitted electron density I_d is the intensity after the photoelectron has travelled through solid of depth d. I_d is damped exponentially with increasing d, and as the angle of emission θ strays away from the detector position. This is due to inelastic interactions with atoms in the sample, quantified by the inelastic mean free path, λ_{IMFP}. λ_{IMFP} is the average distance an electron travels

through a solid before an inelastic scattering event reduces its intensity to 1/e of its initial value. λ_{IMFP} is a function of E_K and atomic density.

High energy resolution of the characteristic peaks of elements is required to accurately determine the specific bonding environment/chemical states. The resulting spectra contain peaks defined by the FWHM, which is a convolution of X-ray characteristic line width, width of the photo emitted electron lines, surface charging and the spectrometer resolution.

X-ray photoelectron spectroscopy (XPS) was performed with a Kratos Axis Ultra DLD, using a monochromated Al-kα (*1486 eV*) X-ray source. Measured spectra were fitted using CasaXPS software. A U 2 Tougaard background was used. Wide scans were performed with a pass energy of 160 eV, 2-minute acquisition time, and resolution of 1 eV. Specific region scans were done with a high resolution of 0.01 eV, 60 s acquisition time, and pass energy of 20 eV. The beam penetrates the first 10 nm of the film, with an X-ray spot size of 700*300 µm. 2 measurements are taken on different points of the film surface for 3 films in each condition, and the results are averaged out. Signal averaging is used to improve the signal:noise ratio, as At% concentration in quantitative analysis can be as low as 60-80% of the true value in weaker peaks with 10-20% of the intensity of the strongest peaks. Due to X-ray induced degradation, Pb is measured in the first pass, to mitigate the effect of beam damage on the chemical state of Pb atoms. The adventitious carbon peak at ~285 eV is used to determine the charge correction factor necessary to compensate for charge induced shift of experimental binding energies. This typically occurs due to a surface charge build-up of positive charge due to photo-emission of electrons. A low energy charge neutralising electron beam is used to partially compensate for this effect. Species were determined by comparing fitted peaks to references available at the National institute of Standards and Technology X-ray Photoelectron database.[298]

5.4   Microscopic Techniques

5.4.1   Scanning Electron Microscopy

Scanning electron Microscopy uses a beam of electrons to interrogate a sample, facilitating, elemental, phase, and microstructural characterisation. An electron beam is accelerated using an applied bias (100V-25kV) and guided through a combination of electromagnetic lenses before interacting with the sample. Electrons can interact with the sample in a variety of different ways, and penetrate to different depths depending on the accelerating voltage, atomic number (*Z*), and density. These factors will determine the interaction volume, a usually tear-drop shaped volume of matter below the incident beam in which different radiation and emission events occur, as shown in Figure 25. In this work, a JSM-6010LA (JEOL) SEM is utilised. The beam is typically operated at accelerating voltages 12 kV and 15 kV and a working distance of 10 mm.

SEM is limited in that the sample needs to be conductive — this is not an issue for perovskites, which are typically semiconducting at room-temperature due to their intrinsically high defect density. Furthermore, electrons can damage the sample as the ionisation of atoms at GBs and surfaces will lead to fragmentation of the crystal structure. Notwithstanding this it is still a very useful technique due to the high-resolution images, with a resolution reaching ~100 nm in the JEOL SEM.
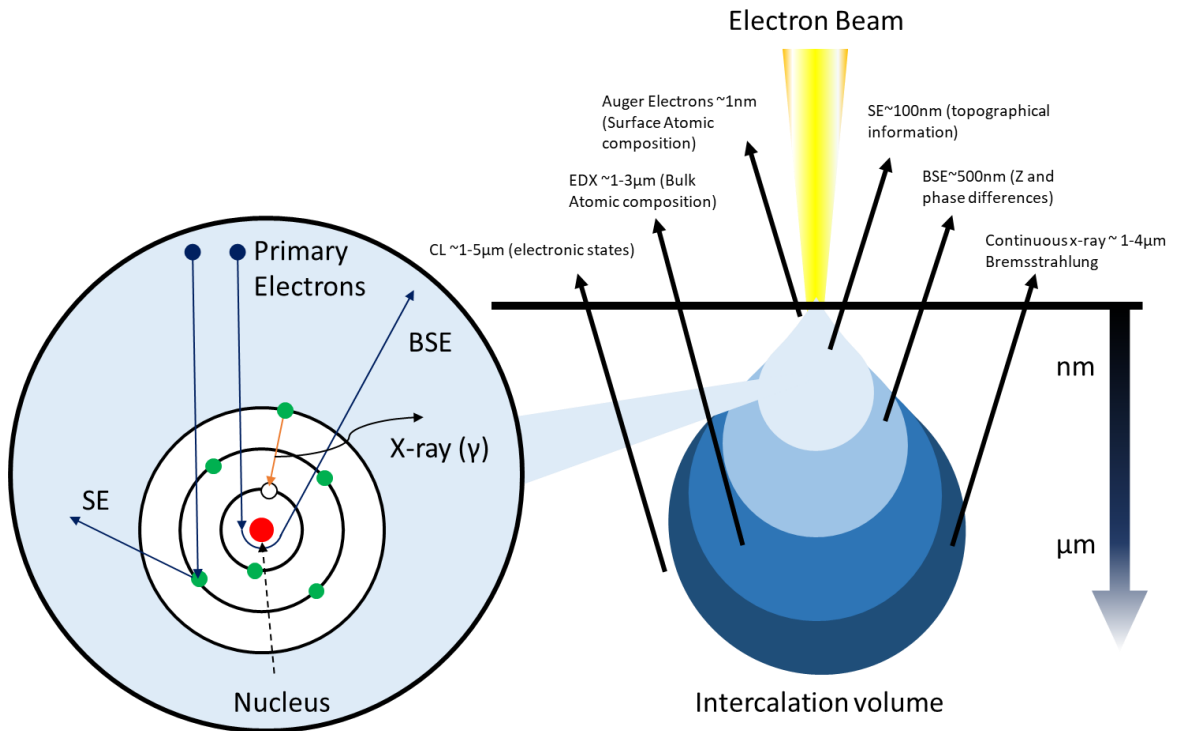
Figure 25: (Right)The intercalation volume in SEM, showing where different radiation and emission events occur. (left) Inset; Bohr model of atom showing how different events occur. SE (Secondary electron): generated by energy transfer from incident electron to electron in atomic orbital. BSE (Back-scattered electron) Blue line representing incident electron that is 'slung' around the positively charged nucleus. γ (X-ray) characteristic emission analysed in EDX (Energy Dispersive X-ray Spectroscopy).

Secondary electrons are emitted from inelastic interactions between incident electrons and surface electrons in the sample. Secondary electrons receive enough energy from the beam to overcome their binding energy and escape the sample. This is very useful for inspecting topography, although the low escape depth makes it less useful for seeing beyond a depth of a few nm. The topographic differences also introduce contrast due to the variation in atomic density as a function of these features crystal packing density, orientation and morphology.

Secondary electrons are emitted and pass up through the electron column of the beam, wherein they are deflected by an array of electromagnetic coils towards the SE detector, mounted above the objective lens, and positioned laterally with respect to the column. This is made possible by both the minimum working distance of the JEOL microscope of 2-4mm, ensuring adequate collection of secondary electrons, as well as the low energy required for their deflection, ~2 keV. This helps to maximise contrast arising from differences in work function between different phases in the sample.

5.4.2   Particle Size Analysis using ImageJ

Analysis of images was done using ImageJ.[299] Images (Mx200) underwent the following processing: 3D Gaussian Blur, 3D Median, Threshold tool (to convert to binary 8-bit image), Erosion or dilation to better define GBs, and Analyse Particles (Overlay) to obtain a list of particle sizes. The results of each stage are shown in the example of Figure 26 for a CsFAMA film on silicon.
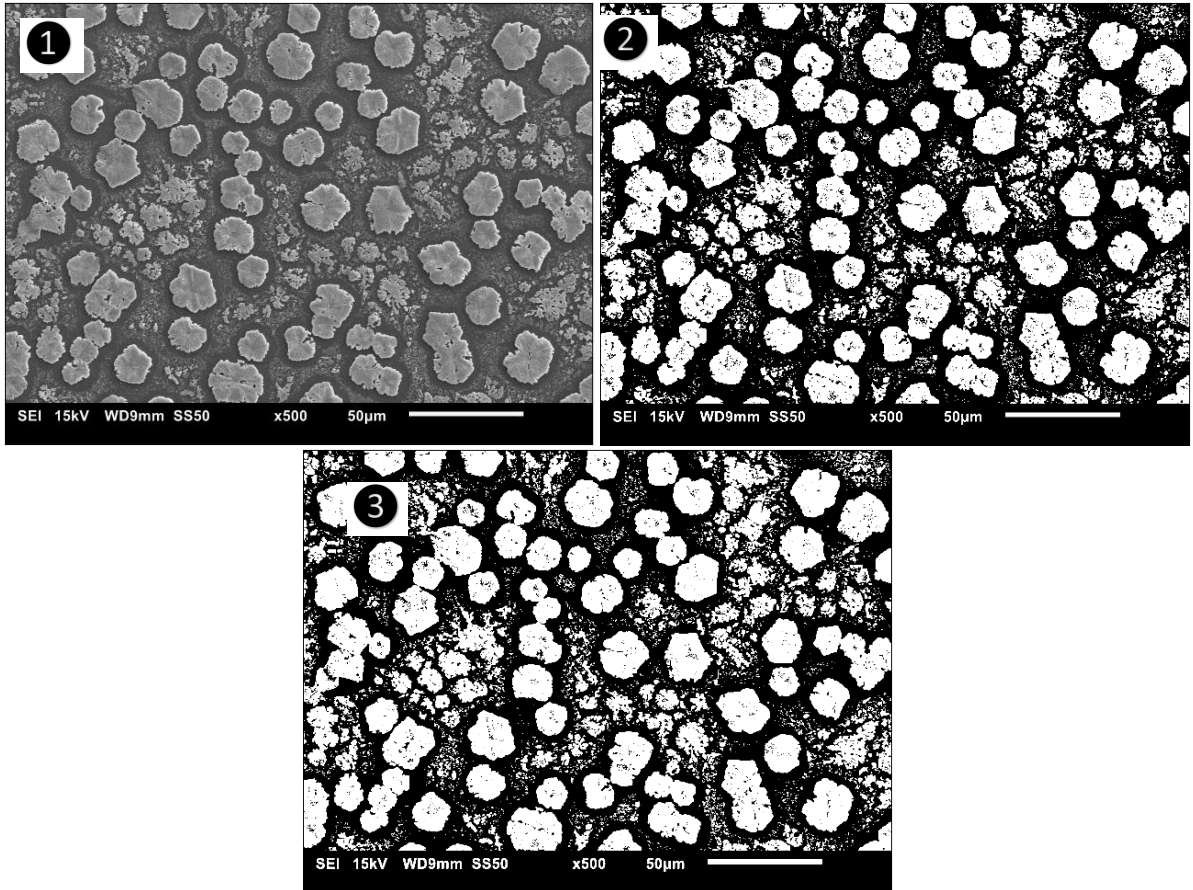
Figure 26: Sample ImageJ processing of a CsFAMA perovskite film on a silicon substrate. 1: 3D Gaussian Blur and 3D Median. 2: Threshold Tool. 3: Erosion tool.

5.5 Device Characterisation

Current density-voltage J(V) characterisation was performed using a Newport 92251A-1000 solar simulator with a Xenon lamp, and an Ossila test board where the switchers for contacts correspond to solar cell pixels. This is an instrument which reproduces radiation proximate to the sun's natural spectrum (Air Mass (AM) 1.5) at the earth's surface, and corresponds to $1000 Wm^{-2}$. Before each set of measurements, the lamp intensity was calibrated with an NREL certified Si reference cell at 100 $mWcm^{-2}$ at room temperature. Solar cells were masked, to define a consistent pixel area (0.02365 ± 0.00012 cm^2 for 8 pixel devices). The conductivity measurement unit was a Keithley 2400 high voltage source measure unit. Measurements were automated by a MATLAB script; the voltage swept between −0.2 V to 1.2 V in scan steps of 0.01 Vs^{-1}. J(V) curves for each pixel can then be plotted showing performance under forward and reverse bias. PCE is taken as the average PCE in the reverse scan direction.

Solar cell performance can be compared via 4 characteristic parameters. Open Circuit Voltage (V_{OC}), Short Circuit Current Density (J_{SC}), Fill Factor (FF%), and Power Conversion Efficiency (PCE%). These are depicted in Figure 27. Efficiency is defined as the power conversion efficiency, calculated from

the maximum current at short circuit (J_{SC}), the voltage at open circuit (V_{OC}), fill factor (*FF*), and incident light power density (P_s), given by Equation 19:

$$\eta = \frac{J_{SC} V_{OC} FF}{P_S}$$
<div align="right">Equation 19</div>
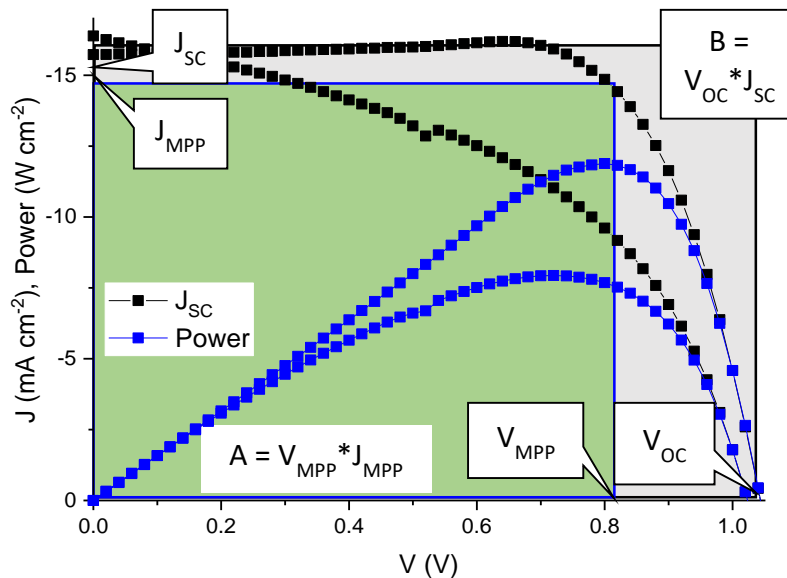
Figure 27: Example Current Density and Power as a function of Voltage for an 11.8% efficient MAPbI$_3$ device. Short Circuit Current Density (J_{SC}) Maximum Power Point current density (J_{MPP}) and voltage (V_{MPP}), Open Circuit Voltage (V_{OC}), and the numerator and denominator represented graphically of the Fill Factor (FF)= A/B.

The value of *J* at $V = 0$ is termed the J_{SC}, which reveals the maximum current density of the device, which for an ideal solar cell (with minimal resistance) is the same as the maximum current density generated by photon absorption. J_{SC} is the short circuit current (I_{SC}) in terms of mA cm^{-2} (due to convenience (small devices), historical convention, and consistency with PV standards) to remove the effect of solar cell area. If surfaces are perfectly passivated, and material type and generation is uniform, J_{SC} is ultimately dependent on the carrier generation rate and carrier diffusion length. Real devices deviate from this ideal, with J_{SC} also affected by optical losses, carrier collection losses, and the incident light intensity (and spectrum).

The value of *V* at $J = 0$ is termed the (V_{OC}), and reveals the maximum voltage available from the solar cell at zero current and 'infinite' resistance. V_{OC} depends on the reverse saturation current (reverse current caused by diffusion of minority carriers from neutral regions to the depletion width; i.e. recombination) and the light-generated current (which depends on the carrier generation rate and diffusion length). As the light-generated current only varies by a small amount in typical devices, the saturation current is the predominant factor, and hence V_{OC} can also be used as a measure of recombination.

The fill factor (*FF*) expressed as a *%* is a function of the cell's maximum power point (occurring at a voltage V_M and corresponding current density J_M; $P_M = J_M V_M$) relative to the J_{SC} and V_{OC}:

$$FF = \frac{J_M V_M}{J_{SC} V_{OC}}$$

<div align="right">Equation 20</div>

,i.e. the area of square A/ square B in Figure 27. *FF* decreases due to shunt resistance and series resistance losses, which reduce the 'squareness' of the J(V) curve. Shunt resistance occurs due to current being lost via lower resistance alternative pathways to the solar cell junction. These pathways typically arise during fabrication; morphological defects such as pinholes create facile shunt paths. Series resistance emerge from inherent resistances in the device, with interfacial contact resistances the dominant contributor. The PCE is defined as the fraction of incident light energy converted to electrical energy (Equation 19). In order to make more general statements and comparisons of solar cells, the conditions they are measured under — chiefly light and temperature must be standardised.

5.5.1   Device Fabrication Procedure

A colloidal dispersion of tin(IV) oxide (SnO_2) in DI H_2O (15%, Alfa Aesar, diluted to 3%) was filtered through a 0.45 µm PVDF filter and 40 µl of the solution spin coated on ITO at 2000 rpm for 30 s. The deposited SnO_2 was patterned to re-expose the ~6 mm ITO cathode using a cotton bud dipped in DI H_2O. The SnO_2 layer was then annealed on a hotplate at 100°C for 30 minutes. 40 µl of 1.3 M or 1.4 M perovskite solutions was dripped statically on the cooled substrate, and spun with either a two-speed or single-speed program. Films were either spun at 1000 rpm for 10 s and 5000 rpm for 20 s (Program 1) or at 3000 rpm for 30 s (Program 2). An EA anti-solvent process was used to improve the film quality.[119] EA was dynamically applied drip-wise to the substrate centre between 10 and 25 s after the start of spinning. The spin coated films were placed on a hotplate to anneal at 100°C for various anneal times. For devices, Program 2 was used to prepare perovskite films on the SnO_2 coated substrate. After annealing, excess perovskite was removed with a combination of a razor blade and cotton bud dipped in acetonitrile. The substrate was dried with an air-gun. A 15 mg/mL solution of PTAA in toluene was prepared. A 170 mg/mL solution of Li-TFSI in acetonitrile and 1:1 volumetric mixture of tBP in acetonitrile was mixed with the PTAA in a PTAA:Li-TFIS:tBP volumetric mixture of 1000:7.5:7.5. This was stirred for 30 minutes at room temperature. 30 µl of solution was statically spin coated at 3000 rpm for 30 s. Excess solution was removed with a cotton bud dipped in acetonitrile to expose the ITO cathode contacts. The samples were mounted on a shadow mask for thermal evaporation of the metal back contact. Au/Ag pellets were heated and a layer of Au/Ag deposited with an initial rate of 0.01 nm/s for the first 2 nm, 0.05 nm/s until 10 nm, and ~0.1 nm/s until a layer 110 nm thick was acquired. Metal deposition was done with an Edwards 306 thermal evaporator at a pressure <$8*10^{-7}$ mbar. Non-encapsulated devices were immediately characterised. All processes (not including thermal evaporation) were performed under ambient conditions of 47%rH +/-2%. For film characterisation thin films of perovskite were deposited as above, directly on glass substrates using either Program 1 or 2 as per the experiment.

For results Section 5, Devices were fabricated with the same conventional n-i-p structure, with an SnO_2 ETL, perovskite precursor solution prepared as in 4.1.3, stirred for 48 hours, and cast as per Program 1. A PTAA:Li-TFSI:tBP HTL was applied as above. An Ag cathode was thermally evaporated onto the HTL. The device was subsequently characterised as described in Section 5.5.

Results

The results element of this thesis have been structured in order of their occurrence and narrated using a paper-style. The findings of Sections 6 are unpubished, whereas Section 8 constitutes a publication in preparation,and the work in Section 7 has been published as a conference paper. In brief, Section 6 follows efforts to describe the effect of super-stoichiometric additions of either MAI or PbI_2 precursor salts in $MAPbI_3$, while optimising the application of ethyl acetate antisolvent to obtain high performing films under ambient conditions. Following on from the insights gained into the stability of $MAPbI_3$ perovskite films during various aspects of processing and under ambient, i.e. wet conditions, moisture induced degradation of various perovskite systems was then investigated using ionic substitution as the stabilising method in Section 6. Finally, in Section 7, the stabilisation of $MAPbI_3$ under wet and ambient conditions with Zn, Cs, and Cl substitution is investigated to observe how this strategy affects degradation of $MAPbI_3$ films fabricated under ambient conditions and how well devices perform.

Sections 5 and 6 use experimental methods which provide unique insights relative to standard approaches with the applied instrumentation. Section 5 applies wide angle X-ray scattering (WAXS) in a transmission geometry with a rotating stage during dynamic experiments, increasing count rate while reducing beam damage to the sample. Section 6 applies Time-of-Flight Grazing Incidence Small Angle Neutron Scattering (TOF-GISANS) to gather data on phase composition and characteristic length scales simultaneously in one measurement, allowing temporal analysis of samples. Section 7 provides a review and investigation of Zn as an additive in the active layer in perovskite solar cells, while demonstrating the importance of testing promising new cell technologies against adequately rigorous performance standards.

6 Beneficial Effect of Super-stoichiometric MAI Addition on $MA_2Pb_3I_8(DMSO)_2$ Formation

6.1 Abstract

Perovskite stoichiometry has previously been shown to influence the optoelectronic characteristics, phase stability, and film formation in perovskite solar cells, as has the application of antisolvent dripping of ethyl acetate (EA). Herein the effect of a 10wt% excess addition in solution of either MAI or PbI_2 on the evolution of the perovskite film during spin coating is characterised with wide-angle X-ray Scattering (WAXS). EA is applied in antisolvent dripping in conjunction with super-stoichiometric precursor solutions to investigate the combined influence of kinetic antisolvent-induced crystallisation and excesses of either precursor salt on film formation. It is found that a 10wt% excess of MAI affects the formation of the DMSO-intercalated intermediate, enhancing its growth-rate by both increasing growth of this crystalline phase, and suppressing loss of DMSO. And extending the antisolvent application window. MAI enrichment improves fill factor and power conversion efficiency in devices, while PbI_2 enrichment improves J_{SC} and V_{OC}. An understanding of the interaction between antisolvent and MAPbI3 films as a function of stoichiometry is developed, enabling the optimal application of EA on MAPbI3 films, producing a device with 16.1±0.2% average efficiency prepared entirely in ambient conditions with a 10wt% MAI excess.

6.2 Background

The stoichiometric dependence of perovskite formation in conjunction with antisolvent application under all-ambient conditions is investigated (all fabrication processes done in air) by varying addition of either Lead (Pb) or Methylammonium Iodide (MAI) salts in a 10% molar excess. Herein perovskite films are spin-coated on substrates at ambient temperature, to identify the stages in intermediate film formation from the sol gel and subsequently perovskite film formation from the crystalline intermediate.

The antisolvent processing window has been shown to be extended by halide and cation substitution on the A-site and X-site of the ABX_3 perovskite.[156] By substituting the A-site of FA dominated perovskite formulations with MA^+, Cs^+, and Rb^+, Wang *et al.* extended the processing window for obtaining uniform, high quality films and found that it is dependent on the crystallisation of the disordered sol gel state and the degree of crystalline by-products. By mixing cations and other halide species with MAPbI3, the production of the by-products is delayed.[156] In their work, perovskite solutions were prepared in a mixture of DMF:DMSO, in a ratio of 4:1, with resulting intermediate peaks in GIWAXS during spin coating around 0.48 A^{-1} and ~0.7 A^{-1}. They attribute the peak at 0.48 A^{-1} to the MAPbI3-DMSO co-crystal, while the 0.7 A^{-1} scattering is not defined. In mixed cation (Cs, FA) precursor solutions, higher amounts of DMSO prolong the duration of the colloidal gel, extending the antisolvent processing window, and thereby making it easier to obtain a uniform, high quality film after dripping EA. The time available to obtain crystalline intermediates beneficial to the formation of perovskite films is extended. Crystalline intermediates are more stable than the amorphous sol-gel state which precede them as the precursor solution dries, and their consistent formation is correlated with more reproducible perovskite conversion during thermal annealing. The Lewis-adduct intermediate has been exploited to obtain high performing perovskite films for PSCs.[98,113,114]

Beneficial Effect of Super-stoichiometric MAI Addition on MA2Pb3I8(DMSO)2 Formation - Results

In this work, EA is used as an antisolvent facilitating conversion to perovskite due to a lower proportion of crystalline by-products and undesired DMF-intercalated complexes. EA has been shown to provide humidity tolerant fabrication, and therefore provide better films under ambient conditions.[127] EA has high volatility, optimal polarity, and high affinity for moisture.[300] The relative humidity of the ambient environment where casting occurs influences the crystallisation kinetics, with a higher rH delaying the onset of intermediate crystallisation due to slower evaporation of DMF. The volume of EA applied can compensate for the slower evaporation rate of DMF in a humid atmosphere, facilitating more consistent formation of films with morphologies comparable to films formed under dry conditions. This is important as the increasing presence of moisture has been shown to reduce the duration of the sol-gel state in intermediate films. This is because H_2O strongly conjugates with Pb forming white PbO and $Pb(OH)_2$ precipitates which lead to reduced crystallinity of the perovskite film after annealing.[73,121] H_2O competes with DMSO, DMF (H_2O>DMSO>DMF) and Iodide ions to coordinate with the Pb atom, limiting and destabilising the formation of the DMSO intermediate. Retaining a fraction of this intermediate is correlated with smooth surface morphology with a higher charge carrier lifetime and fill factor.[110] Meanwhile perovskite hydrates may act as shunting pathways that can significantly reduce V_{OC}.[118] In summary, ideally antisolvent should be applied when the intermediate sol-gel layer is dry enough to reach supersaturation. The presence of moisture closes the window of opportunity for antisolvent application; perovskite film quality under humid conditions is more sensitive to the timing of the antisolvent drip.

6.3   Results

6.3.1   Formation of the intermediate phase

During the in-situ WAXS experiments, the precursor solutions were ejected from the syringe and spun on the substrate at 4000 rpm for 30 s in air with a relative humidity of 55%. Figure 28A shows the formation mechanism of the crystalline intermediate from the sol-gel during spin-coating. As shown in the 1D diffratogram in Figure 28B the hump at low q (0.2-0.6 Å^{-1}) is of the disordered colloidal sol-gel precursor. Peaks occur at 0.47 Å^{-1}, 0.52 Å^{-1}, 0.66 Å^{-1}, and 0.84 Å^{-1} consistent with the MAI-PbI$_2$-DMSO intermediate phase (similar to work by Munir *et al.*).[77] There is also strong scattering around 1.7-1.8 Å^{-1}, which also arises from the MAI-PbI$_2$-DMSO intermediate (as per Hu *et al.* in GIXRD)[149], as well as the peak at ~0.7 Å^{-1}, corresponding with MAI (see Figure 73 in Appendix). The contour plots in Figure 29(A-C) show that all films are characterised by the emergence of intense peaks within a minute. According to WAXS diffractograms of the crystalline MAI precursor, the (001) plane of the MAI crystal has a peak at 0.71 Å^{-1}. This correlates very closely with the observed scattering at 0.706 Å^{-1}. PbI$_2$ peaks occur at 1.54 Å^{-1} and 1.83 Å^{-1}. DMSO molecules compete with DMF, H_2O and MAI to coordinate with PbI$_2$, with the result being the formation of various intermediates and hydrated phases. In the equimolar film (Figure 29B), the crystalline intermediate takes the longest to appear after 40±5 s have elapsed. In the films with excess of either precursor it crystallises from the sol-gel phase sooner, appearing after 30±5 s in the film with an excess of MAI and (Figure 29A), and 25±5 s in the film with an excess of PbI$_2$ (Figure 29C). Comparisons of each stoichiometry 30 s after the beginning of spin-coating are shown in Figure 28C, showing the emergence of the crystalline intermediate peaks at low-q in both films with an excess of either precursor salt. Super-stoichiometric precursor solutions hasten the crystallisation of the intermediate under humid conditions.
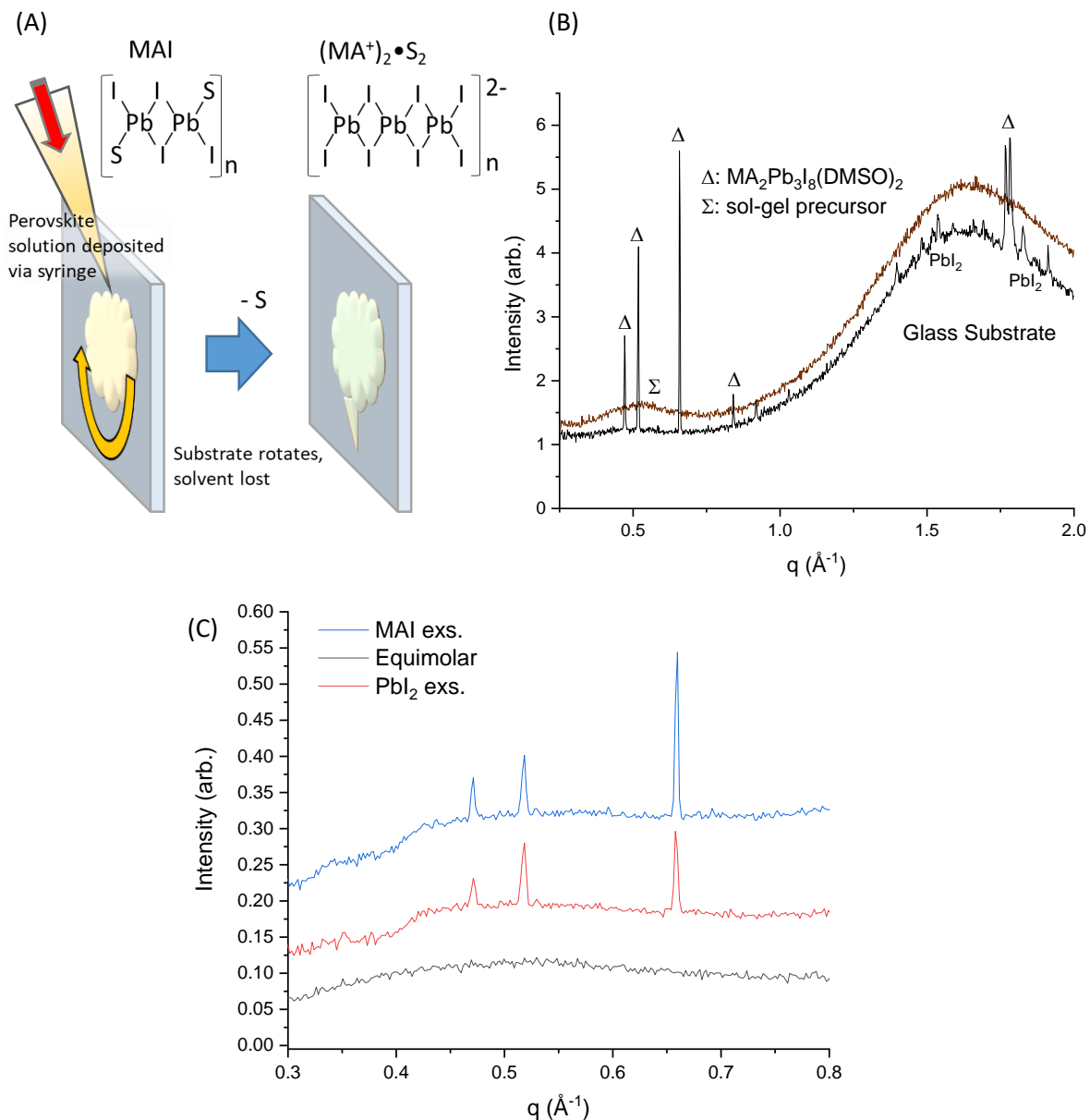
Figure 28: (A) Formation of crystalline solvent-intercalated intermediate during spin-coating. Solvent molecules S (DMSO, DMF) are lost from the sol-gel as the spinning chuck rotates, and the crystalline intermediate forms. (B) Diffuse scattering from the sol-gel precursor (Σ) and scattering peaks from the DMSO-intercalated intermediate (Δ). Also shown are peaks from PbI_2 at q = 1.54 Å^{-1} and 1.83 Å^{-1}. The broad diffuse scattering from the glass substrate lies between 0.7-2.5 Å^{-1}. (C) The emergence of the low-q intermediate peaks after 30 s of spin-coating in different stoichiometries. Notably the intermediate has as of yet not appeared in the equimolar film, in contrast to the MAI and Pbi_2 enriched films.
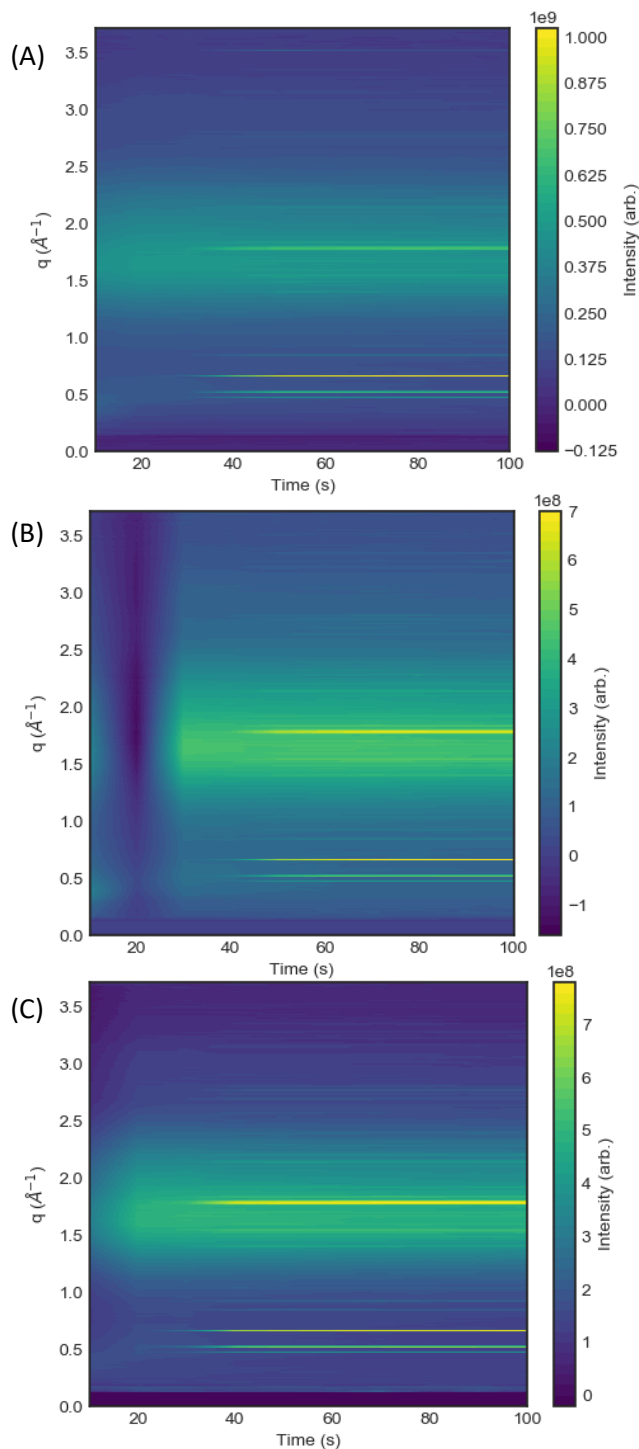
Figure 29: Contour plots over the first 100 s of spin-coating for (A) MAI enriched, (B) equimolar & (C) PbI$_2$ enriched precursor solutions ejected via syringe onto the substrate surface and spin-coated for 600 s in air. Observable are peaks at 0.47 Å^{-1}, 0.52 Å^{-1}, 0.66 Å^{-1}, 0.84 Å^{-1}, & 1.77/1.78 Å^{-1}.

Beneficial Effect of Super-stoichiometric MAI Addition on MA2Pb3I8(DMSO)2 Formation - Results

The evolution of the intermediate can be understood by plotting peak area (Figure 29A,B) and FWHM (Figure 29C,D) for the intermediate peaks present in the evolving precursor film. The difference in onset time visually apparent between the contour plots and plots of peak area vs time arise due to the smoothing function used in python to generate the intensity scale between discrete measurements. In the equimolar film, the onset of DMSO intermediate crystallisation occurs between 30-40 s, after which there is a rapid increase in the peak area of the crystalline DMSO intermediate between 40-50 s, driven by nucleation (as shown in Figures 29A,B of the changing area of the intermediate peaks). As solvent evaporates many small intermediary nuclei precipitate, increasing the width of the peak (Figure 29C (See Section 5.2.1)). Crystallisation of the intermediate occurs more rapidly in super-stoichiometric films. Thereafter there is a gradual increase in the crystallinity of this phase. Driven by growth of the intermediate, evidence by the decreasing summed FWHM, indicative of increasing crystallinity (Figure 29C,D) (See Section 1.2.1). Further evidence comes from the shifting q-position of the 1.77/1.78 peak for which peak splitting is observed. Here q increases rapidly over the first 50-60 s, suggesting increasing compressive strain as solvent is lost and grains squeeze together.

Cao *et al.* have identified two similar DMSO intermediates forming prior to annealing; an orthorhombic PbI$_2$ rich, DMSO rich, and I deficient MA$_2$Pb$_3$I$_8$(DMSO)$_2$ which forms when the ratio of MAI:PbI$_2$ is 1:1; and a monoclinic MAI rich, I rich, MA$_3$(DMSO)PbI$_5$ which forms when the ratio >1:1. They also find an I-rich phase which forms after annealing with the loss of solvent: MA$_4$PbI$_6$. The monoclinic and orthorhombic phases have peak positions close together, often appearing as a split peak[80]. These peaks are plotted in Figure 30A, showing the variation between sample stoichiometry. The summed FWHM of the intermediates peaks at q=1.77/1.78 Å^{-1} decreases after 50-60 s across all films (Figure 32D), pointing to either decreasing strain, increasing crystal size, or decreasing crystallite sampling.
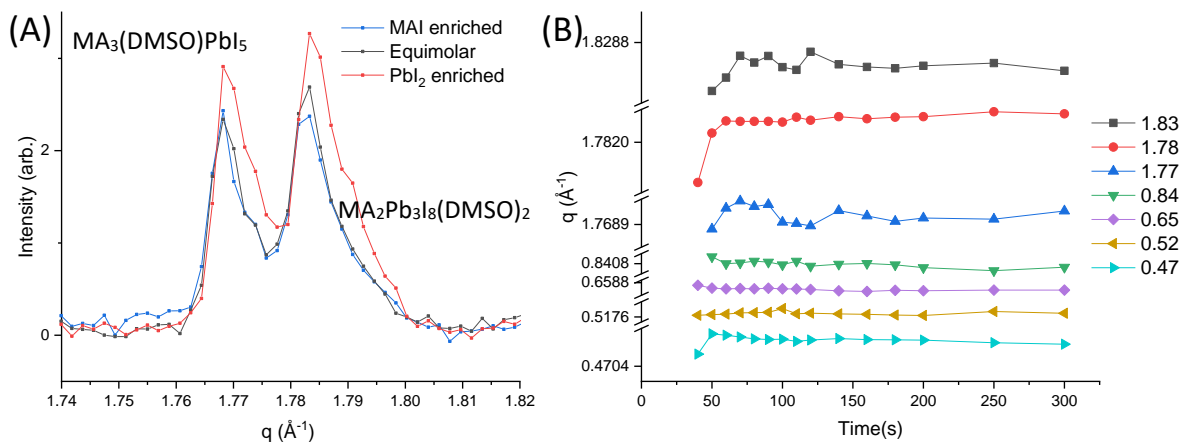
Figure 30:(A) Crystalline MAI-PbI$_2$-DMSO intermediate peak splitting at 1.77/1.78 Å^{-1} after 300 s, showing increasing peak intensity, rightward peak shift, and broadening of right shoulder as the ratio of MAI:PbI$_2$ decreases. (B) Peak position of intermediate phases in equimolar film during spin casting and subsequent drying over 300 s.

Increasing area suggests increasing crystallinity, and hence the decreasing FWHM of the high-q intermediate peak may indicate decreasing strain between crystallites as solvent evaporates. The smaller d-spacing crystals denoted by the split-peak are subsumed by the larger d-spacing crystals

Beneficial Effect of Super-stoichiometric MAI Addition on MA2Pb3I8(DMSO)2 Formation - Results
denoted by the low-q peaks which show a slight decrease in q-position (d-spacing expansion (Figure
30B)) and an increase in peak scattering area (Figures 29A). The position of the q=1.77/1.78 Å^{-1} peak
increases with decreasing MAI:PbI$_2$ ratio (Figure 31C), showing that increasing the concentration of
nucleation centres leads to lattice contraction of the intermediate phase or reorientation. The peaks
shift to higher q as the ratio of MAI:PbI$_2$ decreases, and the intensity of the MAI rich phase increases
relative to the DMSO rich phase. This suggests more rapid loss of DMSO in the PbI$_2$ enriched film
during spin-coating.
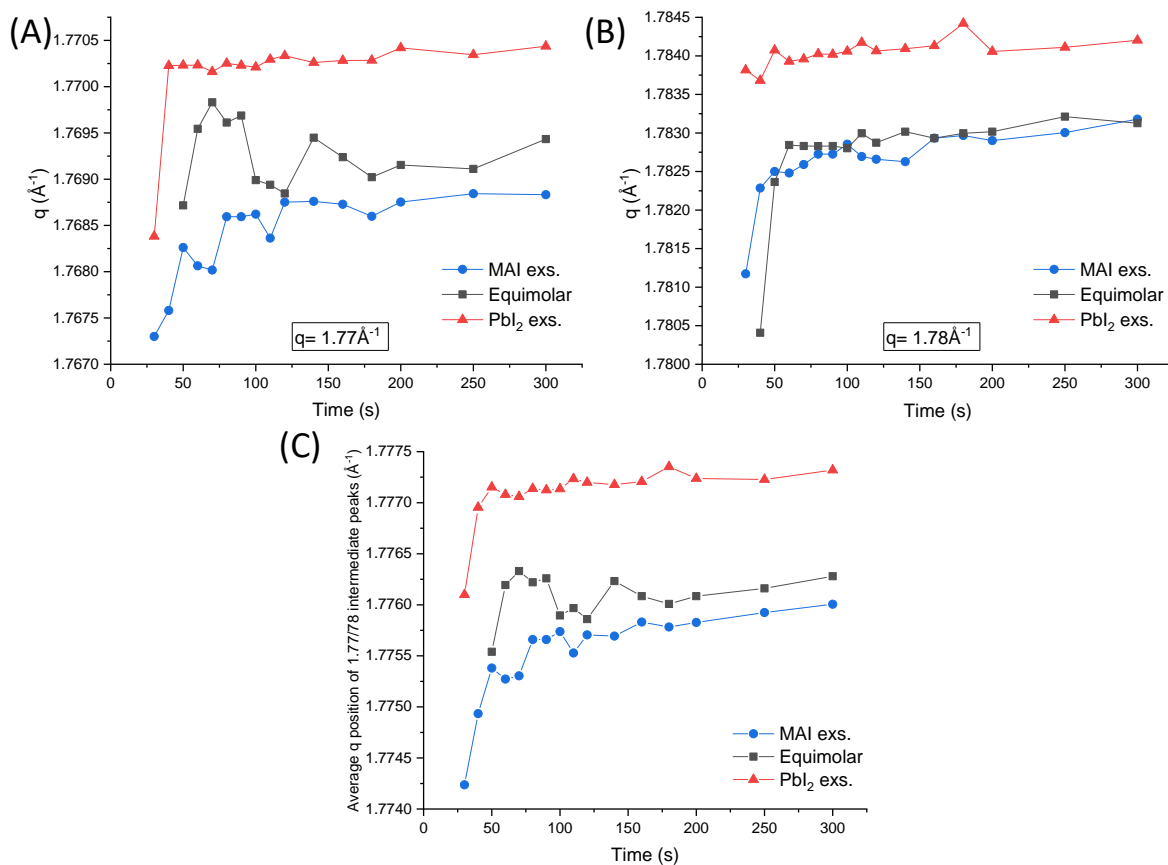
Figure 31: q-position of (A) q=1.77 Å^{-1} and (B) q=1.78 Å^{-1} split-peaks during 30 s of spin casting and subsequent
drying for perovskite films with a 10wt% MAI excess, equimolar stoichiometry and a 10wt% PbI$_2$ excess. (C)
Averaged q position of 1.77/78 split-peaks.

The sample with a 10wt% excess of MAI (Figure 29a) shows an onset for intermediate crystallisation
of 30±5 s. The maxima in nuclei density occurs at 70 s (Figure 32C). Low q intermediate peaks increase
in area rapidly between 30-50 s and thereafter gradually increases, while the FWHM decreases after
80 s, suggesting crystals are getting bigger. Peak positions of the low-q peaks change very little,
suggesting the FWHM decrease arises from crystal growth with very little strain associated with
solvent loss. The scattering from the q=1.54 Å^{-1} and 1.83 Å^{-1} peaks of PbI$_2$ in Figure 32E fluctuates
over the first 200 s, and then becomes negligible. The maximum summed FWHM (Figure 32F) of the
PbI$_2$ peaks corresponding to the peak nuclei density occurs after 60 s. The high-q intermediate peaks'
area rapidly increases between 30-50 s, but thereafter the area remains fairly constant. The high-q
peak position shifts to higher q over the first 70 s (shown in Figure 31A,B) suggesting compressive

84

Beneficial Effect of Super-stoichiometric MAI Addition on MA2Pb3I8(DMSO)2 Formation - Results

strain, while the FWHM (Figure 32D) reaches a maximum at 40 s and then decreases suggesting there is an initial burst of crystallisation which is then hindered with increasing strain. After 50 s, the film dries with little nucleation of new intermediate crystals. Rather the intermediate phase grows through reorientation and fusion of the crystallites present, evidenced by an increase in the low-q peaks intensity. MAI enrichment ensures more complete reaction with the PbI_2, evidenced by a diminished PbI_2 peak in this sample (Figure 32E). After 180 s, there is evidence of the perovskite phase forming, with the (110) peak at q=1.07 Å^{-1} appearing and growing in intensity.

The PbI_2 excess sample (Figure 29C) show an onset for intermediate crystallisation of 30±5 s, with one experiment giving an onset time of 50±5 s. This may be due to its sensitivity to inter-sample variation in spin-coating atmosphere — as the ambient solvent concentration increases the nucleation rate decreases as solvent evaporation is suppressed. The PbI_2 excess film may show more variation due to higher sensitivity to small changes in processing conditions.[301] Considering a sample with onset time (30 s) closest to the group average (37±5 s), area increases rapidly between 30-50 s and thereafter remains fairly constant. The FHWM (Figure 29j) of the intermediate peaks trends downwards over the 300 s, suggesting fewer nuclei being sampled or growing crystal size, while solvent evaporation mostly occurs between 30-50 s evidenced by a shift in the q-position of the high-q peaks (shown in Figure 31c). This downward trend in FWHM is particularly pronounced for the high-q peaks of the intermediate. The FWHM of PbI_2 similarly decreases, however its area increases, suggesting increasing crystallinity of the remaining PbI_2. The nucleation density of the intermediate phase is high immediately after the sol-gel collapses to a semi-crystalline state. This high intermediate nucleation density results in a high nucleation density of perovskite nuclei upon annealing. Typically, during spin-coating the substrate will be removed from the chuck after 20-40 s, when the nucleation density is still high, which implies the PbI_2 enriched film will produce a dense perovskite film with many smaller crystals. This is observed in SEM (D).
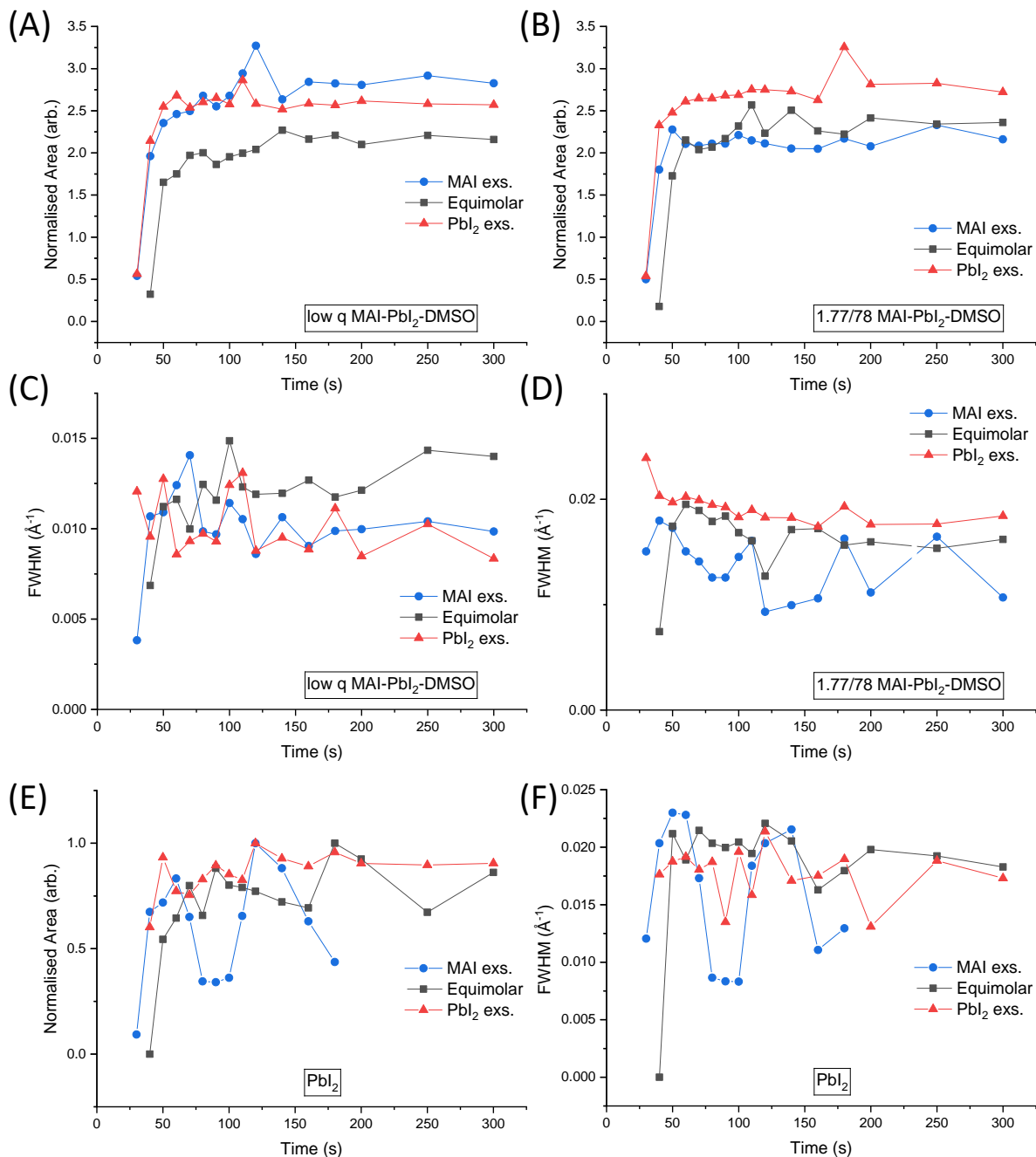
Figure 32: Plots of integrated peak area and FWHM vs time from fits of 1D diffractograms at each measurement interval; for (A,C) low-q intermediate peaks, (B,D) high q 1.77/78 intermediate peaks, and (E,F) PbI_2 for MAI enriched, equimolar and PbI_2 enriched precursor solutions during spin coating. The high-q (1.77/1.78 Å^{-1}) and low-q (0.47 Å^{-1}, 0.52 Å^{-1}, 0.66 Å^{-1}, 0.84 Å^{-1}) points are the summed areas of the denoted peaks, correlating with peaks from GIWAXS by Munir et al. (low q) and GIXD by Hu et al. (high q).[21,22]

6.3.2   Effect of ethyl acetate on intermediate and perovskite formation

In order to understand the influence of stoichiometry after spin coating and upon annealing following application of antisolvent, characterisation was conducted of films spin cast with and without EA antisolvent in the ambient conditions of a fume cupboard (on a conventional spin-coater) before being rapidly transferred to the hutch of the beamline for measurement during in-situ annealing. Due to the beamline setup, it was not possible to apply both the precursor solution in spin casting and the antisolvent on the horizontal axis spin coater. When EA is applied, the solute precursors become super saturated encouraging the formation of the solvent-intercalated intermediates.[127] EA has a high affinity for both DMF and moisture, meaning both solvents are removed during application and providing humidity-resistant fabrication.[127] EA application removes moisture (EA can dissolve 3% H_2O at room temperature) and drives the nucleation of perovskite either directly from the sol-gel or from the crystalline DMSO-intermediate phase, while reducing the presence of hydrated perovskite, s intercalated solvent including DMSO is removed from the intermediate film.[302]

The change in crystallisation onset time is particularly interesting due to the implications for antisolvent dripping during spin-coating. In all in-situ annealed films treated with EA, the antisolvent was applied after 15 s. There will be a difference in the crystallisation dynamics due to the different state of the film upon antisolvent application. As antisolvents reduce solubility of precursors in the solvent (thus increasing the precursor species saturation in the solvent mixture, and raising their reaction rate), the removal of DMF by EA encourages the rapid generation of DMSO-intermediate nuclei across the substrate. Upon annealing, DMSO evaporates and exchanges with MAI, producing a dense, homogenous perovskite film, with a high concentration of smaller crystallites (See Section 2.3.3). Earlier intermediate crystallisation implies a higher saturation rate of nuclei in the sol-gel. If EA is applied after the crystalline intermediate has formed, some DMSO in the intermediate will be removed, leading to early perovskite nucleation.

Annealing of films without ethyl acetate application.

The contour plots in Figure 33 show the presence of faint streaks denoting the crystalline intermediate precursor, which rapidly transforms to the perovskite phase within the first 120 s of annealing at 100°C. The tetragonal-cubic perovskite phase transformation temperature lies between 60-70°C (perovskite nucleation is temperature dependent), and as the hotplate reaches 60-70°C after approximately 90-100 s have elapsed, it takes ~20 s for the intermediate to transform to perovskite. As labelled in Figure 35B for equimolar films, q values (with miller indices) of 1.07 Å^{-1} (110), 2.11 Å^{-1} (220), 2.35 Å^{-1} (310) correspond with peaks of perovskite. Less visible but also present are peaks at 2.94 Å^{-1} (400) and 3.11 Å^{-1} (411), which are also attributed to perovskite. There are distinct peaks at q values of 0.51 Å^{-1}, 0.56 Å^{-1}, and 0.71 Å^{-1}, corresponding with peaks for the DMSO-intermediate, DMF-intermediate, and crystalline MAI respectively, while trigonal PbI_2 also nucleates, as indicated by the peaks at q values of 1.51 Å^{-1} and 1.83 Å^{-1}. The PbI_2 appears after 170 s in the equimolar film, and after 150 s in both enriched films. The integrated intensity under the corresponding peaks over 1000 s shows the phase evolution during annealing in Figure 35. Figure 35(A-C) show the changing integrated scattering intensity from the intermediate peaks specifically. Evidence of the conversion of intermediates and MAI to perovskite (and trigonal PbI_2) for MAPbI$_3$

Beneficial Effect of Super-stoichiometric MAI Addition on MA2Pb3I8(DMSO)2 Formation - Results upon annealing can be seen in Figure 74(A-C) (Supplementary 13.2), where declining solvent intermediate and MAI scattering is associated with increasing perovskite scattering.
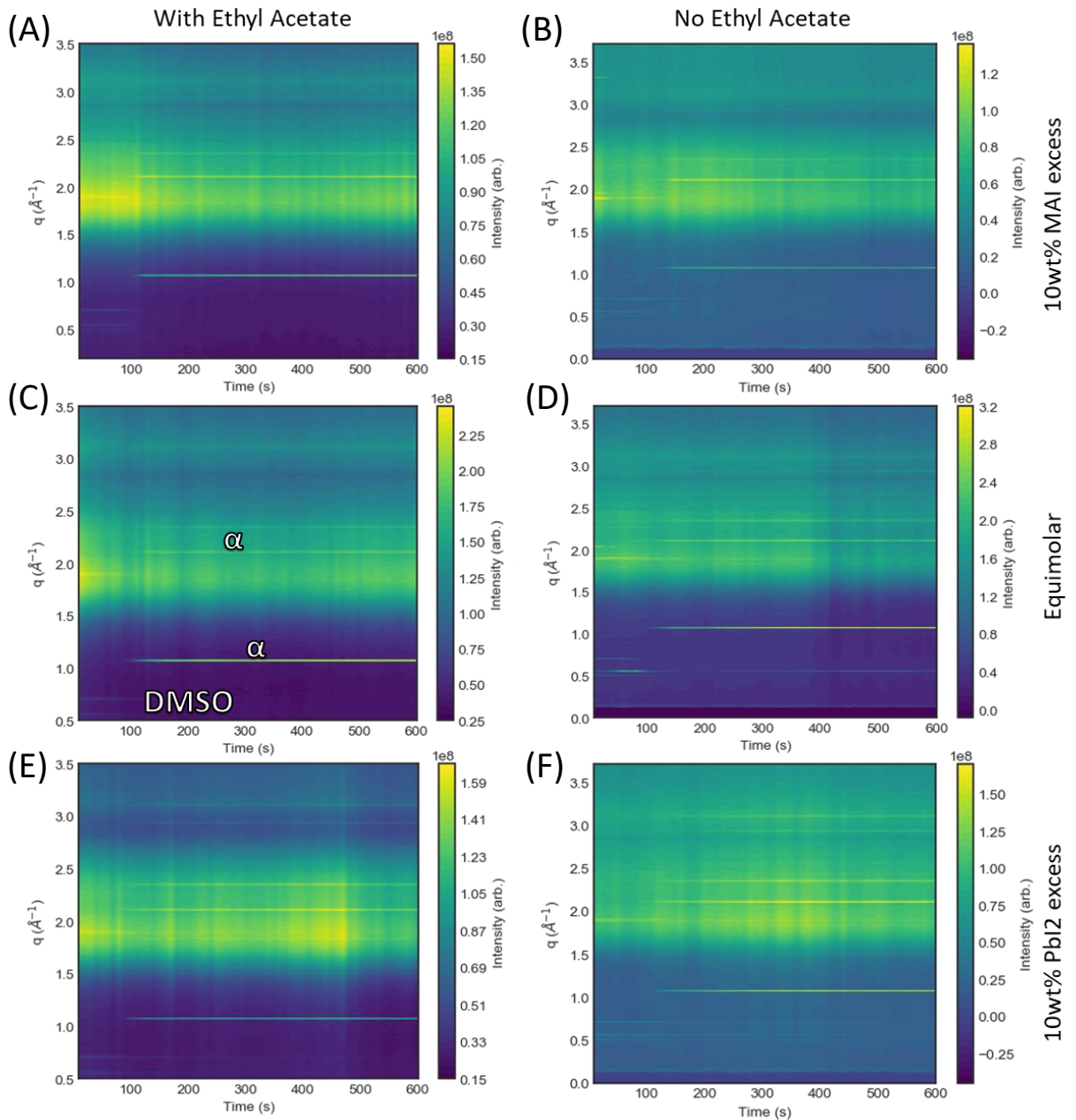
Figure 33: Contour plots over the first 600 s of annealing for perovskite films with (left column) and without (right column) EA application for (A,B) MAI enriched, (C,D) equimolar, and (E,F) PbI$_2$ enriched precursor solutions. 'α' denotes the emerging perovskite phase at ~ q=1.07 Å^{-1}, 2.11 Å^{-1}, and 2.35 Å^{-1}. The crystalline intermediate DMSO is shown by streaks at q=0.51 Å^{-1}, 0.56 Å^{-1}, and 0.71 Å^{-1}. The code that was written to construct these plots can be seen in Appendix 13.2.

Beneficial Effect of Super-stoichiometric MAI Addition on MA2Pb3I8(DMSO)2 Formation - Results

There is a steep increase in the integrated intensity of MAI between 40-80 s, followed by a steep decrease thereafter (Figure 34A). The FWHM of the MAI peak increases up to 110 s and is mainly correlated with its transformation to the intermediate phase via reaction with PbI_2 and DMSO as well as MAI sublimation. This results in shrinking MAI crystallites, increasing FWHM, highlighted in Figure 34B. Some small crystallites of the final perovskite are also formed after 80 s. Figure 35B and Figure 35C show the crystallinity of the intermediates increases during annealing as excess solvent evaporates and Pb coordinates with DMSO, DMF and MAI. In the equimolar $MAPbI_3$ film not treated with EA, a peak is observed from a DMF intermediate after 60 s, with a smaller peak associated with the DMSO intermediates after 50 s. The DMF intermediate lingers in the film for 900 s. The DMSO intermediate in contrast disappears after 150 s — despite the lower boiling point for DMF, suggesting the DMF is more strongly coordinated than the DMSO. In the PbI_2 excess film, the DMSO intermediate peak appears 15±5 s before the DMF intermediate peak.
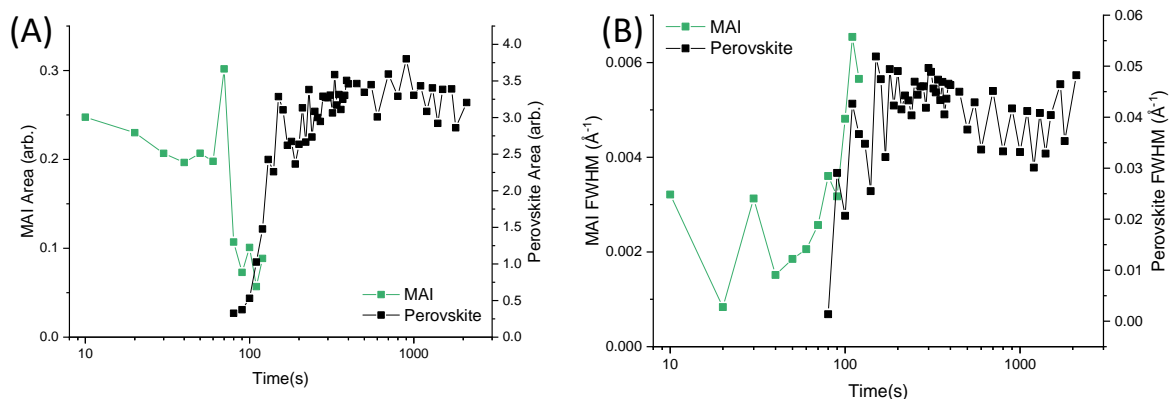
Figure 34: Conversion of MAI to Perovskite in Equimolar $MAPbI_3$ films. (A) Change in peak area, (B) Change in peak FWHM

The FWHM of perovskite peaks in the equimolar film reaches a maxima at 150 s, decreasing gradually thereafter, suggesting fewer crystallites are sampled and grain growth. After ~1500 s, the FWHM of the perovskite peak increases (see Figure 34B) and this is probably due to grain degradation. The area decreases after 900 s in both the equimolar and PbI_2 enriched films, suggesting decreasing crystallinity. This also (in the equimolar film) coincides with the loss of the DMF intermediate, hinting at the role of intermediate phases in grain growth. In contrast, the perovskite peak area and FWHM both diminish after 300 s in the MAI enriched film, suggesting grain growth concurrent with decreasing crystallinity; although excess MAI promotes rapid conversion of the intermediate phases to perovskite, it also seems to be associated with earlier degradation during annealing at 100°C.

Beneficial Effect of Super-stoichiometric MAI Addition on MA2Pb3I8(DMSO)2 Formation - Results
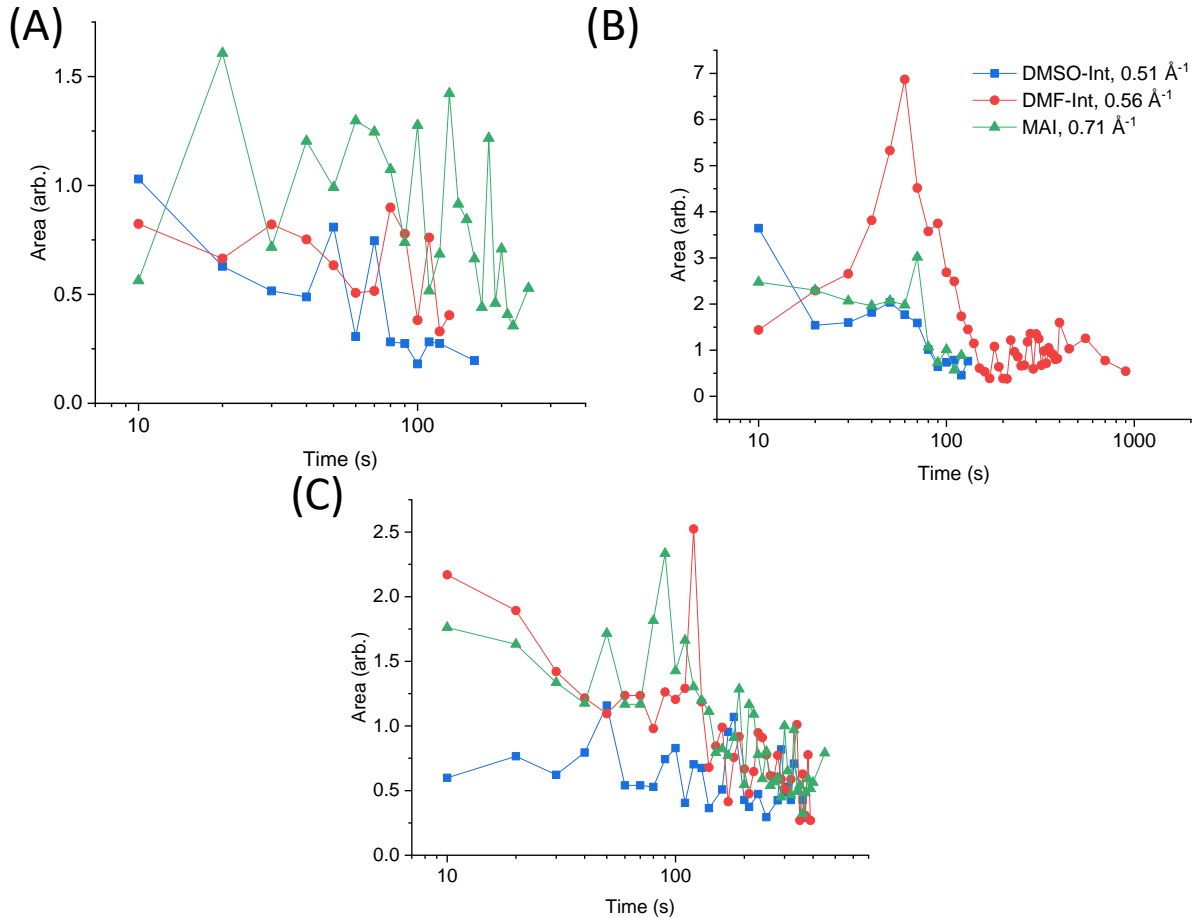
Figure 35: Plots of area vs time showing intermediate phases, and MAI for A) MAI enriched, B) Equimolar and C) PbI₂ enriched films fabricated without antisolvent over first 5 minutes of annealing on a hotplate (which takes ~150 s to reach 100°C from room temperature) The peaks at q = 0.51 Å⁻¹, 0.56 Å⁻¹, and 0.71 Å⁻¹ correspond with the crystalline solvent intercalated DMSO-intermediate, DMF intermediate and MAI respectively.

Annealing of films with ethyl acetate application.

EA application, as shown in Figure 36(A-C) suppresses the DMF peak, with scattering from both intermediate complexes disappearing after ~150 s in the equimolar sample Figure 36B, presumably because the DMF is preferentially removed during antisolvent rinsing. The proportion of DMF intermediate to DMSO intermediate is greatly reduced, while the scattering from the MAI intermediate is relatively higher. EA application significantly reduces scattering from the solvent-complexes due to the enhanced solvent removal rate, with solvent-precursor complexes converting after 150 s, as opposed to 900 s in untreated equimolar films. The reduced solubility of precursors in the solution with EA antisolvent also leads to perovskite nucleating 40 s earlier than in untreated films. In equimolar films, EA application delays the conversion or decomposition of MAI by ~120 s. The more rapid solvent removal may retard the diffusion mediated growth of MAPbI₃ crystallites, leading to unreacted crystalline MAI being retained within the sample and persisting there for ~120 s during the anneal, and so although the nucleation rate is higher, the growth rate may be lower as MAI less readily reacts to form perovskite. Finally, EA application induces earlier PbI₂ nucleation, with the 1.83 Å⁻¹ peak appearing after 90 s in the equimolar film. The 1.51 Å⁻¹ PbI₂ peak appears after 180

90

Beneficial Effect of Super-stoichiometric MAI Addition on MA2Pb3I8(DMSO)2 Formation - Results
s, as opposed to 400 s in the equimolar film. Earlier PbI₂ nucleation suggests the antisolvent volume used is too large under these conditions, leading to the washing away of some organic precursors or excessive removal of precursor solvents — leading to film compositions including both perovskite and PbI₂. This is similar to excessively high temperature annealing resulting in higher MAX sublimation and DMSO diffusion observed by Rong *et al.*, resulting in PbI₂ formation (Figure 6).[110]
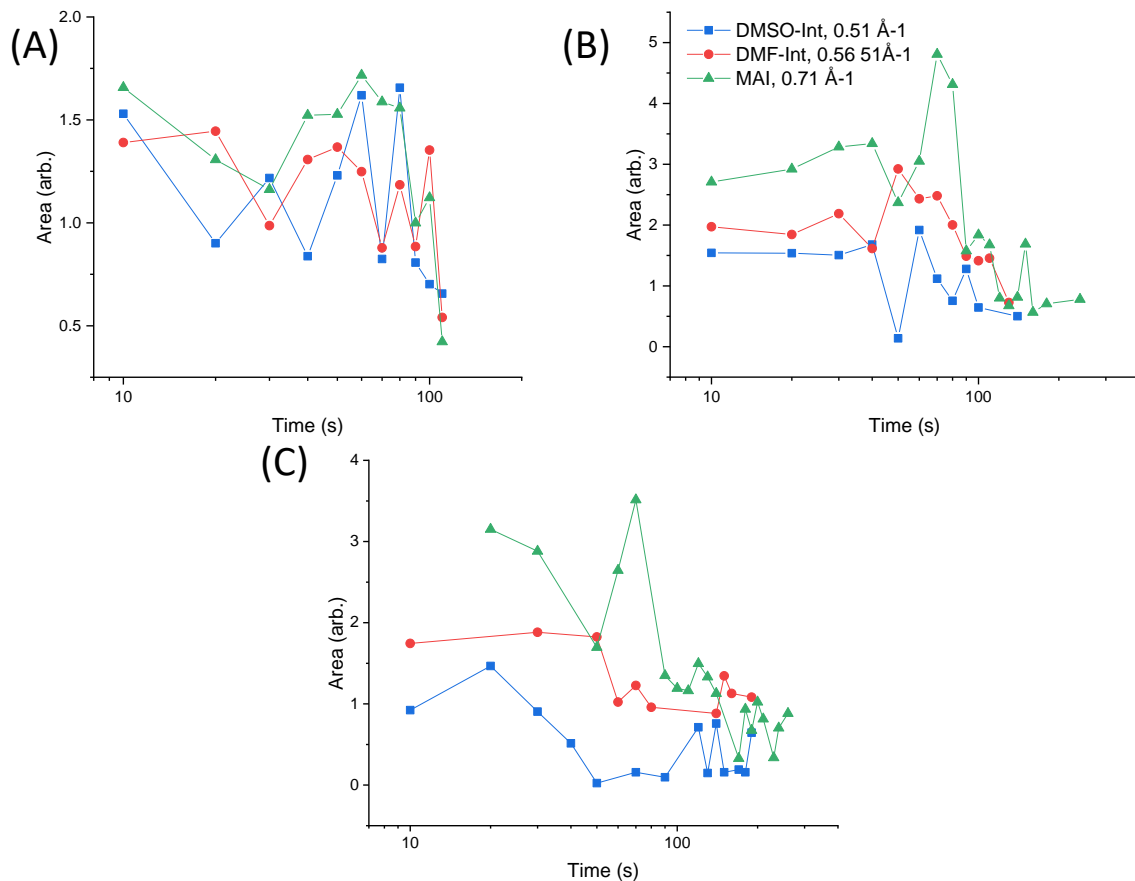
Figure 36: Plots of area vs time showing intermediate phases, and MAI for (A) MAI enriched, (B) Equimolar and (C) PbI₂ enriched films treated with ethyl acetate over first 5 minutes of annealing on a hotplate (which takes ~150 s to reach 100°C from room temperature) The peaks at q = 0.51 Å⁻¹, 0.56 Å⁻¹, and 0.71 Å⁻¹ correspond with the crystalline solvent intercalated DMSO-intermediate, DMF intermediate and MAI respectively.

6.3.3   Effect of excess MAI and excess PbI$_2$

In equimolar films, EA application leads to quicker completion of the intermediate-perovskite conversion, and earlier perovskite nucleation. However, MAI incorporation into the perovskite is delayed when EA is applied to the equimolar film. When excess MAI is used, scattering from the intermediate phases is reduced earlier than in either the equimolar or PbI$_2$ enriched films (Figure 37). The nucleation of perovskite is delayed by 30-40 s relative to equimolar 1.3M perovskite in MAI enriched films. Crystalline MAI lingers for more than twice as long before reacting to form perovskite or volatilising.

Adding an excess of MAI delays nucleation of perovskite, but also hastens intermediate-perovskite conversion once it occurs. This may be due to the excess MAI ensuring a quicker reaction of PbI$_2$ to MAPbI$_3$ once a critical saturation is reached, with excess MAI ions mitigating reduced diffusion caused by solvent removal, by diffusing to the perovskite reaction front. Without application of EA, solvent molecules dominate over MAI in coordinating with PbI$_2$, explaining why there is the lingering crystalline MAI peak in the untreated MAI enriched film after 250 s. The presence of excess MAI may delay perovskite nucleation due to suppressed solvent evaporation over the first few minutes of annealing. The higher solution concentration due to excess MAI cations may encourage more solvent retention in intermediate phases, prolonging the scattering from intermediate peaks. The MAI enriched film also shows continuous growth in area over the course of annealing, compared to the other films which show a decline in area after ~300 s. This points to the beneficial effect of MAI on grain growth. An MAI excess of 20% has been linked to production of the monoclinic, MAI rich (MA)$_3$(DMSO)PbI$_5$ intermediate as opposed to PbI$_2$ and DMSO rich MA$_2$Pb$_3$I$_8$(DMSO)$_2$ (see Figure 30A) prior to annealing.[303] This intermediate also coordinates fewer PbI$_2$ — potentially leading to the production of PbI$_2$ precipitating as a result of under-coordination as solvent evaporates. This may explain the earlier prevalence of PbI$_2$ scattering in the MAI excess films upon EA application relative to equimolar films, as shown in Figure 75A)(Supplementary 13.2). The raw data showed that trigonal PbI$_2$ emerges after merely 30 s in the film treated with EA, denoted by the 1.83 peak, with the 1.51 peak emerging after 130 s (500 s in untreated film).

When an excess of PbI$_2$ is added, perovskite nucleation is delayed by 10 s in both treated and untreated films. Intermediates are converted more rapidly than in the equimolar film, but slower than in the MAI enriched film. This may be due to a larger proportion of intermediate-complexes having crystallised in the film with more Pb atoms providing more opportunities for solvent coordination. Insufficient MAI availability however means that formation of MAPbI$_3$ may be less favourable then in the equimolar film, delaying its nucleation. MAI takes longer to be incorporated into perovskite as the high nucleation density limits the diffusion of MAI to the perovskite growth front, resulting in the nucleation and retention of crystalline MAI for ~400 s. The higher proportion of PbI$_2$ also promotes nucleation of PbI$_2$ after just 20 s (1.83) and 110 s (1.51). compared to 150 s (1.83) and 290 s (1.51) in the untreated film.

Figure 37 summarises the temporal changes in key stages during film formation. As Figure 37 shows, EA application reduces the intermediate conversion time (here defined as the time at which intermediate peaks are no longer resolved above the background) and perovskite nucleation time. Excess MAI is associated with the most rapid completion of the reaction, due to the rapid conversion of intermediates, and reaction of MAI. It is also evident that perovskite saturation — i.e., the time it

Beneficial Effect of Super-stoichiometric MAI Addition on MA2Pb3I8(DMSO)2 Formation - Results takes for the film to reach a critical saturation density of perovskite nuclei upon annealing prior to growth predominating — occurs more rapidly in films treated with EA.
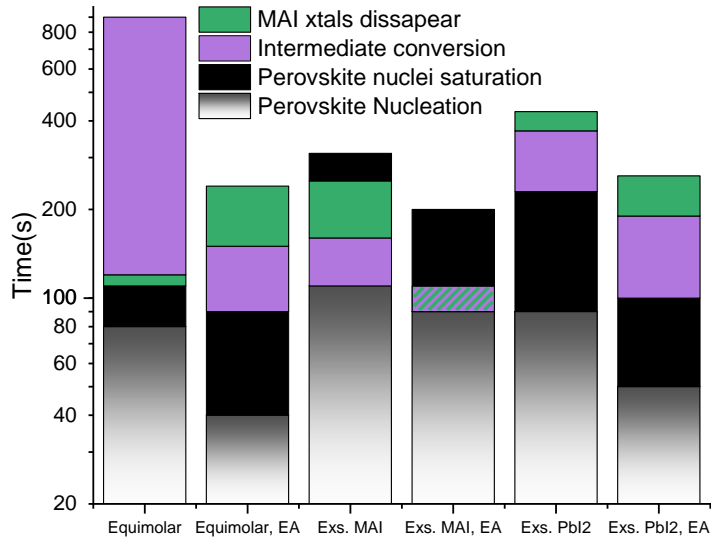
Figure 37: Stages in film formation as observed by WAXS under the influence of varying stoichiometry and application of ethyl acetate. Equimolar films have a 1:1 ratio of MAI:PbI₂, whereas Exs. MAI and Exs. PbI₂ (addition of 10wt% excess of MAI and PbI₂ precursors respectively) films have molar ratios of 1.1:1 and 1:1.1 respectively. "Disappearing" of MAI crystals refers to their consumption in MAPbI₃ formation of sublimation.

6.3.4   UV-VIS Spectroscopy

UV-Vis spectroscopy is used to investigate the influence of EA drip delay and drip volume on the optoelectronic properties of films spin cast at with a single-speed deposition at 3000 rpm (in-situ spin-cast films in WAXS were spun at 4000 rpm to ensure adequate substrate coverage). The presence of secondary phases such as hydrates and PbI₂ correspond with a more disordered band-edge (Urbach Energy, E_U) and red-shifted optical band-gap (E_g). Tauc plots of $(\alpha h \nu)^{1/2}$ versus $h\nu$ and Urbach plots of $\ln(\alpha)$ versus $h\nu$ are calculated from absorbance data (see Methods Section 5.3.1) Values for E_G and E_U are calculated by taking slopes of the linear region which can be extrapolated to the x-axis where $\alpha = 0$. It is expected that EA application improves the perovskite crystallinity, reducing the presence of secondary phases. As drip time is delayed, it is expected the presence of secondary phases to increase due to the intercalation of H₂O as H₂O competes with DMF and DMSO to coordinate with Pb²⁺. Ambient H₂O also reduces the duration of the sol-gel state, reducing the processing window for antisolvent application.[156] As drip volume increases, the excess solvent removal rate increases. Above a certain threshold this will result in perovskite nucleation. Figure 38 shows that use of a larger EA volume seems to increase the electronic disorder, with E_U increasing with each measured addition of EA in films treated < 25 s.
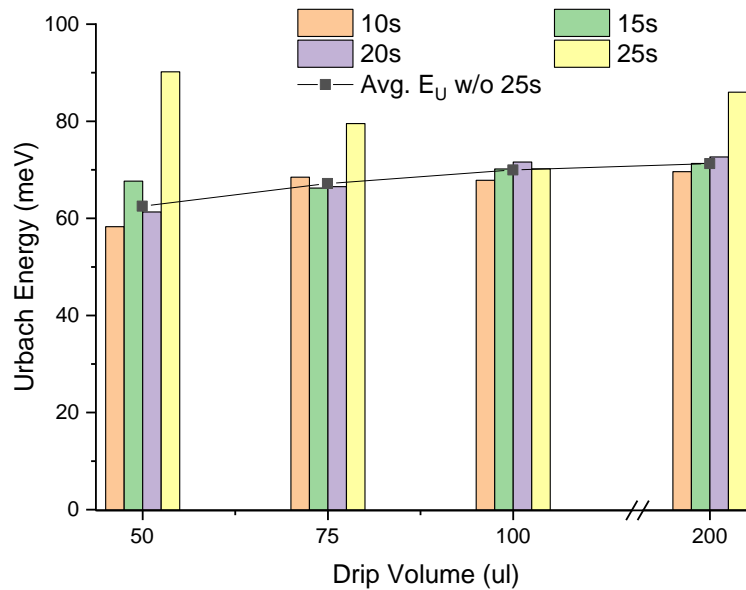
Figure 38: Bar chart of Urbach Energy (E_U) as a function of drip volume and drip-time in films processed at 54%rH with ethyl acetate and line plot of average E_U not including films with a 25 s ethyl acetate drip-time.

This is attributed to the driving force of antisolvent on nucleation of both the intermediate and perovskite. For volumes of EA <100 µl, the film generally forms the intermediate during spin-coating, denoted by a green translucent film. This turns brown and then black upon annealing as it converts first to β and then α-perovskite. Conversely 100 µl or more EA causes nucleation of perovskite during spin casting, driving through the Lewis-adduct intermediate with a β-perovskite film produced prior to annealing. To understand the effect of drip-time, and explain the disparity at 25 s, E_g, E_U, and thickness are determined as a function of drip-time.

According to the Meyerhofer Model, early in spinning coating, thinning of the film by centrifugal flow of solution dominates. Later in the process, when the film is thinner and the flow is slower, evaporation dominates.[304] This may point towards a delayed drip time providing more time for intermediate crystallisation as excess solvent evaporates. Simultaneously, prolonged exposure to ambient moisture increases the generation of hydrated intermediates, where ambient H_2O displaces coordinated DMF and DMSO due to its higher coordination potential. Stable hydrates form which have larger cell parameters than the solvent-intercalated intermediates. After delayed EA dripping, some moisture and intercalated solvent is removed, but a proportion of the stable intermediates and secondary phases persist, shown by the increasing E_U as a function of time in Figure 38. Upon annealing, films with later drip time have higher thickness due to this greater prevalence of secondary phases, with visibly greyer, more matte in appearance, and rougher films. Another observation of delayed drip time during spin casting is enhanced pinhole formation. Adsorption of ambient moisture leads to formation of a hydrated intermediate at the film surface, entrapping solvent. Upon annealing, voids form in the film as trapped solvent bursts through this intermediate crust.[91] These voids reduce charge transfer leading to shunting losses.
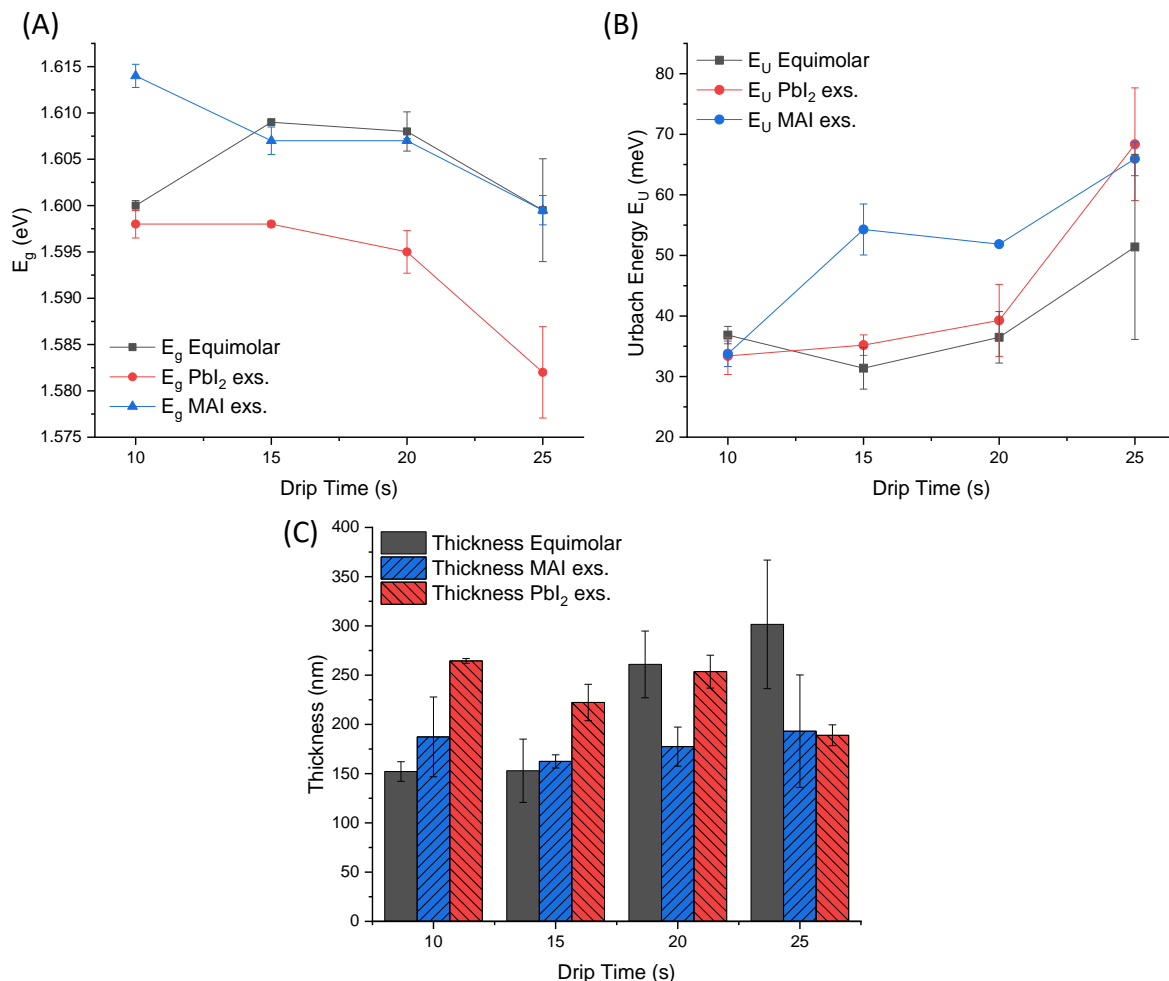
Figure 39: (A) Urbach energy (E_U), (B) Optical band gap (E_g), and (C) Thickness with standard deviation bars, as a function of EA drip-time for films of Equimolar, MAI enriched and PbI2 enriched stoichiometries

By changing the EA drip time for films spin-cast at 3000 rpm, it is found as EA drip time increases there is a small increase in Urbach energy (E_U) (Figure 39B), and red-shift in band-gap (Figure 39A). The intermediate Lewis-adduct formed in Tdrip$_{10 s}$ (drip delay time of 10 s from start of spinning), Tdrip$_{15s}$, and Tdrip$_{20 s}$ films, denoted by the films adopting a translucent green colour during spinning. Tdrip$_{25S}$ films formed a 'cloudier' green intermediate prior to conversion to brown, β (tetragonal) and then black α (pseudo-cubic) perovskite. This suggests the formation of hydrated phases in this film, and explains the greater E_U as shown in Figure 39B.[73] Dripping EA before intermediate crystallisation due to solvent evaporation improves the band-edge ordering of the resulting perovskite, plausibly by the rapid nucleation of the Lewis-adduct phase across the whole film surface simultaneously. E_U and thickness are loosely correlated, with an increase in thickness coinciding with an increase in E_U, shown by the equimolar (10-25 s) and MAI exs. (15-25 s) films in Figure 39c. In the PbI2 exs. films, delaying until Tdrip$_{25S}$ decreases thickness. This may be due to loss of organic cations as the Pb cations have reacted to form stable Pb-hydrates.

95

Beneficial Effect of Super-stoichiometric MAI Addition on MA2Pb3I8(DMSO)2 Formation - Results

It is found that a 10wt% excess PbI_2 addition is associated with a stronger relationship between drip time, electronic disorder and optical band-gap (E_g) than in equimolar films, as shown in Figure 39A and B. The film treated at 15 s has similar properties to the equimolar film treated at 15 s, whereas films treated later have a more red-shifted band-gap, and greater E_U. The higher concentration of Pb^{2+} nucleation centres may lead to a higher rate of formation for hydrated intermediates, exacerbating the deleterious influence of ambient moisture described above and leading to larger electronic disorder in films >15 s. MAI enriched films had a higher E_g than PbI_2 enriched films, and the highest E_g at Tdrip$_{10s}$. An earlier drip time is associated with lower E_U, and higher E_g.

It is hypothesised earlier EA application minimises H_2O incorporation into the intermediate film and increases the conversion to perovskite which it achieves by enhanced solvent extraction. Applying EA earlier minimises production of hydrate phases and improve perovskite film purity (the ratio of perovskite to secondary phases & by-products).

6.3.5 Scanning Electron Microscopy

SEM is used to investigate film morphology under different spinning conditions and with different excess precursor additions. Films cast with a two-spin speed regime (1000 rpm for 10 s and 5000 rpm for 20 s) as per in-situ annealed samples, are contrasted to films cast with a single speed regime (3000 rpm, 30 s) as per in-situ spin cast samples. This was useful to identify any distinct morphological differences arising from the different spinning regimes. As the saturation of solutions increases, the crystallisation rate rises. As previously described, as the Pb^{2+} ions concentration increases, nucleation density increases, leading to denser films. Spin speed and EA application also influences morphology, affecting the precursor super saturation rate, solvent evaporation rate, and thickness. The two-spin speed regime has a relatively higher evaporative thinning component at the start of spin-coating due to the lower spin speed than the single speed regime.

(A-C) show equimolar films spun with a two-speed regime with a 100 µl EA drip after 15, 20, and 25 s. They show a combination of needle and grain like crystal structures. These needles are more obvious in the samples with a shorter drip time. These needle-like features originate from the deleterious orthorhombic DMF-intercalated intermediate.[305] The film becomes less compact with increasing drip time with larger voids between neighbouring crystallites. This is due to more solvent being removed during the spin casting process prior to EA dripping leading to a lower nucleation density of intermediary crystals as compared to earlier drip times. At earlier drip times a larger proportion of Pb is coordinated by the DMF and DSMO solvents (as opposed to ambient moisture or MAI). As the film dries, the less strongly coordinated DMF evaporates more rapidly than DMSO, changing the ratio of DMF to DMSO in favour of DMSO leading to a lower proportion of needles at later drip time. In contrast, (D-F) shows the film cast with an optimal deposition of 3000 rpm for 30 s with a 200 µl drip. Here, an early drip time is associated with a compact film with crystallites on the sub-micrometre scale. The higher initial spin speed and greater acceleration removes more DMF early in the process prior to EA dripping. When EA is dripped after 25 s have elapsed there is evidence of spherulitic perovskite growth in Figure 41C. This sort of growth typically occurs when there is slow crystallisation from a saturated solution.[306] The high precursor saturation of the film due to enhanced solvent evaporation may drive perovskite nucleation upon EA dripping, leading to these spherulitic clusters alongside the significantly smaller grains.[306] This open, coarse structure of radiating fibril structures fans out from heterogeneously formed nuclei where the nucleation rate is low, and normally under isothermal conditions — indicating the nucleation of these structures during spin casting. In subsequent annealing, secondary crystallisation occurs, with slow coarsening of the
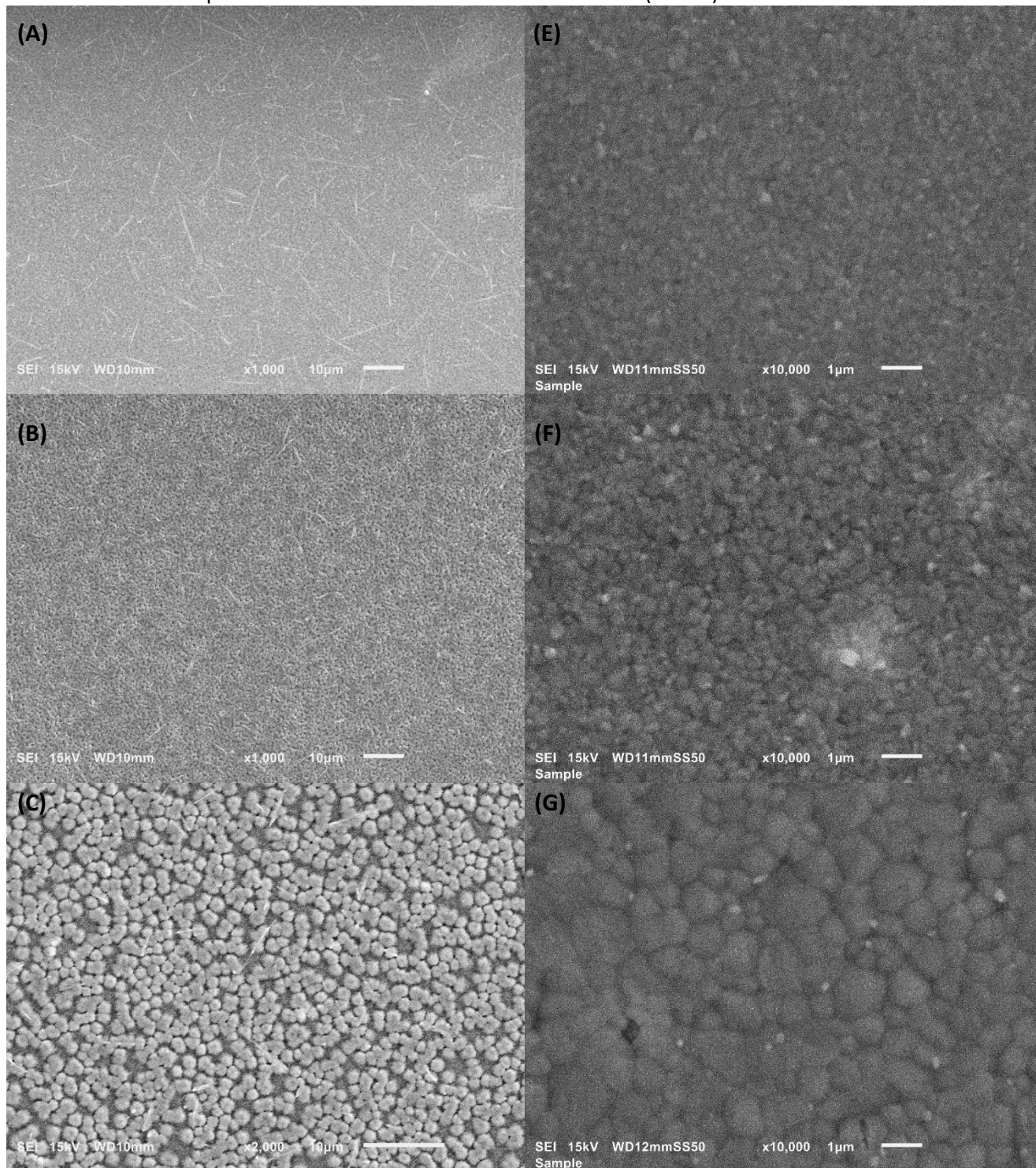
Figure 40: Equimolar MAPbI$_3$ cast with two-phase spinning programme at 1000 rpm for 10 s and 5000 rpm for 20 s with an antisolvent drip of 100 μl with a drip-time of (A) 15 s, (B) 20 s, (C) 25 s. MAPbI$_3$ cast with two-phase spinning programme at 1000 rpm for 10 s and 5000 rpm for 20 s with an antisolvent drip of 100 μl with a drip-time of 15 s with a (D) 10 wt% PbI$_2$ excess stoichiometry, (E) equimolar stoichiometry, (F) 10wt% MAI excess stoichiometry.

fibres.[307] During EA application the film colour progresses from a light green, semi-transparent colour to a brown, semi-transparent colour, suggesting the formation of first the Lewis-adduct intermediate via removal of DMF and excess DMSO and then brown β-perovskite after subsequent DMSO removal. This alludes to the higher crystallisation driving force in this film. Slow growth of the spherulitic clusters occurs prior to annealing.
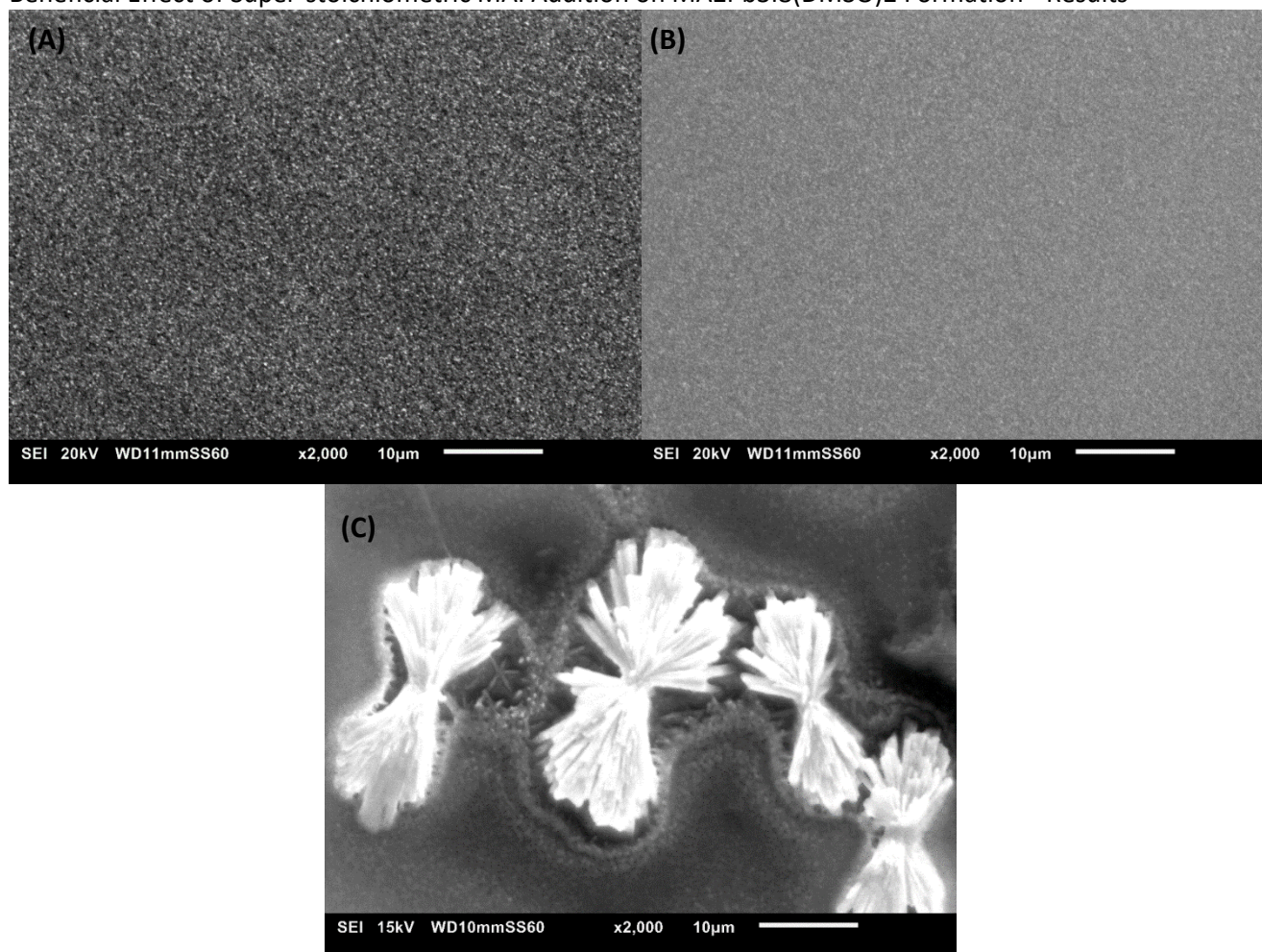
Figure 41: Equimolar MAPbI$_3$ cast at 3000 rpm for 30 s with an EA drip-time of a) 10 s, b) 15 s, c) 25 s. Mx2000

Comparing films of differing stoichiometry while maintaining constant EA volume and drip time, shows clear differences in grain size in Figure 40(D-F). The ratio of MAI:PbI$_2$ correlates with a larger grain size, from <100 nm in the case of the PbI$_2$ rich film to ~500nm-2 µm for the MAI rich film. This is strong evidence for the beneficial effect of excess MAI on enhancing perovskite grain growth. The lower GB area of the MAI enriched films should result in fewer defects at GBs contributing to parasitic charge loss. The earlier drip time ensures a compact film with fewer pinholes, reducing shunting losses, and improving fill factor. These films will have a greater proportion of non-radiative defects due to the excess Iodine, leading to a reduced J_{SC} and V_{OC}, which may mitigate device improvements due to the film morphology.

Figure 42 and Figure 43 shows films cast from solutions with a PbI$_2$ excess with evidence of the DMF-intermediate derived needle crystals on the scale of 10-300 µm. There are also residual PbI$_2$ crystallites — the brighter larger crystals evident in SEM — which result from insufficient MAI for conversion to MAPbI$_3$. These PbI$_2$ crystals have lowest prevalence in films cast with a Tdrip$_{15s}$ (Figure 42b). PbI$_2$ enriched films have a greater sensitivity to EA drip time, with the delay more strongly linked to the crystallisation of unreacted PbI$_2$ and needle like structures. The needles occur more sporadically at Tdrip$_{15s}$ than at either Tdrip$_{10s}$, or Tdrip$_{20s}$, Tdrip$_{25s}$. At Tdrip$_{15s}$ the needles are also more defined and larger, suggesting more optimum growth of the DMF-intermediate. At later drip time, ambient moisture is displacing DMF and DMSO, leading to the formation of PbI$_2$ secondary phases. This is evidenced by the smaller needles and increasing proportion of PbI$_2$ crystallites at later drip time. A MAI excess as shown in Figure 44 is associated with the formation of exceptionally smooth films with grains on the order of hundreds of nanometres. As drip time increases so does the presence of inhomogeneities in the film morphology; pinholes and secondary phases rich in PbI$_2$ (Figure 45).
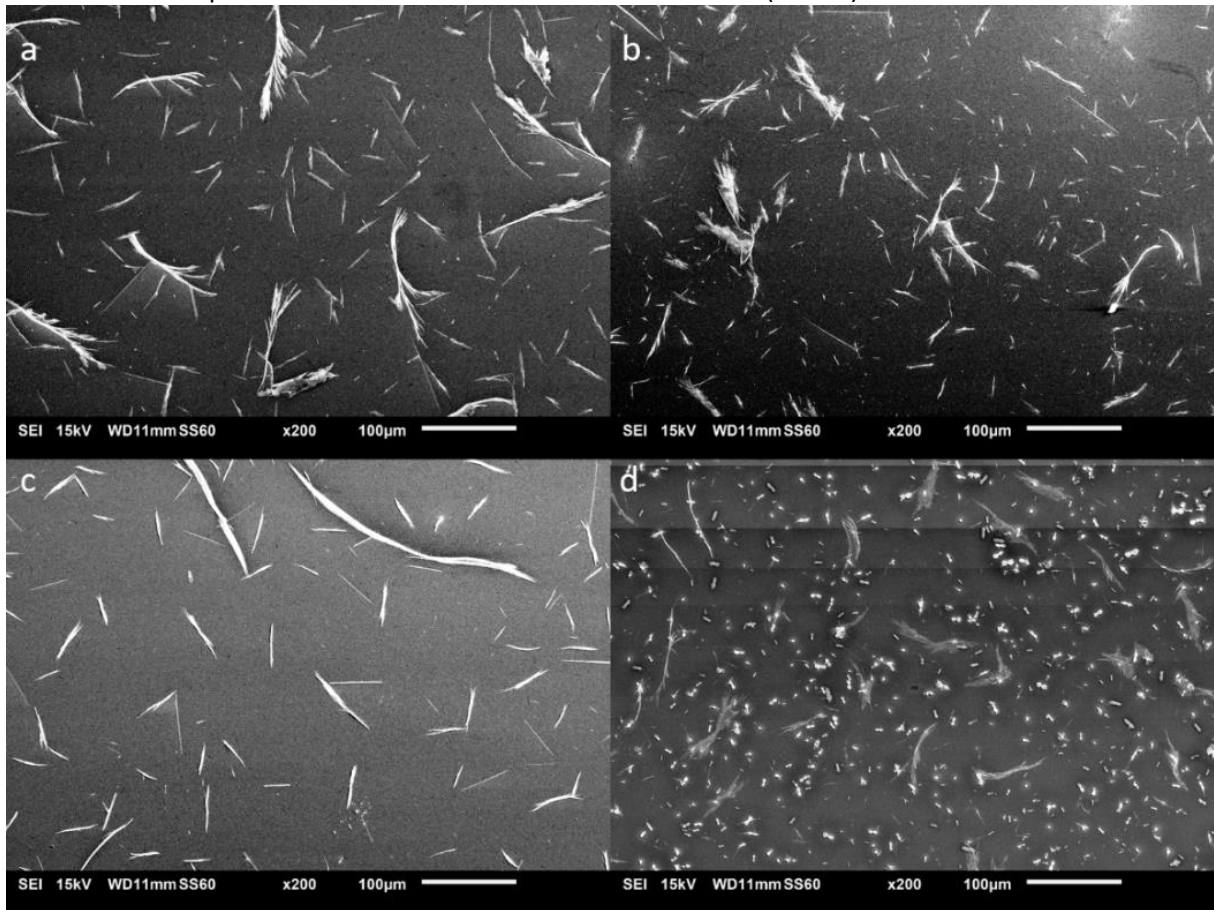
Figure 42: 10wt% PbI$_2$ excess MAPbI$_3$ cast at 3000 rpm for 30 s with an EA drip-time of a) 10 s, b) 15 s, c) 20 s, d) 25 s. Mx200
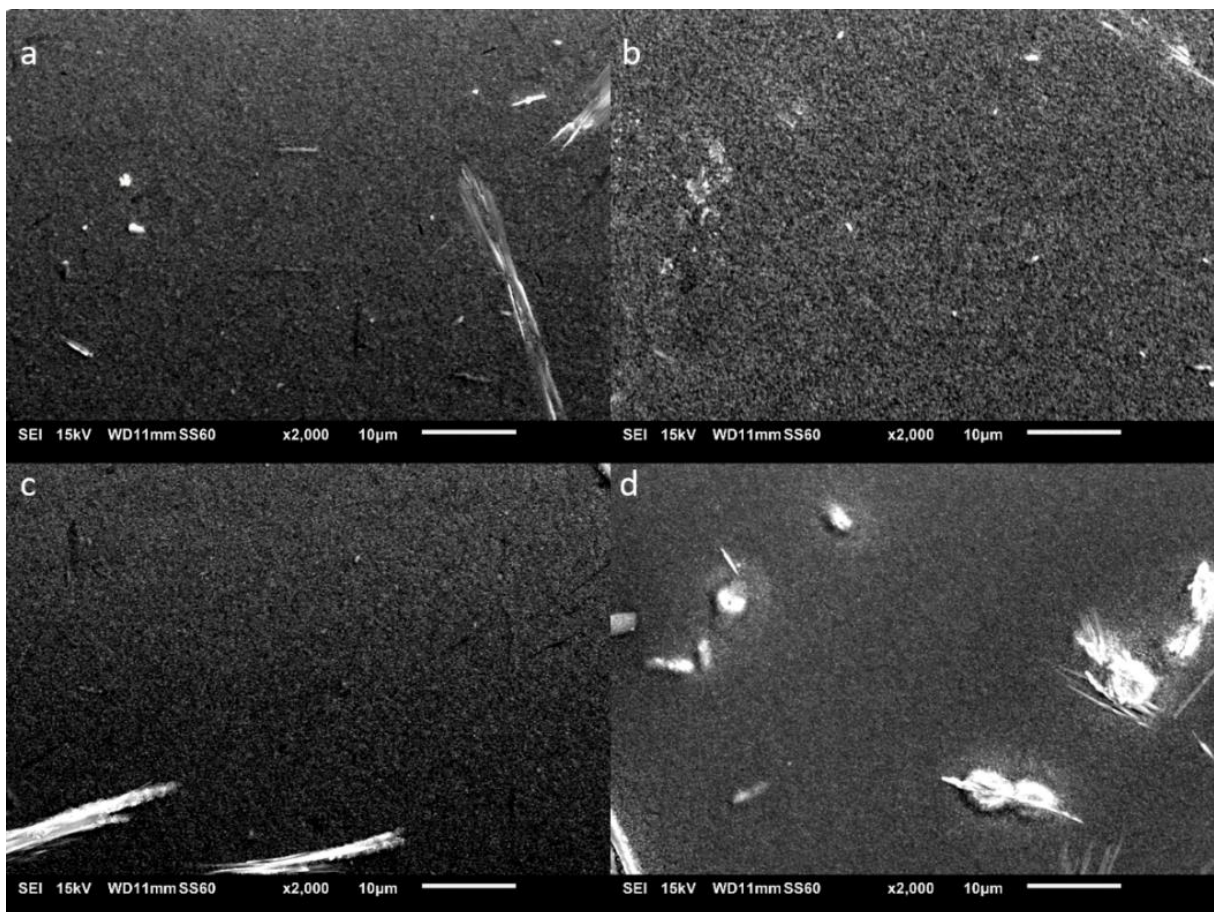
Figure 43: 10wt% PbI$_2$ excess MAPbI$_3$ cast at 3000 rpm for 30 s with an EA drip-time of a) 10 s, b) 15 s, c) 20 s, d) 25 s. Mx2000
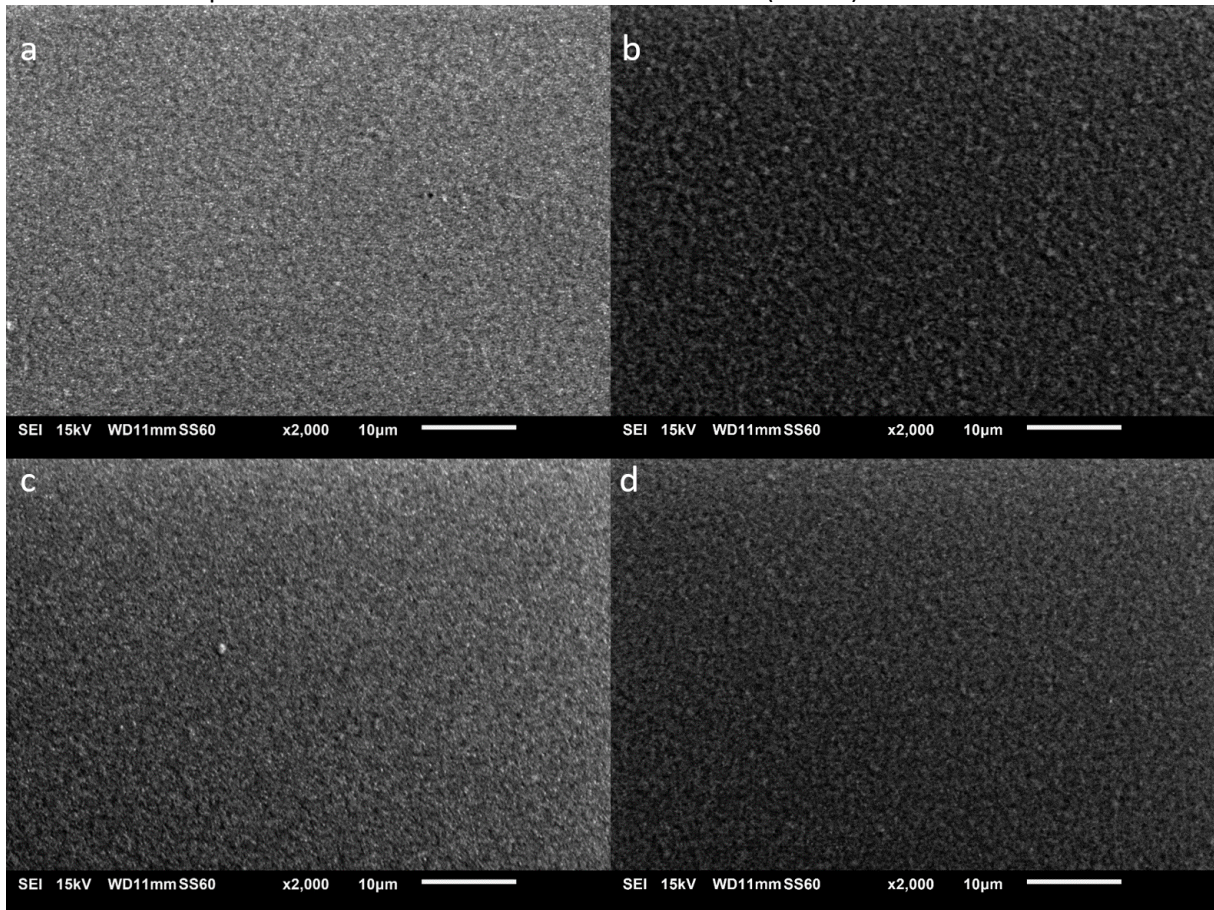
Figure 44: 10wt% MAI excess MAPbI$_3$ cast at 3000 rpm for 30 s with EA drip-times of a) 10 s, b) 15 s, c) 20 s, d) 25 s. Mx2000
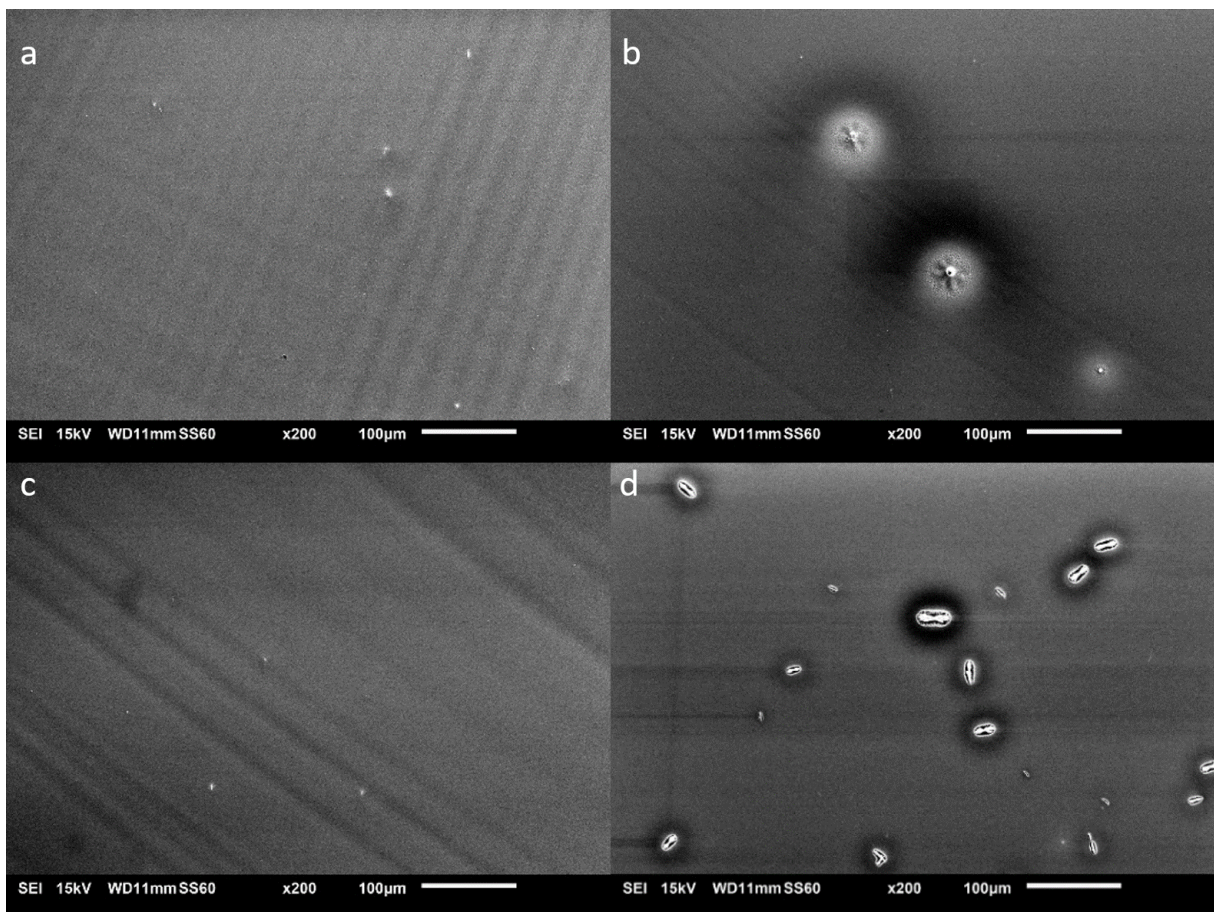
Figure 45: 10wt% MAI excess MAPbI$_3$ cast at 3000 rpm for 30 s with an EA drip-time of (A) 10 s, (B) 15 s, (C) 20 s, (D) 25 s. Mx200

100

6.3.6   Ambient Air Devices

Devices were fabricated under ambient conditions (rH=49±1%) using differing stoichiometric ratios of the precursors to investigate their effect on photovoltaic parameters. Figure 46A and B show that under reverse bias, addition of 10wt% excess MAI increased mean PCE the most, mostly due to improved *FF*. Under forward bias, the PbI$_2$ enriched device shows highest mean efficiency. Additionally, the PbI$_2$ enriched device shows less hysteresis during the measurement, with a reduced difference between the forward and reverse biased PCE. This may be due to reduced sensitivity to EA flow rate (which can change due to variation in pressure applied by scientist pipetting antisolvent), as noted by Taylor *et al.*, who noticed a similar result in triple-cation films with an organic cation deficiency.[126] As shown in Table 7 (Appendix 13.2), MAI enriched devices had the lowest V_{OC} (Figure 46C) and this may be due to recombination arising from intra-band defects. This is supported by the greater E_U in these films (see Figure 39B). V_{OC} increases as the MAI:PbI$_2$ ratio decreases, suggesting the addition of PbI$_2$ passivates these recombination sites. This complements the observation of reduced hysteresis, suggesting PbI$_2$ enrichment reduces the prevalence of ion diffusion pathways, dominated by $V_I^{\bullet}$. J_{sc} of the MAI enriched devices are lower than the PbI$_2$ enriched devices, though both are better than equimolar devices (Figure 46D). This suggests PbI$_2$ as an Iodine ion source more effectively reduces hysteresis by reducing the prevalence of $V_I^{\bullet}$. While MAI addition does passivate some $V_I^{\bullet}$, it may also introduce $V_{Pb}^{\bullet}$ and Iodine interstitial defects, contributing to non-radiative recombination, and thereby reducing J_{SC}. Under forward bias, mobile Iodine ions will accumulate at the perovskite-ETL interface, generating a space charge layer which screens electron transfer between the two, leading to exacerbated hysteresis (See Section 2.7).

Fill factor (*FF*) decreases with PbI$_2$ enrichment. The smaller grains and presence of PbI$_2$ reduces the relative active area of the film. Devices were thus fabricated using MAI exs. MAPbI$_3$ while varying EA drip times and using 200 µl EA. It was found that a Tdrip$_{15s}$ produced the highest performing devices, with a champion efficiency of 16.13%, and *FF* of 76.48%. Tdrip$_{10\ s}$ reduced deviation between pixels under both forward and reverse bias, as shown in Figure 46b, but devices had lower *FF*, as shown in Table 7. As Tdrip is increasingly delayed, V_{OC} and J_{SC} drops. Devices with Tdrip$_{20\ s}$ had lower performance and larger hysteresis due to reduced J_{SC} and *FF*. Devices were also made using equimolar MAPbI$_3$ synthesised under ambient conditions with differing antisolvent drip volumes and constant drip time at 10 s (to minimise the production of hydrates), shown in Figure 46c. An equimolar film is used to isolate the influence of EA volume as opposed to stoichiometry which also influences phase purity and defect density. Together with the J-V curves shown in Figure 46D and the device parameters summarised in Table 7, it is apparent that 100 µl produces the highest performing films on average. This is due to improved J_{SC} and *FF*, meaning the film has improved current extraction, relative to the other conditions. Insufficient EA leads to limited surface interaction, and changes in morphology as a result. This changes the films' properties across the surface. Increasing the EA volume reduces sample variability. Although the best cell with 16.57% efficiency was found when minimal antisolvent (50 µl) was used, the 50 µl film also had the lowest performing cell at 12.81% (8 cells at this volume). The film produced using a 100 µl EA rinse had the highest average PCE (15.61%). Using an EA excess —200 µl— provoked perovskite nucleation during spin coating (evidenced by the brown, β phase), the formation of which (prior to crystallisation of the black α-phase) appears to be associated with reduced hysteresis. The V_{OC} was lowest for films in which 200 µl EA volume was applied. This suggests that while increasing the volume of EA applied can improve consistency over the substrate surface, the fill-factor improvement is mitigated by decreasing band-gap due to increased electronic disorder. This may be due to precursor material being lost from the combination of EA application and centrifugal forces of the spinning chuck, introducing trap states at the band-edge. EA mechanically removes some material as the precursor's solubility rapidly decreases.

Figure 46 shows the best performing devices made in air from publications investigating ambient synthesis of MAPbI$_3$ films with ethyl acetate. Studies fall within a trend of decreasing efficiency as humidity increases.[99,308,309] Troughton *et al.* use 200 µl of EA at 75%rH, whereas at 30%rH Kim *et al.* uses as little as 50 µl of EA. This supports the hypothesis that at lower humidity, less EA is required to suppress moisture adsorption. This work follows the trend, with room for improvement upon devices; reducing the volume of EA applied, swapping the PTAA HTL for spiro-Ometad based HTL, using a Au as opposed to Ag contact, and other optimisation methods.
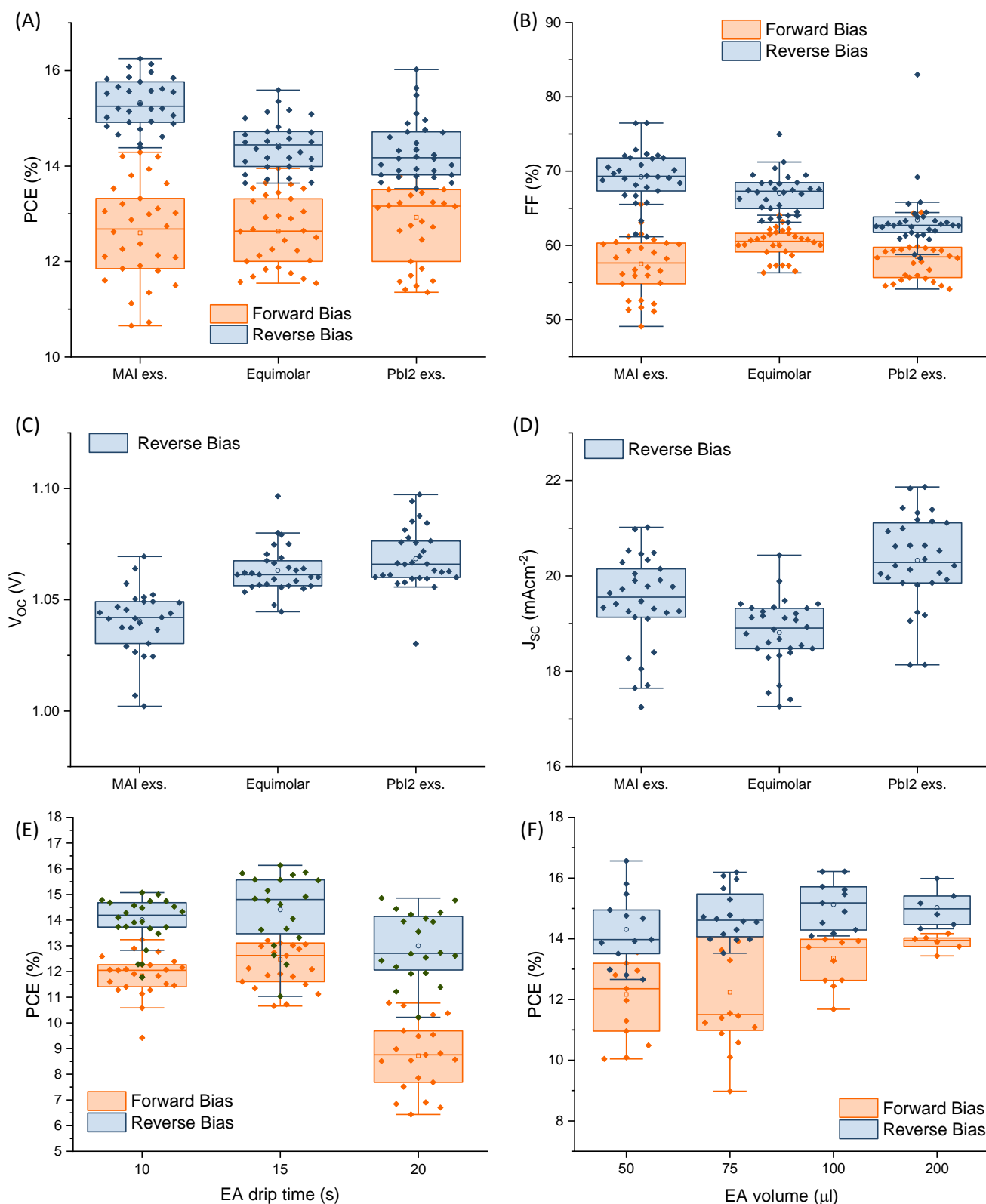
Figure 46: (A) PCE, (B) FF, (C) V_{OC}, (D) J_{SC} of devices (Ag contact) depending on perovskite stoichiometry, N=36 per stoichiometry (E) PCE of devices (Ag contact) as a function of EA drip-time in MAI exs. perovskite films, N=20 per drip-time. (F) PCE of Equimolar devices (Au contact) as a function of EA volume with a drip-time of 10 s, N=8 per volume.

1.   (A)

Figure 47: (A) Device stack in n-i-p configuration. (B) J-V curves (average) of Equimolar MAPbI$_3$ devices as per Figure 46(F) with antisolvent drip volumes of 50, 100 and 200 µl.

Figure 48: MAPbI$_3$ devices made in ambient air with ethyl acetate showing PCE(%) as a function of relative humidity(rH%). This work is with an MAI excess. The negative relationship between increasing rH% and decreasing PCE% is evident.
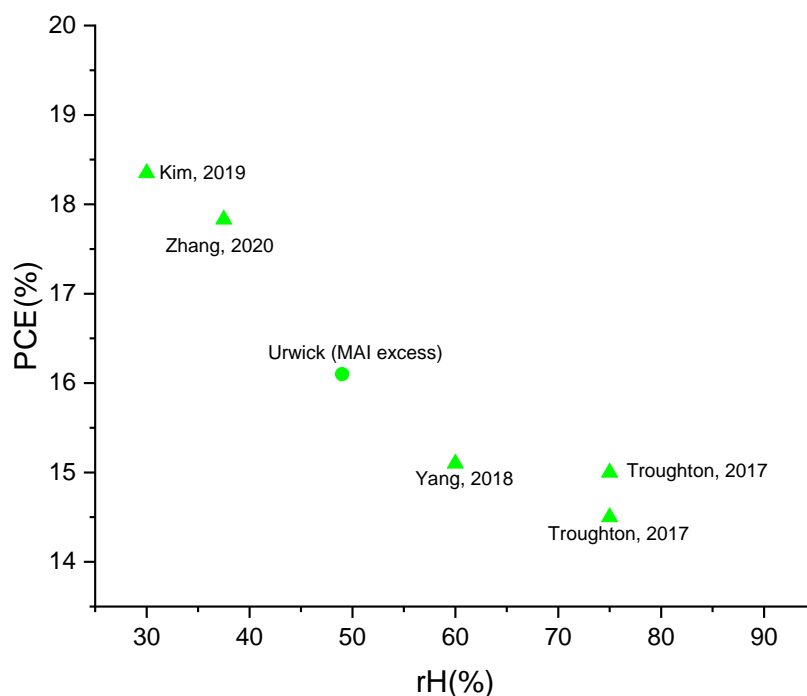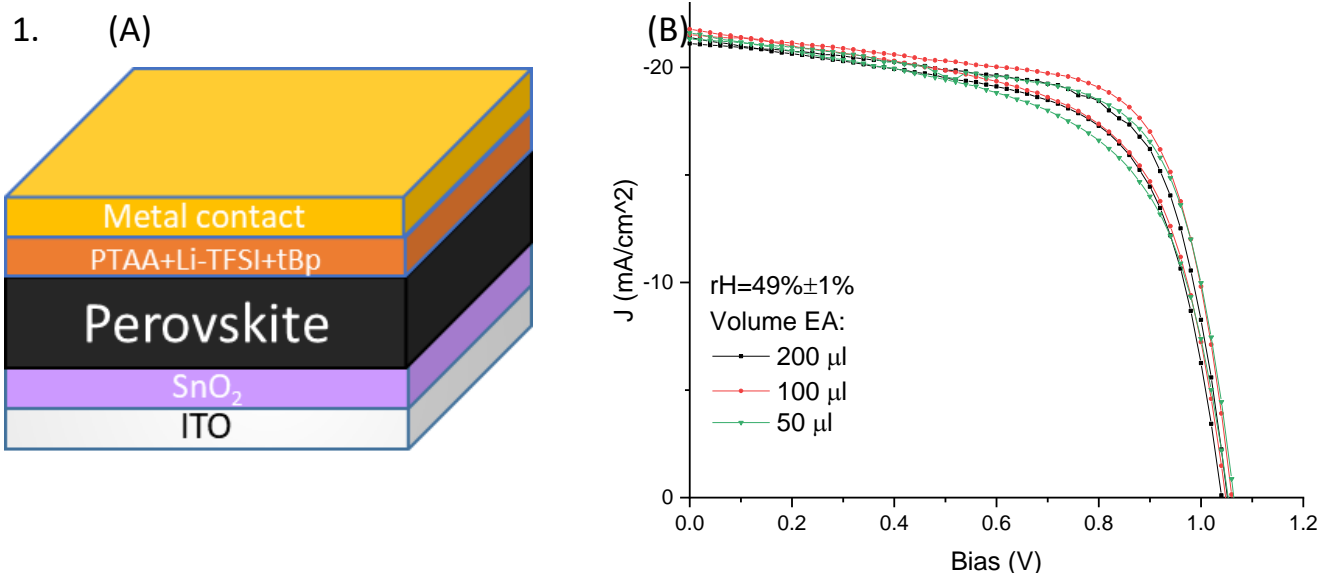
The current best MAPbI$_3$ devices made in air utilise diethyl ether as an antisolvent in a one-step deposition process (See Figure 76 in Appendix). Diethyl ether is a toxic solvent, and as previously discussed does not have optimal polarity with regards to the precursor solvents and salts or affinity for moisture. These studies also either fabricate their devices in relatively low humidity (30%rH, Aranda *et al.*) or with preheating of the substrate prior to perovskite deposition (Wang, and Cheng). Heating the substrate reduces adsorption of H$_2$O and O$_2$ on the spinning film in ambient conditions.[118,121,310] Yang *et al.* show methyl acetate (MA), which has as even stronger moisture affinity than EA, produces better devices than longer chain length acetates.[120] However in their comparison they use relatively large volumes — 500 µl — which based on the trend in Figure 46C would result in a significant decrease in antisolvent efficacy (results in worse film quality and device performance) as the volume applied increases above 100 µl. Excessive antisolvent will drive the nucleation of β-phase perovskite prior to annealing as opposed to the DSMO-intermediate, and this will affect the crystallisation rate of the α-

Beneficial Effect of Super-stoichiometric MAI Addition on MA2Pb3I8(DMSO)2 Formation - Discussion

phase. Indeed, their work shows MA application generating a dark brown film whereas butyl acetate generates a pale white-brown film before annealing. This is telling as upon annealing the darker films will readily convert to α-perovskite, whereas the lighter films, which lack a high concentration of the β-phase, will convert more slowly, impacting film quality and device performance. The rapid conversion in the absence of the mediating DMSO intermediate also results in the application of shorter carbon-chain length acetates being associated with more residual PbI2. As Taylor *et al.* show, any antisolvent can be applied with high efficacy with the correct procedure.[126] Considered together, the thesis that methyl acetate is a better antisolvent merits future investigation and the use of ethyl acetate is justified on the basis of consistency and comparability with the literature which focuses on ethyl acetate.

6.4   Discussion

The effect of stoichiometry, humidity and ethyl acetate on the formation of the DMSO-intermediate can be described using Figure 49. First, decreasing the ratio of MAI:PbI2 results in a higher nucleation rate, and the films attains a higher critical super-saturation density. Ambient moisture reduces nucleation of the DSMO-Intermediate as H_2O competes with DMSO to coordinate with Pb^{2+} cations. Ethyl acetate application promotes the formation of the DMSO-intermediate, by selectively removing DMF and moisture, leading to an even higher nucleation rate. The intermediate phase's crystallinity increases as excess solvent evaporates during further spinning. Growth and aggregation of crystallites leads to conversion and reorientation of particles from crystals with low d-spacing to high d-spacing. Eventually, due to exposure to ambient atmosphere, the intermediate phase begins to decompose, with nuclei density increasing as moisture displaces DMSO, and perovskite also begins to nucleate. An excess of MAI results in lingering crystalline MAI in the intermediate film, which upon annealing leads to a larger grain-growth component in perovskite crystallisation. It is also associated with suppressed solvent loss, delaying the nucleation of perovskite relative to equimolar or PbI2 enriched films. This promotes uniform conversion from the DMSO-intermediate too perovskite, reducing the prevalence of defects and strain.
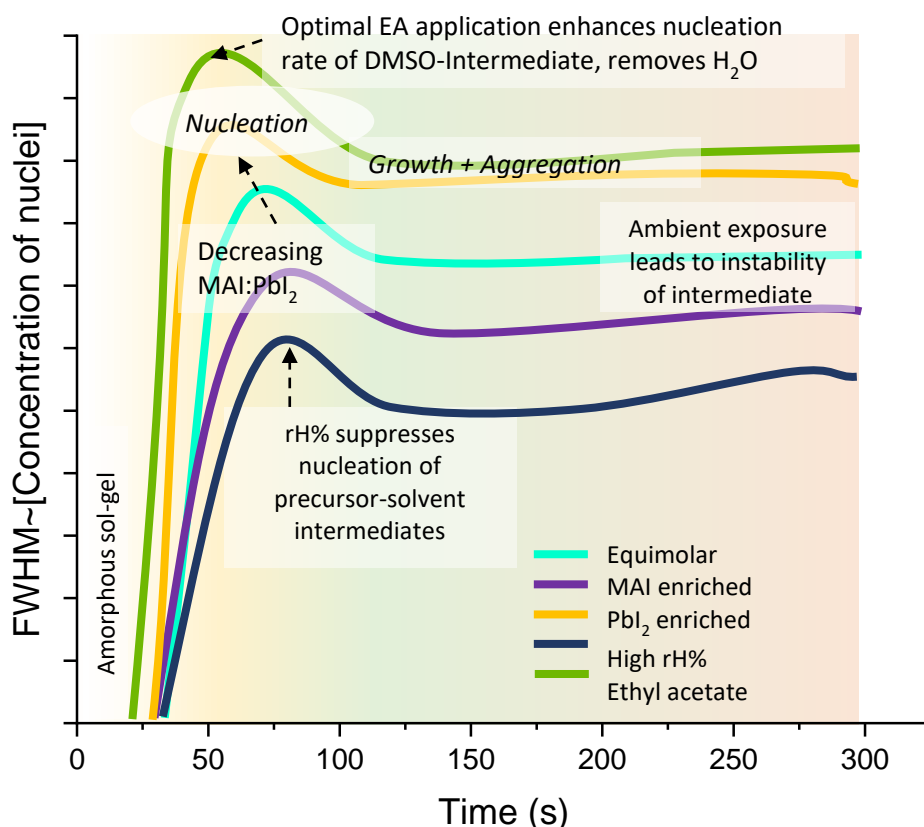
Figure 49: Lamer-model based description of the effect of stoichiometry, moisture and EA antisolvent on the reaction to form the DMSO-intermediate phase.

In detail, adding MAI compensates for the MAI deficient conversion occurring when orthorhombic and monoclinic intermediates convert to perovskite (observed in films dominated by the orthorhombic intermediate). MAI exchanges with DMSO to react with available PbI2 converting $MA_2Pb_3I_8(DMSO)_2$ to $MAPbI_3$.

Beneficial Effect of Super-stoichiometric MAI Addition on MA2Pb3I8(DMSO)2 Formation - Conclusion

The excess MAI suppresses the loss of solvent, promoting the formation of the DMSO rich orthorhombic intermediate while also (but to a lesser extent due to the low excess used) providing the I-rich conditions that promote the DMSO-deficient monoclinic phase, thereby favouring the very conversion route that ensures full perovskite reaction. Combining this with the optimised action of ethyl acetate, which selectively removes DMF and moisture, enhances the nucleation rate and density of intermediary nuclei, further stabilising the orthorhombic intermediate. The intermediate crystals grow larger due to solvent assisted rearrangement, resulting in fewer defects. Residual MAI then also promotes perovskite grain growth upon annealing, which is MAI diffusion regulated. The result is films with large grains and reduced defects, leading to high *FF* in devices.

6.5   Conclusion

Excess precursors (MAI or PbI$_2$) lead to earlier onset for intermediate nucleation. four stages in intermediate formation were identified, similar to the findings of Pineda *et al.*; Sol gel formation, nucleation, growth, and aggregation. Lead enriched films show greater variation in the intermediate nucleation start time as well as greater susceptibility to the production of hydrated by-products during solution processing. This suggests Pb enrichment raises the moisture sensitivity of humidity mediated intermediate crystallisation pathways. The appearance of the perovskite positively correlates with the ratio of PbI$_2$:MAI — a greater concentration of PbI$_2$ induces early perovskite nucleation onset; conversely, MAI delays precipitation of the perovskite. A greater proportion of defects in the final perovskite film can also be inferred from the greater Urbach Energy of PbI$_2$ enriched films. PbI$_2$ enrichment is associated with a longer intermediate-perovskite conversion time and a perovskite film with a more disordered band-edge after annealing. Enriched films containing an excess of MAI or PbI$_2$ have earlier complete conversion of the crystalline intermediate to perovskite relative to films cast from stoichiometric MAPbI$_3$ solution. Intermediates in the PbI$_2$ rich films last longer than in the MAI enriched film. MAI enrichment has the effect of completing the intermediate-perovskite conversion earlier due to enhanced provision of MAI facilitating MAI diffusion regulated growth whereas additional PbI$_2$ hinders the conversion to perovskite due to the high nucleation density reducing MAI mobility or encouraging the nucleation of PbI$_2$.

Ethyl acetate (EA) suppresses formation of the DMF intermediate, while promoting formation of the DMSO-intermediate and leads to more rapid perovskite nucleation (Figure 35 vs Figure 36). Coupled with the higher nuclei concentration in the PbI$_2$ enriched film, this leads to the lowest nucleation onset time in this film. Earlier antisolvent dripping reduces the formation of defects and hydrated by-products. The optimal EA volume balances 1) driving the direct nucleation of perovskite (driving force increases with chemical activity) — which whilst desirable will be more likely to contain undesirable by-products — and 2) sufficient EA to remove DMF while nucleating the DMSO-intercalated Lewis-adduct (which facilitates perovskite coarsening). EA application is associated with earlier intermediate-perovskite conversion upon annealing, but in equimolar films prolongs the endurance of crystalline MAI. This coincides with the prolonged duration of the intermediate in equimolar films indicating the reaction is delayed relative to super-stoichiometric films: Super-stoichiometric films show more rapid conversion to perovskite upon annealing.

There is a positive relationship between the MAI:PbI$_2$ ratio and grain size in EA treated films, explained by the delayed appearance of perovskite in MAI enriched precursors films. XRD suggests the excess MAI is associated with suppressed solvent evaporation, resulting in fewer, but larger intermediate crystals prior to conversion into perovskite. This facilitates the formation of a perovskite film with larger grains due to the lower nucleation density of the intermediate film. MAI enrichment also extends the antisolvent application window as the proportion of uncoordinated Pb^{2+} nucleation centres is reduced, reducing the formation of hydrated intermediates during spin-casting. Devices made with each stoichiometry reveal that MAI enrichment increases average PCE due to improved *FF*, while PbI$_2$ enrichment improved J_{SC} and V_{OC} due to defect passivation (lower E_U). Based on this work, the best scenario would be use of a 10wt% MAI enriched perovskite solution with 100 μl of EA applied after 15 s under ~50%rH. It would also be beneficial to introduce simple additives or treatments to passivate defects, thereby improving J_{SC}, V_{OC}, and reducing hysteresis, such as MACl, HI, or other Lewis acids.

This work furthers our understanding of the interplay of EA application and precursor solution stoichiometry during fabrication of perovskite films under ambient conditions. This developed understanding of the crystallisation of intermediates, conversion to perovskite, and perovskite crystallisation during film formation, as well as how the stages are affected by super-stoichiometric mixtures of precursor salts will inform strategies to optimise performance of MAPbI$_3$ films for optoelectronic applications such as flexible PSCs and multi-junction devices.

7 Deciphering Perovskite Decomposition in a Humid Atmosphere with TOF-GISANS

This work has been published in the journal Energy Reports in the form of a conference paper.[311] In terms of contribution, I researched and designed the experiment, prepared samples, conducted the analysis, and wrote the paper. My co-authors supported me in conducting the GISANS portion of the work carried out at the ISIS Pulsed Neutron and Muon Source. My supervisor and co-author Alan Dunbar, contributed in discussing the analysis, providing feedback from which modifications were made to the work. This is an altered version of the original publication to account for the different textual styles and formatting required for each publication.

7.1 Abstract

Substitution or alloying of the cations on the A-site and halides on the X site of ABX_3 perovskites has been successfully used as a technique to improve moisture stability of perovskite films for optoelectronic applications. Despite structural and electrical stability improvements, these perovskite films still undergo moisture induced degradation into PbI_2 and other photo-inactive phases, reducing device lifetime and performance. Understanding of moisture induced degradation has been hindered by the contrast mechanisms and sensitivity of optical and X-ray scattering techniques. Time-of-Flight Grazing Incidence Small Angle Neutron Scattering (TOF-GISANS) presents itself as a powerful alternative capable of identifying low atomic weight phases and offering depth resolution. Herein TOF-GISANS is used to begin to uncover moisture induced degradation pathways in various mixed perovskite systems fabricated under ambient conditions and exposed to 90%rH in the dark for up to 12 hrs, showing poor stoichiometric homogeneity through the bulk of the film and facile formation of deuterated by-products at ambient temperatures. The evidence is indicative of formation of PbI_2, and $PbBr_2$ due to moisture degradation, from peaks apparent in scattering from the surface of $MAPbI_3$, $FA_{0.83}MA_{0.17}Pb(I_{0.83}Br_{0.17})_3$, and $FA_{0.83}Cs_{0.17}Pb(I_{0.83}Br_{0.17})_3$ thin films. Degradation is markedly less pronounced in the latter films containing Cs. Using deuterated water allows the moisture ingress to be followed. Deuterated by-products form readily, resulting in decreasing average particle size as perovskite crystals swell and fragment from the grain periphery inwards. For the first time, evidence indicative of the formation of alloyed FA based perovskite hydrates is found. $Cs_{0.05}(FA_{0.83}MA_{0.17})_{0.95}Pb(I_{0.84}Br_{0.16})_3$ shows impressive phase stability compared to the other mixtures, with minimal segregation to other phases observed in vertical cuts (out-of-plane integration) through the 2D scattering image, though still exhibits deleterious morphological degradation.

7.2 Introduction

Moisture induced degradation of perovskites is responsible for performance reduction over device lifetimes. The aristotypical $MAPbI_3$ is particularly susceptible to moisture due to the crystal cell parameters permitting facile penetration by water molecules, resulting in the formation of intermediary monohydrate and dihydrated perovskite phases.[164] H_2O molecules form strong H-bonds with organic cations, weakening the bond between the cation and octahedral Pb ion. This enables rapid deprotonation of the A-site cation and leaves the perovskite vulnerable to other exogenous degradation factors.[95,168] Water reacts with the iodine at the X-site in the perovskite, creating hydroiodic acid, methylamine and PbI_2.[170] Liao *et al.* performed nanoscale mapping of the humidity induced degradation of polycrystalline $MAPbI_3$ films treated with EA antisolvent at 90% relative humidity (rH). Their findings suggest that the reaction proceeds initially through humidity induced grain growth and atomic rearrangement, followed by formation of a monohydrate layer which, due to its low stability at room temperature, degrades to PbI_2 through the evaporation of Methylammonium Iodide (MAI) and H_2O. Moisture continues to diffuse through the semi-amorphous hydrated GBs repeating this process, and these GBs are the last surfaces to develop PbI_2. PbI_2 eventually covers surfaces and GBs, limiting further moisture ingress, or loss of the metastable hydrated phase.[171] Similarly, Wang *et al.* reported the susceptibility of an amorphous region at the perovskite GB to react with moisture, finding it to have a much higher propensity to react than the grain surface. They link this to the higher proportion of defects at the GB allowing H_2O to permeate into the bulk and initiate degradation.[172] This resonates with reports of perovskite stoichiometry being initially preserved at the surface while PbI_2 is produced in the bulk and at GBs.[312]

The reaction of $MAPbI_3$ and H_2O to form the monohydrate $MAPbI_3 \cdot H_2O$ has been shown to be reversible, whereas the subsequent reaction to form the dihydrate phase $(CH_3NH_3)_4PbI_6 \cdot 2H2O$ is irreversible, and characterised by the loss of volatile MA^+, HI, I_2, NH_3 and the production of PbI_2.[165] In a time resolved X-ray diffraction (XRD) study under 70%rH, Leguy *et al.* found this hydration pathway proceeded trough the loss of

Deciphering Perovskite Decomposition in a Humid Atmosphere with TOF-GISANS – Results and Discussion
MAI; once the MAI is lost the reaction is irreversible.[165] Evidence for the hydrate and PbI_2 formation was also found in an in-situ grazing incidence XRD (GIXRD) study at 100%rH of moisture induced degradation by Yang *et al.* and Petrus *et al.* using in-situ XRD (75%rH), as well as in the in-operando XRD study at 50%rH by Schelhas *et al.*.[68,163,313] Exposure of MAPbI$_3$ solar cells to rH > 50% rapidly deteriorates device performances.[195] Schlipf *et al.* used Grazing Incidence Small Angle Neutron Scattering (GISANS) to analyse MAPbI$_3$ films during prolonged exposure to humidity (D_2O), finding that under high rH, metastable hydrate phases formed as the faceted crystals are transformed to rounded ones.[166] The films incorporated more water than is simply integrated into the hydrates, with smaller crystals more strongly affected. Even at low humidity water is adsorbed on the surfaces of crystal domains. Above 93%rH the dihydrate phase forms. The uptake of water and formation of hydrates is accompanied by swelling of the grains. Moisture induced degradation has also been observed in encapsulated devices: Chu *et al.* found that in polymethyl methacrylate (PMMA) coated films with micrometre sized MAPbI$_3$ grains at 35%rH over 6 days, moisture diffusion through the PMMA layer leads to the fragmentation of grains, and this disintegration was not centred on GBs.[57] Notably, PMMA is not known for its moisture barrier properties, which stresses the importance of appropriate encapsulation selection.

By using broad neutron wavelengths, GISANS geometry and Time-of-Flight (TOF) detectors to investigate both surface and bulk characteristics of perovskite films. TOF-GISANS was demonstrated by Wolff *et al.* in their depth-resolved study of block co-polymer micelles close to the surface of silicon substrates.[277] The moisture (D_2O) induced degradation in the dark of perovskite films with differing A-site cation combinations and comparable X-site halide mixtures to MAPbI$_3$ are compared. It is found, true to form, that $Cs_{0.05}(FA_{0.83}MA_{0.17})_{0.95}Pb(I_{0.84}Br_{0.16})_3$ shows the least degradation. It is shown the production of PbI_2, $PbBr_2$, and deuterated and hydrated perovskite phases to varying degrees in each sample as well as evidence for the production of $CsPb_2I_4Br$ and various deuterated phases by comparing peaks in the SANS profiles with calculated values for scattering length density, *b*. This uses a similar approach to Schlipf *et al.* by assigning different phases to peaks from out-of-plane ("vertical cuts") surface scattering in GISANS.[166] The methodology for determining and fitting predicted phases to the peaks is described in (Methods Section 5.1.4).

A mixture of Cs, FA and MA on the A site and I and Br on the X-site lead to a film with enhanced moisture stability compared to $FA_{0.83}MA_{0.17}Pb(I_{0.83}Br_{0.17})_3$ or MAPbI3 films, and this is due to the stabilisation of the perovskite α-phase (See Section 2.6.1). This agrees with literature reports of greater thermodynamic stability in perovskite films engineered to be structurally closer to the ideal cubic phase. [141,184,191,314] Importantly, more rapid decline in characteristic length-scales of mesoscale scattering features in the film bulk as opposed to at the surface is observed, with the morphological degradation being accentuated at the grain periphery, leading to a decrease in average particle size. This supports the previously cited evidence that degradation proceeds in the bulk as opposed to at the surface of the film, and suggests that the grain decomposes cyclically as material at the periphery is exposed to moisture, eventually leading to fragmentation of the grain.

7.3   Results and Discussion

Perovskite samples are fabricated upon silicon substrates to investigate moisture induced decomposition in TOF-GISANS. MAPbI$_3$, $FA_{0.83}MA_{0.17}Pb(I_{0.83}Br_{0.17})_3$, $Cs_{0.05}(FA_{0.83}MA_{0.17})_{0.95}Pb(I_{0.84}Br_{0.16})_3$ and $FA_{0.83}Cs_{0.17}Pb(I_{0.83}Br_{0.17})_3$ perovskite samples are prepared for exposure to 90%rH for 8-10 hrs in the dark, allowing the comparison of FA vs combined FA and Cs substitution on the A-site. The fitting procedure, examples of fits of neutron scattering data, and particle size determination is described in Sections 5.1.4 and 5.1.5):

Sample	Acronym	Ratio of FA on A-site	Ratio of Cs on A-site
MAPbI$_3$	MAPbI$_3$	-	-
$FA_{0.83}MA_{0.17}Pb(I_{0.83}Br_{0.17})_3$	FAMAX	0.83	-
$FA_{0.83}Cs_{0.17}Pb(I_{0.83}Br_{0.17})_3$	FACsX	0.83	0.17
$Cs_{0.05}(FA_{0.83}MA_{0.17})_{0.95}Pb(I_{0.84}Br_{0.16})_3$	CsFAMAX	0.79	0.05

The raw GISANS at the selected incident wavelengths can be partitioned into vertical (out-of-plane) and horizontal (in-plane) components. Figure 50(a) shows neutron reflectometry-like specular reflectance from a vertical cut of scattering of an 8 Å incident beam. Figure 50(b) —a vertical cut of 3.8 Å incident beam— shows the degradation of MAPbI$_3$ during moisture exposure to PbI_2 (q ~0.016 Å^{-1}), MAPbI$_3$ heavy monohydrate (D_2O)
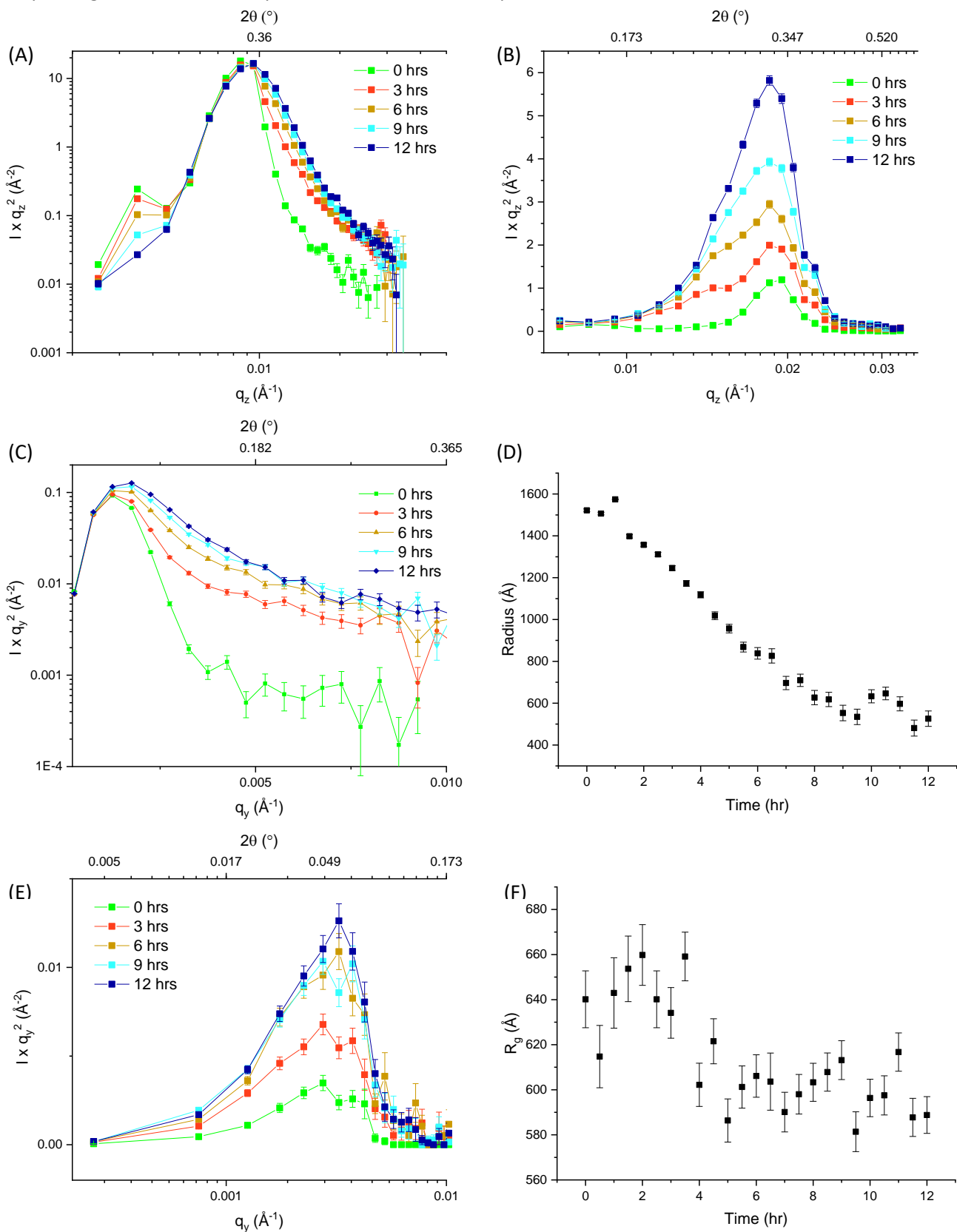
Figure 50: (A), (B),(C), E); Kratky Plots of MAPbI₃ films over the duration of 90%rH exposure. At '0' hours a 'dry' measurement of films was taken in an LiCl solution controlled atmosphere with rH~25%. (A): A vertical cut (out-of-plane integration) through a 2D image from scattering from an incidence neutron beam with λ of 8 Å (vertical cut 'at' 8 Å for shorthand) showing the diffuse reflection peak (Yoneda Peak), where the off-specular scattering peak coincides with the specular peak ($\theta_f = \theta_c$). (B) A vertical cut at 3.8 Å. (C) A horizontal cut at 8 Å. (D) The trend in radius based on the sphere model fit of particles based on scattering from a horizontal cut at 8 Å of MAPbI₃ during exposure to D₂O. (E) Horizontal cut at 3.8 Å. (F) Guinier model fit of particles based on scattering in E

Deciphering Perovskite Decomposition in a Humid Atmosphere with TOF-GISANS – Results and Discussion

and heavy dihydrate (0.015 Å^{-1} and 0.012 Å^{-1}) respectively. The film measured in a 25%rH atmosphere after fabrication in ambient conditions has a peak at q~0.019 Å^{-1}, showing MAPbI$_3$ at the surface rapidly exchanges H atoms for D even at low humidity. The dominant peak acquires a growing shoulder with increasing q-position as H atoms in MAPbI$_3$ are replaced by D. The shoulder shifts from q~0.021 Å^{-1} to q~0.023 Å^{-1} after 10 hrs implying full replacement of H with D in any remaining MAPbI$_3$. The q-shift associated with increasing deuteration for MAPbI$_3$ (and FAPbI$_3$) is shown in Figure 51.

The horizontal cut in Figure 50(c) at 8 Å shows the increasing scattering intensity over time due to decreasing average particle size (q increasing) and an increasing concentration of particles around a characteristic length scale, which changes over time as per Figure 50(d). The sphere model of particle size based on horizontal cut measurements as per Figure 50(c) over time show that the characteristic length-scale R decreases from ~1600 Å to ~500 Å (50 nm) over 12 hrs. This implies the typical distance between particles reducing as large grains fragment into smaller granules surrounded by fragments. Figure 50(e) depicts horizontal cuts at 3.8 Å showing the reducing particle size at the surface of the film (q shifts right), and the consolidation of particles in two size regimes around a shared mean after 12 hrs. Figure 50(f) uses a Guinier model to fit the measurements as per Figure 50(e) over time (See Methods Section 5.1.4).
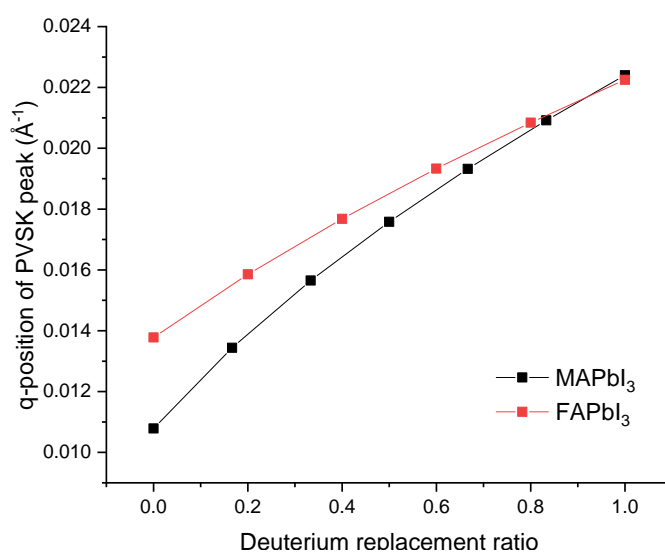
Figure 51: Modelled q-position of MAPbI$_3$ and FAPbI$_3$ peak as H atoms in the organic cation are displaced by Deuterium

Larger error bars are due to poorer sensitivity of this SANS experiment at these length-scales (10 s of nm). The scatter plot suggests a negative trend in particle size over time. The first hour sees an increase in particle size due to the uptake of moisture and formation of PbI$_2$ and mono-deuterated perovskites. Thereafter particle size decreases — perovskite degrades to the heavy dihydrate phase. Around 9 hrs a small peak above the background from Pb(OD)$_2$ (q = 0.028 Å^{-1}), and PbO (q = 0.024 Å^{-1}) is also seen. Contrasting Figure 50(f) and Figure 50(d), it appears that the characteristic length-scales (correlated with particle size) are diminishing more rapidly in the bulk than at the surface, which corroborates with previous findings by Chen *et al.* of moisture induced decomposition resulting first in the production of PbI$_2$ in the bulk of the film, and preservation of perovskite stoichiometry at the surface. [312]

The SEM images (Figure 52A vs B) of MAPbI$_3$ after 8 hrs exposure to moisture shows the degradation of the spherulitic particles into smaller crystallites, highlighted in Figure 52C. The histogram (Figure 52D) comparing the particle size distribution before (0 hrs) and after exposure to rH 90% (12 hrs) finds that hydration has the effect of both reducing the number of particles <10 μm and >70 μm in diameter. This is in agreement with the observation from Figure 50E of a narrowing of the particle size distribution. MAPbI$_3$ follows the degradation pathway identified by previous researchers, and it is noticeable that the formation of Pb(OH$_2$) and PbO after extended exposure is likewise indicated in this work.[165,167,232,315]
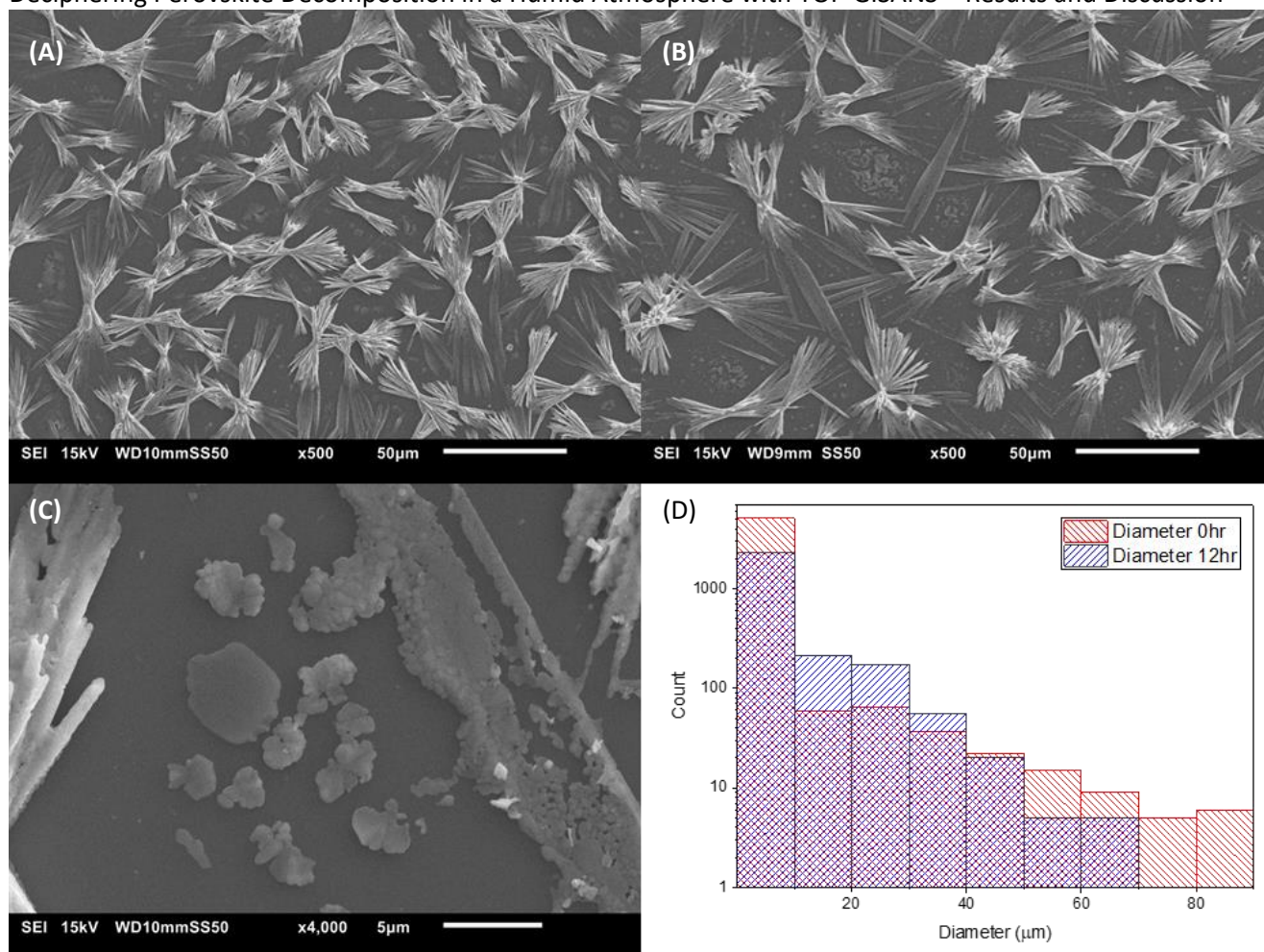
Figure 52: (A) SEM image at Mx500 after exposure to 25%rH. (B) SEM image at Mx500 after exposure to 90%rH for 8 hours. (C) SEM image at Mx2000 after 8hrs exposure to moisture. (D) Particle size distribution before and after (12hrs) hydration from SEM (MX500)

According to Figure 53(a), Initially the FAMAX film shows a peak centred on $q = 0.019$ Å^{-1}, which is a convolution of deuterated FAMAX ($q\sim0.017$ Å^{-1}) and PbBr$_2$ ($q\sim0.02$ Å^{-1}) (perovskite crystallite degradation produces a core-shell structure with degradation products— i.e. PbBr$_2$ — forming the outer layer around the perovskite centre). There is also a broad low-q shoulder centred on $q\sim0.014$ Å^{-1}, from FAPbI$_3$ (0.014 Å^{-1}) and a slight shoulder on the right. This shows poor homogeneity of the film stoichiometry post-annealing. The high-q shoulder at $q\sim0.022$ Å^{-1} grows after 2 hrs, coinciding with deuterated FAMAX ($q\sim0.023$ Å^{-1}), deuterated FAPbBr$_3$ ($q\sim0.023$ Å^{-1}), and deuterated FAPbI$_3$ ($q\sim0.022$ Å^{-1}). After 2 hrs, the low-q shoulder has also sharpened into a second defined peak, likely due to increased production of PbI$_2$ ($q\sim0.016$ Å^{-1}). At 4hrs a peak at $q\sim0.019$ Å^{-1} is produced as well, which coincides with PbBr$_2$ and FAPbBr$_3$ mono-heavy-hydrate. After 10 hrs the low-q peak centre has increased in height and shifted to higher q, likely due to degradation of FAMAX to PbI$_2$ and FAPbI$_3$. It is likely the broadening of the high q peak is also due to deuteration of the FAPbI$_3$ degradation product to deuterated FAPbI$_3$, and formation of FAPbI$_3$ and MAPbBr$_3$ mono-heavy-hydrates ($q\sim0.017$ Å^{-1}). There is no strong contribution from MAPbI$_3$ ($q\sim0.011$ Å^{-1}) although a decrease in q-position of the right peak centre indicates formation of MAPbBr$_3$ ($q\sim0.013$ Å^{-1}) or FAPbBr$_3$ ($q\sim0.015$ Å^{-1}). It has previously been shown that MAPbBr$_3$ is significantly more stable than MAPbI$_3$, so the evidence may be showing loss of MAI from MAPbI$_3$ to form PbI$_2$ whereas MAPbBr$_3$ is retained or converted to deuterated and hydrated by-products.[316] After 10 hrs, small peaks emerge above the background at $q\sim0.28$ Å^{-1} and $q\sim0.24$ Å^{-1}, due to production of PbOH$_2$ and PbO.

The horizontal cut at 8 Å (Figure 53B) shows the scattering peak shifts to high q and decreases slightly in intensity. This suggests decreasing particle size and also reducing crystalline order. This is supported by Figure 53C: a sphere model of the scattering as per Figure 53B, with the characteristic length-scale (radius on the y-axis) decreasing steeply over the course of the experiment. If SEM images in Figure 53(D-E) before and after 8hrs exposure to moisture are compared, it can be observed there is significant deterioration of the initially defined

grains to a mixture of rounded, smaller grains similar to the core structures at the centre of the larger initial grains, and smaller crystallites occupying the space between. Comparing the distribution of particle sizes in Figure 53F, the absence of grains above 30 μm after moisture exposure becomes apparent, in contrast to the broad spread prior with some grains larger than 100 μm.
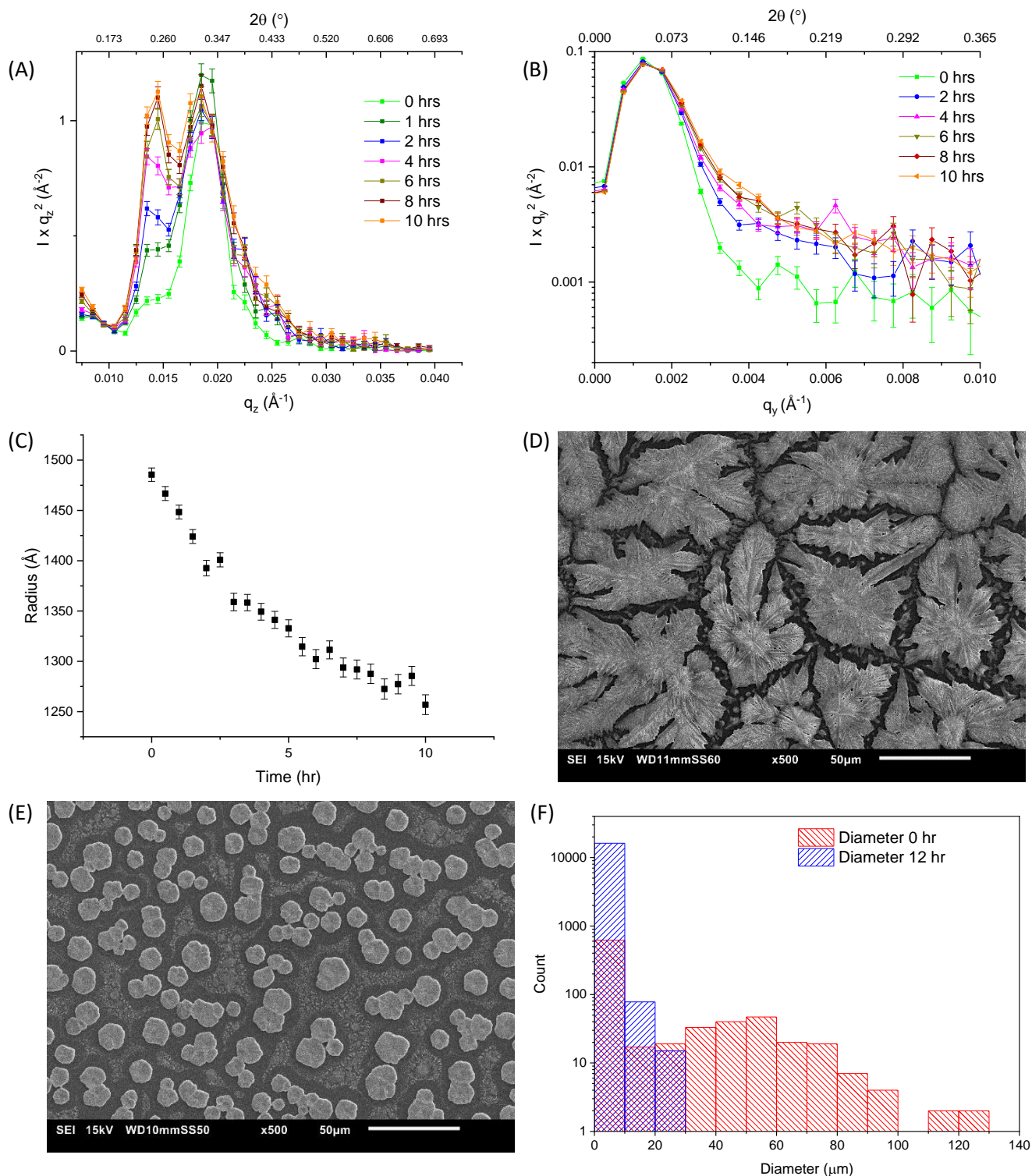
Figure 53: (A), (B) Kratky plots of FAMAX films over time at 90%rH. (A) A Vertical Cut at 3.8 Å showing the degradation of FAMA. (B) A horizontal cut at 8 Å showing small rightwards peak shift. (C) A sphere model of the particles as per the scattering from B. (D) SEM images of FAMAX film before and (E) after (8hrs) exposure to moisture. (F) Particle size distribution before and after (12hrs) hydration from SEM (MX500).
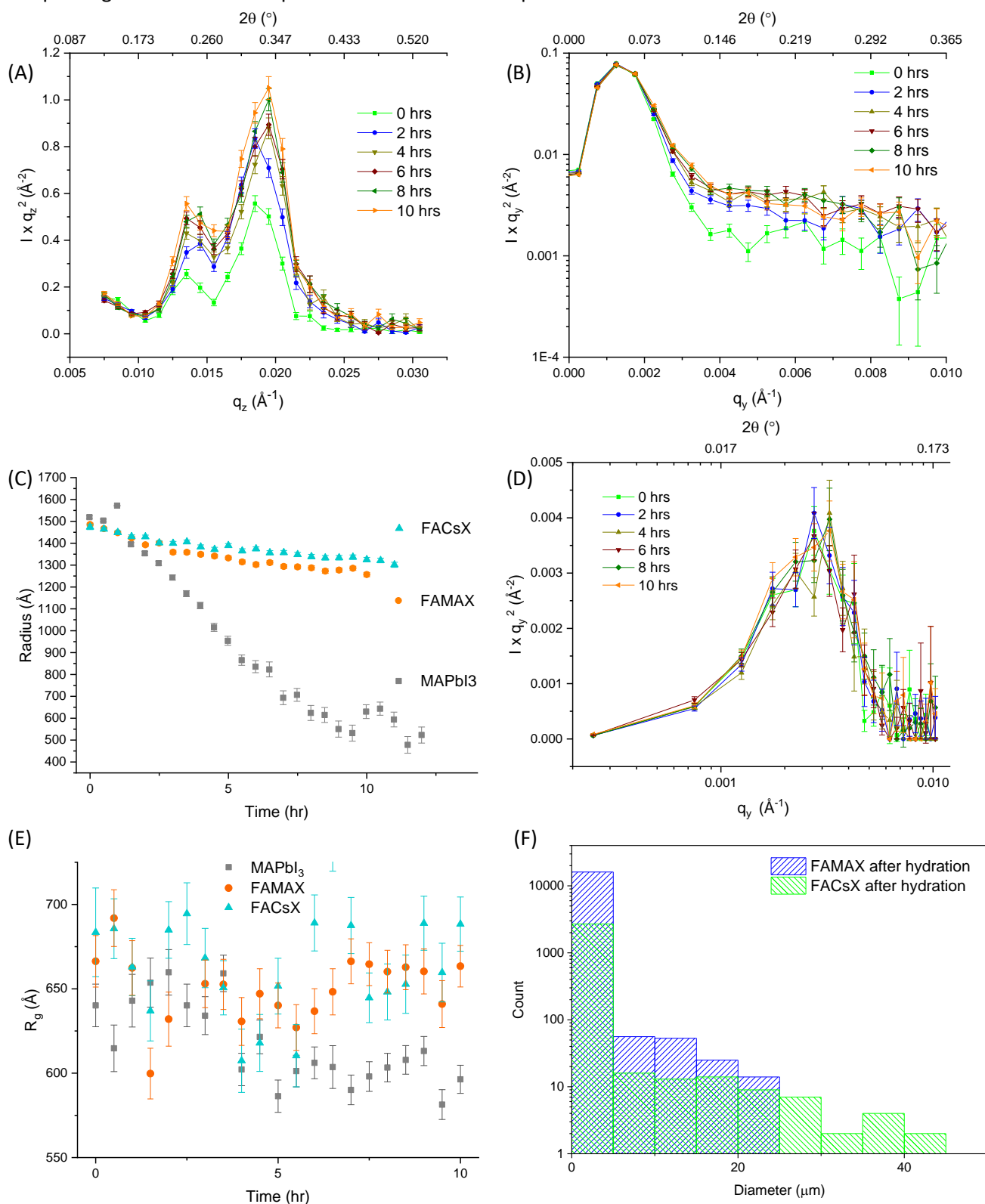
Figure 54: A, B, D; Kratky Plots of FACsX; (A) A vertical cut at 3.8 Å showing degradation of FACsX over 10 hrs. (B) A horizontal cut at 8 Å showing a slight increase in scattering around q = 0.003. (C) Sphere model fits of horizontal cut scattering as per B, showing decrease in characteristic radius for MAPbI₃, FAMAX, and FACsX. (D) Horizontal cut at 3.8 Å. (E) Guinier model fits of horizontal cut scattering comparing MAPbI₃, FAMAX and FACsX (F) Particle Size distribution between FAMAX and FACsX after hydration from SEM (MX500).

At 0 hrs in Figure 54A of FACsX vertically integrated scattering at 3.8 Å, there are two prominent peaks—the low-q peak arises from FAPbI₃, at $q \sim 0.014$ Å⁻¹, while the high-q peak from deuterated FACsX at $q \sim 0.019$ Å⁻¹. There is also a small shoulder around $q \sim 0.023$ Å⁻¹, which arises from deuterated FAPbX₃ and FACsX₃. Due to the overlap in q-position of the deuterated perovskite peaks, it is difficult to resolve which contribution dominates. This once

Deciphering Perovskite Decomposition in a Humid Atmosphere with TOF-GISANS – Results and Discussion again exposes poor stoichiometric heterogeneity through the bulk of the film after film formation in ambient conditions. After 8 hrs, a peak at $q\sim0.014$ Å^{-1} becomes visible, which corresponds with FAPbI$_3$ but also the previously identified CsPb$_2$I$_4$Br. ($q\sim0.014$ Å^{-1}) in degrading Cs$_{0.05}$FA$_{0.83}$MA$_{0.17}$Pb(I$_{0.83}$Br$_{0.17}$)$_3$.[199] There is also increased scattering intensity peaking at $q\sim0.0195$ Å^{-1}, which may relate to PbBr$_2$ production ($q\sim0.02$ Å^{-1}). There is a small peak at $q\sim0.029$ Å^{-1}, which relates to PbOD$_2$. After 10 hrs, the valley between the two peaks has risen, reducing the prominence of the peaks. This indicates production of PbI$_2$ ($q\sim0.016$ Å^{-1}). The shift of the low-q peak to lower q implicates the degradation of FACsX to FAPbI$_3$. The broad high-q peak is the result of addition of deuterated FACsX, FAPbI$_3$ and FAPbBr$_3$ perovskite, as well as their respective monohydrates resulting in the much larger peak intensity after hydration.

In Figure 54B, a horizontal cut at 8 Å shows very slight scattering increase at higher q (~0.03 Å^{-1}) over time, suggesting decreasing particle size. The sphere model fit of the data in Figure 54C as per scattering in Figure 54B shows this relates to a decrease in the characteristic radius, decreasing by ~150 Å. As the figure shows, this is an improvement over both compositions containing MAI. Taking a horizontal cut at 3.8 Å (Figure 54D) shows less variation at the surface of the film. Modelling this scattering using a Guinier model shows a fluctuation in characteristic length-scales, though the error bars amount to little confidence in a trend beyond fairly constant radius of gyration(r_g). The consistency of this characteristic length-scale at the surface compared to deeper in the film may also tie-in with the observation as per MAPbI$_3$ of bulk concentrated degradation as moisture percolates through GBs and surfaces into the core of the film and degrades perovskite to PbI$_2$ and deuterated/hydrated phases. Morphology shown in the SEM image in Figure 55 show the film has undergone similar decomposition to the FAMAX film, with two size regimes; grains between 10-50 μm and granules on the scale of 100 s of nm-5 μm. Degradation is less pronounced, with the particle distribution histogram Figure 54D comparing particles in FACsX and FAMAX after moisture exposure for 8 hrs showing larger grains present, and fewer grains < 5 μm.
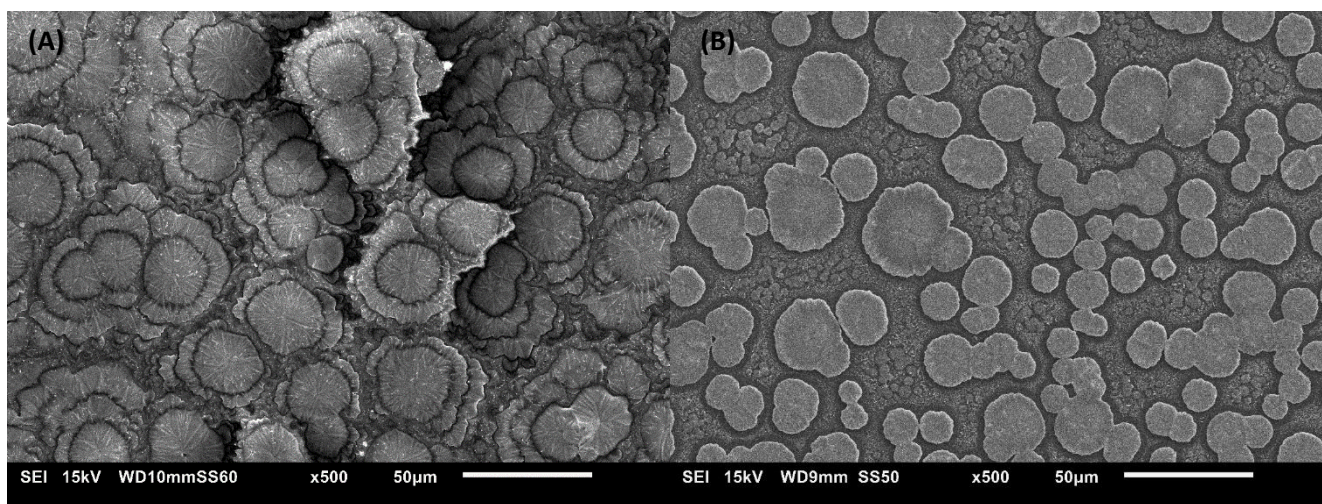
Figure 55: SEM images of FACsX (A) before and (B) after hydration (Mx500).

In Figure 56A, the broad deuterated CsFAMAX peak ($q\sim0.017$ Å^{-1}) initially centred on $q\sim0.0165$ Å^{-1} shifts to high-q and downwards to ~0.0175 Å^{-1} which indicates the increasing deuteration of organic cations in the perovskite. The slight shoulder at $q\sim0.023$ Å^{-1} suggests formation of deuterated FA based perovskite. Overall this film is distinguished by remarkably little phase segregation over the course of the measurements relative to other films, with a lack of segregation into two peaks. This is in agreement with other research showing the enhanced moisture stability of this mixed A-site cation perovskite.[184,317]

Figure 56B of a 3.8 Å horizontal cut of CsFAMA shows moisture exposure decreases the particle size of some surface features, with increased intensity at $q\sim0.045$ Å^{-1}. After 3 hrs, particle size degradation is expressed as two shoulders at $q\sim0.018$ Å^{-1} and 0.04 Å^{-1} indicating multiple size regimes. After 9 hrs, the average particle size has decreased, although there are still two distinct size regimes. Figure 56C shows there is a rapid decrease in the characteristic length-scale r_g over the first half hour. The rate of change decreases between 30 minutes and 2 hrs, at which point r_g increases, possibly due to moisture assisted reorientation of GBs and consolidation of smaller particles. The intensity of scattering from the peak reduces, suggesting reduced structural order. It is

Deciphering Perovskite Decomposition in a Humid Atmosphere with TOF-GISANS – Results and Discussion
unclear why there is an initial decrease in intensity between 1-2 hrs, followed by an increase at 3 hrs, and a final decrease by 9hrs. It is possible the initial decrease in r_g is followed by moisture facilitated grain growth between
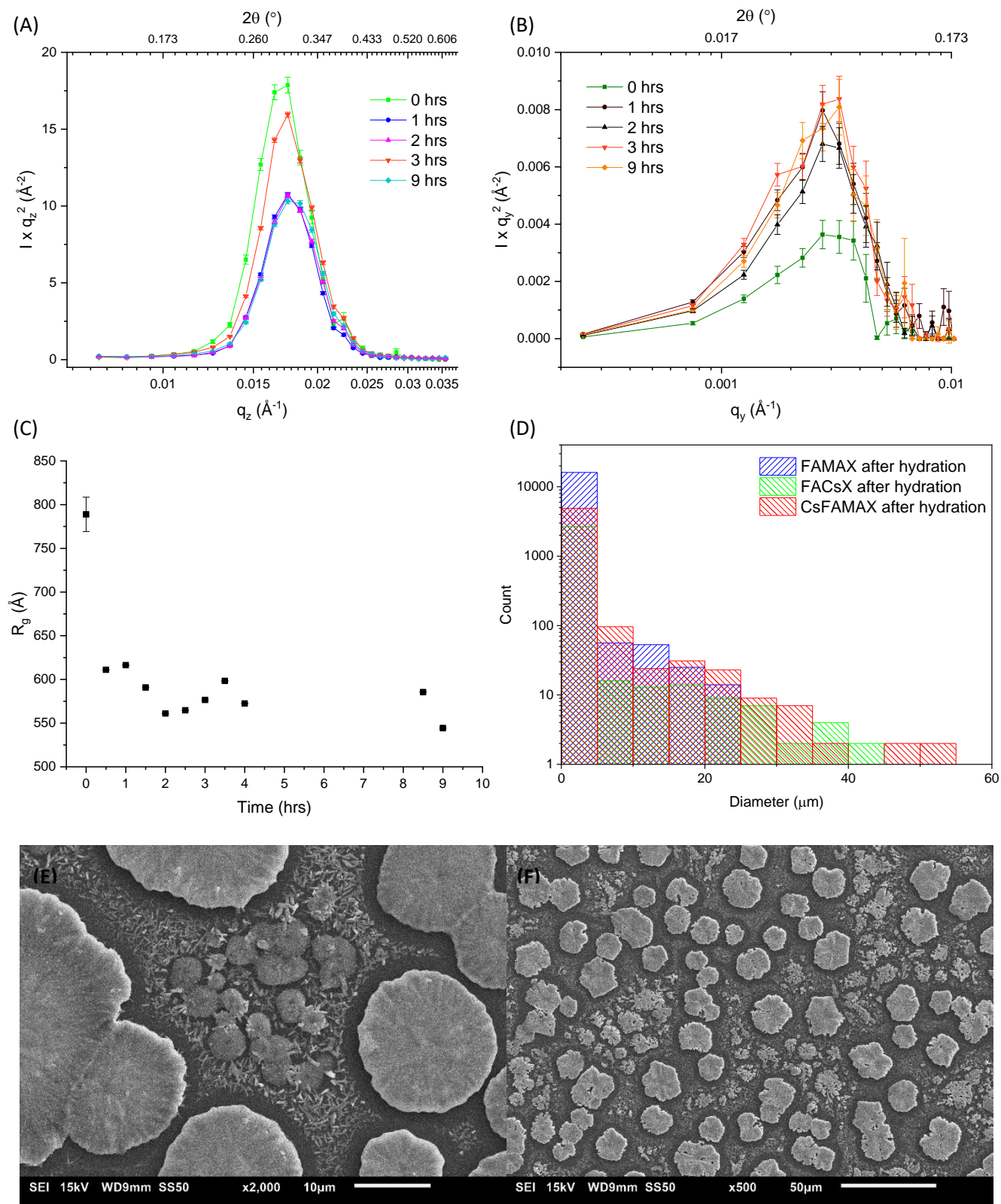
Figure 56:)A), (B); Kratky Plots of CsFAMAX; Temporal data incomplete due to issues in data acquisition. (A) Vertical cut at 3.8 Å showing shift of peak centre to higher q and lower intensity. (B) Horizontal Cut at 3.8 Å of CsFAMAX showing increasing scattering intensity from the lateral features at the surface. (C) Guinier model fit of horizontal scattering cut at 3.8 Å as per B, showing steep initial drop off in characteristic length-scale r_g at the surface. (D) Particle size distribution after hydration from SEM (MX500). (E,F) SEM images at Mx2000 and Mx500 of CsFAMAX after 8 hrs hydration.

2-3 hrs, increasing average particle size and hence r_g. After deuteration particles sizes follow a normal logarithmic distribution as shown in the histogram in Figure 56D. Comparison of SEM before (Figure 56E) and after (Figure 56F) hydration shows that average particle size reduces by approximately 50%. While grains which do not degrade do not show much change in size, those which do decompose to crystallite clusters orders of magnitude smaller. Across all three A-site alloyed samples, moisture induced degradation results in decreasing average particle size as perovskite grains swell and fragment from the grain periphery moving inwards.

In the datasets as the angular range increases above q = 0.02-0.03 Å^{-1}, diffraction features come to dominate the scattering pattern. Error bars become larger due to low flux and hence these peaks become less reliable. This is exacerbated for cuts through scattering from an incident beam of 3.8 Å (3.8-4.2 Å wave-band) due to the lower scattering volume in this geometry (sampling along the surface). These could be corroborated with dedicated wide-angle neutron scattering experiment or neutron diffraction. The similar values for θ_c of several phases — particularly the deuterated perovskites — also makes it difficult to differentiate between them, and this would be further motivation to compliment this work with further neutron diffraction experiments.

7.4   Conclusion

The high relative humidity of 90% may not be representative of typical operating conditions for these perovskite films when encapsulated in modules, but this experiment can be seen as a greatly accelerated simulation of the degradation processes which gradually occur over longer timescales. Average relative humidity ranges can readily reach 90% in a country with similar climate to the UK. In this work it is show that at 90%rH in the dark degradation of mixed A-site cation perovskite films proceeds through a process of degradation from the grain peripheries inwards. Characteristic scattering lengths (r_g) derived from scattering originating at the film surface shows no clear trend in FA containing samples. In contrast characteristic scattering lengths derived from scattering originating deeper in the film shows a negative trend over time. This may support theories that degradation is initiated in the bulk. Moisture first adsorbs to the film along GBs before permeating inside the grains and beginning a gradual process of decomposition from the outside in. Across all films evidence is found for the formation of deuterated degradation products, although reduction of the Methylammonium component and substitution with Cs is particularly beneficial for moisture resistance, ensuring the preservation of larger grains, reduced perovskite phase segregation and reduced production of photo-inactive lead halide species.

For the first time, evidenced indicative of the formation of FA and mixed- perovskite hydrates is found, which will be useful for continuing efforts to develop a mechanistic understanding of moisture induced degradation in FA –based perovskites. Overall, it is reiterated that it is important to develop methods of mitigating degradation of the photoactive component of solar cells. Improving our understanding of how they fail will help us develop strategies to prevent this or slow it down, using additives, interfacial layers or better processing and synthesis. Our experiment demonstrates that multi-cation, multi-halide alloying of perovskites is an effective way of reducing the segregation of mixed perovskites into their component crystals. However morphological degradation leading to discontinuous smaller grains and larger GB area is still observed under high humidity, and developing effective methods of reducing GB mobility, moisture ingress, and hydrophilicity are sorely needed. TOF-GISANS is demonstrated as a potent and vital technique in the arsenal of material scientists seeking to characterise compounds containing organic moieties and understanding moisture induced degradation.

8 The Limited Benefits of ZnCl$_2$ as a Stabilizing Additive for Perovskite Films

8.1 Abstract

ZnCl$_2$ has been proposed as an effective additive for improving the structural stability and photovoltaic performance of perovskite films.[35,318,319] Zn compounds can be strongly hygroscopic, forming hydrated complexes which may introduce a new avenue for decomposition of the perovskite film following moisture exposure. We hypothesize that moisture stability of Zn-incorporating perovskite films, occurs at the expense of non-perovskite phase formation. It is found that ambient storage of MA$_{.97}$Cs$_{0.03}$Pb$_{0.97}$Zn$_{0.03}$(I$_{0.97}$Cl$_{0.03}$)$_3$ films is associated with reduced degradation relative to methylammonium lead iodide (MAPbI$_3$), but whole devices degrade faster than devices, likely due to reactive interactions of the materials present at the perovskite hole transport layer (HTL) interface. The prevalence of ZnO and Zn(OH)$_2$ is associated with greater hysteresis and reduced PCE relative to MAPbI$_3$ devices after fabrication in ambient conditions. It is found that ZnCl$_2$ + CsI addition led to more rapid and extensive thermal degradation of films upon heating ≥ 80°C, due to larger film strain resulting from secondary phases (metal halides/oxides/carbonates) favourably forming at the film surface, as well as the facile reaction of Zn compounds with moisture. Strain and the facile Zn-H$_2$O reaction destabilizes the perovskite lattice, facilitating the ingress of H$_2$O and O$_2$ and hastening degradation.

8.2 Introduction

Perovskite solar cells (PSCs) have seen considerable research interest because of the remarkable performance they can achieve even when made by facile solution processing. They are desirable due to their excellent optoelectronic characteristics, including strong absorption, high charge carrier lifetime, high defect tolerance, tunability, and light-weight. Hybrid organic-inorganic perovskite solar cells have a combination of organic and inorganic ions on the A-site of the ABX$_3$ perovskite crystal structure. The B-site is most commonly occupied by divalent Pb^{2+} cations as they are more stable than alternatives such as Sn^{2+}, and produce more efficient devices. Reasons for this have been detailed elsewhere, but it is chiefly due to the facile oxidation of Sn^{4+} to Sn^{2+}.[320,321] Substitution of Pb with Zn has attracted attention due to improved PSC PCE and PCE retention over time. Reasons for this are discussed in Section 2.1.

Table 8 (Appendix 13.6) summarises studies investigating Zn incorporation in the perovskite film from various sources. Zheng *et al.* suggest greater moisture resistance and enhanced thermal resistance of devices fabricated with 3% doping with ZnI$_2$.[338] Zn incorporation has been shown to increase the relative PCE versus unaltered samples by as much as 33% by Chen *et al.* and Klug *et al.*, while the current record amongst Zn-incorporating devices is 20.06% (12% improvement on pure devices), given by Shai *et al.*.[322,324,336] The researchers suggest the Zn is incorporated through B-site substitution for Pb^{2+} ions, though the evidence for this is inconclusive. Multiple authors purport optimum percentages of Zn^{2+} substitution between 2%-6%, and this is likely due to the different solvents, additives, or varieties of Zn based precursors used in their various fabrication methods. Kooijman *et al.* suggest an optimum around 2.5% for the use of Zn as an additive based on a review of the evidence — particularly for FA/MA materials.[319] 2.5% Zn substitution strikes an optimum between improvement of optoelectronic properties and minimizing structural distortion.[333,325]

The damp heat conditions from the International standards for assessing the long term stability of perovskite solar cells suggest conditions of 85°C and 85%rH should be the standards for testing.[339] Solar cells can regularly reach these conditions in typical installation environments with high solar potential around the equator and seasonally at higher latitudes during the summer. Devices made with perovskite films incorporating Zn as per Table 8 have not been tested under the combined influence of both humidity and UV-light. Under these conditions the films are exposed to greater external stressors, with H$_2$O accelerating the degradation of perovskite into secondary phases under illumination in the presence of O$_2$.[175]

In this work, the thermal and moisture induced degradation of films substituted with 3mol% Zn, Cs and Cl on the A, B and X sites respectively is investigated using wide angle X-ray scattering, X-ray photoelectron spectroscopy, UV-Vis spectroscopy, ellipsometry, and scanning electron microscopy after exposure to elevated heat (40-100°C) and humidity (85%rH). Cl addition in general improves perovskite film quality by improving crystallinity, increased grain size, and increasing charge carrier lifetime.[340,341] MACl gas evolves from MAPbI$_3$

films during annealing, and the subsequent reaction of this gas with perovskite at surfaces enhances crystalline quality and grain size.[96,269,342,343] So while Cl is added as a counter-ion for Zn, it brings benefits to film formation as well. Cs addition improves thermal, optical, and moisture stability, suppressing ion migration, moisture induced phase segregation and improving carrier diffusion length.[184,198,199,311,344] This is largely due to the increased strength of the interaction between the organic cations and iodide due to lattice contraction of the cubo-octahedral volume.

Thin films and devices were fabricated under ambient conditions and then their ambient stability was tested. Zn-substitution in combination with Cs was found to increase moisture resistance at 85%rH. However, the devices had reduced thermal stability of the perovskite phase at temperatures >80°C relative to MAPbI$_3$ and when both high humidity and elevated temperatures are combined the films showed significant degradation without encapsulation. The devices show increased hysteresis and a decrease in efficiency over 120 hrs of ambient exposure. This decrease in PCE was not as large as the decrease in control MAPbI$_3$ devices. This improved resilience to ambient degradation is attributed to the facile reaction of Zn with moisture and oxygen, but this facile reaction is also considered to be the cause of the reduced thermal stability in the presence of moisture and/or oxygen.

8.3   Results

8.3.1   Scanning Electron Microscopy

Scanning Electron Microscopy of the MAPbI$_3$ and MA$_{.97}$Cs$_{0.03}$Pb$_{0.97}$Zn$_{0.03}$(I$_{0.97}$Cl$_{0.03}$)$_3$ (referring to the mixture of precursors as prepared in the perovskite solution prior to deposition, and hereafter referred to as 'MACsPbZn(ICl)$_3$') films prepared in ambient conditions (52±3%rH) are shown in

Figure 57. Both solutions were stirred for 2 days at 60°C before use — stirring for >40hrs has been shown to give higher performing perovskite devices due to improved crystallinity and grain growth.[345] Both films were prepared using the antisolvent induced crystallisation method, with a gradual conversion from the sol-gel to the solvent-intermediate through to the brown and then black perovskite phase. While the MAPbI$_3$ film shows evidence of some excess PbI$_2$ nucleated on the surface (the bright particles), as well as in grains with PbI$_2$ enrichment, the MACsPbZn(ICl)$_3$ films substituted with a combination of CsI and ZnCl$_2$ show more homogenous microstructure, larger grains, and suppressed formation of PbI$_2$ crystallites, confirming reports by others.[324] It may be expected that the MACsPbZn(ICl)$_3$ films have improved structural stability compared to the MAPbI$_3$ films (which show evidence of a non-stoichiometric reaction due to ambient processing, and therefore a higher susceptibility to moisture induced decomposition due to reaction of under-coordinated MAI with H$_2$O). The Goldschmidt tolerance factor (See Equation 1) for the MACsPbZn(ICl)$_3$ film (t=0.925) is barely higher than for MAPbI$_3$ (t=0.924). The octahedral factors are also very similar (rounded to 3 s.f.: MACsPbZn(ICl)$_3$; 0.537, MAPbI$_3$; 0.541) for both materials.[346] This suggests only a minimal improvement in stability may arise from the lattice approaching the cubic ideal. Instead, the observed stability improvements may arise from either differences in reactivity between Zn^{2+} and Pb^{2+}, or differences in lattice strain due to the presence of secondary phases stabilising the perovskite phase.
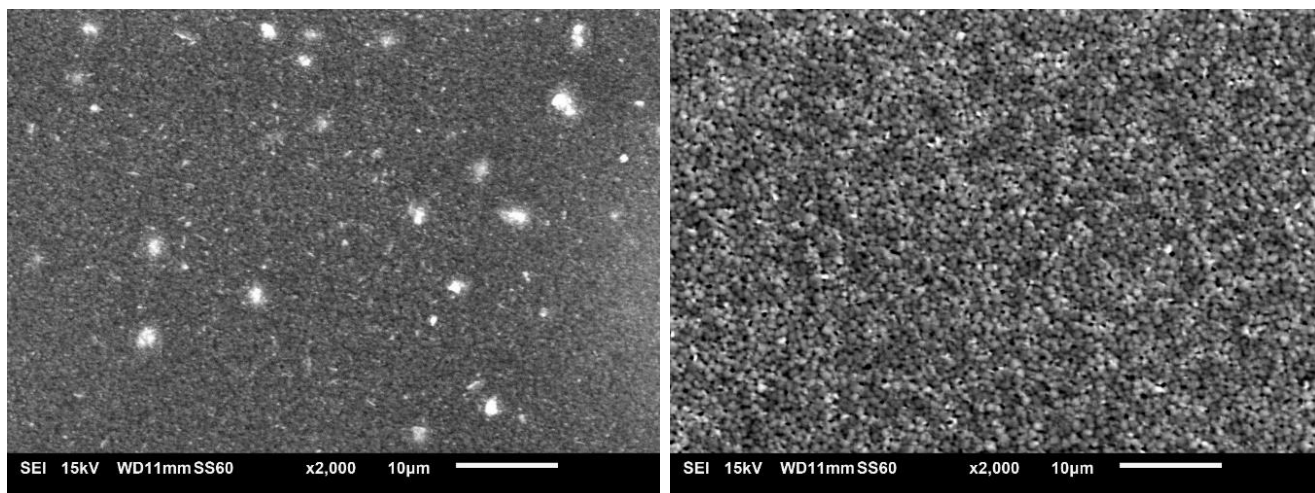
Figure 57: SEM of MAPbI$_3$ (A) vs MACsPbZn(ICl)$_3$ (B) films prepared in all-ambient conditions and annealed at 100°C.

After heating these samples at different annealing temperatures for 8 hrs, significant differences as a function of temperature are observed, shown in Figure 77 in Appendix (Section 13.6). While to the eye the MACsPbZn(ICl)$_3$ film shows little visual macroscopic change from annealing at 40°C between 4hrs and 8hrs, upon raising the temperature > 60°C, the film begins to get microscopically rougher, and a secondary phase makes an appearance. After 8 hr at 100°C, a hexagonal crystallite is observed throughout the film. This hexagonal phase is not observed in MAPbI$_3$ films annealed under the same conditions (shown in Figure 78, Section 13.6) indicating this is due to the presence of the additives influencing the crystallisation of this phase. MAPbI$_3$ films do show evidence of a secondary phase with rod-shaped crystallites forming after annealing at 80°C for 8 hrs or at 100°C after 4hrs. They also show an increasing density of pinholes, suggesting the loss of volatile components such as MAI, trapped moisture, and solvent.

The α-perovskite formation reaction typically occurs between 60-65°C, whereas degradation to PbI$_2$ under ambient conditions will typically proceed in MAPbI$_3$ at room temperature in the presence of oxygen or moisture.[347,193,348] Meanwhile ZnCl$_2$ readily captures moisture in its environment as it is highly hygroscopic.[349,350] It is assumed that perovskite films exposed to ambient air will first adsorb moisture on the surface, and this moisture will slowly diffuse along grain boundaries and into the bulk of the film. Moisture induced degradation proceeds from the grain boundary region inwards, with the grain boundary being the last region to fully convert to PbI$_2$.[172,311] As the temperature increases, H$_2$O will diffuse more rapidly into grains. Ab-initio computational techniques suggest H$_2$O then catalyses the degradation of perovskite by stabilising the superoxide species (O$_2$-), decomposing MAPbI$_3$ into PbI$_2$ and mobile or volatile MA+.[176,351] The concentration of PbI$_2$ increases more rapidly at the surface of the thin film relative to the bulk due to the greater availability of H$_2$O. This layer then acts to limit the ingress of further H$_2$O to and from (self-generation of H$_2$O results from MAI reaction with O$_2$-) the bulk, slowing down degradation, as has been shown by Liao et $al.$.[171,177]

Degradation of MACsPbZn(ICl)$_3$ perovskite incorporating ZnCl$_2$ will produce ZnI$_2$ and ZnCl$_2$, which are both very hygroscopic. A single Zn halide unit can form stable hydrates with many more waters than PbI$_2$ (ZnCl$_2$(H$_2$O)$_n$ can react with n = 1, 1.5, 2.5, 3 and 4).[350] Zn halides will slow down the decomposition of the perovskite phase and the reaction of PbI$_2$ with H$_2$O by competing to react with both internally generated H$_2$O and adsorbed H$_2$O. Zn also reacts with O$_2$- ions to form ZnO, which may also slow down the decomposition of the perovskite phase. The formation energy of PbI$_2$ is less exothermic (-175.5 kJ/mol) than PbO (-188.9 kJ/mol), Pb(OH)$_2$ (-452.2 kJ/mol), ZnO (-318.2 kJ/mol) or ZnOH$_2$ (-642 kJ/mol); as such Zn readily reacts with water under standard conditions.[352] ZnO crystals may form in a dry atmosphere after prolonged heating due to loss of H$_2$O. These crystals have the same space group (P63mc) as PbI$_2$. The thermal decomposition of Zn(OH)$_2$ and ZnX hydroxides proceeds between 90 and 100°C+, with the loss of H$_2$O; hence the yield of ZnO can be increased during heating in a humid atmosphere by the facile reaction to form Zn hydroxides being followed by loss of H$_2$O. The preferential formation of Zn compounds may diminish the formation of PbI$_2$ over the same period by outcompeting Pb to coordinate H$_2$O and O$_2$. This slows down the degradation of the perovskite layer, but as suggested by SEM and UV-VIS, increases surface roughness, and optical scattering.

8.3.2   Wide Angle X-ray Diffraction:

WAXS from the perovskite films was used to investigate the structure and composition of the films after exposure to various heating regimes, 85% relative humidity (rH) and ambient humidity and light. 1D diffractograms were plotted and analysed using a combination of DAWN and GSAS II.[353,354] MAPbI$_3$ films were compared to films with just ZnCl$_2$, and films with both ZnCl$_2$ and CsI. 'Pristine' (measured immediately after fabrication) MACsPbZn(ICl)$_3$ films were compared to MACsPbZn(ICl)$_3$ films exposed to different conditions for 5 days: 'Ambient', meaning exposed to ambient air and light; 'Wet', meaning exposed to 85%rH and 'Aged' in ambient air and light at 85°C. Films were measured under 'Wet' and 'Ambient' conditions to discern the effect of moisture on films in the absence of and in the presence of light respectively. Ambient humidity was between 50-60%rH.

Using GSAS II, the miller indices and cell parameters of the perovskite peaks in the diffractograms of MAPbI$_3$, MAPbZnICl$_3$, and MACsPbZn(ICl)$_3$ ('Pristine', 'Ambient', 'Aged') were determined, allowing comparison of the

space groups of perovskite crystal films.[354] By indexing peaks in the diffractograms and performing a peak refinement with various predicted Bravais lattices, the Bravais lattice and space group of the perovskite crystallites can be assigned by inspecting the best-matching indexing results. $ZnCl_2$ films were included in the comparison to compare the addition of $ZnCl_2$ alone to both $ZnCl_2$ and CsI. If perovskite $MAPbI_3$ films are contrasted to films with a 3mol% substitution of $ZnCl_2$, it can be observed that addition of $ZnCl_2$ changes the crystal structure from cubic Im3m to an Imcm, squashed tetragonal structure, shown in Figure 58A. Despite the small size of the Zn additive, there is a strain-induced change to the lattice, possibly due to the occurrence of Zn based secondary phases. Addition of both $ZnCl_2$ and CsI, produces a lattice contraction, with a shift of the primary perovskite peak to higher q (Figure 58A). This suggests addition of both elements results in reduced lattice parameters — which is expected if the smaller Cs^+ and Zn^{2+} cations are integrated within the perovskite structure on the A and B sites respectively. As the $MACsPbZn(ICl)_3$ degrades (e.g. due to ambient exposure over 5 days at 85 °C) the position of the perovskite peak shifts closer to that of the pure $MAPbI_3$ film, the Ambient and Aged samples in Figure 58A are very close to the Pristine $MAPbI_3$ data. The loss of the substituting cations to Zn and Pb secondary phases can explain this result.

There is a depth dependence to the lattice shift as well. At the surface, the perovskite lattice (110) peak is shifted to lower q – indicating the lattice is expanded. There is also a tensile strain gradient reaching a maximum at 0.5° incident angle. The surface is also under tension relative to the bulk — and this can be linked to the presence of secondary phases which produced the strongest scattering at 0.1° incident angle. As Figure 58B shows, the scattering intensity of the ZnO phase remains roughly constant between the Pristine and Ambient exposed samples, although after ambient exposure there is more scattering at the very surface of the film. The position of the ZnO peak in Figure 58C also shifts to higher q after exposure within the first 0-0.2° of penetration, suggesting lattice contraction. The PbI_2 phase increases in intensity throughout the interrogated depth, reaching a maximum at 0.1° and 0.5°, after ambient exposure. The q-position of the PbI_2 peak is slightly lower at the surface under ambient conditions, again suggesting strain in the film. Scattering intensity of $Zn(OH)_2$ increases following ambient exposure throughout the measured area. It's q-position follows the same trend through the depth of the film under both conditions. From these observations it is theorised that the degradation of perovskite at the surface, producing Zn and Pb secondary phases exerts a tensile strain on the lattice. Meanwhile, thermal expansion coefficient mismatch between the substrate and perovskite film during thermal annealing leads to in-plane tensile strain.[160,355] The lattice strain reduces the activation energy for ion migration, accelerating perovskite decomposition.
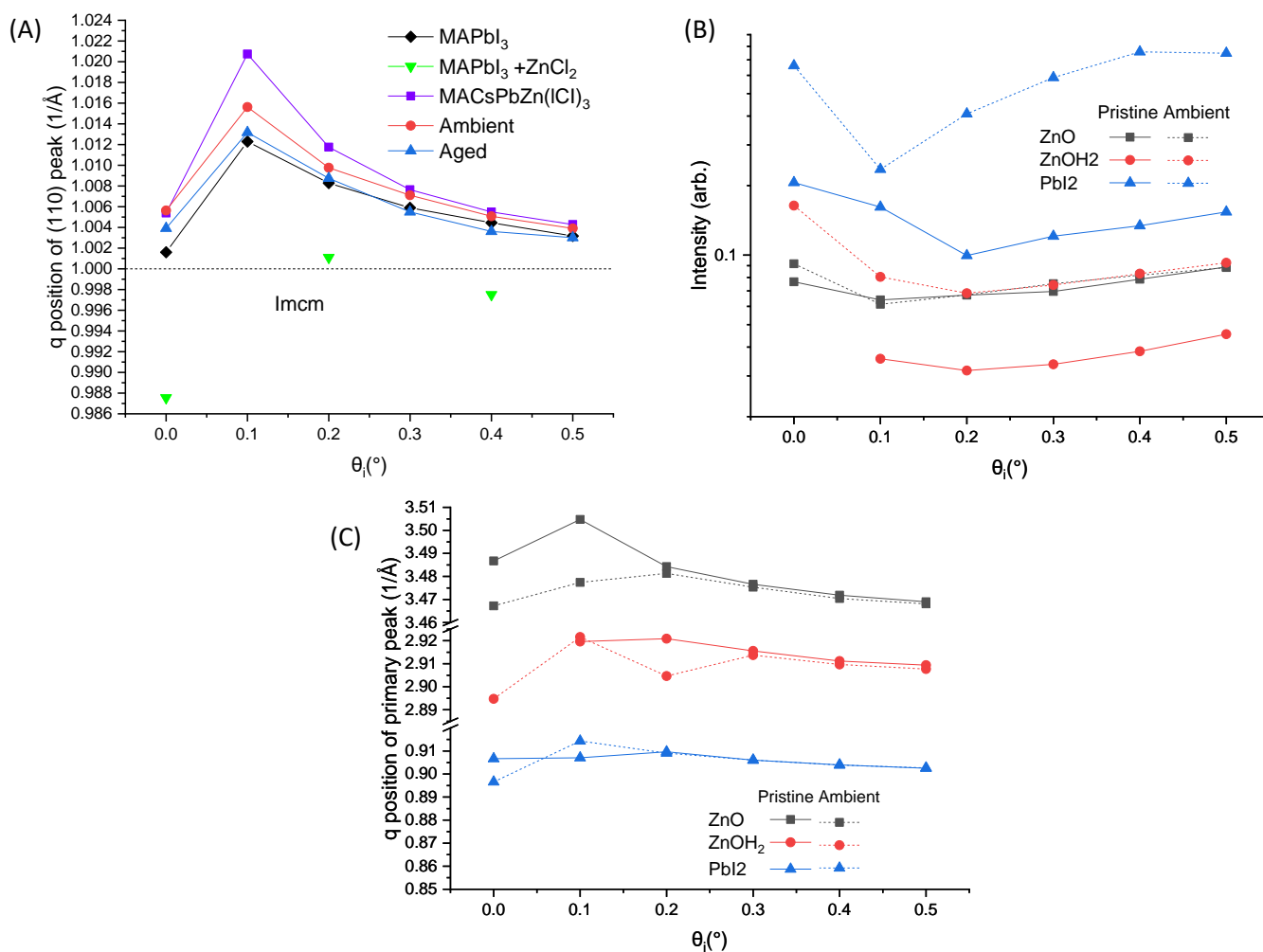
Figure 58: (A) q-position of (110) perovskite peak as a function of incident beam angle for different perovskite film samples. Above the dotted line the crystal structure takes the Im3m structure while below it is Imcm, as per the sample containing only ZnCl$_2$. (B) Intensity and (C) q-position of highest intensity secondary phase peaks in Pristine and Ambient exposed MACsPbZn(ICl)$_3$ films as a function of incident beam angle (Identification of crystal structures and phases is described in the experimental section).

The Pristine film in Figure 59Figure 59: (A) XRD spectra of MACsPbZn(ICl)$_3$ perovskite in Pristine condition, cast from a non-filtered solution. (B) WAXS spectra between q = 2.85 and q = 3.95 Å^{-1}, comparing phases present in Pristine MACsPbZn(ICl)$_3$ film, and MACsPbZn(ICl)$_3$ film after heating in ambient conditions at 85°C for 5 days. (C) Intensity of perovskite peak and PbI2 peak (0.3° critical angle) in Pristine samples compared to films exposed to 'Wet' and 'Ambient' conditions.

To determine the crystal structure of the phases produced, WAXS was performed on MACsPbZn(ICl)$_3$ perovskite thin films. Plots of peaks associated with by-products of fabrication and degradation are shown in Figure 60. Exposure to ambient moisture increases the concentration of Zn(OH)$_2$ and Pb(OH)$_2$ (Figure 60A and B). Relative to the Pristine films, the ZnO component (Figure 60C) is slightly reduced — this suggests some conversion of ZnO to Zn(OH)$_2$ upon reaction with H2O, either from adsorbed moisture or decomposing MA. Under ambient exposure the formation of Zn(OH)$_2$ is increased further, though the ZnO is greater than in the Wet film. Annealing at 100°C increases the concentration of Pb(OH)$_2$, PbI2 (Figure 60E) and Zn(OH)$_2$ more than at 80°C. The high temperature degrades the perovskite more extensively, leading to the reaction of more Zn and ZnO with H2O. As a result, the scattering intensity from Zn(OH)$_2$ is higher for the films heated at 100°C than at 80°C or kept at ambient temperatures.

ZnO has high electron mobility and a small band-gap (0.72 eV); this may have the effect of red-shifting the measured band gap Eg of the MACsPbZn(ICl)$_3$ film (which may also increase electron extraction in devices). However, if ZnO forms preferentially at a surface at which hole extraction occurs, this would have a deleterious effect on charge extraction due to ZnO providing a recombination pathway at the interface. Pb and Zn

hydroxides have wide-band-gaps and relatively poor conductivity. Their prevalence will limit current collection. There was also evidence of the production of ZnI2, shown in Figure 60F. This phase increases in prevalence after more extended degradation, particularly after thermal degradation. Despite the addition of ZnCl2 in the fabrication process, ZnCl2 is not identifiable in our X-ray scattering data. This would suggest Cl only participates in the crystallisation stages of perovskite formation, after which Cl volatilizes or resides at interstitial sites and grain boundaries. This is in agreement with previous data, where ultimately Cl has the effect of increasing grain size, and typically evaporates.[96,269,342,343]

A, shows evidence of both the perovskite and PbI_2 phases. The films were not filtered prior to deposition in order to maximise the prevalence of unreacted precursors in the film, and thereby better understand what phases precipitate under various external stressors by creating nucleation centres for their formation— effectively accelerating the degradation process. Figure 59B compares the Pristine film to an Aged film (exposed to ambient atmosphere and annealed at 85°C), highlighting the peaks towards the end of the q-range of measurements. Here there is evidence of the degradation products of perovskite with Zn incorporated. After 5 days the perovskite peaks have diminished considerably. PbI_2, ZnO, $Pb(OH)_2$ and ZnO all increase in prevalence due to the reaction with ambient O_2 and H_2O. These peaks are assigned by comparison to simulated powder diffraction patterns available at materials project.org.[286] The formation of these species is investigated by exposing $MACsPbZn(ICl)_3$ films to Wet conditions (85%rH in the dark for 5 days, to preclude the influence of light on H_2O/O_2 induced decomposition), Ambient conditions (ambient light and air exposure for 5 days), and continuous annealing at 80°C and 100°C in the dark for 10 hours (to preclude the influence of light irradiation on thermal decomposition). The elevated temperature in the latter conditions should lead to degradation of the perovskite, though likely more complex due to the addition of Zn and Cs. There is a decrease in perovskite scattering intensity and increase in PbI_2 intensity after exposure to both ambient and wet conditions, as shown in Figure 59C.

Figure 59: (A) XRD spectra of MACsPbZn(ICl)$_3$ perovskite in Pristine condition, cast from a non-filtered solution. (B) WAXS spectra between q = 2.85 and q = 3.95 Å^{-1}, comparing phases present in Pristine MACsPbZn(ICl)$_3$ film, and MACsPbZn(ICl)$_3$ film after heating in ambient conditions at 85°C for 5 days. (C) Intensity of perovskite peak and PbI2 peak (0.3° critical angle) in Pristine samples compared to films exposed to 'Wet' and 'Ambient' conditions.

To determine the crystal structure of the phases produced, WAXS was performed on MACsPbZn(ICl)$_3$ perovskite thin films. Plots of peaks associated with by-products of fabrication and degradation are shown in Figure 60. Exposure to ambient moisture increases the concentration of Zn(OH)$_2$ and Pb(OH)$_2$ (Figure 60A and B). Relative to the Pristine films, the ZnO component (Figure 60C) is slightly reduced — this suggests some conversion of ZnO to Zn(OH)$_2$ upon reaction with H$_2$O, either from adsorbed moisture or decomposing MA. Under ambient exposure the formation of Zn(OH)$_2$ is increased further, though the ZnO is greater than in the Wet film. Annealing at 100°C increases the concentration of Pb(OH)$_2$, PbI$_2$ (Figure 60E) and Zn(OH)$_2$ more than at 80°C. The high temperature degrades the perovskite more extensively, leading to the reaction of more Zn and ZnO with H$_2$O. As a result, the scattering intensity from Zn(OH)$_2$ is higher for the films heated at 100°C than at 80°C or kept at ambient temperatures.

ZnO has high electron mobility and a small band-gap (0.72 eV); this may have the effect of red-shifting the measured band gap E_g of the MACsPbZn(ICl)$_3$ film (which may also increase electron extraction in devices). However, if ZnO forms preferentially at a surface at which hole extraction occurs, this would have a deleterious effect on charge extraction due to ZnO providing a recombination pathway at the interface. Pb and Zn hydroxides have wide-band-gaps and relatively poor conductivity. Their prevalence will limit current collection. There was also evidence of the production of ZnI$_2$, shown in Figure 60F. This phase increases in prevalence after more extended degradation, particularly after thermal degradation. Despite the addition of ZnCl$_2$ in the fabrication process, ZnCl$_2$ is not identifiable in our X-ray scattering data. This would suggest Cl only participates

in the crystallisation stages of perovskite formation, after which Cl volatilizes or resides at interstitial sites and grain boundaries. This is in agreement with previous data, where ultimately Cl has the effect of increasing grain size, and typically evaporates.[96,269,342,343]

Figure 60: Scattering intensity of phases in samples exposed to different degradation conditions; (A) $Zn(OH)_2$, (B) $Pb(OH)_2$, (C) Bar chart of ZnO peaks showing contributions from different crystal planes, (D) Bar chart of (110) perovskite peak intensities across samples, (E) Bar chart of PbI_2 peaks showing contributions from different crystal planes, (F) ZnI_2.

8.3.3 X-ray photoelectron spectroscopy

X-ray photoelectron spectroscopy was performed to investigate the elements and bonding environment at the surface of thin film samples. 3 films were made for each condition (Pristine, Wet (exposed to 100%rH for 5 days), Ambient (exposed to ambient light and atmosphere for 5 days)), and two measurements were made on each sample, giving 6 measurements for each condition. The resulting spectra were averaged to determine average peak positions and intensities. Pb was measured in the first pass to minimise X-ray exposure which can lead to photolysis of PbI_2 to Pb. The XPS wide scan survey spectrum (Figure 61) for Pristine $MACsPbZn(ICl)_3$ films shows peaks at binding energies of 137.9 eV(Pb), 198.9 eV(Cl), 286.3 eV(C), 402.3 eV(N), 532.8 eV(O), 619.3 eV(I), 724.7 eV(Cs), and 1022.7 eV(Zn). Well defined split spin-orbit components occur for I (I 3d5/2, 3d3/2, Δ=11.5 eV), Cl (Cl 2p3/2, 2p1/2, Δ=1.6 eV), Pb (Pb 4f7/2, 4f5/2, Δ_{metal}=4.87 eV), Zn (2p3/2, 2p1/2, Δ_{metal}= 23 eV), and Cs (Cs 3d5/2 3d3/2, Δ= 14 eV). The XPS spectra were calibrated to adventitious carbon (C 1s) at 285 eV.

Figure 62 show average XPS spectra for films in their Pristine condition, after exposure to 100% humidity over 5 days (comparable to the 'Wet' samples in XRD and absorbance spectroscopy), and after exposure to direct sunlight and ambient atmosphere for 5 days (comparable to 'Ambient' samples). As XPS is conducted under high vacuum, any unstable hydrates which form are converted back to perovskite (if monohydrated) or PbI_2 if di-hydrated and the H_2O evaporates, and so although films are exposed to high relative humidity the presence of hydrated phases in the films cannot be verified using XPS. 'Wet' films prior to measurement had a speckled grey appearance, which darkened and increased in opacity after measurement under vacuum. This suggests a change of phase from hydrated perovskite to perovskite and PbI_2, supporting the assumption that the requirement of high-vacuum limits the sensitivity of XPS to hydrated phases. Films in the Pristine condition show a Pb 4f7/2 peak at 138.7 eV (Figure 62A). This indicates the presence of PbI_2 and $PbCl_2$. While it remains in the same position in the 'Wet' film, the 'Ambient' film shows a shift to 138.2 eV. This is characteristic of the formation of PbI_2, PbO, $Pb(OH)_2$, and $PbCO_3/PbC_2O_4$, similarly identified by Rocks et al.[356]
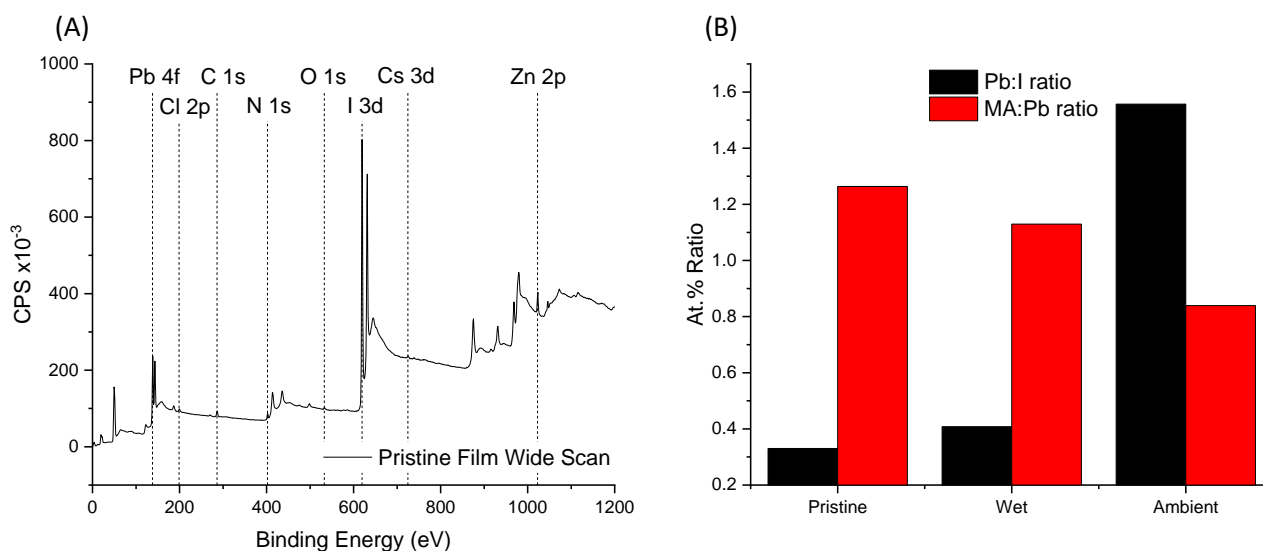
Figure 61: (A) Averaged wide survey scan of 3 Pristine $MACsPbZn(ICl)_3$ films. (B) %At. Concentration ratio of Pb:I and MA:Pb, showing decreasing MA, decreasing I and increasing Pb with exposure severity.

The volume interrogated is increasingly composed of Pb as opposed to C, N or other elements which are lost during degradation. Similarly, the Zn 2p3/2 peak (Figure 62B) shows a leftward shift, from predominantly $ZnCl_2$ and ZnI_2 to both ZnO, $ZnOH_2$ and Zn halides in the 'Wet' films, and finally predominantly ZnO in the 'Ambient' films. Peak broadening is particularly accentuated in the 'Wet' films due to the variety of Zn compounds present. The peak from Cs_2O (725.2 eV) shifts to the right as CsOH (724.15 eV) and Cs Halides (724±0.1 eV) form in wet and ambient conditions (Figure 62C). Similar to Pb, the Cs peak area increases under ambient conditions due to its inability to leave the film unlike organic cations and halides. The O peak (Figure 62D) increases due to the formation of metal oxides, hydrates and carbonates. The peak shifts from a tiny hump at 533 eV (organic C-O

bonds) to 532.6 eV in the 'Wet' films (a combination of C=O and C-O) to two peaks in the 'Ambient' film at 531.3 eV (metal carbonates and adsorbed OH⁻ and O²⁻ ions or lattice O with (Pb/Zn)O/(Pb/Zn)OH$_2$ like states) and 529.4 eV(metal oxides). The increasing contribution from C=O bonds as metal oxides and carbonates forms demonstrates the role of O in destabilising the perovskite lattice and its role in degradation.
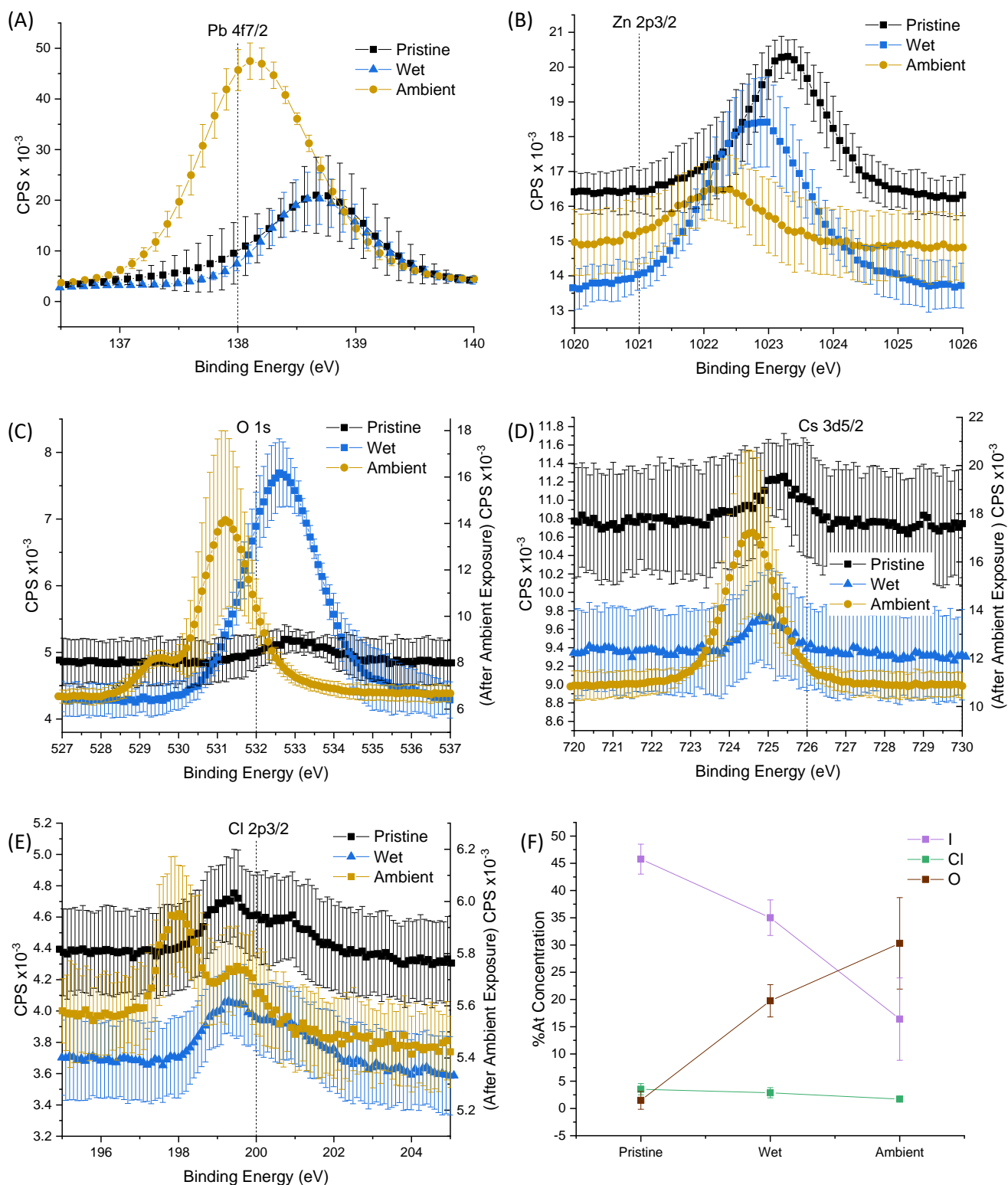
Figure 62: XPS high resolution spectra of peaks in the survey scan of Pristine, 'Wet' and 'Ambient' films showing the (A) Pb 4f, (B) Zn 2p, (C) Cs 3d, (D) O 1s (E) Cl 2p regions. Bars represent standard deviation across samples (3 samples per condition) (F) %At concentration of O, I and Cl across the 3 film conditions.

The Limited Benefits of ZnCl2 as a Stabilizing Additive for Perovskite Films – Results

The atomic concentration (At. %) of surface oxygen species correlates with decreasing At.% of halide species, I and Cl. This indicates the facile loss of I and Cl from the surface during moisture induced and ambient degradation, and the diffusion of O into the lattice vacancies. O then bonds with the metal cations as degradation proceeds. The extent of degradation into oxidised species is greater in the film exposed to 'Ambient' conditions, with the At.% raising to ~30%. The plot of the ratio of Pb to I in Figure 61B shows the changing structure as well. The ratio increases from almost exactly 0.33 (as per the perovskite structure, ABX_3 to 1.6, showing Pb-compounds beyond just PbI_2 (Pb:I ratio of 0.5) have formed within the top 10 nm of the remaining film after ambient exposure, such as PbO.

At the surface of the Pristine film atoms are found to be present in amounts contrary to the intended stoichiometry. If a perovskite structure is assumed, lattice-site occupancy of ~24% for Zn(B-site), 2% for Cs (A-site), and 7% for Cl(X-site) can be calculated. This is compared to expected values of 3% for each assuming the atoms were homogeneously distributed throughout the perovskite film (Zn on the B-site, Cs on A-site, Cl on X-site). This suggests preferential segregation of Zn to the film surface occurs, whereas Cs has a sub-stoichiometric concentration at the film surface. It also suggests that Cl is retained in the as-cast film, in contrast to films characterised in XRD. This Cl intensity arises in both the Pristine and Wet films; with the Cl 2p3/2 peak (Figure 62E) centred at 199.3 eV, indicating metal chlorides (~198.5–199 eV). The peak breadth also suggests a contribution from Cs_2ZnCl_4 (199.20 eV), a fluorescent (blue emission) orthorhombic crystal.[357] In the 'Ambient' films the Cl 2p peak position (198 eV) indicates $ZnCl_2$.

8.3.4 UV-VIS Spectroscopy and Ellipsometry

Films exposed to ambient temperatures and humidity (45-55%rH, 20°C), and light (exposure to sunlight through windows as well as indoor lighting whereby most UV-B and UV-C is absorbed) show significant degradation of $MAPbI_3$ films over 5 days in Figure 63A, with the film changing from a dark grey/black to yellow as PbI_2 forms. In contrast, $MACsPbZn(ICl)_3$ films show significantly suppressed degradation. UV-VIS absorbance spectroscopy shows evolution of the PbI_2 peak around 500nm. Figure 63B shows the $MACsPbZn(ICl)_3$ film maintains a similar absorbance (A) profile, although it decreases significantly between the Pristine condition (directly after fabrication) and Day 1. Directly comparing the two Pristine films in Figure 64A shows higher A in the $MACsPbZn(ICl)_3$ film. Part of the increase in A measured for the Pristine $MACsPbZn(ICl)_3$ films may arise from an increase in scattering as a result of high concentrations of PbI_2 and $PbOH_2$, or presence of ZnO and $Zn(OH)_2$.
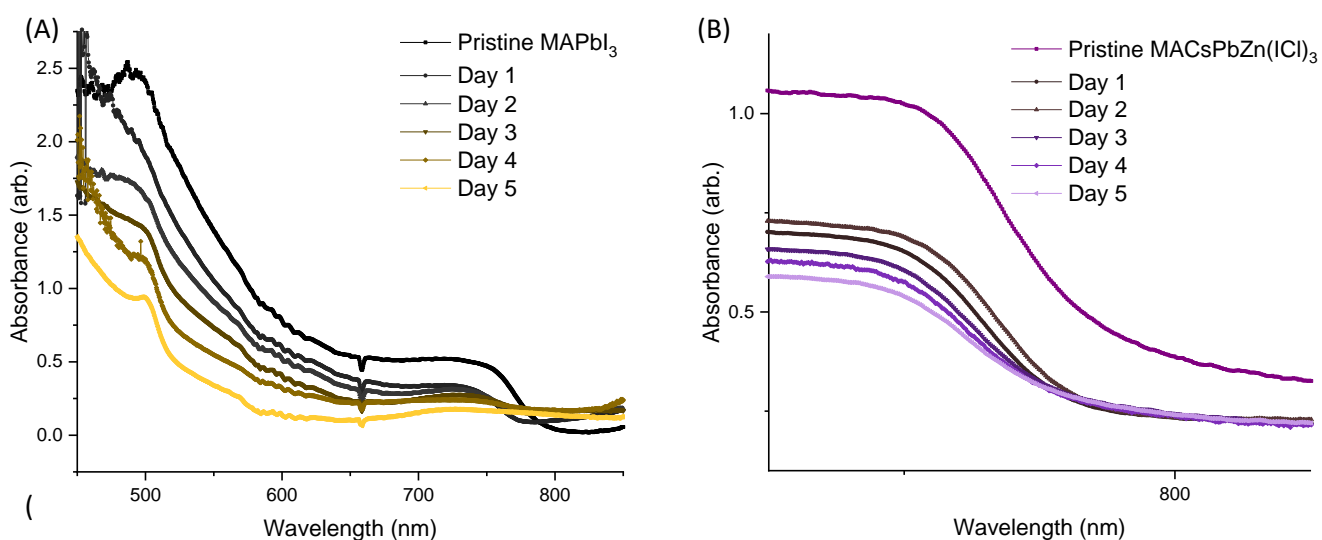
Figure 63: UV-Vis Absorbance Spectra of (A) $MAPbI_3$ films and (B) $MACsPbZn(ICl)_3$ films on glass substrates during ambient degradation in air (45-55%rH, ~20°C, light).

In order to determine absorption (α), measurements of refractive index (n) and extinction coefficient (k) are measured as a function of wavelength using Ellipsometry. The value for α represents the extrinsic or effective α coefficient, as it does not exclude the influence of surface roughness which can cause in-coupling of photons,

126

The Limited Benefits of ZnCl2 as a Stabilizing Additive for Perovskite Films – Results

and increase measured α. Using these measurements, relative changes in α can be observed, and related to changes in material phase, roughness, and electronic disorder. Figure 64B shows the α decreases for both sample types over time, plotting α at 780 nm (at a longer wavelength in nm than the band-gap according to UV-Vis analysis of Pristine films, where the perovskite will absorb strongly). While the MAPbI$_3$ film has a higher α in the Pristine Condition, the ellipsometry results suggest the MACsPbZn(ICl)$_3$ film has higher α thereafter.
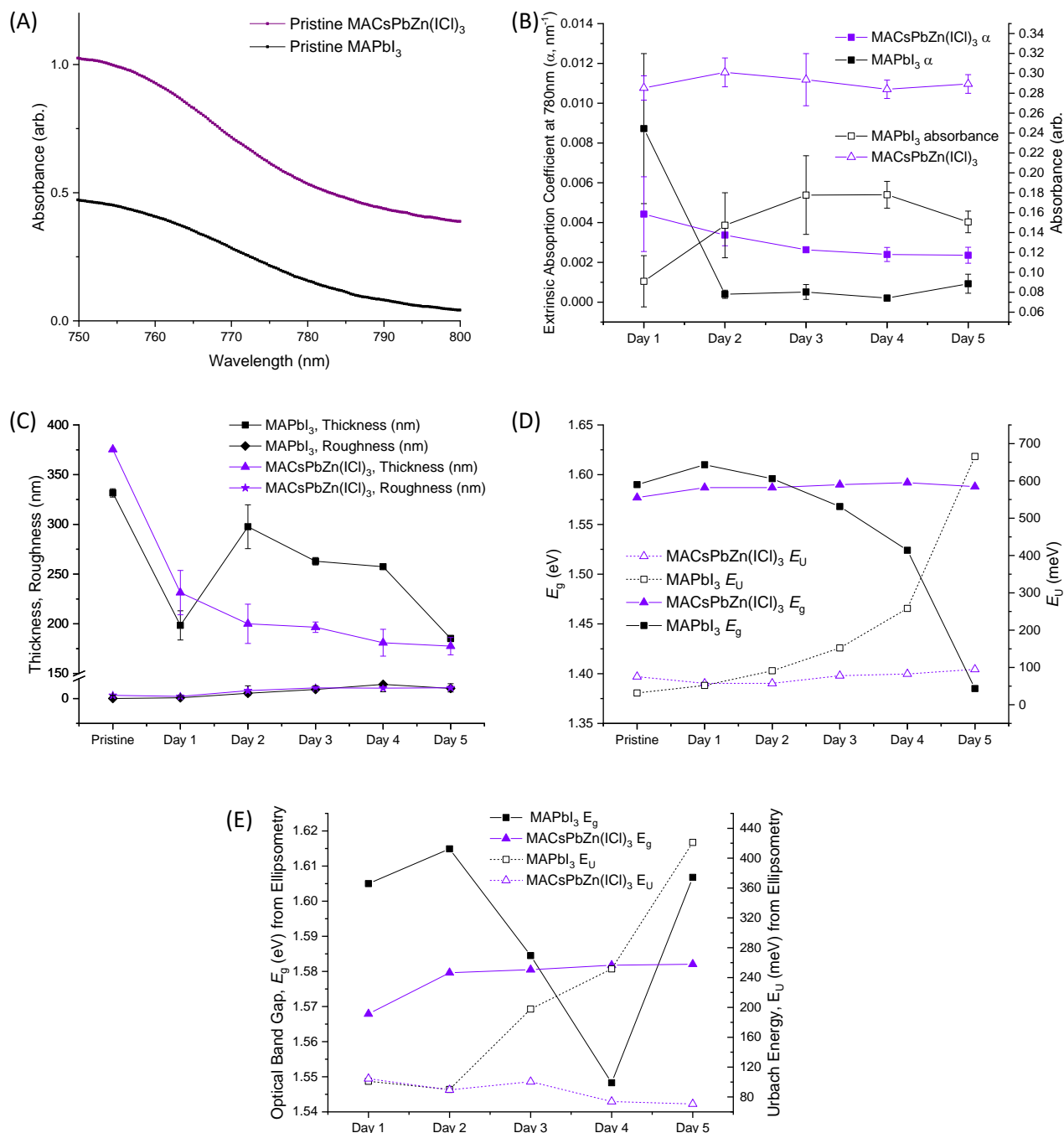
Figure 64: (A) UV-VIS Absorbance spectra for Pristine EA-washed MAPbI$_3$ and MACsPbZn(ICl)$_3$. (B) Absorbance and extrinsic absorption coefficient (α) of MAPbI$_3$ and MACsPbZn(ICl)$_3$ films over 5 days of exposure to ambient conditions. α determined using Ellipsometry. (C) Thickness and roughness of MAPbI$_3$ and MACsPbZn(ICl)$_3$ films according to Ellipsometry modelling. Capped bars represent standard deviation between samples (n=3). (D) Band-gap (E_g) and Urbach Energy E_U of MAPbI$_3$ and MACsPbZn(ICl)$_3$ films determined by UV-Vis spectroscopy (E) E_g and E_U determined by Ellipsometry for MAPbI$_3$ and MACsPbZn(ICl)$_3$ films.

Ambient degradation results in a thickness decrease in both films as initially continuous and connected grains devolve into disconnected islands. This reduces film coverage and hence thickness, also reducing A. In MAPbI$_3$

The Limited Benefits of ZnCl2 as a Stabilizing Additive for Perovskite Films – Results

there is an initial thickness decrease between the Pristine condition and after 1 day of exposure. Subsequently the thickness increases, and this may imply volume expansion due to formation of a secondary phases such as PbI_2 and hydrated perovskite phases. This moisture-adsorption induced swelling as perovskite hydrates form in the moist atmosphere has been observed previously by Schlipf et al.[166] These secondary phases have larger cell lattice parameters than regular perovskite crystals, and also reduce absorptivity of the film per unit mass. They also increase scattering resulting in an upwards shift in A between Days 1-4 in Figure 64B. This phase transformation serves to decrease α in the MAPbI$_3$ film significantly after just 1 day of exposure. Further evidence comes from the PbI$_2$ peak at ~500 nm in Figure 63A. The reaction with moisture at the surface may result in higher PbI$_2$ concentration. The thickness decreases to approximately the same thickness as the MACsPbZn(ICl)$_3$ films. In Figure 64C roughness increases very slightly over the duration of the experiment in both films.

In the MACsPbZn(ICl)$_3$ films, thickness decreases drastically between the Pristine and Day 1 conditions. The A remains fairly constant, while α decreases, suggesting increasing scattering is contributing to the constant A. The roughness increasing as film thickness decreases implies that the film transformations (chemical or structural) are changing the surface topology. A blue-shift in E_g (Figure 64D) and increasing α are correlated with increasing roughness. Simultaneously E_U slightly rises due to increased structural disorder. This suggests that the MACsPbZn(ICl)$_3$ films undergo a different degradation route during ambient exposure, with a roughly linear decrease in thickness after an initial steep decrease, similar to MAPbI$_3$. Under ambient conditions, MAPbI$_3$ shows a rapid increase in electronic disorder at the band-edge of the perovskite phase over the 5 days. Similarly, the E_g of the perovskite phase exponentially red-shifts. In contrast, the MACsPbZn(ICl)$_3$ sample initially shows a decrease in E_U, before increasing after day 2 to ~125% it's starting value by day 5. The E_g blue-shifts slightly during exposure after Day 2. Despite the changing film thickness and roughness over the course of exposure, the bulk of the MACsPbZn(ICl)$_3$ film shows a less disordered band-edge than the MAPbI$_3$ film, and less variation in E_g, suggesting a more stable phase composition.

Ellipsometry tells a more complex story. The E_U in the Pristine condition is similar between the two samples. E_g and E_U of MAPbI$_3$ decrease and increase respectively according to Ellipsometry, in agreement with UV-Vis, though there is a redshift on day 5 coinciding with an increase in α. In, MACsPbZn(ICl)$_3$ there is a blue-shift of E_g, while E_U slightly decreases at the surface. The recovery in E_g of the perovskite phase in MAPbI$_3$ films at the surface may relate to our previous observations using TOF-GISANS of more rapid deterioration in the bulk than at the surface of MAPbI$_3$ films, and may reveal remnant perovskite phase at the surface following degradation.[311] The step-change in E_g between days 2-4 in the MAPbI$_3$ film may reflect the degradation to perovskite-hydrates and PbI$_2$, concurrent with increasing thickness, roughness and decreasing α. Increased E_U may relate to the existence of intra-band states arising from the evolution of secondary phases, which will typically have the effect of decreasing α. This will have a negative effect on PCE, by increasing the rate of non-radiative recombination due to a higher prevalence of trap states.

Comparison of Ambient degradation to Wet and Dry (25%rH in the dark) conditions suggests that Ambient conditions increase the degradation rate of both films, with higher growth rates in E_U over the 5 days, as shown in Figure 65A. Comparing the UV-VIS data across the 3 conditions, Ambient conditions causes the largest fluctuation in the band-gap — likely due to secondary phase formation. Increases in E_U are comparably less after Day 1 in the Dry MACsPbZn(ICl)$_3$ film, and similarly expressed to a lesser extent in the Wet MACsPbZn(ICl)$_3$ film suggesting the additives have improved resilience to moisture induced degradation, particularly in the absence of UV. Plots of α in Figure 65B, show that exposure to both Dry and Wet conditions increased α near the band-edge, whereas α decreased under Ambient conditions (after an initial increase). Measurements of thickness and roughness in Figure 65C and Figure 65D respectively show that the films in a dark atmosphere maintain similar roughness and less thickness reduction in comparison to Ambient exposed films. Ambient films become much rougher, have lower α, and higher disorder after 5 days. The higher roughness can be associated with the more severe degradation which occurs under illumination.[166]

In the MACsPbZn(ICl)$_3$ film, the band-gap as measured by UV-Vis spectroscopy blue-shifts under the Dry (25%rH) conditions and until day 4 under Ambient conditions (50%rH). Thereafter E_g is red-shifted. Similarly, E_g is red-

The Limited Benefits of ZnCl2 as a Stabilizing Additive for Perovskite Films – Results

shifted throughout Wet exposure. This may indicate a moisture exposure threshold above which degradation causing red-shift begins to dominate, possibly arising from the volume of adsorbed moisture along crystal facets and grain boundaries, which will eventually lead to the production of first perovskite hydrates and upon decomposition, PbI_2, associated with red-shift of E_g. Under Wet conditions this threshold is reached by Day 2, while under ambient conditions this threshold is only reached by day 4, with other reactions dominating prior — for example the reaction of Zn with moisture and O_2; $Zn(OH)_2$ is more prevalent in films degraded under ambient conditions according to XRD, suggesting the reaction is easier. XPS also indicates a higher proportion of O=C bonds and peak positions in line with metal oxides, hydroxides and carbonates. This may imply the Zn acts to bind the first moisture to adsorb into the film, but is eventually saturated, with films then degrading in a similar way to regular $MAPbI_3$ films.
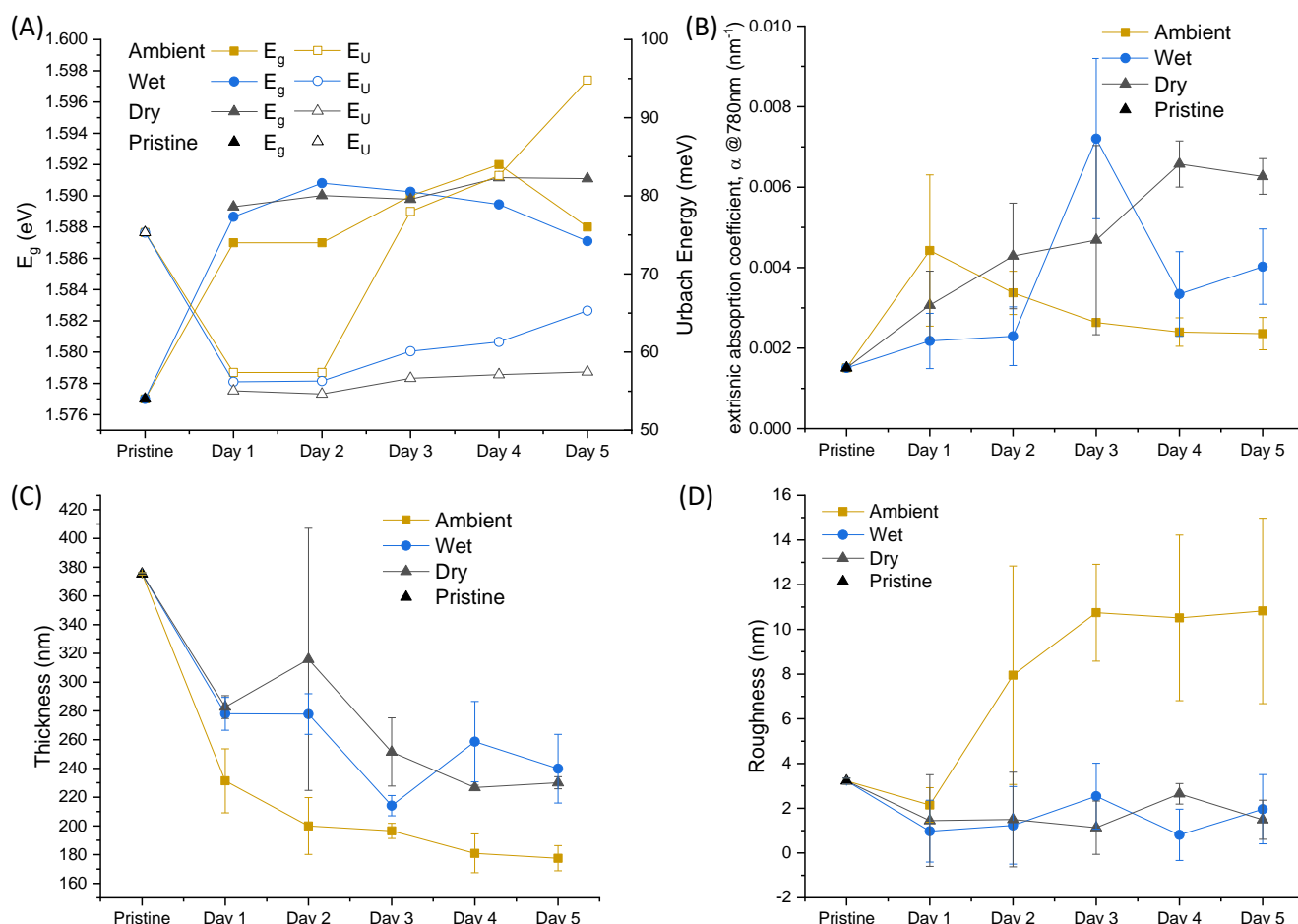
Figure 65: A) E_g and E_U calculated from UV-Vis absorbance spectra, (B) extrinsic absorption coefficient from Ellipsometry, (C) Thickness and (D) Roughness determined by Ellipsometry of the $MACsPbZn(ICl)_3$ film under different exposure conditions over time.

This can also be seen by comparing plots of A and α (determined by UV-Vis and Ellipsometry respectively, Figure 66A. After Day 2 in the Wet $MACsPbZn(ICl)_3$ film, A increases alongside α. There is also an increase in E_U as measured by UV-Vis, , suggesting structural changes in the film. Under ambient conditions, α drops after Day 1, while A fluctuates suggesting increasing scattering. This is supported by the much high E_U and roughness. Under dry conditions, α increases while A stays the same. Thickness decreases and roughness remains between 0-3 nm, while E_U only slightly increases. A significant thickness increase is not observed in the $MACsPbZn(ICl)_3$ films. This means that in the $MACsPbZn(ICl)_3$ film, production of the expansionary by-products is reduced when compared to $MAPbI_3$ films, within which hydrated phases readily form after exposure to moisture, inducing swelling of the thin film. This lack of swelling may be due to preferential formation of Zn based secondary phases at the surface. Indeed, XRD and XPS provide evidence for their formation.
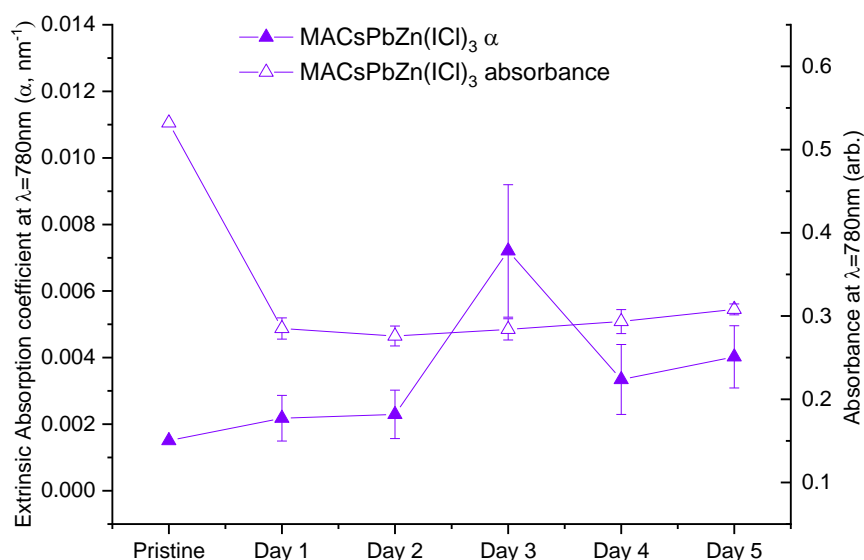
Figure 66: Absorbance (UV-Vis) vs extrinsic absorption coefficient (α) from Ellipsometry in MACsPbZn(ICl)$_3$ films.

8.3.5 Devices

Devices were fabricated as described in the experimental section, and stored under ambient atmosphere in the dark for 5 days. MACsPbZn(ICl)$_3$ devices have smaller V_{OC} with an average of 1.02 V as compared to 1.04 V for MAPbI$_3$; this is expected as the band-gap is red-shifted in UV-Vis. J_{SC} is also reduced, with the best performing pixel having a J_{SC} ~ 17 mA cm^{-2}, compared to ~19 mA cm^{-2} for MAPbI$_3$ pixels. Figure 67 shows the variation in V_{OC} (A), J_{SC} (B), FF (C) and PCE (D) as a function of time for MACsPbZn(ICl)$_3$ devices. Performance degradation is dominated by 'Device 1' which shows more significant decreases in device parameters, as shown in Figure 67. PCE of functioning pixels degrades more rapidly than in the MAPbI$_3$ devices, though there are more functional pixels at the end of measured degradation, as shown in Figure 67E and Figure 67D respectively. The MACsPbZn(ICl)$_3$ devices also show greater hysteresis, particularly evident between the measurements on Day 1. Although the preferential Zn-moisture reaction slows down the moisture induced perovskite degradation route, ZnCl$_2$ addition appears to have a detrimental effect on device performance.

After fabrication, MACsPbZn(ICl)$_3$ devices have greater hysteresis, poorer forward PCE, and reduced J_{SC}. Typically, hysteresis results from charge screening from mobile I$^-$ ions reducing net current under forward bias (and the inverse under reverse bias). V_I^+ defects generated under forward bias act as non-radiative recombination sites for electrons. Poor electron charge extraction to the SnO$_2$ ETL or similarly poor hole extraction to the PTAA based HTL can also contribute to the creation of a screening layer of charge carriers. The Zn secondary phases such as ZnO, and ZnOH$_2$ have an effect on device performance as well. ZnO has high electron mobility. XPS and XRD shows ZnO is forming at the surface of the film during fabrication (due to reaction with oxygen). ZnO will impede current extraction due to electron-hole recombination before electrons reach the perovskite-PTAA interface. This effect would be further accentuated by the trapping of electrons in V_I^+ which form due to perovskite degradation. Zn hydroxides have limited conductivity and hinder current extraction. Zn hydroxides could make the film a poorer semiconductor. It is thus possible that fabrication of these devices in an O-free environment, for example a glovebox filled with inert gas would result in higher performance while maintaining the moisture tolerance and trapping that Zn addition offers.

In the bulk, when Zn is incorporated the perovskite band-gap red-shifts with better absorption in the near-IR range. V_{OC} decreases due to the associated contraction in E_g. At the surface (by the PVSK-PTAA interface), ZnO formation (a wide band-gap semiconductor) blue-shifts the band-gap. The blue-shift may also be due to tensile strain at the surface inducing band-bending.[355] The film absorbs better in the UV region. Under irradiation, holes drift towards the HTL, but generated electrons recombine with holes via the high electron mobility of the ZnO phases. This has the effect of both reducing hole extraction, and creating a charge screening layer which contributes to enhanced hysteresis relative to a MAPbI$_3$ film. This effect dominates at the interface under forward bias. The in-plane strain present in these films will also reduce hole mobility as shown by Zhu *et al.*, due

to greater energy level mismatch between the perovskite valence band and hole transport layer. This would further enhance the recombination rate and reduce carrier lifetime.[355]
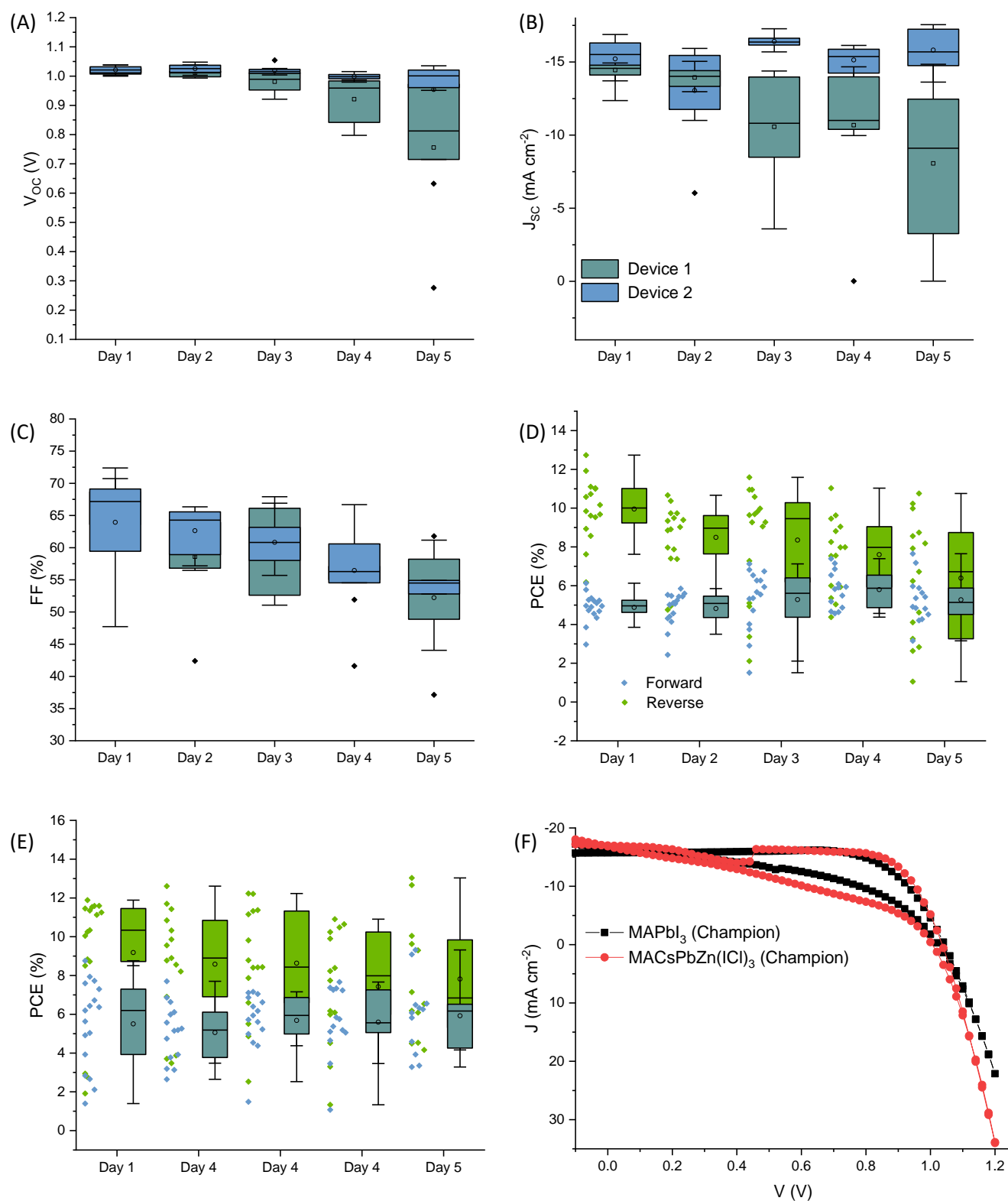
Figure 67: (A) V_{OC} (B) J_{SC} and (C)FF under reverse bias over 120 hours (5 days) of degradation, showing how performance deterioration of MACsPbZn(ICl)$_3$ devices fabricated under ambient conditions is dominated by a single sample. (D) Forward and Reverse PCE of MACsPbZn(ICl)$_3$ devices vs (E) MAPbI$_3$ devices over 5 days of shelf storage in ambient conditions (no incident light). (F) Champion pixels in MAPbI$_3$ compared to MACsPbZn(ICl)$_3$.

The Limited Benefits of ZnCl2 as a Stabilizing Additive for Perovskite Films – Conclusion

Another factor is the choice of HTL. PTAA is air-stable, mechanically strong, highly optically transparent and has higher hole mobility then other organic HTLs such as P3HT and spiro-OMeTAD[358]. However degradation can occur at the perovskite-HTL interface when HI gas releases from MAI.[359] Additionally, the dopants used to increase the hole mobility of the PTAA layer sacrifice device stability, with t-BP and Li both accentuating degradation of the perovskite film.

As a result, a limitation in this experiment was the choice of HTL. PTAA has a strong interaction at the perovskite interface, good transparency, thermal stability, and ambient stability. And yet is likely responsible for the poor device performance longevity observed in this work. The PTAA layer interacts with the perovskite during annealing; when MAI degrades during annealing it releases acidic HI gas which degrades the PTAA.[359] Additionally, the additives incorporated in the PTAA layer to improve hole mobility – tBP and Li-TFSI have been shown to accelerate degradation of the perovskite film during storage in ambient air.[360] Li-TFSI attracts moisture accelerating device degradation. tBP readily evaporates due to its low boiling point, which introduces pinholes. tBP also reacts with PbI$_2$, driving the perovskite decomposition reaction forwards. Only 64% of initial PCE is preserved in devices (fabricated in ambient air) after cupboard storage in ambient air (~50%rH) for 120 hrs. This is in comparison to 80-90% of initial PCE after >700 hrs in devices (fabricated in inert and dry conditions, and with a spiro-OMe-TAD HTL) exposed to similar rH% in the literature. Taking this into account strategies could be put in place to ameliorate or evade this problem, and address the disparity in stability observed between Zn incorporating devices in this work and those in the literature.

The following comprises future work which could be conducted in the area of ambient fabrication of Zn-incorporating devices. Perhaps the most obvious method to avoid issues arising from the HTL would be inverting the device architecture to the alternate (p-i-n) stack, with the PTAA based layer at interface between TCO and perovskite. This could result in better devices both due to reduced degradation of the perovskite layer stemming from the interplay of the HTL layer and moisture, but could also improve electron extraction if Zn (added to the precursor solution) still forms ZnO preferentially at the surface due to its high electron mobility. Another method that could be used to improve device performance and stability while maintaining the n-i-p structure could be optimising the annealing regimes of the various layers to reduce the in-plane strain gradient. Work done by a Masters student involved in obtaining preliminary data for this work suggests the optimum anneal temperature may be between 60-80°C for Zn incorporating perovskites, evidenced by larger grains and higher surface coverage of films in SEM. This could reduce the formation of secondary phases at the surface, which may be encouraged by tensile strain at the surface and also reduce the degradation of the PTAA due to degradation of MAI during annealing. Finally, the formation of Zn compounds at the surface due to reaction with ambient air could be mitigated by fabricating perovskite films in inert gas in a glovebox. The obstacle to this approach arises due to the Li-TFSI additive to the PTAA. The HTL must be exposed to O$_2$ too oxide Li ions which can otherwise diffuse through the perovskite to the ETL/perovskite interface, affecting electrical properties and possibly accelerating degradation.[360] This exposure may also create an opportunity to oxidise Zn. An alternative approach could be using alternate HTL dopants such as BCF or F4-TCNQ which may be less deleterious.[360]

8.4 Conclusion

A-site substitution of MAPbI$_3$ with Cs (and FA) can help mitigate decomposition to first a mono-hydrated and then a di-hydrated phase in a dark, wet atmosphere.[165,311] B-site substitution with Zn could also have a beneficial effect on the shelf-stability of perovskite films, potentially due to the facile reaction of Zn with both O$_2$ and H$_2$O forming ZnO and Zn hydroxides. However, this same reaction is shown to cause problems under thermal stress, as it facilitates the rapid thermal decomposition of the perovskite phase due to the prevalence of defects, as shown by SEM and XRD. The degradation is catalysed by the presence of light which for example catalyses the reaction of perovskite with superoxide species in vacancies, and photolysis of MAPbI$_3$ to PbI$_2$. The same redox chemistry may be responsible for greater thermal degradation in MACsPbZn(ICl)$_3$ films compared to pure MAPbI$_3$ films.

9   Conclusions and Future Work

This thesis has aimed to elaborate upon our mechanistic understanding of processes affecting the stability of PSCs, primarily from the perspective of manipulating perovskite stoichiometry to control defect prevalence. This thesis has journeyed from the prototypical MAPbI$_3$ system through to more exotic and current triple-cation perovskites, before experimenting with a novel mixed cation, mixed halide MA-based composition to try and improve MA-rich film stability. This work has ascertained and expanded upon

1) A detailed understanding of the influence of initial precursor stoichiometry on the formation of the solvent-intercalated precursor intermediate phase during ambient atmosphere perovskite formation. It is demonstrated for the frst time that MAI enrichment enhances the growth rate of the solvent-intercalated intermediate, while also hastening the intermediate-perovskite conversion and the growth rate of perovskite crystals, leading to larger grains, higher *FF*, and improved PCE. MAI enrichment also extends the EA antisolvent application window by suppressing loss of DMSO and coordinating with Pb^{2+} nucleation centres, mitigating formation of hydrated intermediates during spin casting.

2) The degradation of FA-rich perovskites (and MAPbI$_3$) in a dark, 90%rH atmosphere in terms of phase evolution and morphology. It is found that addition of Cs significantly reduces phase segregation of FA-rich perovskite compositions into constituent perovskite phases (e.g. FAPbI$_3$, MAPbBr$_3$ etc). Evidence is also found for the formation of MA *and* FA perovskite-hydrates. Moisture induced decomposition occurs more rapidly in the bulk, with the GB region mediating the degradation of perovskite grains. Evidence supports theories that decomposition is initiated in the bulk, while moisture adsorption on GBs and surfaces smooths the grain periphery, leading to fragmentation of grains into rounded crystallites surrounded by smaller crystallites.

3) The limits of Zn as a B-site additive to MAPbI$_3$, traced to the poor thermal stability of the films and the need for careful selection of the HTL in a conventional n-i-p device architecture. It is shown that Zn-incorporating MA based films fabricated in ambient atmosphere have improved moisture stability compared to MAPbI$_3$, and do not show swelling of the perovskite film associated with formation of hydrated perovskite phases. Rather, Zn acts to mop up adsorbed moisture and O$_2$, forming ZnO and ZnOH$_2$ secondary phases. However, this same reaction exacerbates surface strain which in combination with in plane tensile strain arising from a thermal expansion coefficient mismatch between the perovskite and substrate lead to more rapid thermal degradation after heating >60°C due to a destabilised perovskite lattice. The choice of HTL also impacts device performance stability, with a PTAA based HTL leading to both higher hysteresis than MAPbI$_3$ devices and lower stability than comparable Zn-incorporating devices in the literature.

Section 6 developed our understanding of the interplay of EA application and precursor solution stoichiometry during fabrication of perovskite films under ambient conditions. Investigation of the stages of intermediate and perovskite crystallisation and how non-stoichiometric mixtures affect them can inform strategies to optimise performance of MAPbI$_3$ films for optoelectronic applications such as flexible PSCs and multi-junction devices. MAI enrichment increased grain size and raised the photo-active area across the thin film, leading to higher average PCE due to higher *FF*, whereas PbI$_2$ enrichment improved J_{SC} and V_{OC} due to suppression of defect assisted recombination. The crystallisation process of the perovskite film was described using evidence from WAXS, SEM, and UV-Vis Spectroscopy , including in detail the stages of sol-gel formation and crystallisation of the solvent-intercalated intermediate. It is shown in detail how stoichiometry influences the onset of each stage of the process. The solvent-intermediate forms more rapidly in the solutions with a higher concentration of reactants, while conversion to perovskite occurs most rapidly for the films with an MAI excess, which also enhances the growth rate of the solvent-intercalated-intermediate crystallites Furthermore while PbI$_2$ excess raises the nucleation component of perovskite crystallisation, MAI excess enhances the growth component of perovskite crystallisation.

Conclusions and Future Work

Moisture is found to be key in understanding the relationship between stoichiometry and antisolvent application. Water competes with the precursor-coordinating solvents DMSO and DMF to coordinate with Pb^{2+} ions, creating hydrated perovskite and non-perovskite compounds. A higher ratio of Pb to MAI increases the coordination rate of H_2O to Pb^{2+} cations. Application of EA early in the spin casting process reduces the formation of defects and hydrated by-products by reducing the concentration of adsorbed water in the perovskite film and preferentially promoting the formation of the DMSO-intermediate. Combining this with a 10mol% excess of MAI in the precursor solution creates the best devices, with MAI suppressing evaporation of DMSO and thereby increasing the growth rate of perovskite grains.

This work has focused on the $MAPbI_3$ system, which at the onset of the work was still of significant interest. However, by the end of this investigation, the field had shifted considerable interest to more complex perovskite systems, with mixed cation, mixed halide constituents. This had been foreseen in preliminary planning for the experiment, and solutions prepared for WAXS experiments had originally included FA and Cs based perovskites, and these were measured using the same approach. However, due to lack of expertise, testing, and knowledge it was found after running the experiments that these solutions had all been exposed to excessive amounts of moisture during fabrication, resulting in incorrect non-α-perovskite, and non-perovskite films. Other researchers have since performed similar experiments investigating the crystallisation of FA and CS based perovskites, some of which is covered in the literature review. Nonetheless, analysis of the collected data on $MAPbI_3$ films was still very insightful and the understanding gained is generalizable to MA based perovskites in particular.

Familiar with the interaction of moisture with the crystallising perovskite film, and after continuing literature review, a gap was identified in existing understanding of the moisture induced degradation of perovskite films; namely whether a hydrated perovskite phase was produced in the decomposition of FA-rich perovskites, which were known to degrade via interconversion between various hexagonal polytypes and δ-phase perovskite. In Section 7, TOF-GISANS was used to investigate mixed cation, mixed halide perovskite systems during exposure to a deuterated atmosphere in the dark. It is confirmed, as per the literature, that substitution of the MA cation with FA and Cs, as well as mixing of I and Br on the X-site of organic-inorganic perovskite has the effect of improving moisture stability of the thin films. It is shown that phase segregation is significantly reduced when Cs is used in addition to FA, with triple (A-site) cation mixed films showing minimal evidence of phase segregation. Evidence suggests formation of FA-based hydrated perovskite phases in FA-rich perovskite films exposed to 90%rH does occur. SEM shows a pattern of decreasing average grain size in all films, traced to the fragmentation of grains into smaller, rounded grains (and not previously identified as far as has been investigated). For the first time, Neutron scattering data from TOF-GISANS fitted in SASview provided in-situ evidence of decreasing characteristic length scales in the films, though the decrease appears more severe in the bulk compared to the surface. This supports theories that degradation is initiated in the bulk. Moisture first adsorbs to the film along GBs before permeating inside the grains and beginning a gradual process of decomposition from the outside in. The data suggests that the reaction of moisture with FA-rich mixed cation, mixed halide perovskites at 90%rH results in the formation of constituent perovskite phases, such as $FAPbI_3$, $FAPbBr_3$, $MAPbBr_3$ and $MAPbI_3$ as well as hydrated perovskite phases, Pb halides, $PbOH_2$, and PbO.

A limitation of GISANS results was the undefined crystal phase of the mixed-perovskite films; as they were fabricated under ambient conditions, mixed perovskites with both δ and α phases are likely to form because the δ, hexagonal phase, likely forms due to the instability of the α phase in ambient conditions. The degradation of these phases may proceed differently. This raises the question of whether there would be a difference in the degradation rate of films depending on the initial perovskite phase. It also raises questions about the reversibility of the observed segregation if moisture is reduced. While evidence for formation of FA based perovskite hydrates using GISANS was collected, due to the overlap of some of the non-hydrated and deuterated perovskite peaks with the peak positions of other perovskite hydrates, this leads to addition and convolution of peaks. These peaks are modelled with an origin peak fitting procedure allowing phase identification, but further work should be done to ensure verification. This may include further TOF-GISANS characterisation of pure $FAPbI_3$, $FAPbBr_3$ and other perovskite films, and measurement of the volume of adsorbed moisture in the degrading film to confirm the capture of H_2O. Reflectometry would probably be the suitable approach, and could provide data

on film thickness and roughness. Quantitative measurements of thin film roughness using techniques such as profilometry or AFM could be conducted in future work to verify roughness measurements from Ellipsometry. This was due to difficulties in fabricating and storing the mixed cation films in an inert atmosphere, arising both due to intermittent and limited access to a glovebox, as well as time constraints.

This work emphasised how alloying the different lattice sites in mixed perovskites has clear benefits in the fabrication of stable, high performing perovskite devices. Limitations due to the environmental conditions required to fabricate films with formamidinium shifted attention towards alternatives substitution strategies. Noticing the poor stability of MAPbI$_3$ in moisture, and the relationship between by-product formation under ambient fabrication and the Pb cation from WAXS, Zn-substitution was investigated as a strategy for improving moisture resilience of perovskite thin films.

Developing a mixed perovskite system combining Zn substitution for Pb, Cs substitution for MA, and Cl substitution for I, the influence of these alloying elements on stability of perovskite films following ambient fabrication was investigated in Section 7. Using an ethyl acetate assisted crystallisation methodology in keeping with the findings from Section 5, thin films were spin cast and characterised using SEM, Ellipsometry, UV-Vis, XPS, and WAXS, following exposure to moisture and heat. Zn-addition led to larger grains and more homogeneous mixing of the perovskite precursors as evidenced by SEM showing larger grains than MAPbI$_3$ films and lower concentrations of unreacted residual PbI$_2$. In contrast however, evidence also suggested that while Zn addition had a beneficial effect in reducing moisture-induced degradation by introducing a more favourable reaction pathway for adsorbed moisture and thereby extending thin film optoelectronic properties, it introduced a new and more dramatic thermal degradation pathway. This is in part due to the detected presence of high concentrations of additives at the surface, likely present in the form of secondary phases such as ZnO, ZnOH$_2$, according to both GIWAXS and XPS. Their presence will increase strain at the surface of the perovskite film, destabilising the perovskite lattice and accelerating degradation. As lattice Zn reacts with ambient O$_2$ and H$_2$O it will further destabilise the lattice while also increasing opportunities for diffusion of O$_2$ and H$_2$O, further accelerating degradation.

Section 8 has highlighted the importance of degradation studies in identifying ionic substitution strategies which can be practically applied to improve long-term operation under terrestrial conditions. These strategies must offer stability along multiple dimensions of environmental stress, as well as improve performance relative to unadulterated devices.

This thesis empirically questions the reliability, sustainability and efficacy of ionic substitution and stoichiometric manipulation to improve perovskite films stability. Despite improvements to moisture stability or crystallinity, the inherent difficulty in preparing a homogeneous distribution of the substituting cations as well as maintaining that distribution over time (avoiding moisture or photo-induced segregation and degradation) will tend to lead to the films eventually degrading. Future and ongoing work as a result shall and does focus on use of additives to template the growth or orientation of the perovskite structure and protect it from moisture and O$_2$ ingress, while not incorporating into the perovskite structure or inhibiting charge extraction. These are challenges, but probably surmountable ones.

Ambient fabrication of perovskite solar cells has received less attention than fabrication in controlled and inert atmposhere, and devising reliable and scalable strategies for attaining moisture tolerant fabrication will relax the atmospheric control requirements for preparing PSC's in the future. Key to achieving this will be a thorough and mechanistic understanding of the various stages of thin film formation (and degradation), and this thesis has added to that understanding in the areas of 1) interplay of MAI excess with EA in MAPbI$_3$ thin film formation in ambient atmosphere, 2) phase segregation and grain fragmentation of mixed cation, mixed halide perovskites from moisture exposure, and finally 3) the characterisation of Zn-incorporating perovskite films before and after exposure to external stressors of heat, moisture, and light, showing the poor thermal stability.

10 Acknowledgements

References

11 References

(1) Temperatures | Climate Action Tracker. 2021.

(2) COP27: UN Chief Warns World Is on Path to "climate Hell" – DW – 11/07/2022.

(3) Masson-Delmotte, V., P. Zhai, H.-O. Pörtner, D. Roberts, J. Skea, P.R. Shukla, A. Pirani, W. Moufouma-Okia, C. Péan, R. Pidcock, S. Connors, J.B.R. Matthews, Y. Chen, X. Zhou, M.I. Gomis, E. Lonnoy, T. Maycock, M. Tignor, and T. W. (eds. . IPCC, 2018: Summary for Policymakers. In: Global Warming of 1.5°C. An IPCC Special Report on the impacts of global warming of 1.5°C above pre-industrial levels and related global greenhouse gas emission pathways, in the context of strengthening the global.

(4) DESA. World Population Prospects 2022 : Summary of Results Ten Key Messages. *United Nations , Dep. Econ. Soc. Aff. , Popul. Div.* **2022**, No. July 2022, 2–3.

(5) Ritchie, H.; Roser, M.; Rosado, P. Energy https://ourworldindata.org/energy.

(6) Coddington, O.; Lean, J. L.; Pilewskie, P.; Snow, M.; Lindholm, D. A Solar Irradiance Climate Data Record. *Bull. Am. Meteorol. Soc.* **2016**, *97* (7), 1265–1282. https://doi.org/10.1175/BAMS-D-14-00265.1.

(7) Philipps, S.; Ise, F.; Warmuth, W.; Projects GmbH, P. Photovoltaics Report.

(8) Green, M. A.; Emery, K.; King, D. L.; Igari, S.; Warta, W. Solar Cell Efficiency Tables (Version 24). *Prog. Photovoltaics Res. Appl.* **2004**, *12* (5), 365–372. https://doi.org/10.1002/pip.574.

(9) Zhang, W.; Eperon, G. E.; Snaith, H. J. Metal Halide Perovskites for Energy Applications. *Nat. Energy* **2016**, *1* (6). https://doi.org/10.1038/nenergy.2016.48.

(10) Teixeira, C.; Spinelli, P.; Castriotta, L. A.; Müller, D.; Öz, S.; Andrade, L.; Mendes, A.; Carlo, A. Di; Würfel, U.; Wojciechowski, K.; et al. Charge Extraction in Flexible Perovskite Solar Cell Architectures for Indoor Applications – with up to 31% Efficiency. *Adv. Funct. Mater.* **2022**, *32* (40), 2206761. https://doi.org/10.1002/adfm.202206761.

(11) Hanusch, F. C.; Wiesenmayer, E.; Mankel, E.; Binek, A.; Angloher, P.; Fraunhofer, C.; Giesbrecht, N.; Feckl, J. M.; Jaegermann, W.; Johrendt, D.; et al. Efficient Planar Heterojunction Perovskite Solar Cells Based on Formamidinium Lead Bromide. *J. Phys. Chem. Lett.* **2014**, *5* (16), 2791–2795. https://doi.org/10.1021/jz501237m.

(12) Rossi, D.; Forberich, K.; Matteocci, F.; Auf der Maur, M.; Egelhaaf, H.-J.; Brabec, C. J.; Di Carlo, A. Design of Highly Efficient Semitransparent Perovskite/Organic Tandem Solar Cells. *Sol. RRL* **2022**, *6* (9), 2200242. https://doi.org/10.1002/solr.202200242.

(13) Kim, S.; Oh, H.; Kang, G.; Han, I. K.; Jeong, I.; Park, M. High-Power and Flexible Indoor Solar Cells via Controlled Growth of Perovskite Using a Greener Antisolvent. *ACS Appl. Energy Mater.* **2020**, *3* (7), 6995–7003. https://doi.org/10.1021/acsaem.0c00997.

(14) Deng, Y.; Wang, Q.; Yuan, Y.; Huang, J. Vividly Colorful Hybrid Perovskite Solar Cells by Doctor-Blade Coating with Perovskite Photonic Nanostructures. *Mater. Horizons* **2015**, *2* (6), 578–583. https://doi.org/10.1039/c5mh00126a.

(15) Swanson, R. M. A Vision for Crystalline Silicon Photovoltaics. *Prog. Photovoltaics Res. Appl.* **2006**, *14* (5), 443–453. https://doi.org/10.1002/pip.709.

(16) Solar PV Prices Will Fall Below $1.00 per Watt by 2020 | FUELSAVE – Green Technology.

(17) Utility-Scale PV | Electricity | 2022 | ATB | NREL https://atb.nrel.gov/electricity/2022/utility-scale_pv (accessed Mar 22, 2023).

(18) Jäger-Waldau, A. *European Commission PV Status Report 2017*; 2017. https://doi.org/10.2760/452611.

(19) Module demand to pick up as prices stabilize-Industry-InfoLink Consulting https://www.infolink-group.com/energy-article/pv-spot-price-20230315 (accessed Mar 22, 2023).

(20) Shankleman, J.; Martin, C. Solar Could Beat Coal to Become the Cheapest Power on Earth - Bloomberg.

(21) Martin, C. Solar Panels Now So Cheap Manufacturers Probably Selling at Loss - Bloomberg.

(22) Evans, S.; Gabbatiss, J. Solar is now 'cheapest electricity in history', confirms IEA.

(23) Valero, A. Why have energy bills in the UK been rising? | British Politics and Policy at LSE https://blogs.lse.ac.uk/politicsandpolicy/why-have-energy-bills-in-the-uk-been-rising-net-zero/ (accessed Mar 22, 2023).

(24) Why are global gas prices so high? - BBC News https://www.bbc.co.uk/news/explainers-62644537 (accessed Mar 22, 2023).

(25) United Kingdom Electricity Price - 2023 Data - 2013-2022 Historical - 2024 Forecast https://tradingeconomics.com/united-kingdom/electricity-price (accessed Mar 22, 2023).

(26) Snaith, H. J.; Lilliu, S. The Path to Perovskite on Silicon PV. *Sci. Video Protoc.* **2018**, *1* (1), 1–8. https://doi.org/10.32386/scivpro.000004.

(27) Hook, L. Alternative to silicon offers cheaper solar power | Financial Times.

(28) Galagan, Y.; Coenen, E. W. C.; Verhees, W. J. H.; Andriessen, R. Towards the Scaling up of Perovskite Solar Cells and Modules. *J. Mater. Chem. A* **2016**, *4* (15), 5700–5705. https://doi.org/10.1039/c6ta01134a.

(29) Feng, A.; Saha, S. Chinese Heavy Metal: How Beijing Could Use Rare Earths to Outplay America - Scientific American Blog Network.

(30) Fröhlich, P.; Lorenz, T.; Martin, G.; Brett, B.; Bertau, M. *World Mineral Production*; 2017; Vol. 56. https://doi.org/10.1002/anie.201605417.

(31) Shockley, W.; Queisser, H. J. Detailed Balance Limit of Efficiency of P-n Junction Solar Cells. *J. Appl. Phys.* **1961**, *32* (3), 510–519. https://doi.org/10.1063/1.1736034.

(32) Nayak, P. K.; Mahesh, S.; Snaith, H. J.; Cahen, D. Photovoltaic Solar Cell Technologies: Analysing the State of the Art. *Nat. Rev. Mater.* **2019**, *4* (4), 269–285. https://doi.org/10.1038/s41578-019-0097-0.

(33) Hwang, T.; Lee, B.; Kim, J.; Lee, S.; Gil, B.; Yun, A. J.; Park, B. From Nanostructural Evolution to Dynamic Interplay of Constituents: Perspectives for Perovskite Solar Cells. *Adv. Mater.* **2018**, *1704208*, 1–22. https://doi.org/10.1002/adma.201704208.

(34) Hazen, R. M. Perovskites Gives Rise to Materials That Have a Wide Array of Electrical Properties. **1988**, *258* (June), 74–81.

(35) Weber, D. CH 3 NH 3 PbX 3 , Ein Pb(II)-System Mit Kubischer Perowskitstruktur / CH 3 NH 3 PbX 3 , a Pb(II)-System with Cubic

References

Perovskite Structure . *Zeitschrift für Naturforsch. B* **1978**, *33* (12), 1443–1445. https://doi.org/10.1515/znb-1978-1214.

(36) Ong, K. P.; Goh, T. W.; Xu, Q.; Huan, A. Mechanical Origin of the Structural Phase Transition in Methylammonium Lead Iodide CH3NH3PbI3. *J. Phys. Chem. Lett.* **2015**, *6* (4), 681–685. https://doi.org/10.1021/jz502740d.

(37) Ghosh, D.; Atkins, P. W.; Islam, M. S.; Walker, A. B.; Eames, C. Good Vibrations : Locking of Octahedral Tilting. **2017**, 2–7. https://doi.org/10.1021/acsenergylett.7b00729.

(38) Goldschmidt, V. M. Die Gesetze Der Krystallochemie. *Naturwissenschaften* **1926**, *14* (21), 477–485. https://doi.org/10.1007/BF01507527.

(39) Mao, L.; Ke, W.; Pedesseau, L.; Wu, Y.; Katan, C.; Even, J.; Wasielewski, M. R.; Stoumpos, C. C.; Kanatzidis, M. G. Hybrid Dion–Jacobson 2D Lead Iodide Perovskites. *J. Am. Chem. Soc.* **2018**, *140* (10), 3775–3783. https://doi.org/10.1021/jacs.8b00542.

(40) Assadi, M. K.; Bakhoda, S.; Saidur, R.; Hanaei, H. Recent Progress in Perovskite Solar Cells. *Renew. Sustain. Energy Rev.* **2018**, *81* (June 2017), 2812–2822. https://doi.org/10.1016/j.rser.2017.06.088.

(41) Watthage, S. C.; Ellingson, R. J.; Heben, M. J.; Tompkins, B. L.; Song, Z.; Phillips, A. B. Impact of Processing Temperature and Composition on the Formation of Methylammonium Lead Iodide Perovskites. *Chem. Mater.* **2015**, *27* (13), 4612–4619. https://doi.org/10.1021/acs.chemmater.5b01017.

(42) Beecher, A. N.; Semonin, O. E.; Skelton, J. M.; Frost, J. M.; Terban, M. W.; Zhai, H.; Alatas, A.; Owen, J. S.; Walsh, A.; Billinge, S. J. L. Direct Observation of Dynamic Symmetry Breaking above Room Temperature in Methylammonium Lead Iodide Perovskite. *ACS Energy Lett.* **2016**, *1* (4), 880–887. https://doi.org/10.1021/acsenergylett.6b00381.

(43) Shimamura, K.; Hakamata, T.; Shimojo, F.; Kalia, R. K.; Nakano, A.; Vashishta, P. Rotation Mechanism of Methylammonium Molecules in Organometal Halide Perovskite in Cubic Phase: An Ab Initio Molecular Dynamics Study. *Journal of Chemical Physics*. 2016. https://doi.org/10.1063/1.4971791.

(44) Bernasconi, A.; Malavasi, L. Direct Evidence of Permanent Octahedra Distortion in MAPbBr3 Hybrid Perovskite. *ACS Energy Lett.* **2017**, *2* (4), 863–868. https://doi.org/10.1021/acsenergylett.7b00139.

(45) Ran, C.; Xu, J.; Gao, W.; Huang, C.; Dou, S. Defects in Metal Triiodide Perovskite Materials towards High-Performance Solar Cells: Origin, Impact, Characterization, and Engineering. *Chem. Soc. Rev.* **2018**, *47* (12), 4581–4610. https://doi.org/10.1039/c7cs00868f.

(46) Kovalenko, M. V; Protesescu, L.; Bodnarchuk, M. I. Properties and Potential Optoelectronic Applications of Lead Halide Perovskite Nanocrystals. *Science* **2017**, *358* (6364), 745–750. https://doi.org/10.1126/science.aam7093.

(47) Buin, A.; Pietsch, P.; Xu, J.; Voznyy, O.; Ip, A. H.; Comin, R.; Sargent, E. H. Materials Processing Routes to Trap-Free Halide Perovskites. *Nano Lett.* **2014**, *14* (11), 6281–6286. https://doi.org/10.1021/nl502612m.

(48) Comin, R.; Ip, A. H.; Sargent, E. H.; Buin, A.; Xu, J. Halide-Dependent Electronic Structure of Organolead Perovskite Materials. *Chem. Mater.* **2015**, *27* (12), 4405–4412. https://doi.org/10.1021/acs.chemmater.5b01909.

(49) Yin, W. J.; Shi, T.; Yan, Y. Unusual Defect Physics in CH3NH3PbI3perovskite Solar Cell Absorber. *Appl. Phys. Lett.* **2014**, *104* (6). https://doi.org/10.1063/1.4864778.

(50) Chen, J.; Park, N.-G. Causes and Solutions of Recombination in Perovskite Solar Cells. *Adv. Mater.* **2018**, *1803019*, 1803019. https://doi.org/10.1002/adma.201803019.

(51) Lee, J. W.; Kim, S. G.; Bae, S. H.; Lee, D. K.; Lin, O.; Yang, Y.; Park, N. G. The Interplay between Trap Density and Hysteresis in Planar Heterojunction Perovskite Solar Cells. *Nano Lett.* **2017**, *17* (7), 4270–4276. https://doi.org/10.1021/acs.nanolett.7b01211.

(52) Zhao, P.; Kim, B. J.; Jung, H. S. Passivation in Perovskite Solar Cells: A Review. *Materials Today Energy*. Elsevier Ltd March 2018, pp 267–286. https://doi.org/10.1016/j.mtener.2018.01.004.

(53) Yoo, H. S.; Park, N. G. Post-Treatment of Perovskite Film with Phenylalkylammonium Iodide for Hysteresis-Less Perovskite Solar Cells. *Sol. Energy Mater. Sol. Cells* **2018**, *179* (February), 57–65. https://doi.org/10.1016/j.solmat.2018.02.015.

(54) Braly, I. L.; Dequilettes, D. W.; Pazos-Outón, L. M.; Burke, S.; Ziffer, M. E.; Ginger, D. S.; Hillhouse, H. W. Hybrid Perovskite Films Approaching the Radiative Limit with over 90% Photoluminescence Quantum Efficiency. *Nat. Photonics* **2018**, *12* (6), 355–361. https://doi.org/10.1038/s41566-018-0154-z.

(55) Aristidou, N.; Eames, C.; Sanchez-Molina, I.; Bu, X.; Kosco, J.; Saiful Islam, M.; Haque, S. A. Fast Oxygen Diffusion and Iodide Defects Mediate Oxygen-Induced Degradation of Perovskite Solar Cells. *Nat. Commun.* **2017**, *8* (May), 1–10. https://doi.org/10.1038/ncomms15218.

(56) Rolston, N.; Watson, B. L.; Dauskardt, R. H. Mechanical Integrity of Solution-Processed Perovskite Solar Cells. *2017 IEEE 44th Photovolt. Spec. Conf. PVSC 2017* **2018**, *9*, 1–2. https://doi.org/10.1109/PVSC.2017.8366127.

(57) Chu, Z.; Yang, M.; Schulz, P.; Wu, D.; Ma, X.; Seifert, E.; Sun, L.; Li, X.; Zhu, K.; Lai, K. Impact of Grain Boundaries on Efficiency and Stability of Organic-Inorganic Trihalide Perovskites. *Nat. Commun.* **2017**, *8* (1), 1–8. https://doi.org/10.1038/s41467-017-02331-4.

(58) Stolterfoht, M.; Wolff, C. M.; Amir, Y.; Paulke, A.; Perdigón-Toro, L.; Caprioglio, P.; Neher, D. Approaching the Fill Factor Shockley-Queisser Limit in Stable, Dopant-Free Triple Cation Perovskite Solar Cells. *Energy Environ. Sci.* **2017**, *10* (6), 1530–1539. https://doi.org/10.1039/c7ee00899f.

(59) Dänekamp, B.; Droseros, N.; Palazon, F.; Sessolo, M.; Banerji, N.; Bolink, H. J. Efficient Photo- and Electroluminescence by Trap States Passivation in Vacuum-Deposited Hybrid Perovskite Thin Films. *ACS Appl. Mater. Interfaces* **2018**, *10* (42), 36187–36193. https://doi.org/10.1021/acsami.8b13100.

(60) Jones, T. W.; Osherov, A.; Alsari, M.; Sponseller, M.; Duck, B. C.; Jung, Y.-K.; Settens, C.; Niroui, F.; Brenes, R.; Stan, C. V.; et al. Local Strain Heterogeneity Influences the Optoelectronic Properties of Halide Perovskites. *aRXIV* **2018**, No. April, arXiv:1803.01192.

(61) Dar, M. I.; Hinderhofer, A.; Jacopin, G.; Belova, V.; Arora, N.; Zakeeruddin, S. M.; Schreiber, F.; Grätzel, M. Function Follows Form: Correlation between the Growth and Local Emission of Perovskite Structures and the Performance of Solar Cells. *Adv. Funct. Mater.* **2017**, *27* (26), 1–9. https://doi.org/10.1002/adfm.201701433.

(62) Zhao, L.; Kerner, R. A.; Xiao, Z.; Lin, Y. L.; Lee, K. M.; Schwartz, J.; Rand, B. P. Redox Chemistry Dominates the Degradation and

References

Decomposition of Metal Halide Perovskite Optoelectronic Devices. *ACS Energy Lett.* **2016**, *1* (3), 595–602. https://doi.org/10.1021/acsenergylett.6b00320.

(63) Meier, T.; Gujar, T. P.; Schönleber, A.; Olthof, S.; Meerholz, K.; Van Smaalen, S.; Panzer, F.; Thelakkat, M.; Köhler, A. Impact of Excess PbI 2 on the Structure and the Temperature Dependent Optical Properties of Methylammonium Lead Iodide Perovskites. *J. Mater. Chem. C* **2018**, *6* (28), 7512–7519. https://doi.org/10.1039/c8tc02237b.

(64) Jacobsson, T. J.; Correa-Baena, J. P.; Halvani Anaraki, E.; Philippe, B.; Stranks, S. D.; Bouduban, M. E. F.; Tress, W.; Schenk, K.; Teuscher, J.; Moser, J. E.; et al. Unreacted PbI2 as a Double-Edged Sword for Enhancing the Performance of Perovskite Solar Cells. *J. Am. Chem. Soc.* **2016**, *138* (32), 10331–10343. https://doi.org/10.1021/jacs.6b06320.

(65) Gujar, T. P.; Unger, T.; Schönleber, A.; Fried, M.; Panzer, F.; van Smaalen, S.; Köhler, A.; Thelakkat, M. The Role of PbI 2 in CH 3 NH 3 PbI 3 Perovskite Stability, Solar Cell Parameters and Device Degradation. *Phys. Chem. Chem. Phys.* **2018**, *20* (1), 605–614. https://doi.org/10.1039/C7CP04749E.

(66) Shi, B.; Yao, X.; Hou, F.; Guo, S.; Li, Y.; Wei, C.; Ding, Y.; Li, Y.; Zhao, Y.; Zhang, X. Unraveling the Passivation Process of PbI 2 to Enhance the Efficiency of Planar Perovskite Solar Cells. *J. Phys. Chem. C* **2018**, *122* (37), 21269–21276. https://doi.org/10.1021/acs.jpcc.8b08075.

(67) Euvrard, J.; Gunawan, O.; Mitzi, D. B. Impact of PbI2 Passivation and Grain Size Engineering in CH3NH3PbI3 Solar Absorbers as Revealed by Carrier-Resolved Photo-Hall Technique. *Adv. Energy Mater.* **2019**, *9* (47), 1–10. https://doi.org/10.1002/aenm.201902706.

(68) Petrus, M. L.; Hu, Y.; Moia, D.; Calado, P.; Leguy, A. M. A.; Barnes, P. R. F.; Docampo, P. The Influence of Water Vapor on the Stability and Processing of Hybrid Perovskite Solar Cells Made from Non-Stoichiometric Precursor Mixtures. *ChemSusChem* **2016**, *9* (18), 2699–2707. https://doi.org/10.1002/cssc.201600999.

(69) Roose, B.; Dey, K.; Chiang, Y. H.; Friend, R. H.; Stranks, S. D. Critical Assessment of the Use of Excess Lead Iodide in Lead Halide Perovskite Solar Cells. *J. Phys. Chem. Lett.* **2020**, *11* (16), 6505–6512. https://doi.org/10.1021/acs.jpclett.0c01820.

(70) Tumen-Ulzii, G.; Qin, C.; Klotz, D.; Leyden, M. R.; Wang, P.; Auffray, M.; Fujihara, T.; Matsushima, T.; Lee, J. W.; Lee, S. J.; et al. Detrimental Effect of Unreacted PbI2 on the Long-Term Stability of Perovskite Solar Cells. *Adv. Mater.* **2020**, *32* (16). https://doi.org/10.1002/adma.201905035.

(71) Sakai, N.; Wang, Z.; Burlakov, V. M.; Lim, J.; McMeekin, D.; Pathak, S.; Snaith, H. J. Controlling Nucleation and Growth of Metal Halide Perovskite Thin Films for High-Efficiency Perovskite Solar Cells. *Small* **2017**, *13* (14), 1–8. https://doi.org/10.1002/smll.201602808.

(72) Liao, K.; Yang, J.; Li, C.; Li, T.; Hao, F. Off-Stoichiometric Methylammonium Iodide Passivated Large-Grain Perovskite Film in Ambient Air for Efficient Inverted Solar Cells. *ACS Appl. Mater. Interfaces* **2019**, *11* (43), 39882–39889. https://doi.org/10.1021/acsami.9b12829.

(73) Guo, R.; Dahal, B.; Thapa, A.; Poudel, Y. R.; Liu, Y.; Li, W. Ambient Processed (110) Preferred MAPbI 3 Thin Films for Highly Efficient Perovskite Solar Cells. *Nanoscale Adv.* **2021**. https://doi.org/10.1039/D0NA01029D.

(74) Docampo, P.; Hanusch, F. C.; Giesbrecht, N.; Angloher, P.; Ivanova, A.; Bein, T. Influence of the Orientation of Methylammonium Lead Iodide Perovskite Crystals on Solar Cell Performance. *APL Mater.* **2014**, *2* (8). https://doi.org/10.1063/1.4890244.

(75) Kavadiya, S.; Strzalka, J.; Niedzwiedzki, D. M.; Biswas, P. Crystal Reorientation in Methylammonium Lead Iodide Perovskite Thin Film with Thermal Annealing. *J. Mater. Chem. A* **2019**, *7* (20), 12790–12799. https://doi.org/10.1039/c9ta02358e.

(76) Dhamaniya, B. P.; Chhillar, P.; Roose, B.; Dutta, V.; Pathak, S. Unravelling the Effect of Crystal Structure on Degradation of Methylammonium Lead Halide Perovskite. *ACS Appl. Mater. Interfaces* **2019**, acsami.9b00831. https://doi.org/10.1021/acsami.9b00831.

(77) Munir, R.; Sheikh, A. D.; Abdelsamie, M.; Hu, H.; Yu, L.; Zhao, K.; Kim, T.; Tall, O. El; Li, R.; Smilgies, D.-M.; et al. Hybrid Perovskite Thin-Film Photovoltaics: In Situ Diagnostics and Importance of the Precursor Solvate Phases. *Adv. Mater.* **2017**, *29* (2), 1604113. https://doi.org/10.1002/adma.201604113.

(78) Zhang, W.; Saliba, M.; Moore, D. T.; Pathak, S. K.; Hörantner, M. T.; Stergiopoulos, T.; Stranks, S. D.; Eperon, G. E.; Alexander-Webber, J. A.; Abate, A.; et al. Ultrasmooth Organic-Inorganic Perovskite Thin-Film Formation and Crystallization for Efficient Planar Heterojunction Solar Cells. *Nat. Commun.* **2015**, *6*. https://doi.org/10.1038/ncomms7142.

(79) Zhang, X.; Turiansky, M. E.; Shen, J. X.; Van De Walle, C. G. Iodine Interstitials as a Cause of Nonradiative Recombination in Hybrid Perovskites. *Phys. Rev. B* **2020**, *101* (14), 140101. https://doi.org/10.1103/PhysRevB.101.140101.

(80) Cao, J.; Jing, X.; Yan, J.; Hu, C.; Chen, R.; Yin, J.; Li, J.; Zheng, N. Identifying the Molecular Structures of Intermediates for Optimizing the Fabrication of High-Quality Perovskite Films. *J. Am. Chem. Soc.* **2016**, *138* (31), 9919–9926. https://doi.org/10.1021/jacs.6b04924.

(81) Zhang, X.; Shen, J. X.; Turiansky, M. E.; Van de Walle, C. G. Minimizing Hydrogen Vacancies to Enable Highly Efficient Hybrid Perovskites. *Nat. Mater.* **2021**, *20* (7), 971–976. https://doi.org/10.1038/s41563-021-00986-5.

(82) Fan, W.; Deng, K.; Shen, Y.; Bai, Y.; Li, L. Moisture Accelerated Precursor Crystallization in Ambient Air for High-performance Perovskite Solar Cells toward Mass Production. *Angew. Chemie* **2022**, *215006*. https://doi.org/10.1002/ange.202211259.

(83) Tsevas, K.; Smith, J. A.; Kumar, V.; Rodenburg, C.; Fakis, M.; Mohd Yusoff, A. R. Bin; Vasilopoulou, M.; Lidzey, D. G.; Nazeeruddin, M. K.; Dunbar, A. D. F. Controlling PbI2Stoichiometry during Synthesis to Improve the Performance of Perovskite Photovoltaics. *Chem. Mater.* **2021**, *33* (2), 554–566. https://doi.org/10.1021/acs.chemmater.0c03517.

(84) Belous, A.; Kobylianska, S.; V'yunov, O.; Torchyniuk, P.; Yukhymchuk, V.; Hreshchuk, O. Effect of Non-Stoichiometry of Initial Reagents on Morphological and Structural Properties of Perovskites CH 3 NH 3 PbI 3. *Nanoscale Res. Lett.* **2019**, *14*. https://doi.org/10.1186/s11671-018-2841-6.

(85) Mohammed, O. F.; Maculan, G.; Wu, T.; Wang, L.; Saidaminov, M. I.; Bakr, O. M.; Goriely, A.; Peng, W.; He, Y.; Dursun, I.; et al. High-Quality Bulk Hybrid Perovskite Single Crystals within Minutes by Inverse Temperature Crystallization. *Nat. Commun.* **2015**, *6* (1), 1–6. https://doi.org/10.1038/ncomms8586.

(86) Lamer, V. K.; Dinegar, R. H. Theory, Production and Mechanism of Formation of Monodispersed Hydrosols. *J. Am. Chem. Soc.*

139

References

1950, *72* (11), 4847–4854. https://doi.org/10.1021/ja01167a001.

(87)   Zhou, Y.; Game, O. S.; Pang, S.; Padture, N. P. Microstructures of Organometal Trihalide Perovskites for Solar Cells: Their Evolution from Solutions and Characterization. *J. Phys. Chem. Lett.* **2015**, *6* (23), 4827–4839. https://doi.org/10.1021/acs.jpclett.5b01843.

(88)   Venables, J. A.; Spiller, G. D. T. Nucleation and Growth of Thin Films. *Surf. Mobilities Solid Mater.* **1983**, *47* (4), 341–404. https://doi.org/10.1007/978-1-4684-4343-1_16.

(89)   Voorhees, P. W. Ostwald Ripening of Two-Phase Mixtures. **1992**, 197–215.

(90)   Chen, S.; Xiao, X.; Chen, B.; Kelly, L. L.; Zhao, J.; Lin, Y.; Toney, M. F.; Huang, J. Crystallization in One-Step Solution Deposition of Perovskite Films: Upward or Downward? *Sci. Adv.* **2021**, *7* (4), 26–29. https://doi.org/10.1126/sciadv.abb2412.

(91)   Zheng, D.; Raffin, F.; Volovitch, P.; Pauporté, T. Control of Perovskite Film Crystallization and Growth Direction to Target Homogeneous Monolithic Structures. *Nat. Commun.* **2022**, *13* (1), 6655. https://doi.org/10.1038/s41467-022-34332-3.

(92)   Mrkyvkova, N.; Held, V.; Nádaždy, P.; Subair, R.; Majkova, E.; Jergel, M.; Vlk, A.; Ledinsky, M.; Kotlár, M.; Tian, J.; et al. Combined in Situ Photoluminescence and X-Ray Scattering Reveals Defect Formation in Lead-Halide Perovskite Films. *J. Phys. Chem. Lett.* **2021**, *12* (41), 10156–10162. https://doi.org/10.1021/acs.jpclett.1c02869.

(93)   Zhu, W.; Bao, C.; Wang, Y.; Li, F.; Zhou, X.; Yang, J.; Lv, B.; Wang, X.; Yu, T.; Zou, Z. Coarsening of One-Step Deposited Organolead Triiodide Perovskite Films: Via Ostwald Ripening for High Efficiency Planar-Heterojunction Solar Cells. *Dalt. Trans.* **2016**, *45* (18), 7856–7865. https://doi.org/10.1039/c6dt00900j.

(94)   Kim, T. W.; Shibayama, N.; Cojocaru, L.; Uchida, S.; Kondo, T.; Segawa, H. Real-Time In Situ Observation of Microstructural Change in Organometal Halide Perovskite Induced by Thermal Degradation. *Adv. Funct. Mater.* **2018**, *1804039*, 1–8. https://doi.org/10.1002/adfm.201804039.

(95)   Divitini, G.; Cacovich, S.; Matteocci, F.; Cinà, L.; Di Carlo, A.; Ducati, C. In Situ Observation of Heat-Induced Degradation of Perovskite Solar Cells. *Nat. Energy* **2016**, *1* (2), 15012. https://doi.org/10.1038/NENERGY.2015.12.

(96)   Dualeh, A.; Tétreault, N.; Moehl, T.; Gao, P.; Nazeeruddin, M. K.; Grätzel, M. Effect of Annealing Temperature on Film Morphology of Organic-Inorganic Hybrid Pervoskite Solid-State Solar Cells. *Adv. Funct. Mater.* **2014**, *24* (21), 3250–3258. https://doi.org/10.1002/adfm.201304022.

(97)   Pool, V. L.; Dou, B.; Van Campen, D. G.; Klein-Stockert, T. R.; Barnes, F. S.; Shaheen, S. E.; Ahmad, M. I.; Van Hest, M. F. A. M.; Toney, M. F. Thermal Engineering of FAPbI3perovskite Material via Radiative Thermal Annealing and in Situ XRD. *Nat. Commun.* **2017**, *8*, 1–8. https://doi.org/10.1038/ncomms14075.

(98)   Jeon, N. J.; Noh, J. H.; Kim, Y. C.; Yang, W. S.; Ryu, S.; Seok, S. Il. Solvent Engineering for High-Performance Inorganic-Organic Hybrid Perovskite Solar Cells. *Nat. Mater.* **2014**, *13* (9), 897–903. https://doi.org/10.1038/nmat4014.

(99)   Gedamu, D.; Asuo, I. M.; Benetti, D.; Basti, M.; Ka, I.; Cloutier, S. G.; Rosei, F.; Nechache, R. Solvent-Antisolvent Ambient Processed Large Grain Size Perovskite Thin Films for High-Performance Solar Cells. *Sci. Rep.* **2018**, *8* (1), 12885. https://doi.org/10.1038/s41598-018-31184-0.

(100)   Kong, M.; Hu, H.; Egbo, K.; Dong, B.; Wan, L.; Wang, S. Anti-Solvent Assisted Treatment for Improved Morphology and Efficiency of Lead Acetate Derived Perovskite Solar Cells. *Chinese Chem. Lett.* **2019**, *30* (6), 1325–1328. https://doi.org/10.1016/j.cclet.2019.03.006.

(101)   Noel, N. K.; Habisreutinger, S. N.; Wenger, B.; Klug, M. T.; Hörantner, M. T.; Johnston, M. B.; Nicholas, R. J.; Moore, D. T.; Snaith, H. J. A Low Viscosity, Low Boiling Point, Clean Solvent System for the Rapid Crystallisation of Highly Specular Perovskite Films. *Energy Environ. Sci.* **2017**, *10* (1), 145–152. https://doi.org/10.1039/c6ee02373h.

(102)   Li, X.; Bi, D.; Yi, C.; Décoppet, J.; Luo, J.; Zakeeruddin, S. M.; Hagfeldt, A.; Grätzel, M. A Vacuum Flash–Assisted Solution Process for High-Efficiency Large-Area Perovskite Solar Cells. *Science (80-.).* **2016**, *353* (6294), 58–62. https://doi.org/10.1126/science.aaf8060.

(103)   Ding, B.; Gao, L.; Liang, L.; Chu, Q.; Song, X.; Li, Y.; Yang, G.; Fan, B.; Wang, M.; Li, C.; et al. Facile and Scalable Fabrication of Highly Efficient Lead Iodide Perovskite Thin-Film Solar Cells in Air Using Gas Pump Method. *ACS Appl. Mater. Interfaces* **2016**, *8* (31), 20067–20073. https://doi.org/10.1021/acsami.6b05862.

(104)   Conings, B.; Babayigit, A.; Klug, M.; Bai, S.; Gauquelin, N.; Sakai, N.; Wang, J. T. W.; Verbeeck, J.; Boyen, H. G.; Snaith, H. Getting Rid of Anti-Solvents: Gas Quenching for High Performance Perovskite Solar Cells. In *2018 IEEE 7th World Conference on Photovoltaic Energy Conversion, WCPEC 2018 - A Joint Conference of 45th IEEE PVSC, 28th PVSEC and 34th EU PVSEC*; 2018; pp 1724–1729. https://doi.org/10.1109/PVSC.2018.8547987.

(105)   Huang, J.; Xiao, Z.; Dong, Q.; Yuan, Y.; Shao, Y.; Bi, C. Solvent Annealing of Perovskite-Induced Crystal Growth for Photovoltaic-Device Efficiency Enhancement. *Adv. Mater.* **2014**, *26* (37), 6503–6509. https://doi.org/10.1002/adma.201401685.

(106)   Jung, M.; Ji, S.-G.; Kim, G.; Seok, S. Il. Perovskite Precursor Solution Chemistry: From Fundamentals to Photovoltaic Applications. *Chem. Soc. Rev.* **2019**. https://doi.org/10.1039/c8cs00656c.

(107)   Kerner, R. A.; Zhao, L.; Xiao, Z.; Rand, B. P. Ultrasmooth Metal Halide Perovskite Thin Films: Via Sol-Gel Processing. *J. Mater. Chem. A* **2016**, *4* (21), 8308–8315. https://doi.org/10.1039/c6ta03092k.

(108)   Guo, Y.; Shoyama, K.; Sato, W.; Matsuo, Y.; Inoue, K.; Harano, K.; Liu, C.; Tanaka, H.; Nakamura, E. Chemical Pathways Connecting Lead(II) Iodide and Perovskite via Polymeric Plumbate(II) Fiber. *J. Am. Chem. Soc.* **2015**, *137* (50), 15907–15914. https://doi.org/10.1021/jacs.5b10599.

(109)   Ahn, N.; Son, D.-Y. Y.; Jang, I.-H. H.; Kang, S. M.; Choi, M.; Park, N.-G. G.; Ahn, N.; Son, D.-Y. Y.; Park, N.-G. G.; Choi, M. Highly Reproducible Perovskite Solar Cells with Average Efficiency of 18.3% and Best Efficiency of 19.7% Fabricated via Lewis Base Adduct of Lead(II) Iodide. *J. Am. Chem. Soc.* **2015**, *137* (27), 8696–8699. https://doi.org/10.1021/jacs.5b04930.

(110)   Rong, Y.; Venkatesan, S.; Guo, R.; Wang, Y.; Bao, J.; Li, W.; Fan, Z.; Yao, Y. Critical Kinetic Control of Non-Stoichiometric Intermediate Phase Transformation for Efficient Perovskite Solar Cells. *Nanoscale* **2016**, *8* (26), 12892–12899. https://doi.org/10.1039/C6NR00488A.

(111)   Bai, Y.; Xiao, S.; Hu, C.; Zhang, T.; Meng, X.; Li, Q.; Yang, Y.; Wong, K. S.; Chen, H.; Yang, S. A Pure and Stable Intermediate Phase Is Key to Growing Aligned and Vertically Monolithic Perovskite Crystals for Efficient PIN Planar Perovskite Solar Cells

140

References

with High Processibility and Stability. *Nano Energy* **2017**, *34* (February), 58–68. https://doi.org/10.1016/j.nanoen.2017.02.019.

(112) Xiao, S.; Bai, Y.; Meng, X.; Zhang, T.; Chen, H.; Zheng, X.; Hu, C.; Qu, Y.; Yang, S. Unveiling a Key Intermediate in Solvent Vapor Postannealing to Enlarge Crystalline Domains of Organometal Halide Perovskite Films. *Adv. Funct. Mater.* **2017**, *27* (12), 1604944. https://doi.org/10.1002/adfm.201604944.

(113) Yang, W. S.; Noh, J. H.; Jeon, N. J.; Kim, Y. C.; Ryu, S.; Seo, J.; Seok, S. Il. High-Performance Photovoltaic Perovskite Layers Fabricated through Intramolecular Exchange. *Science (80-.).* **2015**, *348* (6240), 1234–1237. https://doi.org/10.1126/science.aaa9272.

(114) Dou, B.; Pool, V. L.; Toney, M. F.; Van Hest, M. F. A. M. Radiative Thermal Annealing/in Situ X-Ray Diffraction Study of Methylammonium Lead Triiodide: Effect of Antisolvent, Humidity, Annealing Temperature Profile, and Film Substrates. *Chem. Mater.* **2017**, *29* (14), 5931–5941. https://doi.org/10.1021/acs.chemmater.7b01467.

(115) Ozaki, M.; Shimazaki, A.; Jung, M.; Nakaike, Y.; Maruyama, N.; Yakumaru, S.; Rafieh, A. I.; Sasamori, T.; Tokitoh, N.; Ekanayake, P.; et al. A Purified, Solvent-Intercalated Precursor Complex for Wide Process Window Fabrication of Efficient Perovskite Solar Cells and Modules. *Angew. Chemie* **2019**, ange.201902235. https://doi.org/10.1002/ange.201902235.

(116) Huang, J.; Tan, S.; Lund, P. D.; Zhou, H. Impact of H2O on Organic-Inorganic Hybrid Perovskite Solar Cells. *Energy Environ. Sci.* **2017**, *10* (11), 2284–2311. https://doi.org/10.1039/c7ee01674c.

(117) Jeong, B.; Cho, S. M.; Cho, S. H.; Lee, J. H.; Hwang, I.; Hwang, S. K.; Cho, J.; Lee, T.-W.; Park, C. Humidity Controlled Crystallization of Thin CH 3 NH 3 PbI 3 Films for High Performance Perovskite Solar Cell. *Phys. status solidi - Rapid Res. Lett.* **2016**, *10* (5), 381–387. https://doi.org/10.1002/pssr.201600004.

(118) Aranda, C.; Cristobal, C.; Shooshtari, L.; Li, C.; Huettner, S.; Guerrero, A. Formation Criteria of High Efficiency Perovskite Solar Cells under Ambient Conditions. *Sustain. Energy Fuels* **2017**, *1* (3), 540–547. https://doi.org/10.1039/C6SE00077K.

(119) Zhang, W.; Li, Y.; Liu, X.; Tang, D.; Li, X.; Yuan, X. Ethyl Acetate Green Antisolvent Process for High-Performance Planar Low-Temperature SnO2-Based Perovskite Solar Cells Made in Ambient Air. *Chem. Eng. J.* **2020**, *379* (July 2019), 122298. https://doi.org/10.1016/j.cej.2019.122298.

(120) Yang, F.; Kapil, G.; Zhang, P.; Hu, Z.; Kamarudin, M. A.; Ma, T.; Hayase, S. Dependence of Acetate-Based Antisolvents for High Humidity Fabrication of CH 3 NH 3 PbI 3 Perovskite Devices in Ambient Atmosphere. *ACS Appl. Mater. Interfaces* **2018**, *10* (19), 16482–16489. https://doi.org/10.1021/acsami.8b02554.

(121) Wang, F.; Zhang, T.; Wang, Y.; Liu, D.; Zhang, P.; Chen, H.; Ji, L.; Chen, L.; Chen, Z. D.; Wu, J.; et al. Steering the Crystallization of Perovskites for High-Performance Solar Cells in Ambient Air. *J. Mater. Chem. A* **2019**, *7* (19), 12166–12175. https://doi.org/10.1039/C9TA02566A.

(122) Chen, W.-H.; Qiu, L.; Zhuang, Z.; Song, L.; Du, P.; Xiong, J.; Ko, F. Simple Fabrication of Perovskite Solar Cells with Enhanced Efficiency, Stability, and Flexibility under Ambient Air. *J. Power Sources* **2019**, *442* (September), 227216. https://doi.org/10.1016/j.jpowsour.2019.227216.

(123) Kim, S.; Jeong, I.; Park, C.; Kang, G.; Han, I. K.; Kim, W.; Park, M. Morphology Control of Perovskite in Green Antisolvent System for MAPbI3-Based Solar Cells with over 20% Efficiency. *Sol. Energy Mater. Sol. Cells* **2019**, *203* (August), 110197. https://doi.org/10.1016/j.solmat.2019.110197.

(124) Yang, W. S.; Noh, J. H.; Jeon, N. J.; Kim, Y. C.; Ryu, S.; Seo, J.; Seok, S. Il. High-Performance Photovoltaic Perovskite Layers Fabricated through Intramolecular Exchange. *Science (80-.).* **2015**, *348* (6240), 1234–1237. https://doi.org/10.1126/science.aaa9272.

(125) Ouyang, Z.; Abrams, H.; Bergstone, R.; Li, Q.; Zhu, F.; Li, D. Rapid Layer-Specific Annealing Enabled by Ultraviolet LED with Estimation of Crystallization Energy for High-Performance Perovskite Solar Cells. *Adv. Energy Mater.* **2020**, *10* (4), 1902898. https://doi.org/10.1002/aenm.201902898.

(126) Taylor, A. D.; Sun, Q.; Goetz, K. P.; An, Q.; Schramm, T.; Hofstetter, Y.; Litterst, M.; Paulus, F.; Vaynzof, Y. A General Approach to High-Efficiency Perovskite Solar Cells by Any Antisolvent. *Nat. Commun.* **2021**, *12* (1), 1–11. https://doi.org/10.1038/s41467-021-22049-8.

(127) Troughton, J.; Hooper, K.; Watson, T. M. Humidity Resistant Fabrication of CH3NH3PbI3 Perovskite Solar Cells and Modules. *Nano Energy* **2017**, *39* (June), 60–68. https://doi.org/10.1016/j.nanoen.2017.06.039.

(128) Kumar, Y.; Jaramillo-Quintero, O. A.; Jerónimo Rendon, J. J.; Perez, T. D.; Rincón, M. E.; Mathew, X. Short Duration High Temperature Thermal Processing to Reduce Interfacial Trapping States in Perovskite Solar Cells Obtained by a Green Route. *Sol. Energy* **2019**, *189* (June), 285–290. https://doi.org/10.1016/j.solener.2019.07.062.

(129) Bu, T.; Wu, L.; Liu, X.; Yang, X.; Zhou, P.; Yu, X.; Qin, T.; Shi, J.; Wang, S.; Li, S.; et al. Synergic Interface Optimization with Green Solvent Engineering in Mixed Perovskite Solar Cells. *Adv. Energy Mater.* **2017**, *7* (20), 1–10. https://doi.org/10.1002/aenm.201700576.

(130) Adhikari, N.; Dubey, A.; Gaml, E. A.; Vaagensmith, B.; Reza, K. M.; Mabrouk, S. A. A.; Gu, S.; Zai, J.; Qian, X.; Qiao, Q. Crystallization of a Perovskite Film for Higher Performance Solar Cells by Controlling Water Concentration in Methyl Ammonium Iodide Precursor Solution. *Nanoscale* **2016**, *8* (5), 2693–2703. https://doi.org/10.1039/c5nr06687e.

(131) Gao, H.; Bao, C.; Li, F.; Yu, T.; Yang, J.; Zhu, W.; Zhou, X.; Fu, G.; Zou, Z. Nucleation and Crystal Growth of Organic–Inorganic Lead Halide Perovskites under Different Relative Humidity. *ACS Appl. Mater. Interfaces* **2015**, *7* (17), 9110–9117. https://doi.org/10.1021/acsami.5b00895.

(132) You, J.; Hong, Z.; Song, T. Bin; Meng, L.; Liu, Y.; Jiang, C.; Zhou, H.; Chang, W. H.; Li, G.; Yang, Y. Moisture Assisted Perovskite Film Growth for High Performance Solar Cells. *Appl. Phys. Lett.* **2014**, *105* (18). https://doi.org/10.1063/1.4901510.

(133) Sánchez, S.; Jerónimo-rendon, J.; Saliba, M.; Hagfeldt, A. Highly Ef Fi Cient and Rapid Manufactured Perovskite Solar Cells via Flash InfraRed Annealing. **2020**, *xxx* (xx). https://doi.org/10.1016/j.mattod.2019.11.003.

(134) Conings, B.; Babayigit, A.; Klug, M.; Bai, S.; Gauquelin, N.; Sakai, N.; Tse-, J.; Wang, W.; Verbeeck, J.; Boyen, H.; et al. Getting Rid of Anti-Solvents : Gas Quenching for High Performance Perovskite Solar Cells. **2020**, 1724–1729.

(135) Brinkmann, K. O.; He, J.; Schubert, F.; Malerczyk, J.; Kreusel, C.; Hassend, F. Van; Weber, S.; Song, J.; Qu, J.; Riedl, T. Extremely Robust Gas Quenching Deposition of Halide Perovskites on Top of Hydrophobic Hole Transport Materials for Inverted (p-i-n)

141

References

Solar Cells by Targeting the Precursor Wetting Issue . **2019**. https://doi.org/10.1021/acsami.9b15867.

(136) Xie, F. X.; Zhang, D.; Su, H.; Ren, X.; Wong, K. S.; Grätzel, M.; Choy, W. C. H. Vacuum-Assisted Thermal Annealing of CH3NH3PbI3 for Highly Stable and Efficient Perovskite Solar Cells. *ACS Nano* **2015**, *9* (1), 639–646. https://doi.org/10.1021/nn505978r.

(137) Moore, D. T.; Sai, H.; Tan, K. W.; Smilgies, D. M.; Zhang, W.; Snaith, H. J.; Wiesner, U.; Estroff, L. A. Crystallization Kinetics of Organic-Inorganic Trihalide Perovskites and the Role of the Lead Anion in Crystal Growth. *J. Am. Chem. Soc.* **2015**, *137* (6), 2350–2358. https://doi.org/10.1021/ja512117e.

(138) Nie, W.; Tsai, H.; Asadpour, R.; Blancon, J.-C.; Neukirch, A. J.; Gupta, G.; Crochet, J. J.; Chhowalla, M.; Tretiak, S.; Alam, M. A.; et al. High-Efficiency Solution-Processed Perovskite Solar Cells with Millimeter-Scale Grains. *Science (80-.).* **2015**, *347* (6221), 522–525. https://doi.org/10.1126/science.aaa0472.

(139) Molenda, Z.; Chambon, S.; Bassani, D. M.; Hirsch, L. Assessing the Impact of Ambient Fabrication Temperature on the Performance of Planar CH3NH3PbI3 Perovskite Solar Cells. *Eur. J. Inorg. Chem.* **2021**, *2021* (25), 2533–2538. https://doi.org/10.1002/ejic.202100329.

(140) Park, B.; Seok, S. Il. Intrinsic Instability of Inorganic-Organic Hybrid Halide Perovskite Materials. *Adv. Mater.* **2019**, *1805337*, 1805337. https://doi.org/10.1002/adma.201805337.

(141) Saliba, M.; Matsui, T.; Seo, J.-Y.; Domanski, K.; Correa-Baena, J.-P.; Nazeeruddin, M. K.; Zakeeruddin, S. M.; Tress, W.; Abate, A.; Hagfeldt, A.; et al. Cesium-Containing Triple Cation Perovskite Solar Cells: Improved Stability, Reproducibility and High Efficiency. *Energy Environ. Sci.* **2016**, *9* (6), 1989–1997. https://doi.org/10.1039/C5EE03874J.

(142) Lilliu, S.; Dane, T. Reciprocal Space Mapping for Dummies. **2015**, 1–16.

(143) Alsari, M.; Bikondoa, O.; Bishop, J.; Abdi-Jalebi, M.; Y. Ozer, L.; Hampton, M.; Thompson, P.; T. Hörantner, M.; Mahesh, S.; Greenland, C.; et al. In Situ Simultaneous Photovoltaic and Structural Evolution of Perovskite Solar Cells during Film Formation. *Energy Environ. Sci.* **2018**, *11* (2), 383–393. https://doi.org/10.1039/C7EE03013D.

(144) Tan, K. W.; Moore, D. T.; Saliba, M.; Sai, H.; Estroff, L. A.; Hanrath, T.; Snaith, H. J.; Wiesner, U. Thermally Induced Structural Evolution and Performance of Mesoporous Block Copolymer-Directed Alumina Perovskite Solar Cells. *ACS Nano* **2014**, *8* (5), 4730–4739. https://doi.org/10.1021/nn500526t.

(145) Pineda De La O, E.; Alhazmi, N.; Ebbens, S. J.; Dunbar, A. D. F. Influence of Additives on the in Situ Crystallization Dynamics of Methyl Ammonium Lead Halide Perovskites. *ACS Appl. Energy Mater.* **2021**, *4* (2), 1398–1409. https://doi.org/10.1021/acsaem.0c02625.

(146) Stone, K. H.; Gold-Parker, A.; Pool, V. L.; Unger, E. L.; Bowring, A. R.; McGehee, M. D.; Toney, M. F.; Tassone, C. J. Transformation from Crystalline Precursor to Perovskite in PbCl2-Derived MAPbI3. *Nat. Commun.* **2018**, *9* (1). https://doi.org/10.1038/s41467-018-05937-4.

(147) Unger, E. L.; Bowring, A. R.; Tassone, C. J.; Pool, V. L.; Gold-Parker, A.; Cheacharoen, R.; Stone, K. H.; Hoke, E. T.; Toney, M. F.; McGehee, M. D. Chloride in Lead Chloride-Derived Organo-Metal Halides for Perovskite-Absorber Solar Cells. *Chem. Mater.* **2014**, *26* (24), 7158–7165. https://doi.org/10.1021/cm503828b.

(148) Pool, V. L.; Gold-Parker, A.; McGehee, M. D.; Toney, M. F. Chlorine in PbCl 2 -Derived Hybrid-Perovskite Solar Absorbers . *Chem. Mater.* **2015**, *27* (21), 7240–7243. https://doi.org/10.1021/acs.chemmater.5b03581.

(149) Hu, Q.; Zhao, L.; Wu, J.; Gao, K.; Luo, D.; Jiang, Y.; Zhang, Z.; Zhu, C.; Schaible, E.; Hexemer, A.; et al. In Situ Dynamic Observations of Perovskite Crystallisation and Microstructure Evolution Intermediated from [PbI 6]4- Cage Nanoparticles. *Nat. Commun.* **2017**, *8*, 1–9. https://doi.org/10.1038/ncomms15688.

(150) Zhang, Q.; Sun, H.; Zhang, H.; Jiang, M.; Wu, X.; Zhang, Z.; Yang, T.; Xia, R.; Cabanillas-Gonzalez, J. Facile and Controllable Fabrication of High-Performance Methylammonium Lead Triiodide Films Using Lead Acetate Precursor for Low-Threshold Amplified Spontaneous Emission and Distributed-Feedback Lasers. *Phys. Status Solidi - Rapid Res. Lett.* **2019**, *13* (10), 1–7. https://doi.org/10.1002/pssr.201900176.

(151) Hong, D.; Xie, M.; Tian, Y. Photostable and Uniform Ch3nh3pbi3 Perovskite Film Prepared via Stoichiometric Modification and Solvent Engineering. *Nanomaterials* **2021**, *11* (2), 1–12. https://doi.org/10.3390/nano11020405.

(152) Sanni, D. M.; Chen, Y.; Yerramilli, A. S.; Ntsoenzok, E.; Asare, J.; Adeniji, S. A.; Oyelade, O. V.; Fashina, A. A.; Alford, T. L. An Approach to Optimize Pre-Annealing Aging and Anneal Conditions to Improve Photovoltaic Performance of Perovskite Solar Cells. *Mater. Renew. Sustain. Energy* **2019**, *8* (1), 1–10. https://doi.org/10.1007/s40243-018-0139-3.

(153) Xie, L. Q.; Chen, L.; Nan, Z. A.; Lin, H. X.; Wang, T.; Zhan, D. P.; Yan, J. W.; Mao, B. W.; Tian, Z. Q. Understanding the Cubic Phase Stabilization and Crystallization Kinetics in Mixed Cations and Halides Perovskite Single Crystals. *J. Am. Chem. Soc.* **2017**, *139* (9), 3320–3323. https://doi.org/10.1021/jacs.6b12432.

(154) Qin, M.; Tse, K.; Lau, T.; Li, Y.; Su, C.; Yang, G.; Chen, J.; Zhu, J.; Jeng, U.; Li, G.; et al. Manipulating the Mixed-Perovskite Crystallization Pathway Unveiled by In Situ GIWAXS. *Adv. Mater.* **2019**, *31* (25), 1901284. https://doi.org/10.1002/adma.201901284.

(155) Gratia, P.; Zimmermann, I.; Schouwink, P.; Yum, J. H.; Audinot, J. N.; Sivula, K.; Wirtz, T.; Nazeeruddin, M. K. The Many Faces of Mixed Ion Perovskites: Unraveling and Understanding the Crystallization Process. *ACS Energy Lett.* **2017**, *2* (12), 2686–2693. https://doi.org/10.1021/acsenergylett.7b00981.

(156) Wang, K.; Tang, M.-C.; Dang, H. X.; Munir, R.; Barrit, D.; De Bastiani, M.; Aydin, E.; Smilgies, D.-M.; De Wolf, S.; Amassian, A. Kinetic Stabilization of the Sol-Gel State in Perovskites Enables Facile Processing of High-Efficiency Solar Cells. *Adv. Mater.* **2019**, *1808357*, 1808357. https://doi.org/10.1002/adma.201808357.

(157) Szostak, R.; Marchezi, P. E.; Marques, A. D. S.; Silva, J. C.; Holanda, M. S.; Soares, M. M.; Tolentino, H. C. N.; Nogueira, A. F. Exploring the Formation of Formamidinium-Based Hybrid Perovskites by Antisolvent Methods: In Situ GIWAXS Measurements during Spin Coating. *Sustain. Energy Fuels* **2019**. https://doi.org/10.1039/C9SE00306A.

(158) Lilliu, S.; Griffin, J.; Barrows, A. T.; Alsari, M.; Curzadd, B.; Dane, T. G.; Bikondoa, O.; Macdonald, J. E.; Lidzey, D. G. Grain Rotation and Lattice Deformation during Perovskite Spray Coating and Annealing Probed in Situ by GI-WAXS. *CrystEngComm* **2016**, *18* (29), 5448–5455. https://doi.org/10.1039/C6CE00965D.

142

References

(159) Jones, T. W.; Osherov, A.; Alsari, M.; Sponseller, M.; Duck, B. C.; Jung, Y.-K.; Settens, C.; Niroui, F.; Brenes, R.; Stan, C. V.; et al. Lattice Strain Causes Non-Radiative Losses in Halide Perovskites. *Energy Environ. Sci.* **2019**, *12* (2), 596–606. https://doi.org/10.1039/C8EE02751J.

(160) Zhao, J.; Deng, Y.; Wei, H.; Zheng, X.; Yu, Z.; Shao, Y.; Shield, J. E.; Huang, J. Strained Hybrid Perovskite Thin Films and Their Impact on the Intrinsic Stability of Perovskite Solar Cells. *Sci. Adv.* **2017**, *3* (11), eaao5616. https://doi.org/10.1126/sciadv.aao5616.

(161) Friend, R. H.; Deschler, F.; Pazos-Outón, L. M.; Abdi-Jalebi, M.; Alsari, M. Back-Contact Perovskite Solar Cells. *Sci. Video Protoc.* **2019**, *1* (1), 1–10. https://doi.org/10.32386/scivpro.000005.

(162) Wong-Stringer, M.; Routledge, T. J.; McArdle, T.; Wood, C. J.; Game, O. S.; Smith, J. A.; Bishop, J. E.; Vaenas, N.; Coles, D. M.; Buckley, A. R.; et al. A Flexible Back-Contact Perovskite Solar Micro-Module. *Energy Environ. Sci.* **2019**, *12* (6), 1928–1937. https://doi.org/10.1039/C8EE03517B.

(163) Yang, J.; Siempelkamp, B. D.; Liu, D.; Kelly, T. L. Investigation of CH3NH3PbI3 Degradation Rates and Mechanisms in Controlled Humidity Environments Using in Situ Techniques. *ACS Nano* **2015**, *9* (2), 1955–1963. https://doi.org/10.1021/nn506864k.

(164) Boyd, C. C.; Cheacharoen, R.; Leijtens, T.; McGehee, M. D. Understanding Degradation Mechanisms and Improving Stability of Perovskite Photovoltaics. *Chem. Rev.* **2019**, *119* (5), 3418–3451. https://doi.org/10.1021/acs.chemrev.8b00336.

(165) Leguy, A. M. A.; Hu, Y.; Campoy-Quiles, M.; Alonso, M. I.; Weber, O. J.; Azarhoosh, P.; Van Schilfgaarde, M.; Weller, M. T.; Bein, T.; Nelson, J.; et al. Reversible Hydration of CH3NH3PbI3 in Films, Single Crystals, and Solar Cells. *Chem. Mater.* **2015**, *27* (9), 3397–3407. https://doi.org/10.1021/acs.chemmater.5b00660.

(166) Schlipf, J.; Bießmann, L.; Oesinghaus, L.; Berger, E.; Metwalli, E.; Lercher, J. A.; Porcar, L.; Müller-Buschbaum, P. In Situ Monitoring the Uptake of Moisture into Hybrid Perovskite Thin Films. *J. Phys. Chem. Lett.* **2018**, *9* (8), 2015–2021. https://doi.org/10.1021/acs.jpclett.8b00687.

(167) Toloueinia, P.; Khassaf, H.; Shirazi Amin, A.; Tobin, Z. M.; Alpay, S. P.; Suib, S. L. Moisture-Induced Structural Degradation in Methylammonium Lead Iodide Perovskite Thin Films. *ACS Appl. Energy Mater.* **2020**, *3* (9), 8240–8248. https://doi.org/10.1021/acsaem.0c00638.

(168) Leijtens, T.; Hoke, E. T.; Grancini, G.; Slotcavage, D. J.; Eperon, G. E.; Ball, J. M.; De Bastiani, M.; Bowring, A. R.; Martino, N.; Wojciechowski, K.; et al. Mapping Electric Field-Induced Switchable Poling and Structural Degradation in Hybrid Lead Halide Perovskite Thin Films. *Adv. Energy Mater.* **2015**, *5* (20), 1500962. https://doi.org/10.1002/aenm.201500962.

(169) Azpiroz, J. M.; Mosconi, E.; Bisquert, J.; De Angelis, F. Defect Migration in Methylammonium Lead Iodide and Its Role in Perovskite Solar Cell Operation. *Energy Environ. Sci.* **2015**, *8* (7), 2118–2127. https://doi.org/10.1039/c5ee01265a.

(170) Frost, J. M.; Butler, K. T.; Brivio, F.; Hendon, C. H.; Van Schilfgaarde, M.; Walsh, A. Atomistic Origins of High-Performance in Hybrid Halide Perovskite Solar Cells. *Nano Lett.* **2014**, *14* (5), 2584–2590. https://doi.org/10.1021/nl500390f.

(171) Liao, W. C.; Liu, B. H.; Leu, C. C. Nanoscale Mapping of Humid Degradation-Induced Local Mechanical Property Variation in CH3NH3PbI3 Polycrystalline Film by Scanning Probe Microscopy. *Appl. Surf. Sci.* **2020**, *507* (December 2019), 145078. https://doi.org/10.1016/j.apsusc.2019.145078.

(172) Wang, Q.; Chen, B.; Liu, Y.; Deng, Y.; Bai, Y.; Dong, Q.; Huang, J. Scaling Behavior of Moisture-Induced Grain Degradation in Polycrystalline Hybrid Perovskite Thin Films. *Energy Environ. Sci.* **2017**, *10* (2), 516–522. https://doi.org/10.1039/C6EE02941H.

(173) Bryant, D.; Aristidou, N.; Pont, S.; Sanchez-Molina, I.; Chotchunangatchaval, T.; Wheeler, S.; Durrant, J. R.; Haque, S. A. Light and Oxygen Induced Degradation Limits the Operational Stability of Methylammonium Lead Triiodide Perovskite Solar Cells. *Energy Environ. Sci.* **2016**, *9* (5), 1655–1660. https://doi.org/10.1039/c6ee00409a.

(174) Sheikh, A. D.; Bera, A.; Haque, M. A.; Rakhi, R. B.; Del Gobbo, S.; Alshareef, H. N.; Wu, T. Atmospheric Effects on the Photovoltaic Performance of Hybrid Perovskite Solar Cells. *Sol. Energy Mater. Sol. Cells* **2015**, *137*, 6–14. https://doi.org/10.1016/j.solmat.2015.01.023.

(175) Aristidou, N.; Sanchez-Molina, I.; Chotchuangchutchaval, T.; Brown, M.; Martinez, L.; Rath, T.; Haque, S. A. The Role of Oxygen in the Degradation of Methylammonium Lead Trihalide Perovskite Photoactive Layers. *Angew. Chemie - Int. Ed.* **2015**, *54* (28), 8208–8212. https://doi.org/10.1002/anie.201503153.

(176) Aristidou, N.; Eames, C.; Islam, M. S.; Haque, S. A. Insights into the Increased Degradation Rate of CH3NH3PbI3 Solar Cells in Combined Water and O2 Environments. *J. Mater. Chem. A* **2017**, *5* (48), 25469–25475. https://doi.org/10.1039/c7ta06841g.

(177) Liao, W. C.; Liu, B. H.; Leu, C. C. Photodegradation Pathways of CH3NH3PbI3 Organic Perovskite Polycrystalline Film Observed by In-Situ Scanning Probe Microscopy. *Appl. Surf. Sci.* **2021**, *545* (January), 149081. https://doi.org/10.1016/j.apsusc.2021.149081.

(178) An, Y.; Hidalgo, J.; Perini, C. A. R.; Castro-Méndez, A. F.; Vagott, J. N.; Bairley, K.; Wang, S.; Li, X.; Correa-Baena, J. P. Structural Stability of Formamidinium- And Cesium-Based Halide Perovskites. *ACS Energy Lett.* **2021**, *6* (5), 1942–1969. https://doi.org/10.1021/acsenergylett.1c00354.

(179) Raval, P.; Kennard, R. M.; Vasileiadou, E. S.; Dahlman, C. J.; Spanopoulos, I.; Chabinyc, M. L.; Kanatzidis, M.; Manjunatha Reddy, G. N. Understanding Instability in Formamidinium Lead Halide Perovskites: Kinetics of Transformative Reactions at Grain and Subgrain Boundaries. *ACS Energy Lett.* **2022**, *7* (4), 1534–1543. https://doi.org/10.1021/acsenergylett.2c00140.

(180) Vasileiadou, E. S.; Hadar, I.; Kepenekian, M.; Even, J.; Tu, Q.; Malliakas, C. D.; Friedrich, D.; Spanopoulos, I.; Hoffman, J. M.; Dravid, V. P.; et al. Shedding Light on the Stability and Structure-Property Relationships of Two-Dimensional Hybrid Lead Bromide Perovskites. *Chem. Mater.* **2021**, *33* (13), 5085–5107. https://doi.org/10.1021/acs.chemmater.1c01129.

(181) Cordero, F.; Craciun, F.; Paoletti, A. M.; Zanotti, G. Structural Transitions and Stability of Fapbi3 and Mapbi3: The Role of Interstitial Water. *Nanomaterials* **2021**, *11* (6), 1–19. https://doi.org/10.3390/nano11061610.

(182) Kazemi, M. A. A.; Folastre, N.; Raval, P.; Sliwa, M.; Nsanzimana, J. M. V.; Golonu, S.; Demortiere, A.; Rousset, J.; Lafon, O.; Delevoye, L.; et al. Moisture-Induced Non-Equilibrium Phase Segregation in Triple Cation Mixed Halide Perovskite Monitored by In Situ Characterization Techniques and Solid-State NMR. *Energy Environ. Mater.* **2022**, 1–10. https://doi.org/10.1002/eem2.12335.

References

(183) Hidalgo, J.; An, Y.; Breternitz, J.; Schorr, S. Beyond Humidity : The Underlying Phase Transitions in Cesium-Formamidinium Lead Halide Perovskites. **2022**.

(184) Lee, J. W.; Kim, D. H.; Kim, H. S.; Seo, S. W.; Cho, S. M.; Park, N. G. Formamidinium and Cesium Hybridization for Photo- and Moisture-Stable Perovskite Solar Cell. *Adv. Energy Mater.* **2015**, *5* (20). https://doi.org/10.1002/aenm.201501310.

(185) Lee, J.; Seol, D.; Cho, A.; Park, N. High-Efficiency Perovskite Solar Cells Based on the Black Polymorph of HC(NH 2) 2 PbI 3. *Adv. Mater.* **2014**, *26* (29), 4991–4998. https://doi.org/10.1002/adma.201401137.

(186) Eperon, G. E.; Stranks, S. D.; Menelaou, C.; Johnston, M. B.; Herz, L. M.; Snaith, H. J. Environmental Science Formamidinium Lead Trihalide : A Broadly Tunable Perovskite for e Ffi Cient Planar Heterojunction Solar. **2014**, 982–988. https://doi.org/10.1039/c3ee43822h.

(187) Jeon, N. J.; Noh, J. H.; Yang, W. S.; Kim, Y. C.; Ryu, S.; Seo, J.; Seok, S. Il. Compositional Engineering of Perovskite Materials for High-Performance Solar Cells. *Nature* **2015**, *517* (7535), 476–480. https://doi.org/10.1038/nature14133.

(188) Tennyson, E. M.; Roose, B.; Garrett, J. L.; Gong, C.; Munday, J. N.; Abate, A.; Leite, M. S. Cesium-Incorporated Triple Cation Perovskites Deliver Fully Reversible and Stable Nanoscale Voltage Response. *ACS Nano* **2019**, *13*, acsnano.8b07295. https://doi.org/10.1021/acsnano.8b07295.

(189) Beal, R. E.; Slotcavage, D. J.; Leijtens, T.; Bowring, A. R.; Belisle, R. A.; Nguyen, W. H.; Burkhard, G. F.; Hoke, E. T.; McGehee, M. D. Cesium Lead Halide Perovskites with Improved Stability for Tandem Solar Cells. *J. Phys. Chem. Lett.* **2016**, *7* (5), 746–751. https://doi.org/10.1021/acs.jpclett.6b00002.

(190) Li, N.; Tao, S.; Chen, Y.; Niu, X.; Onwudinanti, C. K.; Hu, C.; Qiu, Z.; Xu, Z.; Zheng, G.; Wang, L.; et al. Cation and Anion Immobilization through Chemical Bonding Enhancement with Fluorides for Stable Halide Perovskite Solar Cells. *Nat. Energy* **2019**, *4* (5), 408–415. https://doi.org/10.1038/s41560-019-0382-6.

(191) Yi, C.; Luo, J.; Meloni, S.; Boziki, A.; Ashari-Astani, N.; Grätzel, C.; Zakeeruddin, S. M.; Röthlisberger, U.; Grätzel, M. Entropic Stabilization of Mixed A-Cation ABX 3 Metal Halide Perovskites for High Performance Perovskite Solar Cells. *Energy Environ. Sci.* **2016**, *9* (2), 656–662. https://doi.org/10.1039/C5EE03255E.

(192) Li, Z.; Yang, M.; Park, J.; Wei, S.; Berry, J. J.; Zhu, K. Stabilizing Perovskite Structures by Tuning Tolerance Factor: Formation of Formamidinium and Cesium Lead Iodide Solid-State Alloys. **2016**, *2*. https://doi.org/10.1021/acs.chemmater.5b04107.

(193) Yang, T. Y.; Jeon, N. J.; Shin, H. W.; Shin, S. S.; Kim, Y. Y.; Seo, J. Achieving Long-Term Operational Stability of Perovskite Solar Cells with a Stabilized Efficiency Exceeding 20% after 1000 H. *Adv. Sci.* **2019**, *6* (14), 1–7. https://doi.org/10.1002/advs.201900528.

(194) Bonnassieux, Y.; Lee, H.; Chapon, P.; Tondelier, D.; Boure, J.; Derycke, V.; Ge, B.; Polytechnique, E.; Paris, I. P. De; Saclay, D. E Ff Ect of Halide Ion Migration on the Electrical Properties of Methylammonium Lead Tri-Iodide Perovskite Solar Cells´ , †. **2019**. https://doi.org/10.1021/acs.jpcc.9b04662.

(195) Noh, J. H.; Im, S. H.; Heo, J. H.; Mandal, T. N.; Seok, S. Il. Chemical Management for Colorful, Efficient, and Stable Inorganic-Organic Hybrid Nanostructured Solar Cells. *Nano Lett.* **2013**, *13* (4), 1764–1769. https://doi.org/10.1021/nl400349b.

(196) Ho, K.; Wei, M.; Sargent, E. H.; Walker, G. C. Grain Transformation and Degradation Mechanism of Formamidinium and Cesium Lead Iodide Perovskite under Humidity and Light. *ACS Energy Lett.* **2021**, *6* (3), 934–940. https://doi.org/10.1021/acsenergylett.0c02247.

(197) Li, N.; Luo, Y.; Chen, Z.; Niu, X.; Zhang, X.; Lu, J.; Kumar, R.; Jiang, J.; Liu, H.; Guo, X.; et al. Microscopic Degradation in Formamidinium-Cesium Lead Iodide Perovskite Solar Cells under Operational Stressors. *Joule* **2020**, *4* (8), 1743–1758. https://doi.org/10.1016/j.joule.2020.06.005.

(198) Maniyarasu, S.; Ke, J. C. R.; Spencer, B. F.; Walton, A. S.; Thomas, A. G.; Flavell, W. R. Role of Alkali Cations in Stabilizing Mixed-Cation Perovskites to Thermal Stress and Moisture Conditions. *ACS Appl. Mater. Interfaces* **2021**. https://doi.org/10.1021/acsami.1c10420.

(199) Hu, Y.; Aygüler, M. F.; Petrus, M. L.; Bein, T.; Docampo, P. Impact of Rubidium and Cesium Cations on the Moisture Stability of Multiple-Cation Mixed-Halide Perovskites. *ACS Energy Lett.* **2017**, *2* (10), 2212–2218. https://doi.org/10.1021/acsenergylett.7b00731.

(200) Conings, B.; Drijkoningen, J.; Gauquelin, N.; Babayigit, A.; D'Haen, J.; D'Oliesleager, L.; Ethirajan, A.; Verbeeck, J.; Manca, J.; Mosconi, E.; et al. Intrinsic Thermal Instability of Methylammonium Lead Trihalide Perovskite. *Adv. Energy Mater.* **2015**, *5* (15), 1–8. https://doi.org/10.1002/aenm.201500477.

(201) Son, D.-Y.; Kim, S.-G.; Seo, J.-Y.; Lee, S.-H.; Shin, H.; Lee, D.; Park, N.-G. Universal Approach toward Hysteresis−Free Perovskite Solar Cell via Defect Engineering. *J. Am. Chem. Soc.* **2018**, jacs.7b10430. https://doi.org/10.1021/jacs.7b10430.

(202) Tennyson, E. M.; Roose, B.; Garrett, J. L.; Gong, C.; Munday, J. N.; Abate, A.; Leite, M. S. Cesium-Incorporated Triple Cation Perovskites Deliver Fully Reversible and Stable Nanoscale Voltage Response. *ACS Nano* **2019**, *13* (2), acsnano.8b07295. https://doi.org/10.1021/acsnano.8b07295.

(203) Saliba, M.; Matsui, T.; Domanski, K.; Seo, J.-Y.; Ummadisingu, A.; Zakeeruddin, S. M.; Correa-Baena, J.-P.; Tress, W. R.; Abate, A.; Hagfeldt, A.; et al. Incorporation of Rubidium Cations into Perovskite Solar Cells Improves Photovoltaic Performance. *Science (80-.).* **2016**, *354* (6309), 206–209. https://doi.org/10.1126/science.aah5557.

(204) Philippe, B.; Saliba, M.; Correa-Baena, J. P.; Cappel, U. B.; Turren-Cruz, S. H.; Grätzel, M.; Hagfeldt, A.; Rensmo, H. Chemical Distribution of Multiple Cation (Rb+, Cs+, MA+, and FA+) Perovskite Materials by Photoelectron Spectroscopy. *Chem. Mater.* **2017**, *29* (8), 3589–3596. https://doi.org/10.1021/acs.chemmater.7b00126.

(205) Tan, W.; Bowring, A. R.; Meng, A. C.; McGehee, M. D.; McIntyre, P. C. Thermal Stability of Mixed Cation Metal Halide Perovskites in Air. *ACS Appl. Mater. Interfaces* **2018**, *10* (6), 5485–5491. https://doi.org/10.1021/acsami.7b15263.

(206) Sun, Y.; Peng, J.; Chen, Y.; Yao, Y.; Liang, Z. Triple-Cation Mixed-Halide Perovskites: Towards Efficient, Annealing-Free and Air-Stable Solar Cells Enabled by Pb(SCN) 2 Additive. *Sci. Rep.* **2017**, *7* (April), 1–7. https://doi.org/10.1038/srep46193.

(207) Jacobsson, T. J.; Svanström, S.; Andrei, V.; Rivett, J. P. H.; Kornienko, N.; Philippe, B.; Cappel, U. B.; Rensmo, H.; Deschler, F.; Boschloo, G. Extending the Compositional Space of Mixed Lead Halide Perovskites by Cs, Rb, K, and Na Doping. *J. Phys. Chem. C* **2018**, *122* (25), 13548–13557. https://doi.org/10.1021/acs.jpcc.7b12464.

References

(208)   McMeekin, D. P.; Sadoughi, G.; Rehman, W.; Eperon, G. E.; Saliba, M.; Hörantner, M. T.; Haghighirad, A.; Sakai, N.; Korte, L.; Rech, B.; et al. A Mixed-Cation Lead Mixed-Halide Perovskite Absorber for Tandem Solar Cells. *Science (80-.).* **2016**, *351* (6269), 151–155. https://doi.org/10.1126/science.aad5845.

(209)   Doherty, T. A. S.; Nagane, S.; Kubicki, D. J.; Jung, Y.-K.; Johnstone, D. N.; Iqbal, A. N.; Guo, D.; Frohna, K.; Danaie, M.; Tennyson, E. M.; et al. Stabilized Tilted-Octahedra Halide Perovskites Inhibit Local Formation of Performance-Limiting Phases. *Science (80-.).* **2021**, *374* (6575), 1598–1605. https://doi.org/10.1126/science.abl4890.

(210)   Snaith, H. J.; Abate, A.; Ball, J. M.; Eperon, G. E.; Leijtens, T.; Noel, N. K.; Stranks, S. D.; Wang, J. T. W.; Wojciechowski, K.; Zhang, W. Anomalous Hysteresis in Perovskite Solar Cells. *J. Phys. Chem. Lett.* **2014**, *5* (9), 1511–1515. https://doi.org/10.1021/jz500113x.

(211)   Fan, Z.; Xiao, J.; Sun, K.; Chen, L.; Hu, Y.; Ouyang, J.; Ong, K. P.; Zeng, K.; Wang, J. Ferroelectricity of CH 3 NH 3 PbI 3 Perovskite. *J. Phys. Chem. Lett.* **2015**, *6* (7), 1155–1161. https://doi.org/10.1021/acs.jpclett.5b00389.

(212)   Meloni, S.; Moehl, T.; Tress, W.; Franckevičius, M.; Saliba, M.; Lee, Y. H.; Gao, P.; Nazeeruddin, M. K.; Zakeeruddin, S. M.; Rothlisberger, U.; et al. Ionic Polarization-Induced Current–Voltage Hysteresis in CH3NH3PbX3 Perovskite Solar Cells. *Nat. Commun.* **2016**, *7* (1), 10334. https://doi.org/10.1038/ncomms10334.

(213)   Li, C.; Guerrero, A.; Zhong, Y.; Huettner, S. Origins and Mechanisms of Hysteresis in Organometal Halide Perovskites. *J. Phys. Condens. Matter* **2017**, *29* (19). https://doi.org/10.1088/1361-648X/aa626d.

(214)   Mizusaki, J.; Arai, K.; Fueki, K. Ionic Conduction of the Perovskite-Type Halides. *Solid State Ionics* **1983**, *11* (3), 203–211. https://doi.org/10.1016/0167-2738(83)90025-5.

(215)   Narayan, R. L.; Suryanarayana, S. V. Transport Properties of the Perovskite-Type Halides. *Mater. Lett.* **1991**, *11* (8–9), 305–308. https://doi.org/10.1016/0167-577X(91)90208-N.

(216)   Eames, C.; Frost, J. M.; Barnes, P. R. F.; O'Regan, B. C.; Walsh, A.; Islam, M. S. Ionic Transport in Hybrid Lead Iodide Perovskite Solar Cells. *Nat. Commun.* **2015**, *6* (May), 2–9. https://doi.org/10.1038/ncomms8497.

(217)   Lan, D. The Physics of Ion Migration in Perovskite Solar Cells: Insights into Hysteresis, Device Performance, and Characterization. *Prog. Photovoltaics Res. Appl.* **2019**, No. July, 8–11. https://doi.org/10.1002/pip.3203.

(218)   Walsh, A.; Stranks, S. D. Taking Control of Ion Transport in Halide Perovskite Solar Cells. *ACS Energy Lett.* **2018**, *3* (8), 1983–1990. https://doi.org/10.1021/acsenergylett.8b00764.

(219)   Walsh, A.; Scanlon, D. O.; Chen, S.; Gong, X. G.; Wei, S. H. Self-Regulation Mechanism for Charged Point Defects in Hybrid Halide Perovskites. *Angew. Chemie - Int. Ed.* **2015**, *54* (6), 1791–1794. https://doi.org/10.1002/anie.201409740.

(220)   Chen, B.; Li, T.; Dong, Q.; Mosconi, E.; Song, J.; Chen, Z.; Deng, Y.; Liu, Y.; Ducharme, S.; Gruverman, A.; et al. Large Electrostrictive Response in Lead Halide Perovskites. *Nat. Mater.* **2018**. https://doi.org/10.1038/s41563-018-0170-x.

(221)   Haruyama, J.; Sodeyama, K.; Han, L.; Tateyama, Y. First-Principles Study of Ion Diffusion in Perovskite Solar Cell Sensitizers. *J. Am. Chem. Soc.* **2015**, *137* (32), 10048–10051. https://doi.org/10.1021/jacs.5b03615.

(222)   Snaider, J. M.; Guo, Z.; Wang, T.; Yang, M.; Yuan, L.; Zhu, K.; Huang, L. Ultrafast Imaging of Carrier Transport across Grain Boundaries in Hybrid Perovskite Thin Films. *ACS Energy Lett.* **2018**, *3* (6), 1402–1408. https://doi.org/10.1021/acsenergylett.8b00560.

(223)   Regonini, D.; Dent, A. C. E.; Bowen, C. R.; Pennock, S. R.; Taylor, J. Impedance Spectroscopy Analysis of TinO2n−1 Magnéli Phases. *Mater. Lett.* **2011**, *65* (23–24), 3590–3592. https://doi.org/10.1016/j.matlet.2011.07.094.

(224)   DeQuilettes, D. W.; Jariwala, S.; Burke, S.; Ziffer, M. E.; Wang, J. T. W.; Snaith, H. J.; Ginger, D. S. Tracking Photoexcited Carriers in Hybrid Perovskite Semiconductors: Trap-Dominated Spatial Heterogeneity and Diffusion. *ACS Nano* **2017**, *11* (11), 11488–11496. https://doi.org/10.1021/acsnano.7b06242.

(225)   Yuan, Y.; Wang, Q.; Shao, Y.; Lu, H.; Li, T.; Gruverman, A.; Huang, J. Electric-Field-Driven Reversible Conversion between Methylammonium Lead Triiodide Perovskites and Lead Iodide at Elevated Temperatures. *Adv. Energy Mater.* **2016**, *6* (2), 1–7. https://doi.org/10.1002/aenm.201501803.

(226)   Birkhold, S. T.; Precht, J. T.; Liu, H.; Giridharagopal, R.; Eperon, G. E.; Schmidt-Mende, L.; Li, X.; Ginger, D. S. Interplay of Mobile Ions and Injected Carriers Creates Recombination Centers in Metal Halide Perovskites under Bias. *ACS Energy Lett.* **2018**, *3* (6), 1279–1286. https://doi.org/10.1021/acsenergylett.8b00505.

(227)   Jeangros, Q.; Duchamp, M.; Werner, J.; Kruth, M.; Dunin-Borkowski, R. E.; Niesen, B.; Ballif, C.; Hessler-Wyser, A. In Situ TEM Analysis of Organic-Inorganic Metal-Halide Perovskite Solar Cells under Electrical Bias. *Nano Lett.* **2016**, *16* (11), 7013–7018. https://doi.org/10.1021/acs.nanolett.6b03158.

(228)   Zhang, H.; Fu, X.; Tang, Y.; Wang, H.; Zhang, C.; Yu, W. W.; Wang, X.; Zhang, Y.; Xiao, M. Phase Segregation Due to Ion Migration in All-Inorganic Mixed-Halide Perovskite Nanocrystals. *Nat. Commun.* **2019**, *10* (1), 1088. https://doi.org/10.1038/s41467-019-09047-7.

(229)   Pellet, N.; Teuscher, J.; Maier, J.; Grätzel, M. Transforming Hybrid Organic Inorganic Perovskites by Rapid Halide Exchange. *Chem. Mater.* **2015**, *27* (6), 2181–2188. https://doi.org/10.1021/acs.chemmater.5b00281.

(230)   Eperon, G. E.; Beck, C. E.; Snaith, H. J. Cation Exchange for Thin Film Lead Iodide Perovskite Interconversion. *Mater. Horizons* **2016**, *3* (1), 63–71. https://doi.org/10.1039/c5mh00170f.

(231)   Eperon, G. E.; Ginger, D. S. B-Site Metal Cation Exchange in Halide Perovskites. *ACS Energy Lett.* **2017**, *2* (5), 1190–1196. https://doi.org/10.1021/acsenergylett.7b00290.

(232)   Fransishyn, K. M.; Kundu, S.; Kelly, T. L. Elucidating the Failure Mechanisms of Perovskite Solar Cells in Humid Environments Using in Situ Grazing-Incidence Wide-Angle X-Ray Scattering. *ACS Energy Lett.* **2018**, *3* (9), 2127–2133. https://doi.org/10.1021/acsenergylett.8b01300.

(233)   Brenes, R.; Eames, C.; Bulović, V.; Islam, M. S.; Stranks, S. D. The Impact of Atmosphere on the Local Luminescence Properties of Metal Halide Perovskite Grains. *Adv. Mater.* **2018**, *30* (15), 1706208. https://doi.org/10.1002/adma.201706208.

(234)   Frost, J. M.; Whalley, L. D.; Walsh, A. Slow Cooling of Hot Polarons in Halide Perovskite Solar Cells. *ACS Energy Lett.* **2017**, *2* (12), 2647–2652. https://doi.org/10.1021/acsenergylett.7b00862.

(235)   Bag, M.; Renna, L. A.; Adhikari, R. Y.; Karak, S.; Liu, F.; Lahti, P. M.; Russell, T. P.; Tuominen, M. T.; Venkataraman, D. Kinetics of

145

References

Ion Transport in Perovskite Active Layers and Its Implications for Active Layer Stability. *J. Am. Chem. Soc.* **2015**, *137* (40), 13130–13137. https://doi.org/10.1021/jacs.5b08535.

(236) Zhou, Y.; Garces, H. F.; Padture, N. P. Challenges in the Ambient Raman Spectroscopy Characterization of Methylammonium Lead Triiodide Perovskite Thin Films. *Front. Optoelectron.* **2016**, *9* (1), 81–86. https://doi.org/10.1007/s12200-016-0573-8.

(237) Kovalsky, A.; Wang, L.; Marek, G. T.; Burda, C.; Dyck, J. S. Thermal Conductivity of CH3NH3PbI3 and CsPbI3: Measuring the Effect of the Methylammonium Ion on Phonon Scattering. *J. Phys. Chem. C* **2017**, *121* (6), 3228–3233. https://doi.org/10.1021/acs.jpcc.6b12231.

(238) He, Y.; Galli, G. Perovskites for Solar Thermoelectric Applications: A First Principle Study of CH 3 NH 3 AI 3 (A = Pb and Sn). *Chem. Mater.* **2014**, *26* (18), 5394–5400. https://doi.org/10.1021/cm5026766.

(239) Barker, A. J.; Sadhanala, A.; Deschler, F.; Gandini, M.; Senanayak, S. P.; Pearce, P. M.; Mosconi, E.; Pearson, A. J.; Wu, Y.; Srimath Kandada, A. R.; et al. Defect-Assisted Photoinduced Halide Segregation in Mixed-Halide Perovskite Thin Films. *ACS Energy Lett.* **2017**, *2* (6), 1416–1424. https://doi.org/10.1021/acsenergylett.7b00282.

(240) Hoke, E. T.; Slotcavage, D. J.; Dohner, E. R.; Bowring, A. R.; Karunadasa, H. I.; McGehee, M. D. Reversible Photo-Induced Trap Formation in Mixed-Halide Hybrid Perovskites for Photovoltaics. *Chem. Sci.* **2015**, *6* (1), 613–617. https://doi.org/10.1039/c4sc03141e.

(241) Brennan, M. C.; Draguta, S.; Kamat, P. V.; Kuno, M. Light-Induced Anion Phase Segregation in Mixed Halide Perovskites. *ACS Energy Lett.* **2018**, *3* (1), 204–213. https://doi.org/10.1021/acsenergylett.7b01151.

(242) Slotcavage, D. J.; Karunadasa, H. I.; McGehee, M. D. Light-Induced Phase Segregation in Halide-Perovskite Absorbers. *ACS Energy Lett.* **2016**, *1* (6), 1199–1205. https://doi.org/10.1021/acsenergylett.6b00495.

(243) Yuan, Y.; Huang, J. Ion Migration in Organometal Trihalide Perovskite and Its Impact on Photovoltaic Efficiency and Stability. *Acc. Chem. Res.* **2016**, *49* (2), 286–293. https://doi.org/10.1021/acs.accounts.5b00420.

(244) DeQuilettes, D. W.; Zhang, W.; Burlakov, V. M.; Graham, D. J.; Leijtens, T.; Osherov, A.; Bulović, V.; Snaith, H. J.; Ginger, D. S.; Stranks, S. D. Photo-Induced Halide Redistribution in Organic-Inorganic Perovskite Films. *Nat. Commun.* **2016**, *7* (May). https://doi.org/10.1038/ncomms11683.

(245) Belisle, R. A.; Bush, K. A.; Bertoluzzi, L.; Gold-Parker, A.; Toney, M. F.; McGehee, M. D. Impact of Surfaces on Photo-Induced Halide-Segregation in Mixed-Halide Perovskites. *ACS Energy Lett.* **2018**, *3*, acsenergylett.8b01562. https://doi.org/10.1021/acsenergylett.8b01562.

(246) Hu, M.; Bi, C.; Yuan, Y.; Bai, Y.; Huang, J. Stabilized Wide Bandgap MAPbBrxI3-Xperovskite by Enhanced Grain Size and Improved Crystallinity. *Adv. Sci.* **2015**, *3* (6), 6–11. https://doi.org/10.1002/advs.201500301.

(247) Eperon, G. E.; Hörantner, M. T.; Snaith, H. J. Metal Halide Perovskite Tandem and Multiple-Junction Photovoltaics. *Nat. Rev. Chem.* **2017**, *1*, 0095. https://doi.org/10.1038/s41570-017-0095.

(248) Leijtens, T.; Bush, K. A.; Prasanna, R.; McGehee, M. D. Opportunities and Challenges for Tandem Solar Cells Using Metal Halide Perovskite Semiconductors. *Nat. Energy* **2018**, *3* (October), 1–11. https://doi.org/10.1038/s41560-018-0190-4.

(249) Tsai, H.; Asadpour, R.; Blancon, J. C.; Stoumpos, C. C.; Durand, O.; Strzalka, J. W.; Chen, B.; Verduzco, R.; Ajayan, P. M.; Tretiak, S.; et al. Light-Induced Lattice Expansion Leads to High-Efficiency Perovskite Solar Cells. *Science (80-.).* **2018**, *360* (6384), 67–70. https://doi.org/10.1126/science.aap8671.

(250) Zhou, Y.; You, L.; Wang, S.; Ku, Z.; Fan, H.; Schmidt, D.; Rusydi, A.; Chang, L.; Wang, L.; Ren, P.; et al. Giant Photostriction in Organic-Inorganic Lead Halide Perovskites. *Nat. Commun.* **2016**, *7*, 1–8. https://doi.org/10.1038/ncomms11193.

(251) Tiede, D. O.; Calvo, M. E.; Galisteo-López, J. F.; Míguez, H. Local Rearrangement of the Iodide Defect Structure Determines the Phase Segregation Effect in Mixed-Halide Perovskites. *J. Phys. Chem. Lett.* **2020**, *11* (12), 4911–4916. https://doi.org/10.1021/acs.jpclett.0c01127.

(252) Sheikh, A. D.; Munir, R.; Haque, M. A.; Bera, A.; Hu, W.; Shaikh, P.; Amassian, A.; Wu, T. Effects of High Temperature and Thermal Cycling on the Performance of Perovskite Solar Cells: Acceleration of Charge Recombination and Deterioration of Charge Extraction. *ACS Appl. Mater. Interfaces* **2017**, *9* (40), 35018–35029. https://doi.org/10.1021/acsami.7b11250.

(253) Li, C.; Guerrero, A.; Zhong, Y.; Gräser, A.; Luna, C. A. M.; Köhler, J.; Bisquert, J.; Hildner, R.; Huettner, S. Real-Time Observation of Iodide Ion Migration in Methylammonium Lead Halide Perovskites. *Small* **2017**, *13* (42), 1–10. https://doi.org/10.1002/smll.201701711.

(254) Luo, Y.; Khoram, P.; Brittman, S.; Zhu, Z.; Lai, B.; Ong, S. P.; Garnett, E. C.; Fenning, D. P. Direct Observation of Halide Migration and Its Effect on the Photoluminescence of Methylammonium Lead Bromide Perovskite Single Crystals. *Adv. Mater.* **2017**, *29* (43), 1703451. https://doi.org/10.1002/adma.201703451.

(255) Li, C.; Tscheuschner, S.; Paulus, F.; Hopkinson, P. E.; Kießling, J.; Köhler, A.; Vaynzof, Y.; Huettner, S. Iodine Migration and Its Effect on Hysteresis in Perovskite Solar Cells. *Adv. Mater.* **2016**, *28* (12), 2446–2454. https://doi.org/10.1002/adma.201503832.

(256) Dar, M. I.; Jacopin, G.; Hezam, M.; Arora, N.; Zakeeruddin, S. M.; Deveaud, B.; Nazeeruddin, M. K.; Grätzel, M. Asymmetric Cathodoluminescence Emission in CH3NH3PbI3-XBrx Perovskite Single Crystals. *ACS Photonics* **2016**, *3* (6), 947–952. https://doi.org/10.1021/acsphotonics.6b00290.

(257) Hartmann, C.; Sadoughi, G.; Félix, R.; Handick, E.; Klemm, H. W.; Peschel, G.; Madej, E.; Fuhrich, A. B.; Liao, X.; Raoux, S.; et al. Spatially Resolved Insight into the Chemical and Electronic Structure of Solution-Processed Perovskites—Why to (Not) Worry about Pinholes. *Adv. Mater. Interfaces* **2018**, *5* (5), 1–9. https://doi.org/10.1002/admi.201701420.

(258) Kumar, V.; Schmidt, W. L.; Schileo, G.; Masters, R. C.; Wong-Stringer, M.; Sinclair, D. C.; Reaney, I. M.; Lidzey, D.; Rodenburg, C. Nanoscale Mapping of Bromide Segregation on the Cross Sections of Complex Hybrid Perovskite Photovoltaic Films Using Secondary Electron Hyperspectral Imaging in a Scanning Electron Microscope. *ACS Omega* **2017**, *2* (5), 2126–2133. https://doi.org/10.1021/acsomega.7b00265.

(259) Hentz, O.; Zhao, Z.; Gradečak, S. Impacts of Ion Segregation on Local Optical Properties in Mixed Halide Perovskite Films. *Nano Lett.* **2016**, *16* (2), 1485–1490. https://doi.org/10.1021/acs.nanolett.5b05181.

(260) Deng, X.; Wen, X.; Lau, C. F. J.; Young, T.; Yun, J.; Green, M. A.; Huang, S.; Ho-Baillie, A. W. Y. Electric Field Induced Reversible

146

References

and Irreversible Photoluminescence Responses in Methylammonium Lead Iodide Perovskite. *J. Mater. Chem. C* **2016**, *4* (38), 9060–9068. https://doi.org/10.1039/C6TC03206K.

(261) Cacovich, S.; Divitini, G.; Ireland, C.; Matteocci, F.; Di Carlo, A.; Ducati, C. Elemental Mapping of Perovskite Solar Cells by Using Multivariate Analysis: An Insight into Degradation Processes. *ChemSusChem* **2016**, *9* (18), 2673–2678. https://doi.org/10.1002/cssc.201600913.

(262) Li, W.; Rothmann, M. U.; Liu, A.; Wang, Z.; Zhang, Y.; Pascoe, A. R.; Lu, J.; Jiang, L.; Chen, Y.; Huang, F.; et al. Phase Segregation Enhanced Ion Movement in Efficient Inorganic CsPbIBr2Solar Cells. *Adv. Energy Mater.* **2017**, *7* (20), 1–8. https://doi.org/10.1002/aenm.201700946.

(263) Divitini, G.; Di Carlo, A.; Cacovich, S.; Ducati, C.; Matteocci, F.; Stranks, S. D.; Abdi-Jalebi, M. Unveiling the Chemical Composition of Halide Perovskite Films Using Multivariate Statistical Analyses. *ACS Appl. Energy Mater.* **2018**, *1* (12), 7174–7181. https://doi.org/10.1021/acsaem.8b01622.

(264) Yoon, S. J.; Draguta, S.; Manser, J. S.; Sharia, O.; Schneider, W. F.; Kuno, M.; Kamat, P. V. Tracking Iodide and Bromide Ion Segregation in Mixed Halide Lead Perovskites during Photoirradiation. *ACS Energy Lett.* **2016**, *1* (1), 290–296. https://doi.org/10.1021/acsenergylett.6b00158.

(265) Hoye, R. L. Z.; Schulz, P.; Schelhas, L. T.; Holder, A. M.; Stone, K. H.; Perkins, J. D.; Vigil-Fowler, D.; Siol, S.; Scanlon, D. O.; Zakutayev, A.; et al. Perovskite-Inspired Photovoltaic Materials: Toward Best Practices in Materials Characterization and Calculations. *Chem. Mater.* **2017**, *29* (5), 1964–1988. https://doi.org/10.1021/acs.chemmater.6b03852.

(266) Sanni, D. M.; Yerramilli, A. S.; Ntsoenzok, E.; Adeniji, S. A.; Oyelade, O. V.; Koech, R. K.; Fashina, A. A.; Alford, T. L. Impact of Precursor Concentration on the Properties of Perovskite Solar Cells Obtained from the Dehydrated Lead Acetate Precursors. *J. Vac. Sci. Technol. A* **2021**, *39* (3), 032801. https://doi.org/10.1116/6.0000714.

(267) Du, S.; Yang, J.; Qu, S.; Lan, Z.; Sun, T.; Dong, Y.; Shang, Z.; Liu, D.; Yang, Y.; Yan, L.; et al. Impact of Precursor Concentration on Perovskite Crystallization for Efficient Wide-Bandgap Solar Cells. *Materials (Basel).* **2022**, *15* (9). https://doi.org/10.3390/ma15093185.

(268) Alturisa, M. I.; Wira, J.; Mardiyati; Herman; Hidayat, R. Influences of Precursor Solution Concentration and Temperature on CH3NH3PbI3 Perovskite Layer Morphology and the Unconverted PbI2 Proportion to Their Perovskite Solar Cell Characteristics. *J. Phys. Conf. Ser.* **2017**, *877* (1). https://doi.org/10.1088/1742-6596/877/1/012046.

(269) Zuo, W. W.; Yang, Y. G.; Fu, W. F.; Li, M.; Malekshahi Byranvand, M.; Di Girolamo, D.; Pascual, J.; Li, M. Q.; Li, L. N.; Abate, A.; et al. In Situ Methylammonium Chloride-Assisted Perovskite Crystallization Strategy for High-Performance Solar Cells. *ACS Mater. Lett.* **2022**, *4* (3), 448–456. https://doi.org/10.1021/acsmaterialslett.1c00830.

(270) Young, J. F. Humidity Control in the Laboratory Using Salt Solutions-a Review. *J. Appl. Chem.* **2007**, *17* (9), 241–245. https://doi.org/10.1002/jctb.5010170901.

(271) Hexemer, A.; Müller-Buschbaum, P. Advanced Grazing-Incidence Techniques for Modern Soft-Matter Materials Analysis. *IUCrJ* **2015**, *2* (1), 106–125. https://doi.org/10.1107/S2052252514024178.

(272) Müller-Buschbaum, P. Grazing Incidence Small-Angle Neutron Scattering: Challenges and Possibilities. *Polym. J.* **2013**, *45* (1), 34–42. https://doi.org/10.1038/pj.2012.190.

(273) Nouhi, S.; Hellsing, M. S.; Kapaklis, V.; Rennie, A. R. Grazing-Incidence Small-Angle Neutron Scattering from Structures below an Interface. *J. Appl. Crystallogr.* **2017**, *50*, 1066–1074. https://doi.org/10.1107/S1600576717007518.

(274) Xiao, C.; Li, Z.; Guthrey, H.; Moseley, J.; Yang, Y.; Wozny, S.; Moutinho, H.; To, B.; Berry, J. J.; Gorman, B.; et al. Mechanisms of Electron-Beam-Induced Damage in Perovskite Thin Films Revealed by Cathodoluminescence Spectroscopy. *J. Phys. Chem. C* **2015**, *119* (48), 26904–26911. https://doi.org/10.1021/acs.jpcc.5b09698.

(275) Van Hove, L. Correlations in Space and Time and Born Approximation Scattering in Systems of Interacting Particles. *Phys. Rev.* **1954**, *95* (1), 249–262. https://doi.org/10.1103/PhysRev.95.249.

(276) Yoneda, Y. Anomalous Surface Reflection of X Rays. *Phys. Rev.* **1963**, *131* (5), 2010–2013. https://doi.org/10.1103/PhysRev.131.2010.

(277) Wolff, M.; Herbel, J.; Adlmann, F.; Dennison, A. J. C.; Liesche, G.; Gutfreund, P.; Rogers, S. Depth-Resolved Grazing-Incidence Time-of-Flight Neutron Scattering from a Solid–Liquid Interface. *J. Appl. Crystallogr.* **2014**, *47* (1), 130–135. https://doi.org/10.1107/S1600576713028665.

(278) Lee, S. W.; Kim, S.; Bae, S.; Cho, K.; Chung, T.; Mundt, L. E.; Lee, S.; Park, S.; Park, H.; Schubert, M. C.; et al. UV Degradation and Recovery of Perovskite Solar Cells. *Sci. Rep.* **2016**, *6* (December), 1–10. https://doi.org/10.1038/srep38150.

(279) Gommes, C. J.; Jaksch, S.; Frielinghaus, H. Small-Angle Scattering for Beginners. *J. Appl. Cryst* **2021**, *54*, 1832–1843. https://doi.org/10.1107/S1600576721010293.

(280) Guinier, A.; Fournet, G. Small-Angle Scattering of X-Rays. *John Wiley Sons, New York* **1955**, *18* (C), 1–19. https://doi.org/10.1107/S0365110X56003089.

(281) Schlipf, J.; Hu, Y.; Pratap, S.; Bießmann, L.; Hohn, N.; Porcar, L.; Bein, T.; Docampo, P.; Mu, P. Shedding Light on the Moisture Stability of 3D/2D Hybrid Perovskite Heterojunction Thin Films. **2019**. https://doi.org/10.1021/acsaem.9b00005.

(282) Neutron Scattering Lengths List | NIST https://www.nist.gov/ncnr/neutron-scattering-lengths-list (accessed Mar 17, 2023).

(283) Alhazmi, N.; Pineda, E.; Rawle, J.; Howse, J. R.; Dunbar, A. D. F. F. Perovskite Crystallization Dynamics during Spin-Casting: An In Situ Wide-Angle X-Ray Scattering Study. *ACS Appl. Energy Mater.* **2020**, *3* (7), 6155–6164. https://doi.org/10.1021/acsaem.9b02470.

(284) Lu, X.; Yager, K. G.; Johnston, D.; Black, C. T.; Ocko, B. M. Grazing-Incidence Transmission X-Ray Scattering: Surface Scattering in the Born Approximation. *J. Appl. Crystallogr.* **2013**, *46* (1), 165–172. https://doi.org/10.1107/S0021889812047887.

(285) Filik, J.; Ashton, A. W.; Chang, P. C. Y.; Chater, P. A.; Day, S. J.; Drakopoulos, M.; Gerring, M. W.; Hart, M. L.; Magdysyuk, O. V.; Michalik, S.; et al. Processing Two-Dimensional X-Ray Diffraction and Small-Angle Scattering Data in DAWN 2. *J. Appl. Crystallogr.* **2017**, *50* (3), 959–966. https://doi.org/10.1107/S1600576717004708.

(286) Jain, A.; Ong, S. P.; Hautier, G.; Chen, W.; Richards, W. D.; Dacek, S.; Cholia, S.; Gunter, D.; Skinner, D.; Ceder, G.; et al. Commentary: The Materials Project: A Materials Genome Approach to Accelerating Materials Innovation. *APL Mater.* **2013**, *1*

References

(1). https://doi.org/10.1063/1.4812323.

(287) D'Innocenzo, V.; Grancini, G.; Alcocer, M. J. P.; Kandada, A. R. S.; Stranks, S. D.; Lee, M. M.; Lanzani, G.; Snaith, H. J.; Petrozza, A. Excitons versus Free Charges in Organo-Lead Tri-Halide Perovskites. *Nat. Commun.* **2014**, *5*, 1–6. https://doi.org/10.1038/ncomms4586.

(288) Luo, S.; Daoud, W. A. Recent Progress in Organic-Inorganic Halide Perovskite Solar Cells: Mechanisms and Material Design. *J. Mater. Chem. A* **2015**, *3* (17), 8992–9010. https://doi.org/10.1039/c4ta04953e.

(289) What is Ellipsometry? - J.A. Woollam.

(290) Forouhi, A. R.; Bloomer, I. Optical Dispersion Relations for Amorphous Semiconductors and Amorphous Dielectrics. *Phys. Rev. B* **1986**, *34* (10), 7018–7026. https://doi.org/10.1103/PhysRevB.34.7018.

(291) Kozak, M. I.; Zhikharev, V. N.; Puga, P. P.; Loya, V. Y. The Kramers-Kronig Relations : Validation via Calculation Technique. **2017**, *4* (12).

(292) Nussenzveig; Moysés, H. *Causality and Dispersion Relations*; Nussenzveig, Ed.; ISSN; Elsevier Science, 1972.

(293) Afzaal, M.; Salhi, B.; Al-Ahmed, A.; Yates, H. M.; Hakeem, A. S. Surface-Related Properties of Perovskite CH3NH3PbI3 Thin Films by Aerosol-Assisted Chemical Vapour Deposition. *J. Mater. Chem. C* **2017**, *5* (33), 8366–8370. https://doi.org/10.1039/c7tc02968c.

(294) Leguy, A. M. A.; Azarhoosh, P.; Alonso, M. I.; Campoy-Quiles, M.; Weber, O. J.; Yao, J.; Bryant, D.; Weller, M. T.; Nelson, J.; Walsh, A.; et al. Experimental and Theoretical Optical Properties of Methylammonium Lead Halide Perovskites. *Nanoscale* **2016**, *8* (12), 6317–6327. https://doi.org/10.1039/c5nr05435d.

(295) Fujiwara, H.; Collins, R. W. *Spectroscopic Ellipsometry for Photovoltaics: Volume 1: Fundamental Principles and Solar Cell Characterization*; Springer Series in Optical Sciences; Springer International Publishing, 2019.

(296) J. A. Woollam Co., I. CompleteEASE Software Manual.

(297) Wang, M.; Gao, Y.; Wang, K.; Liu, J.; De Wolf, S.; Laquai, F. Photo-Induced Enhancement of Lattice Fluctuations in Metal-Halide Perovskites. *Nat. Commun.* **2022**, *13* (1). https://doi.org/10.1038/s41467-022-28532-0.

(298) Alexander V. Naumkin, Anna Kraut-Vass, Stephen W. Gaarenstroom, and C. J. P. NIST X-ray Photoelectron Spectroscopy Database NIST Standard Reference Database 20, Version 4.1. https://doi.org/http://dx.doi.org/10.18434/T4T88K.

(299) Schneider, C. A.; Rasband, W. S.; Eliceiri, K. W.; Instrumentation, C. NIH Image to ImageJ : 25 Years of Image Analysis. **2017**, *9* (7), 671–675.

(300) Li, J.; Yang, R.; Que, L.; Wang, Y.; Wang, F.; Wu, J.; Li, S. Optimization of Anti-Solvent Engineering toward High Performance Perovskite Solar Cells. *J. Mater. Res.* **2019**, *34* (14), 2416–2424. https://doi.org/10.1557/jmr.2019.122.

(301) Taylor, A. D.; Sun, Q.; Goetz, K. P.; An, Q.; Schramm, T.; Hofstetter, Y.; Litterst, M.; Paulus, F.; Vaynzof, Y. A General Approach to High-Efficiency Perovskite Solar Cells by Any Antisolvent. *Nat. Commun.* **2021**, *12* (1), 1878. https://doi.org/10.1038/s41467-021-22049-8.

(302) Ethyl_acetate https://www.chemeurope.com/en/encyclopedia/Ethyl_acetate.html (accessed Apr 4, 2023).

(303) Petrov, A. A.; Sokolova, I. P.; Belich, N. A.; Peters, G. S.; Dorovatovskii, P. V.; Zubavichus, Y. V.; Khrustalev, V. N.; Petrov, A. V.; Grätzel, M.; Goodilin, E. A.; et al. Crystal Structure of DMF-Intermediate Phases Uncovers the Link between CH3NH3PbI3 Morphology and Precursor Stoichiometry. *J. Phys. Chem. C* **2017**, *121* (38), 20739–20743. https://doi.org/10.1021/acs.jpcc.7b08468.

(304) Meyerhofer, D. Characteristics of Resist Films Produced by Spinning. *J. Appl. Phys.* **1978**, *49* (7), 3993–3997. https://doi.org/10.1063/1.325357.

(305) Song, T. Bin; Yuan, Z.; Mori, M.; Motiwala, F.; Segev, G.; Masquelier, E.; Stan, C. V.; Slack, J. L.; Tamura, N.; Sutter-Fella, C. M. Revealing the Dynamics of Hybrid Metal Halide Perovskite Formation via Multimodal In Situ Probes. *Adv. Funct. Mater.* **2020**, *30* (6). https://doi.org/10.1002/adfm.201908337.

(306) Zhong, Y.; Munir, R.; Li, J.; Tang, M.-C.; Niazi, M. R.; Smilgies, D.-M.; Zhao, K.; Amassian, A. Blade-Coated Hybrid Perovskite Solar Cells with Efficiency > 17%: An In Situ Investigation. *ACS Energy Lett.* **2018**, *3* (5), 1078–1085. https://doi.org/10.1021/acsenergylett.8b00428.

(307) Low, I. N. A. G. Spherulitic_Growth_Theory. **2010**, *201*, 417.

(308) Wu, K.-L.; Kogo, A.; Sakai, N.; Ikegami, M.; Miyasaka, T. High Efficiency and Robust Performance of Organo Lead Perovskite Solar Cells with Large Grain Absorbers Prepared in Ambient Air Conditions. *Chem. Lett.* **2015**, *44* (3), 321–323. https://doi.org/10.1246/cl.140919.

(309) Vijayan, A.; Johansson, M. B.; Svanström, S.; Cappel, U. B.; Rensmo, H.; Boschloo, G. Simple Method for Efficient Slot-Die Coating of MAPbI 3 Perovskite Thin Films in Ambient Air Conditions. *ACS Appl. Energy Mater.* **2020**, *3* (5), 4331–4337. https://doi.org/10.1021/acsaem.0c00039.

(310) Cheng, Y.; Xu, X.; Xie, Y.; Li, H.-W.; Qing, J.; Ma, C.; Lee, C.-S.; So, F.; Tsang, S.-W. 18% High-Efficiency Air-Processed Perovskite Solar Cells Made in a Humid Atmosphere of 70%rH. *Sol. RRL* **2017**, *1* (9), 1700097. https://doi.org/10.1002/solr.201700097.

(311) Urwick, A. N.; Bastianini, F.; Pérez, G. E.; Dunbar, A. Deciphering Perovskite Decomposition in a Humid Atmosphere with TOF-GISANS. *Energy Reports* **2022**, *8*, 23–33. https://doi.org/10.1016/j.egyr.2022.05.044.

(312) Chen; Solanki; Pan; Sum. Compositional and Morphological Changes in Water-Induced Early-Stage Degradation in Lead Halide Perovskites. *Coatings* **2019**, *9* (9), 535. https://doi.org/10.3390/coatings9090535.

(313) Schelhas, L. T.; Li, Z.; Christians, J. A.; Goyal, A.; Kairys, P.; Harvey, S. P.; Kim, D. H.; Stone, K. H.; Luther, J. M.; Zhu, K.; et al. Insights into Operational Stability and Processing of Halide Perovskite Active Layers. *Energy Environ. Sci.* **2019**, *12* (4), 1341–1348. https://doi.org/10.1039/c8ee03051k.

(314) Gong, J.; Guo, P.; Benjamin, S. E.; Van Patten, P. G.; Schaller, R. D.; Xu, T. Cation Engineering on Lead Iodide Perovskites for Stable and High-Performance Photovoltaic Applications. *J. Energy Chem.* **2018**, *27* (4), 1017–1039. https://doi.org/10.1016/j.jechem.2017.12.005.

(315) Hada, M.; Abdullah Al Asad, M.; Misawa, M.; Hasegawa, Y.; Nagaoka, R.; Suzuki, H.; Mishima, R.; Ota, H.; Nishikawa, T.; Yamashita, Y.; et al. A Mechanistic Investigation of Moisture-Induced Degradation of Methylammonium Lead Iodide. *Appl.*

References

Phys. Lett. **2020**, *117* (25). https://doi.org/10.1063/5.0021338.

(316) Mcgovern, L.; Futscher, M. H.; Muscarella, L. A.; Ehrler, B. Understanding the Stability of MAPbBr 3 versus MAPbI 3 : Suppression of Methylammonium Migration and Reduction of Halide Migration. **2020**. https://doi.org/10.1021/acs.jpclett.0c01822.

(317) Liu, Y.; Wu, Z.; Dou, Y.; Zhang, J.; Bu, T.; Zhang, K.; Fang, D.; Ku, Z.; Huang, F.; Cheng, Y. B.; et al. Formamidinium-Based Perovskite Solar Cells with Enhanced Moisture Stability and Performance via Confined Pressure Annealing. *J. Phys. Chem. C* **2020**, *124* (23), 12249–12258. https://doi.org/10.1021/acs.jpcc.0c02289.

(318) Jin, J.; Li, H.; Chen, C.; Zhang, B.; Xu, L.; Dong, B.; Song, H.; Dai, Q. Enhanced Performance of Perovskite Solar Cells with Zinc Chloride Additives. *ACS Appl. Mater. Interfaces* **2017**, *9* (49), 42875–42882. https://doi.org/10.1021/acsami.7b15310.

(319) Kooijman, A.; Muscarella, L. A.; Williams, R. M. Perovskite Thin Film Materials Stabilized and Enhanced by Zinc(II) Doping. *Appl. Sci.* **2019**, *9* (8). https://doi.org/10.3390/app9081678.

(320) Lanzetta, L.; Aristidou, N.; Haque, S. A. Stability of Lead and Tin Halide Perovskites: The Link between Defects and Degradation. **2020**. https://doi.org/10.1021/acs.jpclett.9b02191.

(321) Zhang, Q.; Hao, F.; Li, J.; Zhou, Y.; Wei, Y.; Lin, H. Perovskite Solar Cells: Must Lead Be Replaced – and Can It Be Done? *Sci. Technol. Adv. Mater.* **2018**, *19* (1), 425–442. https://doi.org/10.1080/14686996.2018.1460176.

(322) Klug, M. T.; Osherov, A.; Haghighirad, A. A.; Stranks, S. D.; Brown, P. R.; Bai, S.; Wang, J. T. W.; Dang, X.; Bulović, V.; Snaith, H. J.; et al. Tailoring Metal Halide Perovskites through Metal Substitution: Influence on Photovoltaic and Material Properties. *Energy Environ. Sci.* **2017**, *10* (1), 236–246. https://doi.org/10.1039/c6ee03201j.

(323) Zhao, W.; Yang, D.; Yang, Z.; Liu, S. (Frank). Zn-Doping for Reduced Hysteresis and Improved Performance of Methylammonium Lead Iodide Perovskite Hybrid Solar Cells. *Mater. Today Energy* **2017**, *5*, 205–213. https://doi.org/10.1016/j.mtener.2017.06.009.

(324) Chen, R.; Hou, D.; Lu, C.; Zhang, J.; Liu, P.; Tian, H.; Zeng, Z.; Xiong, Q.; Hu, Z.; Zhu, Y.; et al. Zinc Ion as Effective Film Morphology Controller in Perovskite Solar Cells. *Sustainable Energy and Fuels*. 2018, pp 1093–1100. https://doi.org/10.1039/c8se00059j.

(325) Muscarella, L. A.; Petrova, D.; Jorge Cervasio, R.; Farawar, A.; Lugier, O.; McLure, C.; Slaman, M. J.; Wang, J.; Ehrler, B.; Von Hauff, E.; et al. Air-Stable and Oriented Mixed Lead Halide Perovskite (FA/MA) by the One-Step Deposition Method Using Zinc Iodide and an Alkylammonium Additive. *ACS Appl. Mater. Interfaces* **2019**, *11* (19), 17555–17562. https://doi.org/10.1021/acsami.9b03810.

(326) Niu, G.; Li, W.; Meng, F.; Wang, L.; Dong, H.; Qiu, Y. Study on the Stability of CH3NH3PbI3 Films and the Effect of Post-Modification by Aluminum Oxide in All-Solid-State Hybrid Solar Cells. *J. Mater. Chem. A* **2014**, *2* (3), 705–710. https://doi.org/10.1039/c3ta13606j.

(327) Zhang, W.; Pathak, S.; Sakai, N.; Stergiopoulos, T.; Nayak, P. K.; Noel, N. K.; Haghighirad, A. A.; Burlakov, V. M.; Dequilettes, D. W.; Sadhanala, A.; et al. Enhanced Optoelectronic Quality of Perovskite Thin Films with Hypophosphorous Acid for Planar Heterojunction Solar Cells. *Nat. Commun.* **2015**, *6* (May), 1–9. https://doi.org/10.1038/ncomms10030.

(328) Hentz, O.; Zhao, Z.; Gradečak, S. Direct Correlation between Local Stoichiometry and Optoelectronic Properties in CH 3 NH 3 PbI 3 Films. **2016**, No. c, 3661–3663.

(329) Falk, L. M.; Goetz, K. P.; Lami, V.; An, Q.; Fassl, P.; Herkel, J.; Thome, F.; Taylor, A. D.; Paulus, F.; Vaynzof, Y. Effect of Precursor Stoichiometry on the Performance and Stability of MAPbBr3 Photovoltaic Devices. *Energy Technol.* **2020**, *8* (4), 1–8. https://doi.org/10.1002/ente.201900737.

(330) Kumar, V.; Barbé, J.; Schmidt, W. L.; Tsevas, K.; Ozkan, B.; Handley, C. M.; Freeman, C. L.; Sinclair, D. C.; Reaney, I. M.; Tsoi, W. C.; et al. Stoichiometry-Dependent Local Instability in MAPbI 3 Perovskite Materials and Devices. *J. Mater. Chem. A* **2018**, *6* (46), 23578–23586. https://doi.org/10.1039/C8TA08231F.

(331) Kim, J.; Lee, S. H.; Lee, J. H.; Hong, K. H. The Role of Intrinsic Defects in Methylammonium Lead Iodide Perovskite. *J. Phys. Chem. Lett.* **2014**, *5* (8), 1312–1317. https://doi.org/10.1021/jz500370k.

(332) Tan, S.; Yavuz, I.; Weber, M. H.; Huang, T.; Chen, C. H.; Wang, R.; Wang, H. C.; Ko, J. H.; Nuryyeva, S.; Xue, J.; et al. Shallow Iodine Defects Accelerate the Degradation of α-Phase Formamidinium Perovskite. *Joule* **2020**, 1–17. https://doi.org/10.1016/j.joule.2020.08.016.

(333) Muscarella, L. A.; Petrova, D.; Cervasio, R. J.; Farawar, A.; Lugier, O.; Mclure, C.; Slaman, M. J.; Wang, J.; Von, E. Enhanced Grain-Boundary Emission Lifetime and Additive Induced Crystal Orientation in One-Step Spin-Coated Mixed Cationic (FA/MA) Lead Perovskite Thin Films Stabilized by Zinc Iodide Doping. **2017**, No. October, 1–18. https://doi.org/10.26434/chemrxiv.5484073.v2.

(334) Badrooj, M.; Jamali-Sheini, F.; Torabi, N. Zn-Doped Pb/Sn Hybrid Perovskite Solar Cells: Towards High Photovoltaic Performance. *Sol. Energy* **2022**, *236* (March), 63–74. https://doi.org/10.1016/j.solener.2022.02.034.

(335) Ou, Y.; Lu, Z.; Lu, J.; Zhong, X.; Chen, P.; Zhou, L.; Chen, T. Boosting the Stability and Efficiency of Cs2AgBiBr6 Perovskite Solar Cells via Zn Doping. *Opt. Mater. (Amst).* **2022**, *129* (February), 112452. https://doi.org/10.1016/j.optmat.2022.112452.

(336) Shai, X.; Wang, J.; Sun, P.; Huang, W.; Liao, P.; Cheng, F.; Zhu, B.; Chang, S. Y.; Yao, E. P.; Shen, Y.; et al. Achieving Ordered and Stable Binary Metal Perovskite via Strain Engineering. *Nano Energy* **2018**, *48* (March), 117–127. https://doi.org/10.1016/j.nanoen.2018.03.047.

(337) Wei, Q.; Yin, J.; Bakr, O. M.; Wang, Z.; Wang, C.; Mohammed, O. F.; Li, M.; Xing, G. Effect of Zinc-Doping on the Reduction of the Hot-Carrier Cooling Rate in Halide Perovskites. *Angew. Chemie - Int. Ed.* **2021**, *60* (19), 10957–10963. https://doi.org/10.1002/anie.202100099.

(338) Zheng, H.; Liu, G.; Xu, X.; Alsaedi, A.; Hayat, T.; Pan, X.; Dai, S. Acquiring High-Performance and Stable Mixed-Dimensional Perovskite Solar Cells by Using a Transition-Metal-Substituted Pb Precursor. *ChemSusChem*. 2018, pp 3269–3275. https://doi.org/10.1002/cssc.201801171.

(339) Holzhey, P.; Saliba, M. A Full Overview of International Standards Assessing the Long-Term Stability of Perovskite Solar Cells. *J. Mater. Chem. A* **2018**, *6* (44), 21794–21808. https://doi.org/10.1039/C8TA06950F.

References

(340) Cheng, F.; Zhang, J.; Pauporté, T. Chlorides, Other Halides, and Pseudo-Halides as Additives for the Fabrication of Efficient and Stable Perovskite Solar Cells. *ChemSusChem*. 2021, pp 3665–3692. https://doi.org/10.1002/cssc.202101089.

(341) Barrows, A. T.; Lilliu, S.; Pearson, A. J.; Babonneau, D.; Dunbar, A. D. F.; Lidzey, D. G. Monitoring the Formation of a CH3NH3PbI3–XClx Perovskite during Thermal Annealing Using X-Ray Scattering. *Adv. Funct. Mater.* 2016, *26* (27), 4934–4942. https://doi.org/10.1002/adfm.201601309.

(342) Dualeh, A.; Gao, P.; Seok, S. Il; Nazeeruddin, M. K.; Grätzel, M. Thermal Behavior of Methylammonium Lead-Trihalide Perovskite Photovoltaic Light Harvesters. *Chem. Mater.* 2014, *26* (21), 6160–6164. https://doi.org/10.1021/cm502468k.

(343) Khadka, D. B.; Shirai, Y.; Yanagida, M.; Masuda, T.; Miyano, K. Enhancement in Efficiency and Optoelectronic Quality of Perovskite Thin Films Annealed in MACl Vapor. *Sustain. Energy Fuels* 2017, *1* (4), 755–766. https://doi.org/10.1039/c7se00033b.

(344) Niu, G.; Yu, H.; Li, J.; Wang, D.; Wang, L. Controlled Orientation of Perovskite Films through Mixed Cations toward High Performance Perovskite Solar Cells. *Nano Energy* 2016, *27*, 87–94. https://doi.org/10.1016/j.nanoen.2016.06.053.

(345) Tsai, H.; Nie, W.; Lin, Y. H.; Blancon, J. C.; Tretiak, S.; Even, J.; Gupta, G.; Ajayan, P. M.; Mohite, A. D. Effect of Precursor Solution Aging on the Crystallinity and Photovoltaic Performance of Perovskite Solar Cells. *Adv. Energy Mater.* 2017, *7* (11), 1–9. https://doi.org/10.1002/aenm.201602159.

(346) Travis, W.; Glover, E. N. K.; Bronstein, H.; Scanlon, D. O.; Palgrave, R. G. On the Application of the Tolerance Factor to Inorganic and Hybrid Halide Perovskites: A Revised System. *Chem. Sci.* 2016, *7* (7), 4548–4556. https://doi.org/10.1039/c5sc04845a.

(347) Schelhas, L. T.; Christians, J. A.; Berry, J. J.; Toney, M. F.; Tassone, C. J.; Luther, J. M.; Stone, K. H. Monitoring a Silent Phase Transition in CH3NH3PbI3 Solar Cells via Operando X-Ray Diffraction. *ACS Energy Lett.* 2016, *1* (5), 1007–1012. https://doi.org/10.1021/acsenergylett.6b00441.

(348) Chun-Ren Ke, J.; Walton, A. S.; Lewis, D. J.; Tedstone, A.; O'Brien, P.; Thomas, A. G.; Flavell, W. R. In Situ Investigation of Degradation at Organometal Halide Perovskite Surfaces by X-Ray Photoelectron Spectroscopy at Realistic Water Vapour Pressure. *Chem. Commun.* 2017, *53* (37), 5231–5234. https://doi.org/10.1039/c7cc01538k.

(349) Irish, D. E.; Mccarroll, B.; Young, T. F. Raman Study of Zinc Chloride Solutions. *J. Chem. Phys.* 1963, *39* (12), 3436–3444. https://doi.org/10.1063/1.1734212.

(350) Holleman, A. F.; Wiberg, E.; Wiberg, N.; Eagleson, M.; Brewer, W. *Inorganic Chemistry*; Academic Press, 2001.

(351) Ouyang, Y.; Shi, L.; Li, Q.; Wang, J. Role of Water and Defects in Photo-Oxidative Degradation of Methylammonium Lead Iodide Perovskite. *Small Methods* 2019, *3* (7), 2–7. https://doi.org/10.1002/smtd.201900154.

(352) Haynes, W. M. *CRC Handbook of Chemistry and Physics*; CRC Handbook of Chemistry and Physics; CRC Press, 2011.

(353) Basham, M.; Filik, J.; Wharmby, M. T.; Chang, P. C. Y.; El Kassaby, B.; Gerring, M.; Aishima, J.; Levik, K.; Pulford, B. C. A.; Sikharulidze, I.; et al. Data Analysis WorkbeNch (DAWN). *J. Synchrotron Radiat.* 2015, *22*, 853–858. https://doi.org/10.1107/S1600577515002283.

(354) Toby, B. H.; Von Dreele, R. B. GSAS-II: The Genesis of a Modern Open-Source All Purpose Crystallography Software Package. *J. Appl. Crystallogr.* 2013, *46* (2), 544–549. https://doi.org/10.1107/S0021889813003531.

(355) Zhu, C.; Niu, X.; Fu, Y.; Li, N.; Hu, C.; Chen, Y.; He, X.; Na, G.; Liu, P.; Zai, H.; et al. Strain Engineering in Perovskite Solar Cells and Its Impacts on Carrier Dynamics. *Nat. Commun.* 2019, *10* (1). https://doi.org/10.1038/s41467-019-08507-4.

(356) Rocks, C.; Svrcek, V.; Maguire, P.; Mariotti, D. Understanding Surface Chemistry during MAPbI3 Spray Deposition and Its Effect on Photovoltaic Performance. *J. Mater. Chem. C* 2017, *5* (4), 902–916. https://doi.org/10.1039/c6tc04864a.

(357) Wang, B.; Zhu, M.; Jia, X.; Zhang, Y.; Li, J.; Wang, J. Bridgman Growth and Intrinsic Luminescence of Pure - Cs 2 ZnCl 4 Single. *J. Electron. Mater.* 2022, *51* (11), 6512–6517. https://doi.org/10.1007/s11664-022-09890-3.

(358) Wang, Y.; Duan, L.; Zhang, M.; Hameiri, Z.; Liu, X.; Bai, Y.; Hao, X. PTAA as Efficient Hole Transport Materials in Perovskite Solar Cells: A Review. *Sol. RRL* 2022, *6* (8). https://doi.org/10.1002/solr.202200234.

(359) Spalla, M.; Perrin, L.; Planes, E.; Matheron, M.; Berson, S.; Flandin, L. Effect of the Hole Transporting/Active Layer Interface on the Perovskite Solar Cell Stability. *ACS Appl. Energy Mater.* 2020, *3* (4), 3282–3292. https://doi.org/10.1021/acsaem.9b02281.

(360) Rombach, F. M.; Haque, S. A.; Macdonald, T. J. Lessons Learned from Spiro-OMeTAD and PTAA in Perovskite Solar Cells. *Energy Environ. Sci.* 2021, *14* (10), 5161–5190. https://doi.org/10.1039/d1ee02095a.

(361) Shockley–Queisser Limit - Wikipedia.

(362) He, J.; Li, T.; Liu, X.; Su, H.; Ku, Z.; Zhong, J.; Huang, F.; Peng, Y.; Cheng, Y.-B. Influence of Phase Transition on Stability of Perovskite Solar Cells under Thermal Cycling Conditions. *Sol. Energy* 2019, *188* (January), 312–317. https://doi.org/10.1016/j.solener.2019.06.025.

(363) GISAXS.

12 COVID Impact Statement

The UK lockdown in response to the Covid-19 pandemic meant that I was not able to conduct lab based research – the main focus of my PhD research - between 16th March 2020 and 14th August 2020. When access to the lab was once again permitted, the number of users in the lab was severely limited to ensure that social distancing was easily achievable.

Subsequent lockdowns were not as severe but access to the lab was still significantly restricted. There were restrictions coinciding with national restrictions and the second and third lockdowns, limiting lab access (1 person per lab at any time) from the 17th October 2020 until 18th July 2021. I again had less restricted lab access from July 19th 2021 onwards. From the 10th September 2021 room capacity restrictions began to be lifted.

Lack of access to the lab meant I was not able to carry out various experimental projects in the Spring and Summer of 2021, which resulted in a backlog of experimental work. Furthermore, I and my girlfriend suffered with symptoms of Covid-19 soon after the first lockdown was announced (March 2020). Shortly before the lockdown we had been socialising with a friend who was unknowingly infectious. Upon their return to Singapore, they discovered their Covid-19 positive condition due to the nations policy of testing and quarantining all arrivals. They contacted me and others to inform us (this was midway through March) and within several days both myself, my girlfriend and two others from that social occasion had symptoms with varying degrees of severity.

While my own symptoms were not too harsh, and I largely recovered after 2 weeks, my girlfriend (who was staying with me at the time) dealt with re-occurring symptoms for the next 6 weeks, including chest pain, exhaustion, coughing, and a secondary chest infection. She was not admitted to the hospital as her case was not deemed severe enough for specialist care amidst the stretched resources early on in the pandemic. My own and her illness took a significant portion of my attention away from my research.

In March 2022, I was again infected with a variant of COVID-19, and despite full vaccination, I suffered intense symptoms and I was bedridden for a couple days and unable to work for a week. I was also unable to access the lab afterwards for more than a week as I was in isolation. At this stage I became increasingly aware that, although I had used the lockdown periods to focus on writing, reading papers, and analysis of obtained data so far, the time saved in that respect did not alleviate the core issue of delayed experimental study, data collection and gaining hands on experience.

Therefore, I requested a 3-month extension beyond my then expected PhD completion date of the 28th December 2022 until March 29th 2022 as I believe the lockdown period and my bouts of infection had adversely impacted my ability to pursue my research.

In addition to the Covid extension I had received a 3-month internship extension to December 28th (from an original funding end date of 28th September 2022) due to a placement internship I took in GO-SCIENCE (part of BEIS). I took this opportunity as it was in the interests of my future career opportunities, despite the research impact. This placement was between April and June 2022. In the role I surveyed Science Advisory Councils and Committees across government and the devolved administrations as part of the Science Systems and Capability Directorate. I presented and disseminated my findings to stakeholders including Chief Science Advisors, Chairs of Science Advisory Councils, and the Government Chief Scientific Advisor at the time, Patrick Vallance.

Therefore, I requested and obtained the 3-month extension specifically to enable me to

1.   Perform and analyse upcoming WAXS measurements of perovskite films with Cs, Zn and Cl additives.

This was completed

1.   Make devices based on findings from above and previous work.

This was completed

151

COVID Impact Statement

1. Take measurements of thin film parameters such as density, topography/roughness, and crystal structure before and after hydration to compliment GISANS data on uptake of moisture in perovskite films.

This was not completed. This is because I chose to use the time to do the activities which follow:-

Beyond the specified objectives pursuant to the 2nd extension I:

1. Performed and analysed XPS measurements on perovskite films with Cs, Zn and Cl additives
2. Took part in a collaboration with my supervisor and Dr Johansson (University of Uppsala, Sweden) over approximately 3 weeks on research into crystallisation of perovskites from suspensions in alcohols. During this collaboration we conducted two experiments at the Diamond Light Source Synchrotron over 2 weeks, and visited Uppsala for a week to conduct data analysis.

In total, my 5 year PhD has consisted of the following stages:

1. (Sep 2018-2019): Focused on training with CDT-PV, training at the University of Sheffield, heated stage development and literature review

2. (Sep 2019-2020): WAXS and SANS beam-time grants awarded + Confirmation Viva passed, Covid-19 pandemic begins

3. (Sep2020-2021): Research Continues, focus on analysis of beam-time results and Bath Abbey Paper

4. (Sep2021-2022): Research Continues, Bath Abbey and GISANS papers published + Internship

5. (September 2022-April 2023): Completion of Thesis and collaboration with Dr Johansson

13 Appendix

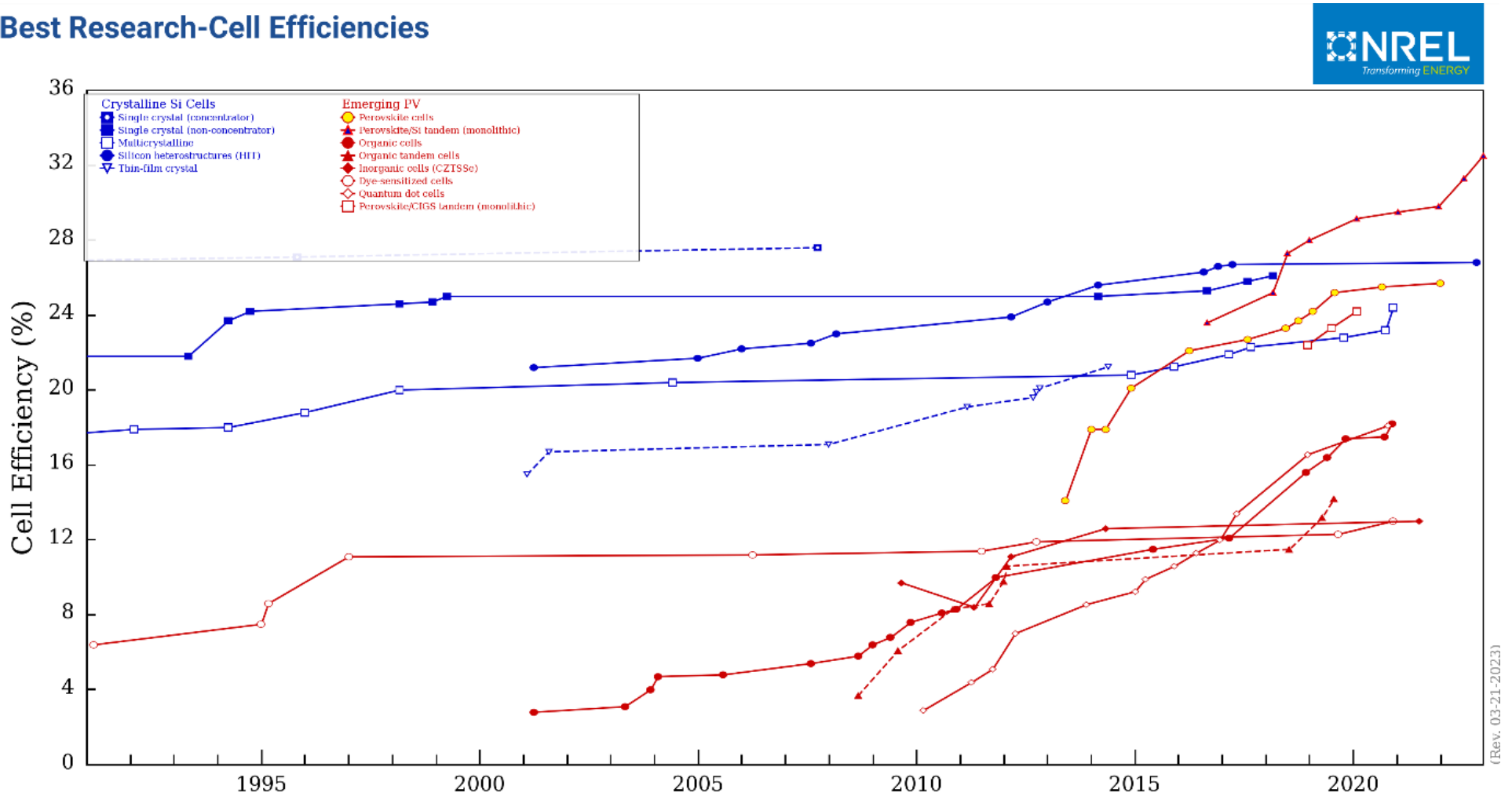## 13.1 Supplementary Tables for Introduction to Solar Cells

Figure 68: NREL 2020 Chart of Best Research-Cell Efficiencies. The rapid improvement of perovskites is shown by the orange bounded yellow circles. (Reproduced from NREL website)
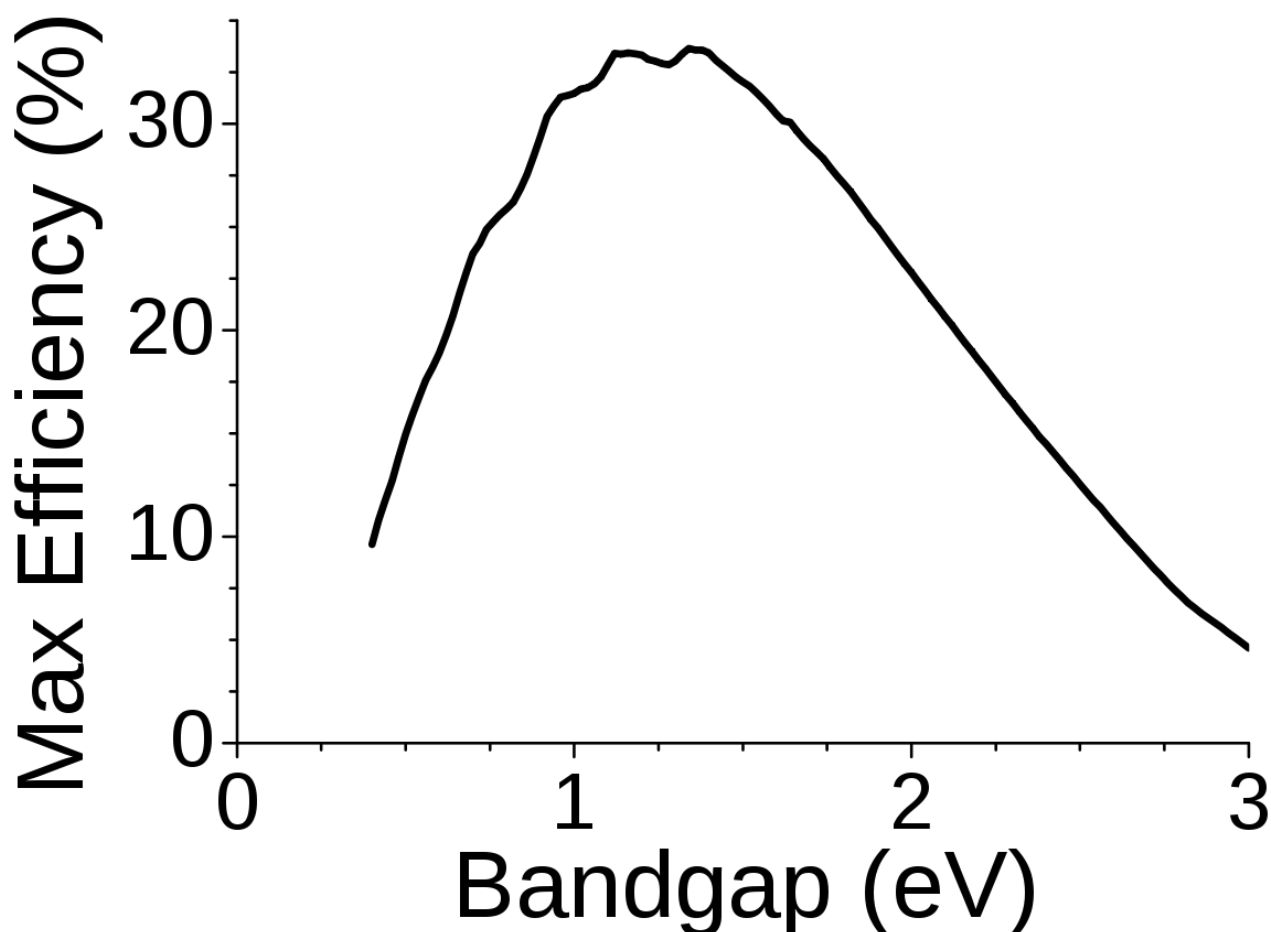
Figure 69: The Shockley–Queisser limit for the efficiency of a solar cell, under 1 sun concentration. Deviations from a smooth curve occur due to absorption bands in the atmosphere. Image reproduced from Wikipedia.[361]

Table 3: Conditions and processes to monitor or control for wherever possible during one-step deposition of perovskite films

Steps of film processing which must be controlled/monitored during one-step deposition:
Colloidal formation…
Precursor Solution Ageing Time (and temperature)
Dynamics vs Static spin coating
Spin speed, time, acceleration
Solvent vapour pressure
Antisolvent window (depends on choice of solvent and antisolvent)
Post-spinning drying (time, rate)
Annealing time (and temperature)
Other conditions to note and if possible, control:
Ambient Humidity
Ambient temperature
rO_2
Solvent atmosphere
Air pressure/Vacuum pressure

Appendix

Table 4: Perovskite devices fabricated using ethyl acetate as an antisolvent

Author	Perovskite	Precursor Solvent: v(ml):v(ml)	Cathode	ETL	HTL	Anode	PCE (%)	rH (%)
Zhang et al. 2020[119]	$MAPbI_3$	DMF: DMSO (4:1)	FTO	SnO_2	Spiro-OMeTAD/4-tert-butypyridine/Li-TFSI	Au	~17	37.5
Yang et al. 2018[120]	$MAPbI_3$	DMF: DMSO (4:1)	FTO	SnO_2	Spiro-OMeTAD/4-tert-butypyridine/Li-TFSI	Au	15.1	60-70
Kumar et al.[A] 2019[128]	$MAPbI_3$	DMSO & DMF	FTO	TiO_2-mp	Spiro-OMeTAD/4-tert-butypyridine/Li-TFSI	Au	13.78	30
Bu et al. [B]2017.[129]	$FA_{0.85}MA_{0.15}Pb(I_{0.85}Br_{0.15})_3$	DMF: DMSO (4:1)	FTO	c-TiO_2/ TiO_2-mp/Li-TFSI	Spiro-OMeTAD/4-tert-butypyridine/Li-TFSI	Au	19.43	-
Troughton et al. 2017[127]	$MAPbI_3$	DMF: DMSO (4:1)	FTO	NiO	PCBM & BCP	Ag	14.5	75
Troughton et al. 2017[127]	$MAPbI_3$	DMF: DMSO (4:1)	FTO	TiO_2-mp	Spiro-OMeTAD/4-tert-butypyridine/Li-TFSI	Au	~15	75
He et al. 2019[362]	$FA_{0.9}Cs_{0.1}PbI_3$	DMF: DMSO (4:1)	FTO	SnO_2	Carbon	-	6.54	
Faibut et al. 2019	$MAPbI_3$	DMF	FTO	c-TiO_2	Carbon	-	5.91	55-65
Faibut et al. 2019	$MAPbI_3$	PbI_2 in DMF, MAI in IPA[C]	FTO	c-TiO_2	Carbon	-	1.56	55-65
Lee et al. 2019 [D]	$FA_{0.85}MA_{0.15}Pb(I_{0.85}Br_{0.15})_3$	DMF: DMSO (4:1)	ITO	SnO_2	Spiro-OMeTAD/4-tert-butypyridine/Li-TFSI	Ag or Au	20.06	-
Zheng et al. 2019	$Cs_{0.05}(FA_{0.85}MA_{0.15})_{0.95}Pb(I_{0.85}Br_{0.15})_3$	DMF: DMSO (4:1)	FTO	SnO_2	Spiro-OMeTAD/4-tert-butypyridine/Li-TFSI	Au	19.26[E]	-
Zheng et al. 2019	$Cs_{0.05}(FA_{0.85}MA_{0.15})_{0.95}Pb(I_{0.85}Br_{0.15})_3$ +3.5mol% KI	DMF: DMSO (4:1)	FTO	SnO_2	Spiro-OMeTAD	Au	~20	-
Kim et al. 2019	$(MAPbI_3)_{95.2}(FAPbIBr_2)_{4.8}$	DMF> DMSO	ITO	SnO_2	Spiro-OMeTAD/4-tert-butypyridine/Li-TFSI	Au	20.93	20
Pandey et al. 2019	$FA_{0.2}MA_{0.8}PbI_3$ +3wt% $Pb(SCN_2)$	-	PET-ITO	PEDOT: PSS	C60/BCP	Ag	15.04	-
Wang et al. 2019	$MAPbI_3$	DMF: DMSO (9:1)	ITO	SnO_2	Spiro-OMeTAD/4-tert-butypyridine/Li-TFSI	Au	19.5	90

Relative humidity (rH) during perovskite processing. If no rH is given, processing was done under N_2 airflow or in an inert atmosphere. (A). Annealed at 230°C for 8s, stored before application of gold contact for 12 hours under 30% humidity. (B): HTL deposited from EA. (C): Two Step deposition. (D): A mixture of EA and hexane was used as an antisolvent. (F): In forward bias

Appendix

Table 5: Definitional Boundaries of various diffraction experiments[363]

Experiment	Incident Angle(°)	q range (Å^{-1})	d –size range	Features
Neutron Experiments				
Neutron Backscattering	180-14	12 - 1	Several Angstroms	Atomic Packing distances
Neutron Diffraction	155-0.2	11 - 0.01	Angstroms - ~60nm	Crystal Structure, Molecules
WANS	90-4	10 - 0.1	Angstroms - ~6nm	Molecules, Crystallites
SANS	40-0.4	0.7 - 0.008	~1 nm - ~80nm	Macromolecules, Mesoscale structures, Nanoparticles, Proteins
VSANS	0.04-0.004	0.001 - 0.0001	~600 nm – 2um	Colloids, Protein Complexes, Small Cells
USANS	0.2-0.00005	0.01 - 7x10^{-6}	~60 nm - ~90um	Microparticles
X-ray Experiments				
Total Scattering	180-0			Utilises Bragg & Diffuse Scattering
X-ray backscattering	180- 90			
XRD	90 - 5	6 - 0.3	Angstroms - ~2 nm	Crystal Structure
WAXS	45 - 1	5 - 0.1	Angstroms - ~6 nm	Molecules, Crystallites
MAXS	8 - 0.08	1 - 0.01	~0.6 nm - ~60 nm	Macromolecular structures Crystallites
SAXS	1 - 0.01	0.1 - 0.001	~6 nm - ~100 nm	Mesoscale structures, Nanoparticles, Proteins
USAXS	0.05 - 0.0001	0.006 - 0.00003	~100 nm - ~20 µm	Colloids, Protein Complexes, Cells Microparticles

13.2 Q-Positions of Predicted Compounds in Perovskite Films during Moisture Induced Degradation

Table 6: Determining the q-position of predicted compounds in perovskite films during moisture induced degradation in the dark. 'Heavy-hydrates' refers to the moisture comprised of two Deuterium as opposed to Hydrogen atoms and 1 Oxygen atom. 'Deuterated' refers to all Hydrogen atoms in a molecule being replaced by Deuterium.

Material	Silicon	MAPbI$_3$	MAPbI$_3$ Mono-heavy-hydrate	MAPbI$_3$ Di-heavy-hydrate	MAPbI$_3$ monohydrate	MAPbI$_3$ di-hydrate	Deuterated MAPbI$_3$	MAPbI3+D$_3$O
Structural formula	Si	CH$_3$NH$_3$PbI$_3$	CH$_3$NH$_3$PbI$_3$•D$_2$O	(CH$_3$NH$_3$)$_4$(PbI$_6$)•2D$_2$O	CH$_3$NH$_3$PbI$_3$•H$_2$O	(CH$_3$NH$_3$)$_4$(PbI$_6$)•2H$_2$O	CD$_3$ND$_3$PbI$_3$	(CH$_3$NH$_3$)(CH$_3$NH$_2$)2 PbI$_3$[D$_3$O]
Molar weight [g mol^{-1}]	28.09	619.98	640.01	1136.95	637.99	1132.92	626.02	1007.18
Density [g cm^{-3}]	2.329	4.159	4.026	3.035	4.026	3.035	4.159	4.159
Molar volume, V$_M$ [cm^3 mol^{-1}]	12.061	149.069	158.969	374.613	158.467	373.287	103.919	242.170
Molecular Volume (V$_M$/NA) [cm^3]	2.003E-23	2.475E-22	2.640E-22	6.221E-22	2.631E-22	6.199E-22	1.726E-22	4.021E-22
Volume ratio		1.000	1.066	2.513	1.063	2.504	1.010	7.378
Σ b$_{coherent (fm)}$	4.149	18.823	37.968	53.685	42.387	13.489	81.271	67.186
b(r) [10^{-6} Å^{-2}]	2.072	0.760	1.438	0.863	1.611	0.218	3.252	1.671
Critical angle [°]	3.4106	2.0663	2.8418	2.2013	3.0074	1.1054	4.2729	3.0629
q-value [1/nm]	0.0178	0.0108	0.0148	0.0115	0.0157	0.0058	0.0223	0.0160

Appendix

Material	Lead	Lead Iodide	Lead Hydroxide	Lead Heavy Hydroxide	Lead(II) Oxide	Lead(IV) Oxide	Lead Bromide	FaCs	FACs monohydrate	FACs dihydrate	Deuterated FACs
Structural formula	Pb	PbI_2	$PbOH_2$	$PbOD_2$	PbO	Pb_3O_4	$PbBr_2$	$(CH_5N_2)_{0.83}Cs_{0.17}Pb(I_{0.83}Br_{0.17})_3$	$(CH_5N_2)_{0.83}Cs_{0.17}Pb(I_{0.83}Br_{0.17})_3 \cdot D_2O$	$((CH_5N_2)_{0.83}Cs_{0.17})_4Pb(I_{0.83}Br_{0.17})_6 \cdot 2D_2O$	$(CD_5N_2)_{0.83}Cs_{0.17}Pb(I_{0.83}Br_{0.17})_3$
Molar weight [g mol^{-1}]	207.19	461.01	241.21	243.22	223.20	685.60	367.01	633.82	653.85	1240.26	638.85
Density [g cm^{-3}]	11.290	6.106	7.410	7.410	9.530	8.300	6.606	4.252	4.116	3.004	4.252
Molar volume, V_M [cm^3 mol^{-1}]	18.352	75.501	32.552	32.823	23.421	82.602	55.557	149.069	158.861	412.933	150.253
Molecular Volume (V_M/NA) [cm^3]	3.047E-23	1.254E-22	5.405E-23	5.450E-23	3.889E-23	1.372E-22	9.225E-23	2.475E-22	2.638E-22	6.857E-22	2.495E-22
Volume ratio	0.123	0.506	0.218	0.220	0.157	0.554	0.373	1.000	1.066	2.770	1.000
Σ b$_{coherent (fm)}$	9.405	19.965	7.730	28.550	15.208	49.540	22.995	36.248	55.393	102.698	88.293
b(r) [10^{-6} Å^{-2}]	3.086	1.592	1.430	5.238	3.910	3.612	2.493	1.464	2.100	1.498	3.539
Critical angle [°]	4.1629	2.9903	2.8337	5.4233	4.6858	4.5033	3.7411	2.8675	3.4338	2.9000	4.4576
q-value [1/nm]	0.0217	0.0156	0.0148	0.0283	0.0244	0.0235	0.0195	0.0150	0.0179	0.0151	0.0233

Appendix

Material	FAMAX	FAMAX Mono-heavy-hydrate	FAMAX di-heavy-hydrate		Cs-FAMAX	Deuterated Cs-FAMAX	Cesium Iodide		
Structural formula	$(CH_3NH_3)_{0.17}(CH_5N_2)_{0.83}Pb(I_{0.83}Br_{0.17})_3$	$((CH_3NH_3)_{0.17}(CH_5N_2)_{0.83})_4Pb(I_{0.83}Br_{0.17})_6 \cdot 2D_2O$	$(CH_3NH_3)_{0.17}(CH_5N_2)_{0.83}Pb(I_{0.83}Br_{0.17})_3 \cdot D_2O$	$(CH_3NH_3)(CH_3NH_2)_2PbI_3[D_3O]$	$(CsI)_{0.05}(((CH_3NH_3)_{0.17}(CH_5N_2)_{0.83})Pb(I_{0.17}Br_{0.83})_3)_{0.95}$		CsI	CsMAFA-D2O	$CsPb_2I_4Br$
Molar weight [g mol^{-1}]	606.81	626.84	1132.21	1007.18	589.46	594.49	259.81	609.49	1261.73
Density [g cm^{-3}]	4.071	3.940	2.971	4.159	3.954	3.954	7.024	3.828	5.150
Molar volume, V_M [cm^3 mol^{-1}]	149.069	159.077	381.148	242.170	149.069	150.342	36.989	159.227	244.997
Molecular Volume (V_M/NA) [cm^3]	2.475E-22	2.642E-22	6.329E-22	4.021E-22	2.475E-22	2.496E-22	6.142E-23	2.644E-22	4.068E-22
Volume ratio	1.000	1.067	2.557	7.378	1.000	1.000	0.359	1.068	6.624
$\Sigma\ b_{coherent\ (fm)}$	33.462	52.607	91.555	67.186	32.324	84.369	10.700	37.561	52.145
b(r) [10^{-6} Å^{-2}]	1.352	1.992	1.447	1.671	1.306	3.380	1.742	1.421	1.282
Critical angle [°]	2.7551	3.3440	2.8500	3.0629	2.7078	4.3561	3.1276	2.8243	2.6827
q-value [1/nm]	0.0144	0.0175	0.0149	0.0160	0.0141	0.0227	0.0163	0.0147	0.0140

Appendix

Material	FAPbBr$_3$	FAPbBr$_3$-Mono-heavy-hydrate	FAPbI$_3$	FAPbI$_3$. Mono-heavy-hydrate	FAPbI$_3$. Di-heavy-hydrate	Deuterated FAPbI$_3$	Deuterated FAPbBr$_3$	MAPbBr$_3$	MAPbBr$_3$ mono-heavy-hydrate	Deuterated MAPbBr$_3$
Structural formula	CH$_5$N$_2$PbBr$_3$	CH$_5$NH$_2$PbBr$_3$+D$_2$O	CH$_5$N$_2$PbI$_3$	CH$_5$N$_2$PbI$_3$.D$_2$O	(CH$_5$N$_2$)$_4$(PbI$_6$).2(D$_2$O)	CD$_5$N$_2$PbI$_3$	CD$_5$N$_2$PbBr$_3$	CH3NH3PbBr3	CH3NH3PbBr3+D2O	CD$_3$ND$_3$PbBr$_3$
Molar weight [g mol^{-1}]	491.99	512.02	632.98	653.01	1208.91	638.01	497.02	478.98	499.01	485.02
Density [g cm^{-3}]	3.300	3.672	4.087	3.956	2.982	4.087	3.300	3.830	3.708	3.830
Molar volume, V$_M$ [cm^3 mol^{-1}]	149.069	139.450	154.876	165.055	405.340	156.107	150.594	125.060	134.594	126.636
Molecular Volume (V$_M$/NA) [cm^3]	2.475E-22	2.316E-22	2.572E-22	2.741E-22	6.731E-22	2.592E-22	2.501E-22	2.077E-22	2.235E-22	2.103E-22
Volume ratio	1.000	0.935	1.039	1.107	2.719	1.047	1.010	0.839	0.903	0.850
Σ b$_{coherent (fm)}$	36.461	55.606	31.916	51.061	106.059	83.961	88.506	23.362	42.507	85.816
b(r) [10^{-6} Å^{-2}]	1.473	2.401	1.241	1.863	1.576	3.239	3.539	1.125	1.902	4.081
Critical angle [°]	2.8759	3.6720	2.6397	3.2343	2.9745	4.2646	4.4579	2.5133	3.2679	4.7869
q-value [1/nm]	0.0150	0.0192	0.0138	0.0169	0.0155	0.0222	0.0233	0.0131	0.0171	0.0250

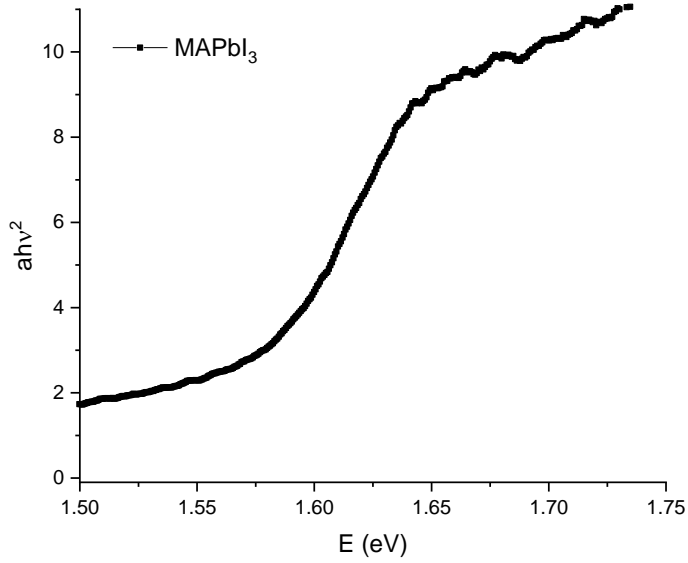## 13.3 Sample Tauc & Urbach Plots from UV-vis absorbance spectra

Figure 70: Sample Tauc Plot of MAPbI₃
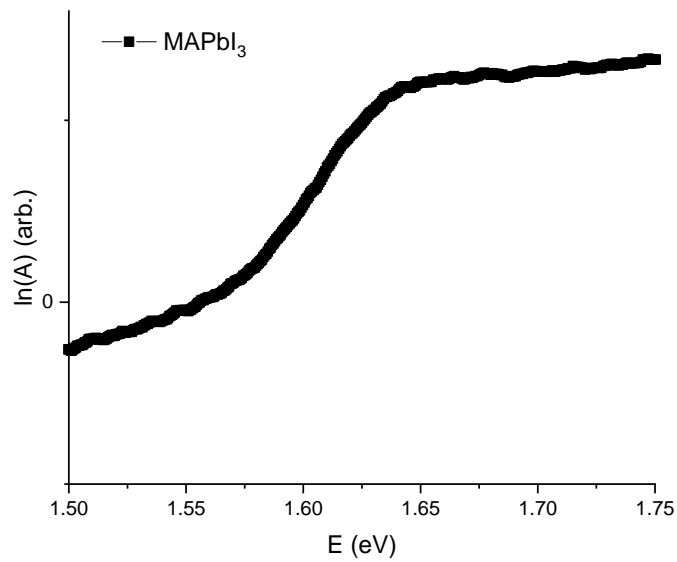

Figure 71: Sample Urbach Plot of MAPbI₃.

13.4 Supplementary Data for 16% Efficient MAPbI3 solar cells under ambient conditions via intermediate phase formation control by synergised ethyl acetate application with stoichiometric regulation
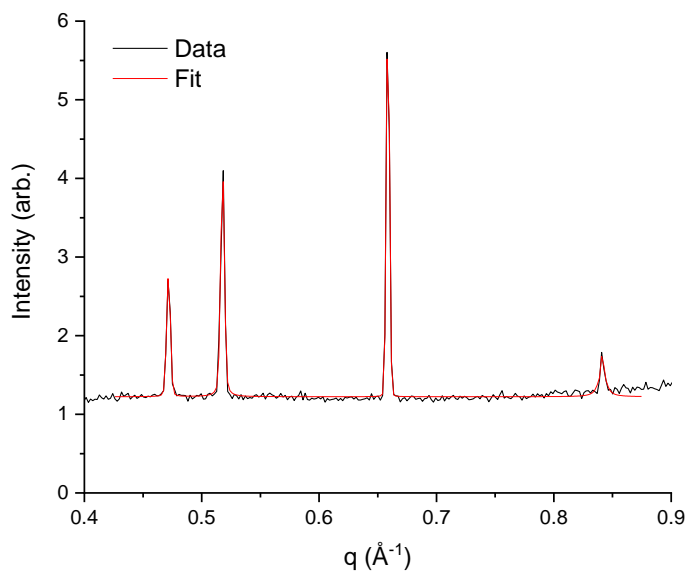

Figure 72: Example fit of low-q scattering peaks with pseudo-voigt type model. Shown are the peaks of the MAI-PbI$_2$-DMSO intermediate (MA
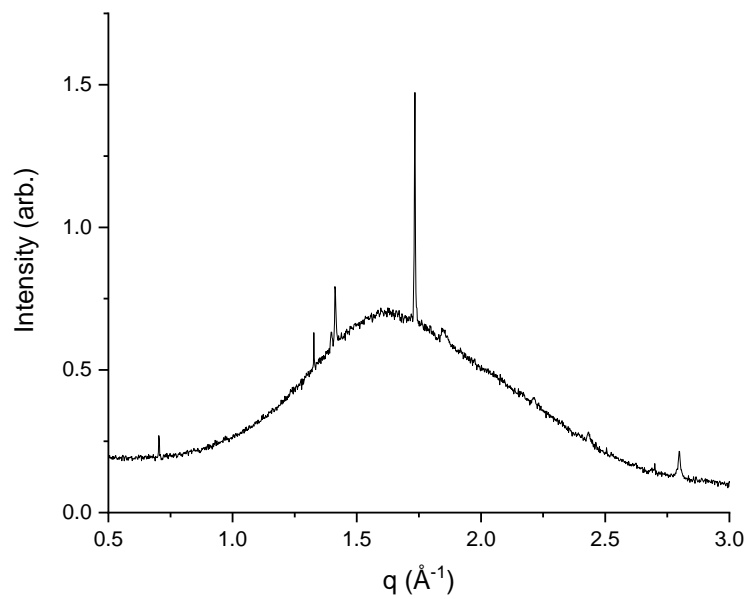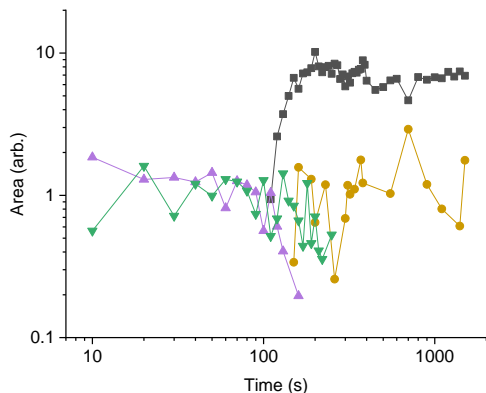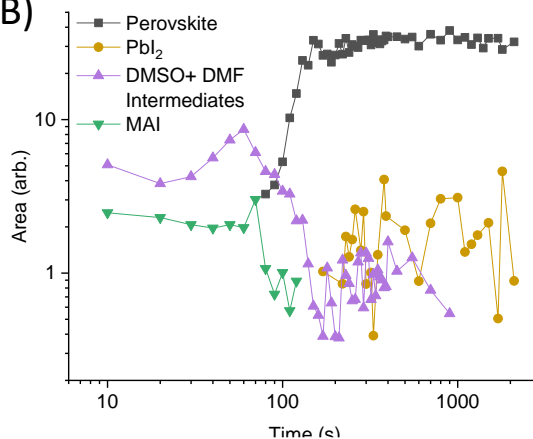
Figure 73: Scattering peaks of MAI crystallised after spin-coating from a solution of DMSO:DMF. The small peak at 0.7 Å^{-1} occurs in scattering from MAPbI$_3$ films
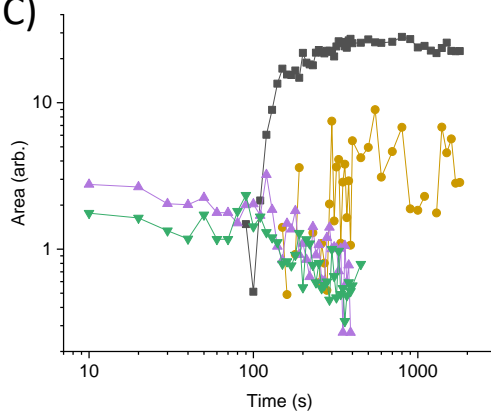
Figure 74: Log-log Plots of area vs time for (A) MAI enriched, (B) Equimolar and (C) PbI$_2$ enriched films over complete 35mins of annealing. The peak area shown the integrated intensity beneath specific peaks indicating each phase; for perovskite: 1.07 Å^{-1}, 2.11 Å^{-1}, 2.35 Å^{-1}, 2.94 Å^{-1}, 3.11 Å^{-1} peaks; for trigonal PbI$_2$: 1.51 Å^{-1} and 1.83 Å^{-1} peaks; for the intermediates: 0.51 Å^{-1}(DMSO) and 0.56 Å^{-1}(DMF) peaks; for MAI, the 0.71 Å^{-1} peak.
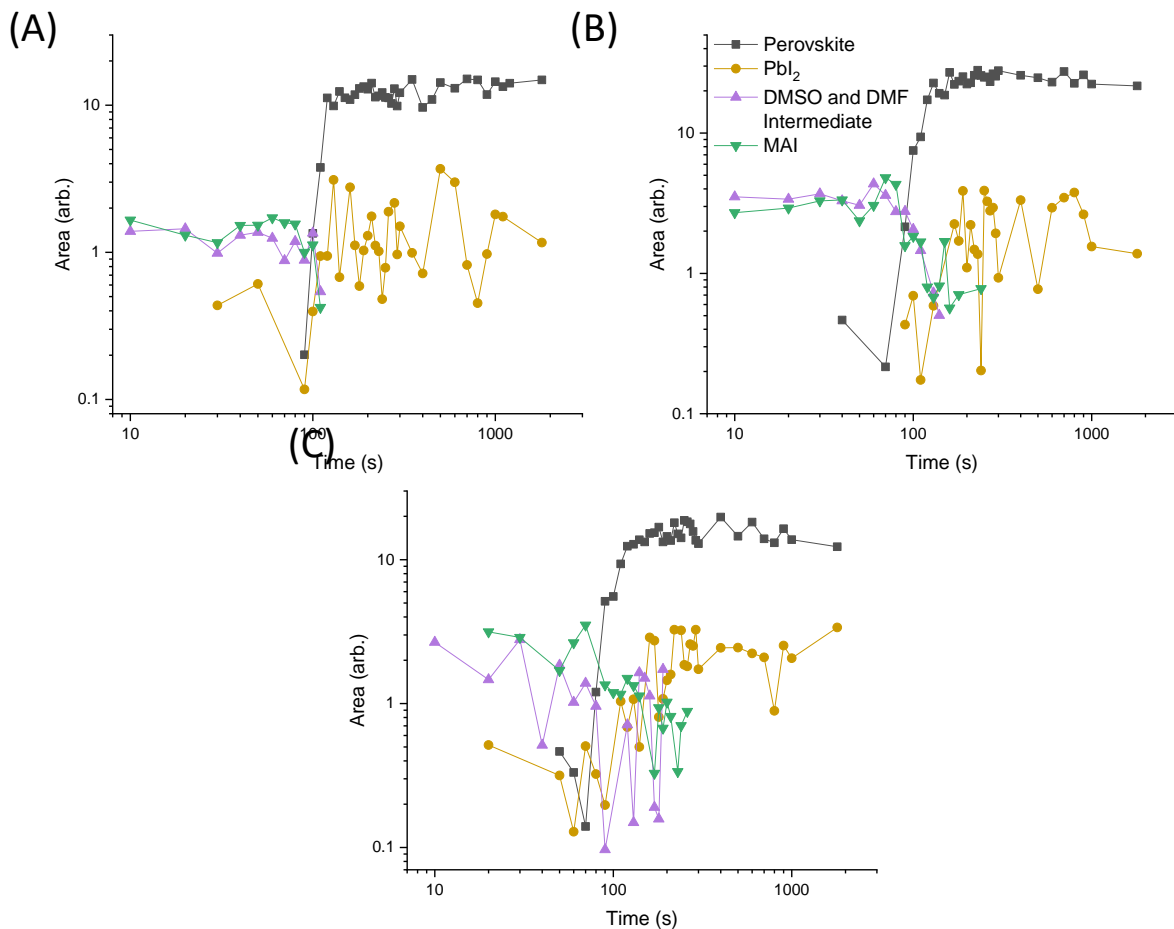
Figure 75: Log-log Plots of area vs time for (A) MAI enriched, (B) Equimolar and (C) PbI_2 enriched films treated with ethyl acetate over complete 35mins of annealing. The peak area shows the integrated intensity beneath specific peaks indicating each phase; for perovskite: 1.07 Å^{-1}, 2.11 Å^{-1}, 2.35 Å^{-1}, 2.94 Å^{-1}, 3.11 Å^{-1} peaks; for trigonal PbI_2: 1.51 Å^{-1} and 1.83 Å^{-1} peaks; for the intermediates: 0.51 Å^{-1}(DMSO) and 0.56 Å^{-1}(DMF) peaks; and for MAI, the 0.71 Å^{-1} peak.

Appendix - Supplementary Data for 16% Efficient MAPbI3 solar cells under ambient conditions via intermediate phase formation control by synergised ethyl acetate application with stoichiometric regulation

Table 7: Device Parameters under Reverse Bias of MAPbI$_3$ devices as a function of ethyl acetate drip time and drip volume.

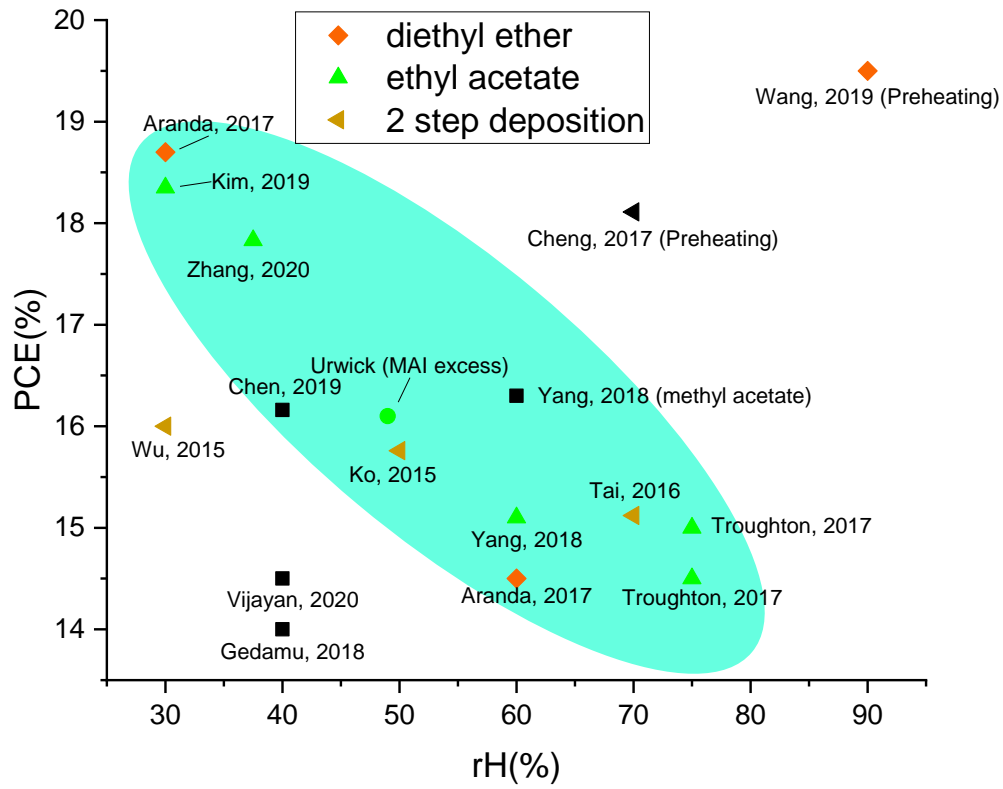| MAI:PbI$_2$ ratio	MAPbI$_3$ devices with varying MAI:PbI$_2$ ratio , Ag contact, 100 µl EA, Tdrip$_{15s}$			
	J_{SC} (mA/cm^2)	V_{OC} (V)	FF (%)	PCE (%)
1.1:1	20.73	1.04	69.22	15.33
1:1	20.41	1.06	67.04	14.44
1:1.1	21.16	1.07	63.41	14.34
EA Drip time (s)	MAI exs. MAPbI$_3$, Ag contact, 200 µl EA			
10	20.60	1.05	64.62	13.78
15	20.31	1.04	67.19	14.41
20	18.96	1.03	63.70	12.99
EA Drip volume (µl)	Equimolar MAPbI$_3$, Au contact, Tdrip$_{10s}$			
50	21.36	1.06	65.47	14.87
75	21.24	1.06	68.05	15.28
100	21.52	1.06	68.39	15.61
200	20.98	1.05	67.66	15.03

Figure 76: MAPbI₃ devices made in ambient air with ethyl acetate showing PCE(%) as a function of relative humidity(rH%). This work is highlighted as the green (referring to ethyl acetate) circle, labelled with an MAI excess. The oval highlights the general relationship between increasing rH% and decreasing PCE%.

Appendix

13.5 Python Code for Contour Plots

```python
In [ ]:  import math
         import numpy as np
         import pandas as pd
         import matplotlib.pyplot as plt
         from scipy.signal import chirp, find_peaks, peak_widths
         import matplotlib.pyplot as plt
         from mpl_toolkits.mplot3d import Axes3D
         %matplotlib inline
         import glob

         static_glass_background_20s = pd.read_csv(r'C:\Users\Usedr\Documents\PhD python\Xray\clean glass\p2mImage662765_00000.txt', name
         spinning_glass_background_5s = pd.read_csv(r'C:\Users\Usedr\Documents\PhD python\Xray\clean glass\p2mImage664571_00000.txt', nam
         #print(spinning_glass_background_5s.loc[:,'intensity'])

         files = glob.glob("*[.dat]")
         Your_data = [pd.read_csv(f, names=['q','intensity','error'] ,sep="\t") for f in files]


         def Contourplot(Your_data):
             intensity_dataframe_list=[]
             q_values_list=[]
             twotheta_values_list=[]
             time_list=[]
             timedf=[]
             TIMES=[]
             peaksarray=[];fwhmdf=[];intensityarray=[];q_array=[]; allpeakswidthsarray=[]
             test=[];test2=[];test3=[]
             a=0
             fig =plt.figure(figsize=(10,7.6), dpi=100)
             hh='_'
             name=input('Plot Title')
```

```python
             for f in Your_data:
                 intensity= f.loc[:,'intensity'].values#- (spinning_glass_background_5s.loc[:,'intensity'].values)* (correction_factor)
                 q_values= f.loc[:,'q'].values
                 q_array.append(q_values)
                 i_df = pd.DataFrame(data=intensity.flatten())
                 q_df = pd.DataFrame(data=q_values.flatten())
                 intensity_dataframe_list.append(i_df)
                 q_values_list.append(q_df)
                 sintheta= f.loc[:,'q'].values*1.1808/(4*math.pi)
                 two_theta= pd.DataFrame(2*np.degrees(np.arcsin(sintheta)))
                 twotheta_values_list.append(two_theta)
                 normalised_intensity= ((intensity)-(np.min(intensity)))/((np.max(intensity))-(np.min(intensity)))
                 intmod=-normalised_intensity
                 intensityarray.append(intensity)
                 a+=1

             A=1;
             for intensityvals, qvals in zip(intensity_dataframe_list, q_values_list):
                 #seq=(str(0.5*(A+1)),'hours')
                 M3=(20*(A-60))
                 M1=A
                 M2=60
                 if M1 > 60:
                     T= math.exp(math.log(10*M2))+math.exp(math.log(M3))
                 else:
                     T= math.exp(math.log(10*A))
                 #seq2=(str(files[A])[:-4])
                 time_list.append(np.full(len(qvals),T))
                 time=pd.DataFrame(np.full(len(qvals),T))
                 timedf.append(time)
                 TIMES.append(T)

                 A+=1
```

```python
         Zz=np.transpose(intensityarray)
         Xx=np.transpose(time_list)
         Yy=np.transpose(q_array)

         plt.style.use('seaborn-white')

         axes2=plt.subplot(221)
         count=0
         for X, Y, Z in zip(Xx,q_array,Zz):
             A, B = np.meshgrid(X, Y)
             #print('length of Y is',len(Y),'shape of Y is', np.shape(Y),'\n', pd.DataFrame(Y))
             #print(np.meshgrid(X,Y))
             #print('B IS',len(B), '\n',B)
             #print(len(Y), len(X))
             #print(len(Zz))
         #print('shape of','t is:', np.shape(Xx),'q is:', np.shape(q_array), 'Z is:',np.shape(Z))
             plt.contourf(A, B, Zz, 50, cmap='viridis')
             count+=1
         cbar=plt.colorbar()
         cbar.set_label('Intensity (arb.)')
         axes2.axis(aspect='image')
         #axes2.set_title('Annealing MAPbI$_3$', loc='left', size=12)
         axes2.set_xlabel('Time')
         axes2.set_ylabel('q ($\AA$${-1}$)')
```

```python
axes3=plt.subplot(222)
Xxs=np.transpose(np.array(time_list)[0:60])
Yys=(np.array(q_array)[10:60])
Zzs=np.transpose(np.array(intensityarray)[0:60])
count2=0
for U, V in zip(Xxs,Yys):
    C, D = np.meshgrid(U, V)
    plt.contourf(C, D, Zzs, 50, cmap='viridis')
    count2+=1

cbar=plt.colorbar()
cbar.set_label('Intensity (arb.)')
axes3.axis(aspect='image')
#axes3.set_title('Annealing MAPbI$_3$, 10min', loc = 'left', size=12)
axes3.set_xlabel('Time')
axes3.set_ylabel('q ($\AA$${-1}$)')
#plt.imshow(Zz, extent=[0, 35, 0, 3.5], origin='lower',
    #cmap='hsv')
axes4=plt.subplot(223)
Xxz=np.transpose(np.array(time_list)[0:10])
Yyz=(np.array(q_array)[0:10])
Zzz=np.transpose(np.array(intensityarray)[0:10])
count3=0
for U, V in zip(Xxz,Yyz):
    C, D = np.meshgrid(U, V)
    plt.contourf(C, D, Zzz, 50, cmap='viridis')
    count3+=1
cbar=plt.colorbar()
cbar.set_label('Intensity (arb.)')
axes4.axis(aspect='image')
#.set_title('Annealing MAPbI$_3$, 10min', loc = 'left', size=12)
axes4.set_xlabel('Time')
axes4.set_ylabel('q ($\AA$${-1}$)')

#axes5=plt.subplot(224)
#Xxz=np.transpose(np.array(time_list)[0:4])
#Yyz=(np.array(q_array)[0:4])
#Zzz=np.transpose(np.array(intensityarray)[0:4])
#count3=0
#for U, V in zip(Xxz,Yyz):
    #C, D = np.meshgrid(U, V)
    #plt.contourf(C, D, Zzz, 50, cmap='viridis')
    #count3+=1
#cbar=plt.colorbar()
#cbar.set_label('Intensity (arb.)')
#axes5.axis(aspect='image')
#axes5.set_title('Annealing MAPbI$_3$, 10min', loc = 'left', size=12)
#axes5.set_xlabel('Time')
#axes5.set_ylabel('q ($\AA$${-1}$)')

fig.subplots_adjust(right=0.9, wspace=0.2)
fig.tight_layout()
fig.show()
fig.savefig(fname=name)
```

13.6 Supplementary Data for The Limited Benefits of ZnCl$_2$ as a Stabilizing Additive for Perovskite Films

Table 8: 3mol% Zn additive non-encapsulated devices after exposure to various conditions.

Device	Zn Source	mol %	Fabrication Atmosphere	PCE$_{after}$/ PCE$_{initial}$	rH (%)	Temp (°C)	Time (hours)	Reference
FTO/cTiO$_2$•mpTiO$_2$/MAPb$_{0.97}$ Zn$_{0.03}$I$_3$/spiro-OMeTAD + 4-tbp + LiTFSI + Co(III)/Au	ZnI$_2$	0.03	20%rH	0.81	40	20-25	800	(Zheng *et al.*, 2018) 10.1002/cssc. 201801171
	ZnI$_2$	0.03	20%rH	0.84	<10	60	100	10.1002/cssc. 201801171
FTO/cTiO$_2$ /MAI(PbI$_2$)$_{0.97}$(ZnCl$_2$)$_{0.03}$/spiro -OMeTAD + 4-tbp + LiTFSI/Au	ZnCl$_2$	0.03	N$_2$	0.7	30-55	85	180	(Jin *et al.*, 2017) 10.1021/acsa mi.7b15310
	ZnCl$_2$	0.03	N$_2$	0.93	30-55	25-28	~700	10.1021/acsa mi.7b15310
ITO/cTiO$_2$/MAPb$_{0.97}$Zn$_{0.02}$I$_3$/s piro-OMeTAD + 4-tbp + LiTFSI/Ag	ZnI$_2$	0.02	-	-	-	-	-	(Que *et al.*, 2018) 10.1016/j.che mphys.2018.0 9.032
ITO/SnO$_2$/ MA$_{.97}$Cs$_{0.03}$Pb$_{0.97}$Zn$_{0.03}$(I$_{0.97}$Cl$_{0.03}$)$_3$/ PTAA + 4-tbp + LiTFSI /Ag	*ZnCl$_2$*	*0.03*	*45-50%rH*	*0.64*	*45-60*	*20-22*	*120*	*(This work)*

Those shaded grey are experiments investigating effect of humidity exposure on performance stability whilst those shaded red are experiments investigating effect of isothermal heating on performance stability.
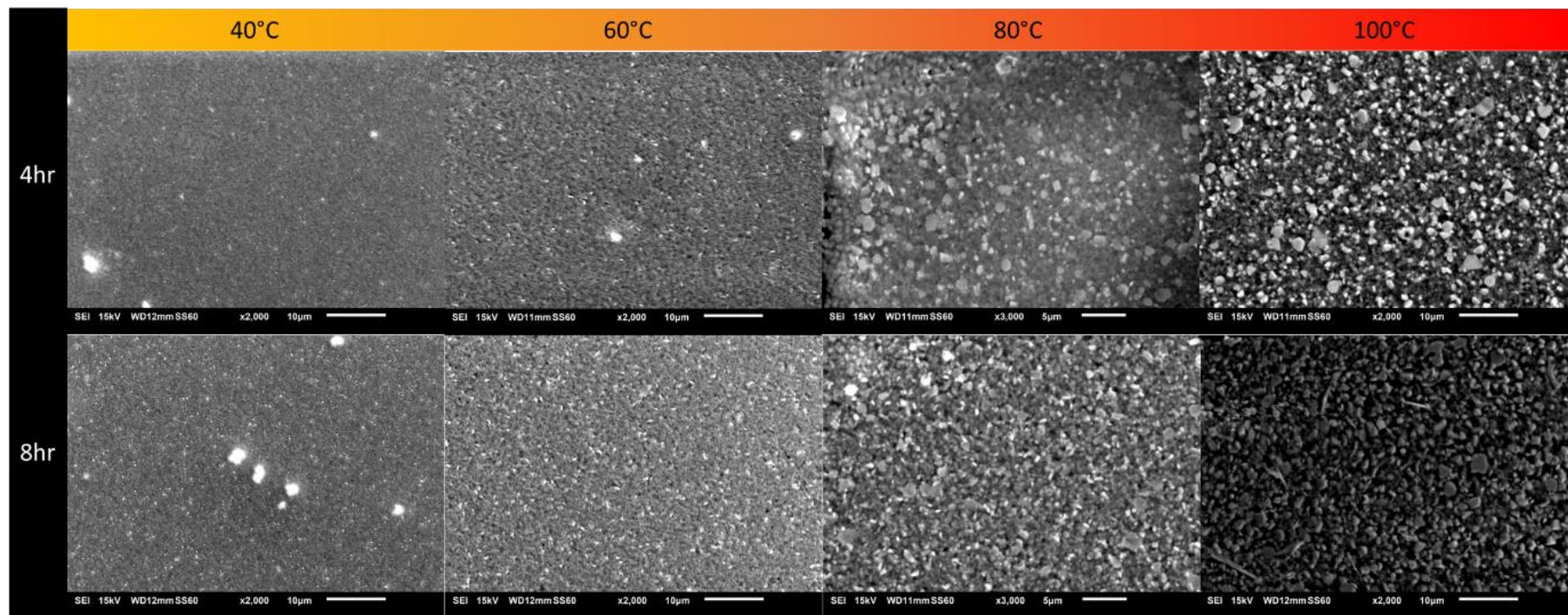
Figure 77: Degradation of MACsPbZn(ICl)$_3$ perovskite films after annealing at different temperatures for 4hrs and 8 hrs.
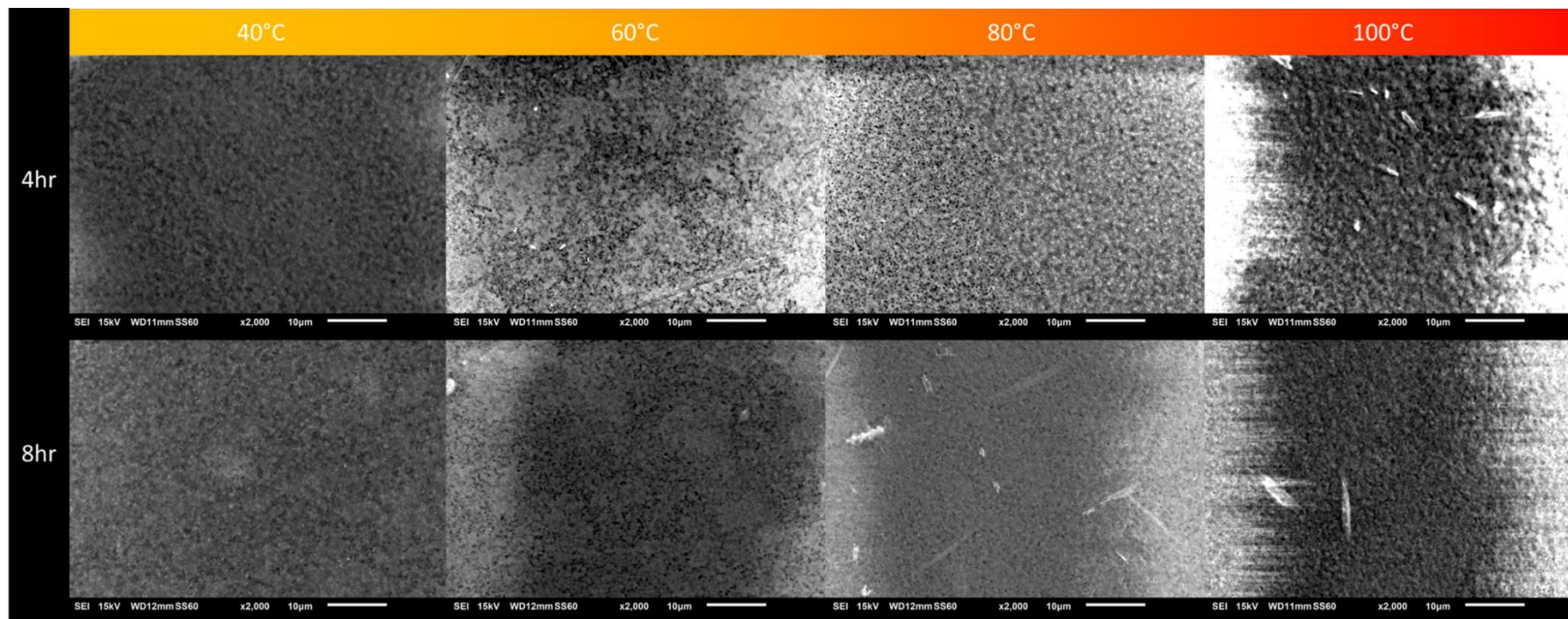
Figure 78: Degradation of MAPbI₃ perovskite films after annealing at different temperatures for 4hrs and 8 hrs.